APPLIED COMPUTATIONAL ELECTROMAGNETICS SOCIETY JOURNAL

January 2017
Vol. 32 No. 1
ISSN 1054-4887

The ACES Journal is abstracted in INSPEC, in Engineering Index, DTIC, Science Citation Index Expanded, the Research Alert, and to Current Contents/Engineering, Computing & Technology.

The illustrations on the front cover have been obtained from the research groups at the Department of Electrical Engineering, The University of Mississippi.

EMERITUS EDITORIAL ASSISTANTS

JANUARY 2017 REVIEWERS

THE APPLIED COMPUTATIONAL ELECTROMAGNETICS SOCIETY

JOURNAL

Vol. 32 No. 1 January 2017

TABLE OF CONTENTS

Mathematical Model for Calibration of Potential Detection of Nonlinear Responses in Biological Media Exposed to RF Energy
Chan H. See, Raed A. Abd-Alhameed, Ahmed F. Mirza, Neil J. McEwan, Peter S. Excell, and Quirino Balzano 1

Time-Domain Electromagnetic Inversion Technique for Biological Tissues by Reconstructing Distributions of Cole-Cole Model Parameters
Guangdong Liu 8

Novel Extraction Method of Inductance Parameter for Nonuniform Transmission Line in Anisotropic Dielectric
Yaxiu Sun and Xiaomeng Wang 15

The Investigation of Substrate's Dielectric Properties for Improving the Performance of Witricity Devices
Mohd H. M. Salleh, Norhudah Seman, and Raimi Dewan 24

Assessment of Kapton-based Flexible Antenna for Near Field Wireless Energy Transfer
Mohamad H. Misran, Sharul K. A. Rahim, Akaa A. Eteng, and Guy A. E. Vandenbosch 31

Determination of Reverse-Current Coil Turns Layout to Mitigate Over-Coupling in Resonant Inductive Power Transfer Links
Akaa A. Eteng, Sharul K. A. Rahim, Chee Y. Leow, Beng W. Chew, and Guy A. E. Vandenbosch 37

A Data Collection Method Based on the Region Division in Opportunistic Networks
Yaqing Ma, Shukui Zhang, Chengkuan Lin, and Lingzhi Li 43

Design of Parabolic Reflector Antenna with Two Directional Cosecant-Squared Pattern Using Curve-Deformation Equations
Ki-Bok Kong 50

Compact Broad Band-Stop Filter with Circular Fractal-Shaped Stubs for X-Band Radar Applications
Mohammad Pourbagher, Javad Nourinia, and Changiz Ghobadi 56

RCS Validation of Asymptotic Techniques Using Measured Data of an Electrically Large Complex Model Airframe
Ciara Pienaar, Johann W. Odendaal, Johan Joubert, Johan C. Smit, and Jacques E. Cilliers 60

A Novel UWB Monopole Antenna with Controllable Band-Notch Characteristics
Nasrin Tasouji, Javad Nourinia, Changiz Ghobadi, and Farnaz Mirzamohammadi 68

A Novel Compact Polarization Diversity Ultra-Wideband MIMO Antenna
Saeid Karamzadeh 74

Dual-Band Wide-Angle Circularly-Polarized Microstrip Antenna by Ferrite Ring Inserted in Its Cavity Domain
Fazel R. Rostami, Gholamreza Moradi, and Reza S. Shirazi 81

Computationally Efficient Technique for Wide-Band Analysis of Grid-Like Spatial Shields for Protection Against LEMP Effects
Andrzej Karwowski, Artur Noga, and Tomasz Topa 87

Shape Reconstruction of Three Dimensional Conducting Objects Using Opposition-Based Differential Evolution
Mojtaba Maddahali, Ahad Tavakoli, and Mojtaba Dehmollaian 93

Mathematical Model for Calibration of Potential Detection of Nonlinear Responses in Biological Media Exposed to RF Energy

C. H. See [1,2], R. A. Abd-Alhameed [2], A. F. Mirza [2], N. J. McEwan [2,3], P. S. Excell [2,3], and Q. Balzano [4]

[1] School of Engineering
University of Bolton, Bolton, BL3 5AB, UK
c.see@bolton.ac.uk

[2] School of Electrical Engineering & Computer Science
University of Bradford, Bradford, BD7 1DP, UK
r.a.a.abd@bradford.ac.uk, A.F.Mirza@student.bradford.ac.uk

[3] Division of Applied Science, Computing and Engineering
Glyndwr University, Wrexham, LL11 2AW, UK
p.excell@glyndwr.ac.uk, n.mcewan@glyndwr.ac.uk

[4] Department of Electronic and Computer Engineering
University of Maryland, College Park, MD, USA
qbalzano@gmail.umd.edu

Abstract ─ An efficient way to test for potential unsymmetrical nonlinear responses in biological tissue samples exposed to a microwave signal is to observe the second harmonic in a cavity resonant at the two frequencies, with collocated antinodes. Such a response would be of interest as being a mechanism that could enable demodulation of information-carrying waveforms. In this work, an electric circuit model is proposed to facilitate calibration of any putative nonlinear RF energy conversion inside a high quality-factor resonant cavity with a known nonlinear loading device. The first and second harmonic responses of the cavity due to loading with the nonlinear and lossy material are also demonstrated. The results from the proposed mathematical model give a good indication of the input power required to detect any very weak second harmonic signal in relation to the sensitivity of the measurement equipment. Hence, this proposed mathematical model will assist in determining the level of the second harmonic signal in the detector as a function of the specific input power applied.

Index Terms ─ Biological responses, nonlinearity, quality factor, resonant cavity, second harmonic.

I. INTRODUCTION

With the explosive growth of mobile communications, large numbers of researchers around the world have studied the interaction mechanisms between electromagnetic fields and biological tissues. The result has been the development of research streams in different aspects of bioelectromagnetic problems at various levels of definition such as tissue level, cell level and ionic level, with intensive effort worldwide [1-17].

However, most of the previous analyses have been performed treating bulk tissue effects as a linear problem. Recently, the tendency of research in this area has moved towards seeking evidence for the existence of nonlinear tissue responses, involving microscopic studies of cellular and molecular processes. Many experiments have been proposed in order to clarify the various nonlinearity hypotheses for biological tissue. Balzano [4-8] has suggested that the detection of the presence of nonlinear interactions can be investigated by exposing living cells to low-amplitude unmodulated RF carriers and observing the possible generation of second harmonics. Such harmonics would be inherent in any unsymmetrically-nonlinear medium; a property essential for demodulation of modulated waveforms. Demodulation has been postulated as a plausible mode for putative non-thermal effects of RF radiation on living organisms.

By implementing a doubly harmonic resonant cavity model, as proposed in [4-8], this paper presents an electric circuit model to verify second harmonic generation from a known nonlinear device and suggests the required level of input power needed to excite the

Submitted On: February 25, 2015
Accepted On: November 19, 2016

bio-preparation in order to maximize the chance of detection of a possible second harmonic signal.

II. METHODOLOGY

The proposed mathematical model is an extension of some earlier work [18]. It consists of two parts: cavity model design and electric circuit model. The cavity model will be first described and S-parameters of the model will be extracted by using CST Microwave Studio software [19]. Once these data are obtained, they will be adopted into the derived equations from the proposed circuit model to calculate the second harmonic power with known input power.

A. Cavity model design

The previously-reported practical work was undertaken with a carrier frequency in the 880-890 MHz band. To investigate whether biological cells exhibit unsymmetrical nonlinearity when exposed to such RF energy, a high quality-factor resonant cylindrical cavity was created, having diameter and height of 248 mm and 272 mm respectively. The cavity was built with two rectangular loop coupling antennas and a support structure for biopreparations, i.e., a butterfly-shaped Lexan lamina and Petri dish, as shown in Fig. 1. As can be seen, the antenna with size 14x105 mm^2 at the bottom of the cavity acts as a transmitter to excite the TE_{111} cavity mode in the 880-890 MHz band; whereas the antenna with size 12.5 x 56.5 mm^2 on the side wall of the cavity was used to detect the energy of the TE_{113} cavity mode in the range 1760-1790 MHz. It should be noted that the lengths of the transmit and receive antennas were fine tuned in order to achieve the TE_{113} mode resonant at exactly double the frequency of the TE_{111} mode.

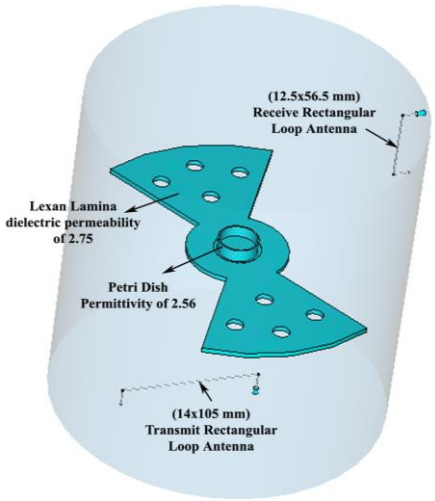

Fig. 1. The dimensions of the cavity modeled, with its Lexan sample support structure and two rectangular loop antennas.

B. Electric circuit model for calibrations

In order to more precisely quantify the amount of input power required in the excitation port to generate a detectable second harmonic signal, a mathematical technique is proposed here to calculate the second harmonic level with known input power.

The procedure of the proposed mathematical model will be demonstrated in the following context. Firstly, the same cavity model used in previous analyses will be implemented. A discrete floating port with metal leads of 1 mm length, resembling a dipole antenna, is placed inside the Petri dish in the cavity and oriented parallel to the transmit antenna, as depicted in Figs. 2 and 3. Then, two simulations will be performed separately at the resonant frequencies of the TE_{111} and TE_{113} modes, in order to extract the 3×3 Z-parameters at both frequencies. This is equivalent to the 3-port network as depicted in Fig. 4. Once the 3×3 Z-parameters are obtained at both frequencies, they will be employed in the proposed mathematical model as depicted in Fig. 5. According to Fig. 5, the input and output ports can be represented as transmit and receive antennas respectively in the cavity, while the nonlinear element is represented as the diode inside the cavity. The equivalent electric circuit of the diode model is illustrated in Fig. 6.

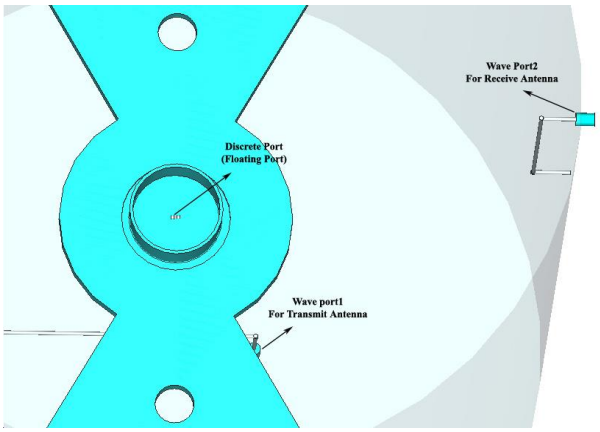

Fig. 2. Proposed cavity model for mathematical analysis.

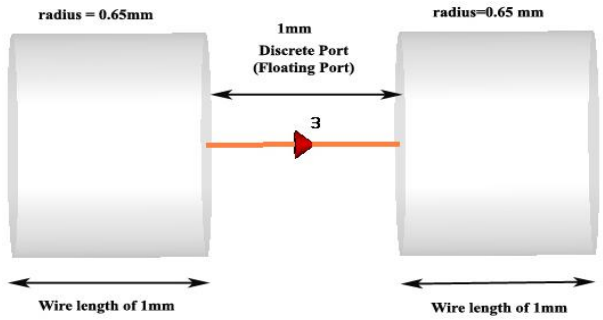

Fig. 3. Discrete port model in the Petri dish of the cavity (enlargement).

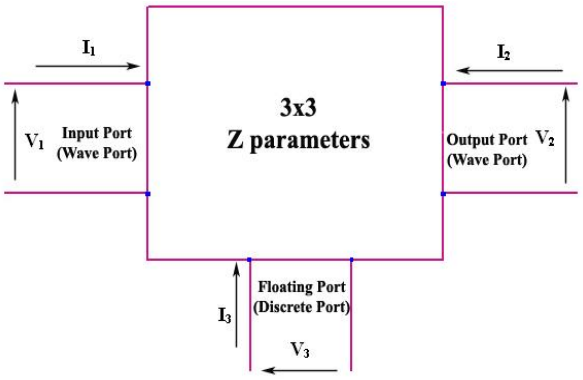

Fig. 4. Simulated model in Microwave Studio [19].

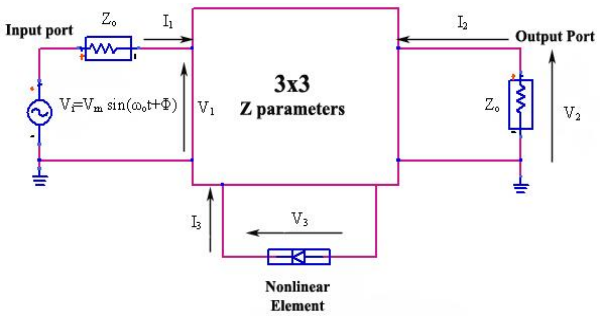

Fig. 5. Proposed mathematical model for TE_{111} mode.

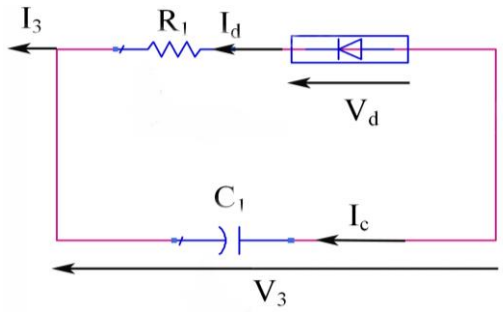

Fig. 6. Electric circuit model of the nonlinear element in Fig. 5.

From Figs. 5 and 6, and by applying Ohm's law, the following equation can be derived:

$$\begin{bmatrix} V_1 \\ V_2 \\ V_3 \end{bmatrix} = \begin{bmatrix} Z_{11} & Z_{12} & Z_{13} \\ Z_{21} & Z_{22} & Z_{23} \\ Z_{31} & Z_{32} & Z_{33} \end{bmatrix}_f \begin{bmatrix} I_1 \\ I_2 \\ I_3 \end{bmatrix}. \quad (1)$$

From the input port in Fig. 5:

$$I_1 = \frac{V_i - V_1}{Z_o}, \quad (2)$$

where V_i is the input voltage to port 1 and Z_o is the characteristic impedance of 50 Ω. From the output port in Fig. 5, I_2 is given by:

$$I_2 = -\frac{V_2}{Z_0}. \quad (3)$$

From the diode model in Figs. 5 and 6:

$$I_3 = I_c + I_d, \quad (4)$$

where I_d is the current across the diode and I_c is the current across the capacitor in the diode model, as seen in Fig. 6.

From Equation (4), I_3 can be further extended to following equation:

$$I_3 = \frac{V_3}{jX_{C1}} + I_d, \quad (5)$$

where:

$$I_d = I_o\left(e^{\frac{e}{KT}(V_d)} - 1\right), \quad (6)$$

where e is the electron charge ($e=1.60217x10^{-19}$ coulombs):
T is the temperature in Kelvin (T=300 K),
I_o is the reverse current ($I_o=1.0x10^{-14}$ A),
k is the Boltzmann Constant ($k=1.38065x10^{-23}$ JK^{-1}),

$$V_3 = V_d + I_d R_1. \quad (7)$$

Substituting the Equations (2 to 7) into (1), the following expression can be obtained:

$$\begin{bmatrix} V_1 \\ V_2 \\ V_d + I_d R_1 \end{bmatrix} = \begin{bmatrix} Z_{11} & Z_{12} & Z_{13} \\ Z_{21} & Z_{22} & Z_{23} \\ Z_{31} & Z_{32} & Z_{33} \end{bmatrix}_{TE_{111}} \begin{bmatrix} \frac{V_i - V_1}{Z_o} \\ -\frac{V_2}{Z_o} \\ \frac{V_d + I_d R_1}{jX_{c1}} + I_d \end{bmatrix}, \quad (8)$$

where $R_1=106.5\ \Omega$ and $C_1=1.5$ fF, obtained from reference [20]. V_i is the input voltage to port 1.

Since e, K, T and I_o are known parameters, Equation (6) can be simplified as follows:

$$I_d = I_o\left(e^{\frac{e}{KT}(V_d)} - 1\right) = 1.0x10^{-14}\left(e^{38.6815(V_d)} - 1\right). \quad (9)$$

By assuming the input voltage and substituting the Z-parameters of TE_{111} into Equation (8), the parameters V_1, V_2 and V_d can be found. Then, the input power of the mathematical model can be computed by $P_{in} = 0.5\mathrm{Re}\left(V_1 \times I_1^*\right)$.

Once V_d is obtained, it can be used as the excitation source to the previous input and output port, hence the electric circuit can be modified as shown in Fig. 7. From this figure, the following set of equations can be established:

$$\begin{bmatrix} V_1 \\ V_2 \\ V_3 \end{bmatrix} = \begin{bmatrix} Z_{11} & Z_{12} & Z_{13} \\ Z_{21} & Z_{22} & Z_{23} \\ Z_{31} & Z_{32} & Z_{33} \end{bmatrix}_{TE_{113}} \begin{bmatrix} \frac{-V_1}{Z_o} \\ -\frac{V_2}{Z_o} \\ \frac{V_3 - V_d}{Z_o} \end{bmatrix}. \quad (10)$$

By substituting V_d from the solution of Equation (8) into Equation (10), V_1, V_2 and V_3 can be computed. Hence, the output power on port 2 can be calculated by $P_{out} = 0.5\,\mathrm{Re}\left(V_2 \times I_2^*\right)$.

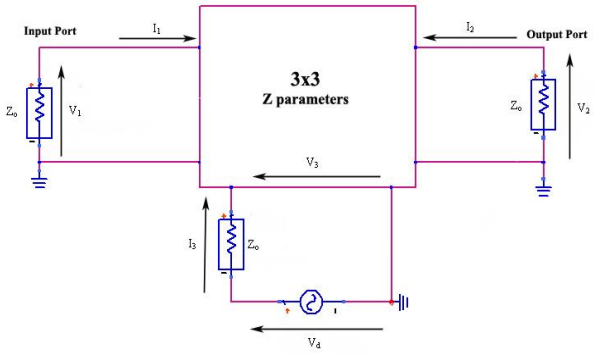

Fig. 7. Proposed mathematical model for TE_{113} mode.

III. SIMULATION AND RESULTS

The bands of operation of the two antennas are shown in Fig. 8. Here the dashed line represents the return loss of the bottom (excitation) antenna at its frequency of operation with an empty 3 cm Petri dish. The frequency has been multiplied by a factor of two to display the second harmonic performance in the same band as the high frequency antenna (receive antenna). The solid line in Fig. 8 illustrates the shift of operating frequency band when a 15μm lamina of lossy water is added to the Petri dish in the cavity, having properties $\varepsilon_r = 78.24$, $\sigma = 0.173$ S/m [2, 13].

Table 1 shows the results obtained from the proposed mathematical model. In order to cross-validate the result, ANSYS HFSS software was adopted for comparison [21]. Figure 9 illustrates the second harmonic power as a function of the input power as the input voltage was increased. As can be clearly seen, both simulation results were in good agreement. Further, it is observed that the relationship between input power and second harmonic output power, applying the Silicon diode model adopted here, is slightly nonlinear. Moreover, the presented results have also compared with the measured results achieved by [8] and it was found that both are agreed well in terms of the level of the second harmonic.

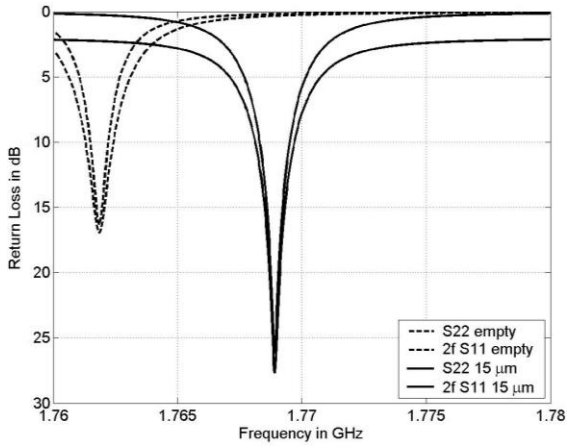

Fig. 8. The fundamental and second harmonic responses of the cavity (fundamental frequency doubled for convenience of display purposes).

Table 1: Input power versus second harmonic power

Input Voltage (Volts)	Input Power (Watts)	Second Harmonic Power (Watts)
1	0.0025	1.1924e-008
2.5	0.0156	7.4573e-008
5	0.0625	2.9818e-007
7.5	0.1405	6.7098e-007
10	0.2499	1.1942e-006
12.5	0.3904	1.8929e-006
15	0.5622	2.5478e-006
17.5	0.7652	3.2223e-006
20	0.9994	3.9630e-006
22.5	1.2649	4.7811e-006
25	1.5616	5.6810e-006
27.5	1.8895	6.6632e-006
30	2.2487	7.7299e-006

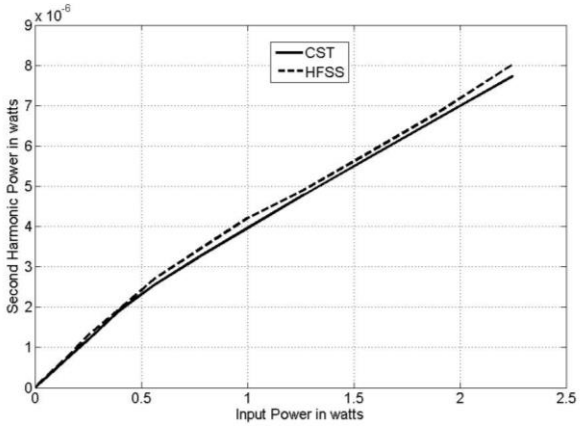

Fig. 9. Input power at Port 1 versus second harmonic power at Port 2.

IV. CONCLUSION

A simulated cylindrical cavity model has been presented, using two rectangular loop antennas for coupling and loaded with a support structure for testing of nonlinear materials. The simulated results show that the tuned TE_{113} mode has double the resonant frequency of the TE_{111} mode. A simple electric circuit model was proposed to calibrate and check the required sensitivity of the detection of the generated second harmonic signal. The nonlinear response of the experiment was tested using a simulated chip diode connected to very short dipole arms. For the diode modelled, a nonlinear relationship was demonstrated between fundamental input power and second harmonic output power. The methodology presented can thus be used to predict such relationships for other nonlinear devices and frequencies applied to the Balzano cavity method or, with some modification, to deduce properties of unknown materials from measured results.

ACKNOWLEDGMENT

The authors would like to acknowledge financial and sponsorship support from the UK Dept. of Health, Mobile Telecommunications & Health Research Programme; in addition to the European Regional Development Fund through Yorkshire Innovation Research and Development Project.

REFERENCES

[1] L. J. Challis, "Review of mechanisms for interaction between RF fields and biological tissue," *Bioelectromagnetics*, pp. S98-S106, 2005.

[2] C. H. See, R. A. Abd-Alhameed, and P. S. Excell, "Computation of electromagnetic fields in assemblages of biological cells using a modified finite difference time domain scheme," *IEEE Transactions on Microwave Theory and Techniques*, vol. 55, no. 9, pp. 1986-1994, Sept. 2007.

[3] A. Ferikoglu, O. Cerezci, M. Kahriman, and S. C. Yener, "Electromagnetic absorption rate in a multilayer human tissue model exposed to base-station radiation using transmission line analysis," *IEEE Antennas and Wireless Propagation Letters*, vol. 13, pp. 903-906, 2014.

[4] Q. Balzano, "Proposed test for detection of nonlinear responses in biological preparations exposed to RF energy," *Bioelectromagnetics*, pp. 278-287, 2002.

[5] Q. Balzano and A. Sheppard, "RF nonlinear interactions in living cells – I: Nonequilibrium thermodynamic theory," *Bioelectromagnetics*, pp. 473-482, 2003.

[6] Q. Balzano, "RF nonlinear interactions in living cells – II: Detection methods for spectral signatures," *Bioelectromagnetics*, pp. 483-488, 2003.

[7] C. Kowalczuk, G. Yarwood, R. Blackwell, M. Priestner, Z. Sienkiewicz, S. Bouffler, I. Ahmed, R. Abd-Alhameed, P. Excell, V. Hodzic, C. Davis, R. Gammon, and Q. Balzano, "Absence of nonlinear responses in cells and tissues exposed to RF energy at mobile phone frequencies using a doubly resonant cavity," *Bioelectromagnetics*, vol. 31, pp. 556-565, 2010.

[8] C. Kowalczuk, G. Yarwood, M. Priestner, R. Blackwell, S. Bouffler, I. Almed, R. Abd-Alhameed, C. See, P. Excell, Q. Balzano, V. Hodzic, R. Gammon, and C. Davis, "Nonlinear and demodulation mechanisms in biological tissue (biological systems)," *Final Report* submitted to Department of Health on 2009. Available: http://www.mthr.org.uk/research_projects/documents/RUM22bFinalReport.pdf

[9] S. Pisa and E. Piuzzi, "Interaction between 3-T MRI systems and patients with an implanted pacemaker," *ACES Journal*, vol. 30, no. 7, pp. 706-716, July 2015.

[10] M. R. I. Faruque, M. T. Islam, and N. Misran, "Evaluation of EM absorption in human head with metamaterial attachment," *ACES Journal*, vol. 25, no. 12, pp. 1097-1107, Dec. 2010.

[11] M. Eleiwa and A. Z. Elsherbeni, "Debye constants for biological tissues from 30 Hz to 20 GHz," *ACES Journal*, vol. 16, no. 3, pp. 202-213, Nov. 2001.

[12] K. Ramli, R. A. Abd-Alhameed, C. H. See, P. S. Excell, and J. M. Noras, "Hybrid computational scheme for antenna-human body interaction," *Progress In Electromagnetics Research (PIER)*, vol. 133, pp. 117-136, 2013.

[13] C. H. See, R. A. Abd-Alhameed, P. S. Excell, and D. Zhou, "Microscopic biological cell level model using modified finite-difference time-domain at mobile radio frequencies," *PIERS Online*, ISSN 1931-7360, vol. 4, no. 1, pp. 6-10, Jan. 2008.

[14] M. O. Goni, "Electric field distribution in a biological cell for various electrode configurations-A simulation study," *ACES Journal*, vol. 27, no. 5, pp. 449-457, May 2012.

[15] C. H. See, R. A. Abd-Alhameed, S. W. J. Chung, D. Zhou, H. Al-Ahmad, and P. S. Excell, "The design of a resistively loaded bowtie antenna for applications in breast cancer detection systems," *IEEE Trans. Antennas and Propagation*, vol. 60, no. 5, pp. 2526-2530, May 2012.

[16] H. Acikgoz, "Internal homogenization of biological tissues for electromagnetic dosimetry," *ACES Journal*, vol. 31, no. 6, pp. 706-711, June 2016.

[17] M. Cvetkovic, S. Lallechere, K. El Khamlichi Drissi, P. Bonnet, and D. Poljak, "Stochastic sensitivity in homogeneous electromagnetic-thermal dosimetry model of human brain," *ACES Journal*, vol. 31, no. 6, pp. 644-652, June 2016.

[18] C. H. See, R. A. Abd-Alhameed, and P. S. Excell, "Mathematical model for calibration of nonlinear responses in biological media exposed to RF energy," *IET Computational in Electromagnetics (CEM)*, March 31-April 1, 2014, Imperial College London, pp. 1-2, 2014.
[19] CST Microwave Studio software, Germany.
[20] Z. Hu, V. T. Ho, A. A. Ali, and A. Rezazadeh, "High tangential signal sensitivity GaAs planar doped barrier diodes for microwave/millimeter-wave power detector applications," *IEEE Microwave and Wireless Components Letters*, vol. 15, no. 3, pp. 150-152, Mar. 2005.
[21] ANSYS HFSS software, ANSYS Inc., Canonsburg, PA, USA.

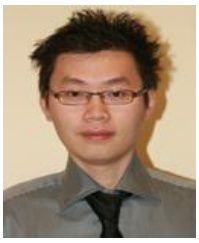

Chan See received a first class B.Eng. Honours degree in Electronic, Telecommunication and Computer Engineering and a Ph.D. degree from the University of Bradford, UK in 2002 and 2007 respectively. He is a Senior Lecturer (Programme Leader) in Electrical & Electronic Engineering, School of Engineering, University of Bolton, UK. Previously, he was a Senior Research Fellow in the Antennas and Applied Electromagnetics Research Group within the University of Bradford. He has published over 150 peer-reviewed journal articles and conference papers. He is a co-author for one book and three book chapters. He was a recipient of two Young Scientist Awards from the International Union of Radio Science (URSI) and Asia-Pacific Radio Science Conference (AP-RASC) in 2008 and 2010 respectively. See is a Chartered Engineer, Member of the Institution of Engineering and Technology (MIET) and Senior Member of the Institute of Electronics and Electrical Engineers (SMIEEE). He is also a Fellow of The Higher Education Academy (FHEA).

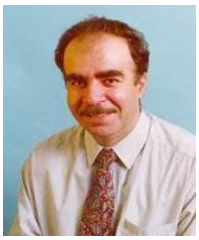

Raed Abd-Alhameed is Professor of Electromagnetic and Radio Frequency Engineering at the University of Bradford, UK. He has many years' research experience in the areas of Radio Frequency, Signal Processing, Propagation, Antennas and Computational Electromagnetics techniques, and has published over 500 academic journal and conference papers; in addition he is co-author of three books and several book chapters. At the present he is the Leader of the Radio Frequency, Propagation, Sensor Design and Signal Processing Group, in addition to leading the Communications Research Group for several years within the School of Engineering and Informatics, Bradford University, UK. He is Principal Investigator for several funded applications to EPSRCs (UK) and leader of several successful knowledge Transfer Programmes such as with Pace PLC, YW PLC, ITEG Ltd, Seven Technologies Group Ltd, Emkay Ltd, and Two World Ltd; including to several funded projects from EU Programmes such as H2020. He is a Fellow of the Institution of Engineering and Technology, Fellow of the Higher Education Academy and a Chartered Engineer.

Ahmed Faraz Mirza was born in Jhelum, Pakistan in 1987. He received his B.Sc. degree in Electrical Engineering from University of Engineering & Technology Lahore Pakistan in 2010, he was awarded M.Sc. degree in Electrical & Electronics Engineering from University of Bradford in 2012. He worked for 2 years as a Field Engineer in a Scotland based packaging company. Currently he is a Ph.D. student and employed as a Casual Research Fellow at the University of Bradford. His research interests include Electromagnetics and Microwave propagation.

Neil McEwan has the degrees of MA in Mathematics from Cambridge University, UK, and Ph.D. in Radio Astronomy from Manchester University, UK. He was formerly Reader in Electromagnetics at the University of Bradford, UK where he worked on aspects of microwave propagation and antennas. McEwan has also worked on quasi-optical antennas as a Visiting Research Scientist at Millitech Corporation, Massachusetts and on mobile base station and handset antennas as a Principal Engineer with Filtronic PLC in Shipley, UK. Presently he is an RF Design Engineer with Saras Technology Ltd, Leeds, UK, and is also part-time Professor of Electromagnetics at Glyndwr University, Wrexham, Wales, UK. McEwan is a Chartered Engineer and Fellow of the Institution of Engineering and Technology (FIET).

Peter Excell joined Glyndwr University in 2007, where he is now Deputy Vice-Chancellor. He was previously Associate Dean for Research in the School of Informatics at the University of Bradford, UK, where he had worked since 1971. His long-standing research interests have been in the applications and computation of high-frequency electromagnetic fields. These have led to numerous research grants,

contracts and patents in the areas of antennas, electromagnetic hazards, electromagnetic compatibility and field computation. His current work includes studies of advanced methods for electromagnetic field computation, the effect of electromagnetic fields on biological cells, advanced antenna designs for mobile communications, and consideration of usage scenarios for future mobile communications devices. He is a Fellow of the IET, the British Computer Society and the Higher Education Academy, a Chartered Engineer and Chartered IT Professional, a Senior Member of the Institute of Electronics and Electrical Engineers and a member of the Applied Computational Electromagnetics Society.

Quirino Balzano was born in Rome, Italy, in December 1940. In 1965, he received the Laurea of Doctor in Electronics Engineering from the University of Rome, La Sapienza, Rome, Italy. During 1966, he was at FIAT, SpA, Turin, Italy. From 1967 to 1974, he was with the Missile Systems Division, Raytheon Corporation, Bedford, MA. He was involved in the research and development of planar and conformal phased arrays for the Patriot and other weapon systems. In 1974, he joined Motorola, Inc., Plantation, FL. In 1987 he became Vice President of the technical staff and in 1993 Corporate Vice President and Director of the Florida Research Laboratories. He retired from Motorola in February, 2001. Since August, 2002 Balzano has been at the University of Maryland, Electrical and Computer Engineering Dept., College Park, Maryland, where he is a Senior Staff Researcher and teaches a graduate course on antennas. His main interests are in the biological effects of human exposure to RF electromagnetic energy and the safe use of wireless technology.

He received the IEEE Vehicular Technology Society Paper Prize Award in 1978 and 1982 and a certificate of merit from the Radiological Society of North America in 1981 for the Treatment of Tumors with RF energy. In 1995 he received the Best Paper of the Year Award from the IEEE EMC Society. He is a Life Fellow of IEEE and former (2002-2005) Chair of Commission A of the International Union of Radio Science. He has written more than 50 papers on RF dosimetry near electromagnetic sources and the biological effects of RF energy. He has 31 patents in antenna and IC technology and has authored or co-authored more than 100 publications.

Time-Domain Electromagnetic Inversion Technique for Biological Tissues by Reconstructing Distributions of Cole-Cole Model Parameters

Guangdong Liu

School of Physics and Electronic Engineering
Fuyang Normal University, Fuyang, 236037, China
liu_guang_dong@126.com

Abstract ─ The Cole-Cole (C-C) models have been frequently used for a precise description of the dispersion characteristics of biological tissues. One of the main difficulties in the direct reconstruction of these dielectric properties from time-domain measurements is their frequency dependence. In order to overcome this difficulty, an electromagnetic (EM) inversion technique in the time domain is proposed, in which four kinds of frequency-independence model parameters, the optical relative permittivity, the static conductivity, the relative permittivity difference, and the relaxation time, can be determined simultaneously. It formulates the inversion problem as a regularized minimization problem, whose forward and backward subproblems could be solved iteratively by the finite-difference time-domain (FDTD) method and any conjugate gradient algorithm, respectively. Numerical results on two types of stratified C-C slabs, with smooth and discontinuous parameter profiles, respectively, confirm the performance of the inversion methodology.

Index Terms ─ Biological tissues, conjugate gradient methods, electromagnetic scattering by dispersive media, electromagnetic scattering inverse problems, finite-difference time-domain (FDTD) methods, regulators.

I. INTRODUCTION

The electromagnetic (EM) inverse scattering problems, which aim to estimate the EM properties from the measurements outside the object of interest, have attracted increasing attention recently, due to their extensive application fields, and some promising results [1-3]. Nevertheless, in general, there are two major difficulties for these problems: one difficulty is their nonlinearity, and the other is the non-uniqueness of their solution [4].

Methodologically, the EM scattering inverse problem may be solved in the frequency domain [5] or the time domain [6]. By contrast, the time-domain reconstructed results are better than those by applying any single-frequency technique in the amount of information and the resolution of images [1, 6, 7]. Currently, several inversion approaches in the time domain for nondispersive media have been developed, such as the forward-backward time-stepping (FBTS) method [8] and the Lagrange multipliers technique [9]. However, in the real world, the wideband dielectric properties of biological tissues are dispersive, which have been widely described by the Debye or Cole-Cole (C-C) models, but the precision of the former is not better than that of the latter [10]. One basic difficulty in the time-domain reconstruction of the electrical characteristics is their frequency correlation. To date, a few time-domain inversion methods for Debye media have been proposed [6, 11]. Unfortunately, for C-C frequency-dependent media, the existing methods are not suitable, and few inverse methods are available directly.

Recently, several finite-difference time-domain (FDTD) forward solvers suitable for C-C media have been presented [12, 13], which have laid the groundwork for the research of inverse solvers for this class of media. There are two novelties in this paper. One novelty is to present a new inverse EM scattering technique, which is to reconstruct the C-C model parameters by means of measurements in the time domain directly. And the other innovation is to introduce a regularization scheme to cope with the ill-posedness of the inverse problem, which was not used in references [1, 6, 11].

II. INVERSE SCATTERING TECHNIQUE IN THE TIME DOMAIN

A. Problem formulation

Suppose that a problem space V, occupied by some biological tissues, is surrounded by a region D, filled with a known background medium. Also, it is assumed that all the media are linear, isotropic, and nonmagnetic, and that the complex-valued relative permittivity, ε_r^*, of the media within V is modeled by the single pole C-C electrical dispersion equation as [10]:

$$\varepsilon_r^*(\omega)=\varepsilon_\infty - \mathrm{j}\sigma_s/(\omega\varepsilon_0)+\Delta\varepsilon/\left[1+(\mathrm{j}\omega\tau)^\alpha\right], \quad (1)$$

where $\Delta\varepsilon = \varepsilon_s - \varepsilon_\infty$, ε_s and ε_∞ are the static and optical relative permittivity, respectively, σ_s is the static

Submitted On: June 10, 2016
Accepted On: October 31, 2016

conductivity, τ and α ($0 \le \alpha \le 1$) denote the relaxation time and the dispersion breadth, respectively, $\mathrm{j}^2 = -1$, ε_0 is the dielectric constant of free space, and ω represents the angular frequency.

For simplicity, we assume that α is *a priori* known (it is appropriate for most biological tissues since they are not distinctly different in a wide frequency range [10]).

Our objective is therefore to determine four kinds of unknowns, (ε_∞, σ_s, $\Delta\varepsilon$, and τ), for every position within V. These C-C model parameters can be explicitly shown in the following field equations when activating the i^{th} incidence for the time interval [0, T]:

$$\nabla\times\mathbf{E}_i + \mu_0\partial_t\mathbf{H}_i = \mathbf{0}, \tag{2}$$

$$\nabla\times\mathbf{H}_i - \varepsilon_0\varepsilon_\infty\partial_t\mathbf{E}_i - \sigma_\mathrm{s}\mathbf{E}_i - \mathbf{J}_i - \mathbf{J}_i^\mathrm{s} = \mathbf{0}, \tag{3}$$

and a fractional auxiliary differential equation (ADE) [13]:

$$\mathbf{J}_i + \tau^\alpha \mathrm{D}_t^\alpha \mathbf{J}_i - \varepsilon_0\Delta\varepsilon\partial_t\mathbf{E}_i = \mathbf{0}, \tag{4}$$

where μ_0 is the free-space permeability, $\mathbf{E}_i$, $\mathbf{H}_i$, and $\mathbf{J}_i$ are the electric field intensity, magnetic field intensity, and dispersion current, respectively, $\mathbf{J}_i^\mathrm{s}$ is the current density, ∇ is the Hamilton operator, and ∂_t and D_t^α denote 1st-order and α^{th}-order temporal partial differential operators with respect to time variable, t, respectively.

B. Constrained minimization problem

In order to cope with the nonlinearity of the aforementioned inverse problem, we formulate it as a constrained minimization problem:

$$\begin{cases} \mathbf{p} = \arg\min_{\mathbf{p}}\left[F(\mathbf{p})\right], \\ \quad \text{s.t. } (2)-(4), \end{cases} \tag{5}$$

where the estimated parameters $\mathbf{p} = [\varepsilon_\infty, \sigma_\mathrm{s}, \Delta\varepsilon, \tau]^\mathrm{T}$, and the cost functional F is given by:

$$F = \frac{1}{2}\sum_{i=1}^{I}\sum_{j=1}^{J}\int_0^T \left\|\mathbf{E}_{ij}(\mathbf{p}) - \mathbf{E}_{ij}^{\mathrm{mea}}\right\|_2^2 \mathrm{d}t + \frac{1}{2}\sum_{m=1}^{4}\int_V \gamma_m \left\|\nabla p_m\right\|_2^2 \mathrm{d}v. \tag{6}$$

In the right hand side of (6), the first term formulates inversion error, in which $\mathbf{E}_{ij}$ and $\mathbf{E}_{ij}^{\mathrm{mea}}$ represent the calculated and measured electric fields at the j^{th} receiving position due to the i^{th} incident wave, respectively, and I and J denote the total number of transmitters and receivers, respectively. While the second term, which is not contained in references [1, 6, 11], is incorporated to regularize the ill-posedness of the inverse problem, in which γ_m (m = 1, 2, 3, 4) are four positive Tikhonov regularization factors.

C. Unconstrained minimization problem

Based on the method of the Lagrange penalty function, the above constrained minimization problem is turned into an unconstrained minimization one, whose augmented cost functional F^a is represented as:

$$\begin{aligned} F^\mathrm{a} = \sum_{i=1}^{I}\int_0^T\int_V \Big[& \mathbf{e}_i\cdot\left(\nabla\times\mathbf{H}_i - \varepsilon_0\varepsilon_\infty\partial_t\mathbf{E}_i - \sigma_\mathrm{s}\mathbf{E}_i - \mathbf{J}_i - \mathbf{J}_i^\mathrm{s}\right) \\ & + \mathbf{h}_i\cdot\left(\nabla\times\mathbf{E}_i + \mu_0\partial_t\mathbf{H}_i\right) \\ & + \mathbf{q}_i\cdot\left(\mathbf{J}_i + \tau^\alpha\mathrm{D}_t^\alpha\mathbf{J}_i - \varepsilon_0\Delta\varepsilon\partial_t\mathbf{E}_i\right)\Big]\mathrm{d}v\mathrm{d}t + F, \end{aligned} \tag{7}$$

where $\mathbf{e}_i$, $\mathbf{h}_i$, and $\mathbf{q}_i$ are the Lagrange vector multipliers.

D. Fréchet derivatives

Solving (7) by the variational method [14], we have $\delta F^\mathrm{a} = 0$, where δ denotes the first-order variation operator. After some calculus of variations similar to [1, 6, 11], it can be derived that the fields $\mathbf{e}_i$, $\mathbf{h}_i$, and $\mathbf{j}_i$ ($\mathbf{j}_i =: -\varepsilon_0\Delta\varepsilon\partial_t\mathbf{q}_i$) must satisfy the following equations for the time interval [T, 0]:

$$\nabla\times\mathbf{e}_i - \mu_0\partial_t\mathbf{h}_i = \mathbf{0}, \tag{8}$$

$$\nabla\times\mathbf{h}_i + \varepsilon_0\varepsilon_\infty\partial_t\mathbf{e}_i - \sigma_\mathrm{s}\mathbf{e}_i - \mathbf{j}_i + \sum_{j=1}^{J}\left(\mathbf{E}_{ij} - \mathbf{E}_{ij}^{\mathrm{mea}}\right) = \mathbf{0}, \tag{9}$$

$$\mathbf{j}_i - \tau^\alpha\mathrm{D}_t^\alpha\mathbf{j}_i + \varepsilon_0\Delta\varepsilon\partial_t\mathbf{e}_i = \mathbf{0}, \tag{10}$$

and that the Fréchet derivatives (gradients) of F^a with respect to p_m are denoted as:

$$g_{\varepsilon_\infty} =: \delta F^\mathrm{a}/\delta\varepsilon_\infty = -\varepsilon_0\sum_{i=1}^{I}\int_0^T\left(\mathbf{e}_i\cdot\partial_t\mathbf{E}_i\right)\mathrm{d}t - \gamma_1\nabla^2\varepsilon_\infty, \tag{11}$$

$$g_{\sigma_\mathrm{s}} =: \delta F^\mathrm{a}/\delta\sigma_\mathrm{s} = -\sum_{i=1}^{I}\int_0^T\left(\mathbf{e}_i\cdot\mathbf{E}_i\right)\mathrm{d}t - \gamma_2\nabla^2\sigma_\mathrm{s}, \tag{12}$$

$$g_{\Delta\varepsilon} =: \delta F^\mathrm{a}/\delta\Delta\varepsilon = -\left[\sum_{i=1}^{I}\int_0^T\left(\mathbf{j}_i\cdot\mathbf{E}_i\right)\mathrm{d}t\Big/\Delta\varepsilon\right] - \gamma_3\nabla^2\Delta\varepsilon, \tag{13}$$

$$g_\tau =: \frac{\delta F^\mathrm{a}}{\delta\tau} = \left[\alpha\tau^{\alpha-1}\sum_{i=1}^{I}\int_0^T\left(\mathrm{D}_t^{1-\alpha}\mathbf{j}_i\cdot\mathbf{J}_i\right)\mathrm{d}t\Big/\left(\varepsilon_0\Delta\varepsilon\right)\right] - \gamma_4\nabla^2\tau, \tag{14}$$

where $\mathrm{D}_t^{1-\alpha}$ indicates a fractional differential operator, whose numerical treatment could be found in [15], the direct fields ($\mathbf{E}_i$, $\mathbf{H}_i$, and $\mathbf{J}_i$) and the adjoint fields ($\mathbf{e}_i$, $\mathbf{h}_i$, and $\mathbf{j}_i$) can be calculated by using the FDTD method based on approximation of the Grünwald-Letnikov fractional derivative, from (2)–(4) and (8)–(10), respectively [13].

E. Inversion algorithm

In this work, we select the Polak-Ribière-Polyak conjugate gradient algorithm [16] to solve the derived problem. Let the discretized forms of the C-C model parameters and gradients be represented by:

$$\mathbf{x} = \left[\varepsilon_\infty^1,\ldots,\varepsilon_\infty^N,\sigma_\mathrm{s}^1,\ldots,\sigma_\mathrm{s}^N,\Delta\varepsilon^1,\ldots,\Delta\varepsilon^N,\tau^1,\ldots,\tau^N\right]^\mathrm{T}, \tag{15}$$

and

$$\mathbf{g}=\Big[\, g_{\varepsilon_\infty^1},\ldots,g_{\varepsilon_\infty^N},g_{\sigma_s^1},\ldots,g_{\sigma_s^N},\; g_{\Delta\varepsilon^1},\ldots,g_{\Delta\varepsilon^N},g_{\tau^1},\ldots,g_{\tau^N}\,\Big]^{\mathrm{T}}, \tag{16}$$

respectively. Given that the estimated value of $\mathbf{x}$ at the k^{th} iteration, $\mathbf{x}_k$, is achieved, the next estimated $\mathbf{x}_{k+1}$ is updated by:

$$\mathbf{x}_{k+1}=\mathbf{x}_k+\lambda_k\mathbf{d}_k, \tag{17}$$

where λ_k is the step size, and the direction $\mathbf{d}_k$ is given by [16]:

$$\mathbf{d}_k=\begin{cases}-\mathbf{g}_k, & (k=1),\\ -\mathbf{g}_k+\dfrac{\mathbf{g}_k^{\mathrm{T}}\cdot(\mathbf{g}_k-\mathbf{g}_{k-1})}{\mathbf{g}_{k-1}^{\mathrm{T}}\cdot\mathbf{g}_{k-1}}\mathbf{d}_{k-1}, & (k\ge 2),\end{cases} \tag{18}$$

where $\mathbf{g}_k$ denotes the estimated value of $\mathbf{g}$ at the k^{th} iteration.

At the k^{th} iteration, the relative mean square error e between the true parameters $\mathbf{x}$ and estimated ones $\mathbf{x}_k$ is defined as:

$$e(k)=:\|\mathbf{x}-\mathbf{x}_k\|_2/\|\mathbf{x}\|_2. \tag{19}$$

The above inverse problem is solved iteratively until a predetermined error threshold e_{th} is reached or a predefined iteration number k_{pre} is finished. The basic steps of the inversion algorithm are illustrated in Fig. 1.

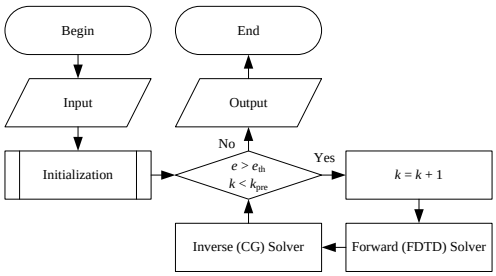

Fig. 1. Basic flow-chart of the proposed inversion technology.

III. NUMERICAL RESULTS AND DISCUSSION

In this section, two simple one-dimensional (1-D) numerical examples, similar to [1, 6], are provided to examine the performance of the newly-elaborated approach. The geometry of the examples is shown in Fig. 2, in which either side of a 4*d*-width objective region is surrounded by a known background medium (air) where d = 10 mm, and all their electrical properties depend only on z coordinate, where the positive direction of z axis is from left to right, and z = 0 is on the left plane of the left background medium.

The objective region consists of layered C-C medium with a parameter of α = 0.8. In the background medium, a bistatic detection system is applied where two transmitters (I = 2), denoted by T, are symmetrically placed at distance equal to d/2 from both sides of the objective region, while two receivers (J = 2), denoted by R, are placed at symmetrical distance equal to d/4 from both sides of the objective region. An ultra-wideband pulse of the excitation source for transmitters is selected the same as [12]:

$$s(t)=\sin\left(2\pi f_c\left(t-4/a\right)\right)\exp\left(-a^2\left(t-4/a\right)^2\right), \tag{20}$$

where $a = 1.26\times10^{10}$, and central frequency f_c = 3 GHz.

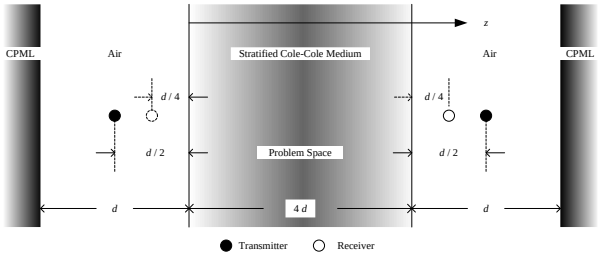

Fig. 2. Geometry model of 1-D problem.

The FDTD method is applied to compute the direct and adjoint fields [13]. The FDTD solution space, which is bounded by the five-cell convolution perfectly matched layer (CPML) [17], consists of 120 homogeneous cells with spatial size Δz = 0.5 mm and time step $\Delta t = 0.5\Delta z/c_0$, where c_0 is the speed of light in free space. Therefore, the total number of unknowns is 320. In this work, the necessary measurement data came from the similar FDTD simulation with $T = 1500\Delta t$, but its cell size is twice finer than the one used in the inverse solver to avoid the "inverse crime".

Besides, it is assumed that the location and width of the reconstruction region are *a priori* known, that a set of values (6.0, 0.5 S·m^{-1}, 20.0, and 7.0 ps), which are the average values of the C-C model parameters (ε_∞, σ_s, $\Delta\varepsilon$, and τ) within the objective region, is selected as an initial guess of the inversion algorithm, and that the specific stopping condition for the iterative algorithm is that reconstruction errors are not declining or k_{pre} = 30.

In the first example, the spatial distribution profiles of the four parameters within the entire objective region are smooth (sinusoidal or cosinusoidal), whose (peaks, valleys) for ε_∞, σ_s, $\Delta\varepsilon$, and τ are (10.0, 2.0), (0.9 S·m^{-1}, 0.1 S·m^{-1}), (30.0, 10.0), and (8.0 ps, 6.0 ps), respectively.

Firstly, the regularization term is not applied in the noiseless case (i.e. ,set γ_m= 0 with m = 1, 2, 3, 4). After 30 iterations, the estimated optical relative permittivity, static conductivity, relative permittivity difference, and relaxation time are obtained as shown in subfigures (a)–(d) of Fig. 3. In these subfigures, the solid black lines, small red dots, and small blue circles depict the true distributions, start values, and end values, respectively (similarly for the later cases).

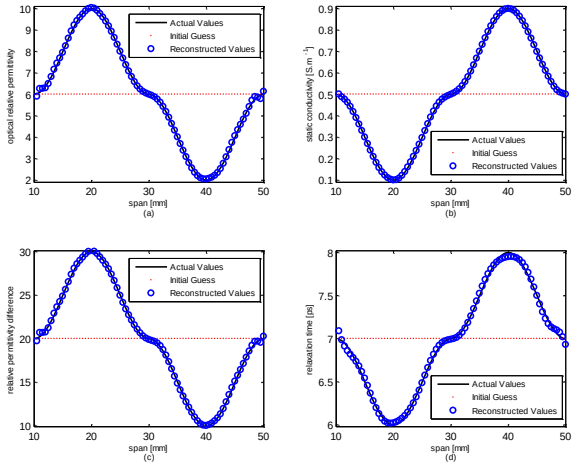

Fig. 3. The reconstructed distributions of: (a) optical relative permittivity, (b) static conductivity, (c) relative permittivity difference, and (d) relaxation time for a stratified Cole-Cole slab with smooth model parameter profiles, using noiseless data without regularization, at the 30th iteration. For comparison purpose, its corresponding original distributions with smooth profiles, and homogeneous initial guess are given, too (similarly for later cases).

As can be seen in Fig. 3, the proposed method for the non-regularized 1-D problem is convergent when noise is not considered, and that all the model parameters of the C-C dispersive media are reconstructed precisely.

Secondly, it is assumed that the measured fields are corrupted by the additive white Gaussian noise (AWGN) with a signal-to-noise ratio (SNR) of 20 dB. The same procedures as the previous case are repeated, where no regularization scheme is adopted yet. Numerical experiments show that the reconstruction errors are not decreased just after 14 iterations. The estimated optical relative permittivity, static conductivity, relative permittivity difference, and relaxation time are obtained as illustrated in subfigures (a)–(d) of Fig. 4 at the 14th iteration, where the estimated relative mean square error is about 0.25.

From Fig. 4, it is obvious that all the estimated distributions are poor, especially for the optical relative permittivity and relaxation time.

Finally, suppose that the simulated measurement field data are corrupted by the AWGN with a SNR of 20 dB, too. To test the performance of the regularized inversion algorithm, four of regularization factors (γ_1, γ_2, γ_3, and γ_4) are chosen to be (0.01, 0.001, 0.01, and 0.0001), respectively. It is noteworthy that these factors could be not optimal. The estimated optical relative permittivity, static conductivity, relative permittivity difference, and relaxation time are obtained as given in subfigures (a)–(d) of Fig. 5 at 30th iteration.

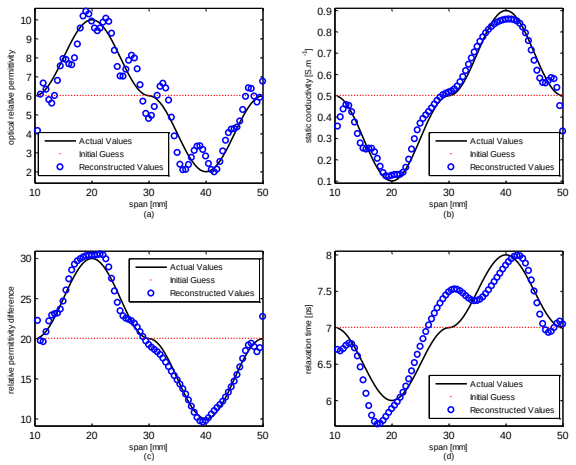

Fig. 4. The reconstructed distributions of: (a) optical relative permittivity, (b) static conductivity, (c) relative permittivity difference, and (d) relaxation time for a stratified Cole-Cole slab with smooth model parameter profiles, applying noisy data (SNR = 20 dB) without regularization, at the 14th iteration.

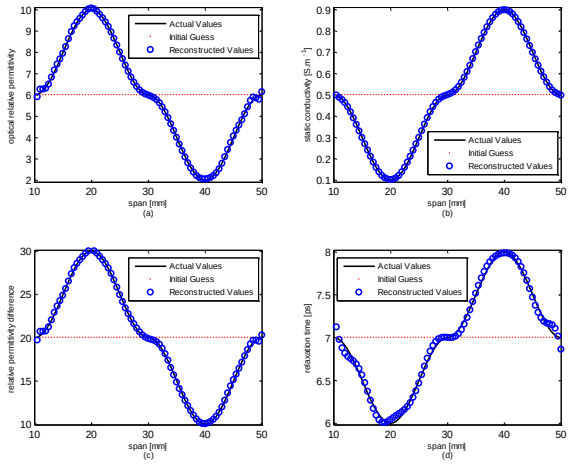

Fig. 5. The reconstructed distributions of: (a) optical relative permittivity, (b) static conductivity, (c) relative permittivity difference, and (d) relaxation time for a stratified Cole-Cole slab with smooth model parameter profiles, using noisy data (SNR = 20 dB) with regularization, at the 30th iteration.

Figure 5 shows that the recreated model parameters of the C-C dispersive media are satisfactory, even based on the noise-contaminated data with a SNR of 20 dB, which could benefit from the additional regularization terms.

In addition, the relative mean square errors versus the number of iterations, for the first and last cases, are presented in Fig. 6, where the final values of the errors are approximately 0.052 and 0.057, respectively.

Figure 6 indicates clearly that the proposed method is convergent, and the relative mean square errors are decreased with the increase of the number of iterations in two cases, and that the final error in the last case is slightly larger than that in the first case.

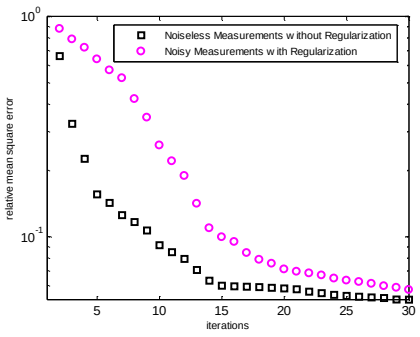

Fig. 6. In the iterative inversion methodology, relative mean square errors versus the number of iterations.

The second example is to reconstruct an inhomogeneous C-C slab with discontinuous (step-shaped) model parameter profiles, consisting of six layers. The width of the second and fifth layers is all 10 mm, and that of other layers is all 5 mm. The parameters (ε_∞, σ_s, $\Delta\varepsilon$, and τ) of the first and third layers are all (8.0, 0.3 S·m^{-1}, 25.0, and 6.5 ps), those of the second layer are (10.0, 0.9 S·m^{-1}, 30.0, and 6.0 ps), those of the fourth and sixth layers are all (4.0, 0.7 S·m^{-1}, 15.0, and 7.5 ps), and those of the fifth layer are (2.0, 0.9 S·m^{-1}, 10.0, and 8.0 ps).

After 30 iterations of the algorithm with regularization (regularization factors are the same as the first example) based on a noisy scenario (SNR is the same as the first example, too), the estimated optical relative permittivity, static conductivity, relative permittivity difference, and relaxation time are obtained as shown in subfigures (a)–(d) of Fig. 7. The error at the 30th iteration is about 0.16.

Figure 7 shows that even when the distributions of the C-C model parameters for a slab are discontinuous and the simulated measurements are added a noise with a SNR of 20 dB, the inversion algorithm is still convergent, and the reconstructed results are acceptable. Note that the final error in the discontinuous case is noticeably larger than that in the smooth one.

Theoretically, the initial guess applied in the inversion algorithm could be also important to its imaging performance. For this reason, the inversion algorithm is applied to the third case of the first example, the only difference is that the initial guess is replaced with the C-C model parameters of the known background medium (air), (1.0, 0.0 S·m^{-1}, 0.0, and 8.0 ps). The reconstructed optical relative permittivity, static conductivity, relative permittivity difference, and relaxation time are presented in subfigures (a)–(d) of Fig. 8. The error at the 30th iteration is approximately 0.063.

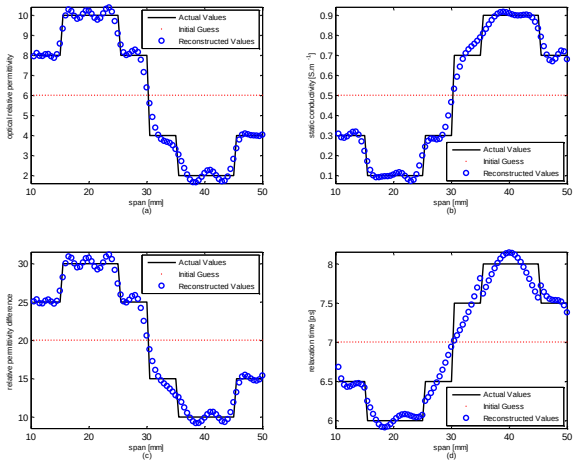

Fig. 7. The reconstructed distributions of: (a) optical relative permittivity, (b) static conductivity, (c) relative permittivity difference, and (d) relaxation time for a stratified Cole-Cole slab with discontinuous model parameter profiles, using noisy data (SNR = 20 dB) with regularization, at the 30th iteration.

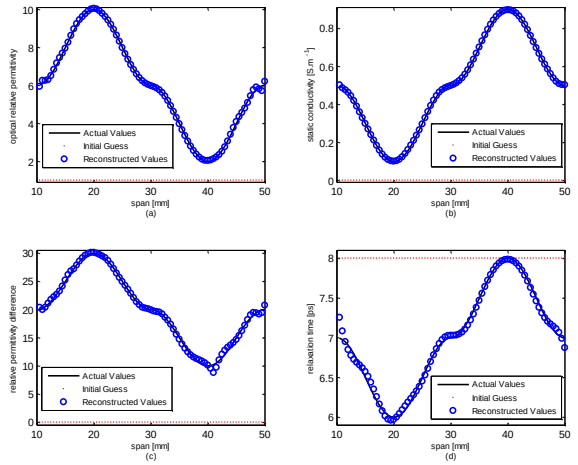

Fig. 8. The reconstructed distributions of: (a) optical relative permittivity, (b) static conductivity, (c) relative permittivity difference, and (d) relaxation time for a stratified Cole-Cole slab with smooth model parameter profiles, using noisy data (SNR = 20 dB) with regularization, at the 30th iteration.

Figure 8 shows that the reconstructed C-C model parameters are also acceptable, based on the new initial guess. Thus, the proposed method is robust to initial guess.

The whole solution program codes written in MATLAB (R2011b, win64-bit) are iteratively executed

on a PC with a four-core i5-2320 CPU, each iteration taking, on average, about 2.87 s.

As previously mentioned, the nonlinearity and ill-posedness are two major difficulties in the solution of the inverse problem. Indeed, in order to bridge over the first difficulty, two similar multi-frequency time-harmonic imaging approaches, the frequency-hopping approach [18] and the simultaneous inversion one [19], have been proposed. While the time-domain technique presented in this paper is a natural extension from several frequencies to an entire frequency range, which could produce imaging results with higher resolution and accuracy. When this time-domain technique is, however, applied to large scale problems such as high-dimensional ones, their high computational cost will become a new difficulty, which may be overcome by either of the multi-frequency methods.

For the second difficulty, the Tikhonov regularization scheme used in this work is one of remedies, in which the reasonable regularization parameters (factors γ_m) for a particular problem can be determined by several regularization parameter-choice techniques such as the L-curve method [20]. Naturally, it will add additional computational cost to the problem. Besides, other regularization schemes, such as the total variation (TV) regularization [21], can also be adopted to remedy the ill-posedness of the inverse problem.

IV. CONCLUSION

This paper estimates four frequency-dependent parameters in the single pole Cole-Cole electrical dispersion equation via a time-domain optimization method. The first contribution in the developed inversion technique is direct reconstruction of four sorts of parameters for the C-C dispersive media from the time-domain measured data. The second one is that comparative studies on the same 1-D problem in three different cases are carried out. The numerical results demonstrate that the proposed technique is feasible for quantitative determination of the parameters of the 1-D example, and it provides a valuable tool for microwave imaging of biological tissues. The further work is to investigate multidimensional reconstruction problems as well as else regularization schemes.

ACKNOWLEDGMENT

This work was supported in part by the National Natural Science Foundation of China under Grant No. 51271059, the Key Program of the Natural Science Foundation of Anhui Higher Education Institutions of China under Grant No. KJ2014A193, the Science and Technology Program of Anhui Province of China under Grant No. 1604a0702037, and the Teaching Research Program of Fuyang Normal University under Grant No. 2015JYXM35.

REFERENCES

[1] T. G. Papadopoulos and I. T. Rekanos, "Estimation of the parameters of Lorentz dispersive media using a time-domain inverse scattering technique," *IEEE Trans. Magn.*, vol. 48, no. 2, pp. 219-222, Feb. 2012.

[2] F. Bai, A. Franchois, and A. Pizurica, "3D microwave tomography with Huber regularization applied to realistic numerical breast phantoms," *Progress In Electromagnetics Research*, vol. 155, pp. 75-91, 2016.

[3] M. T. Bevacqua and R. Scapaticci, "A compressive sensing approach for 3D breast cancer microwave imaging with magnetic nanoparticles as contrast agent," *IEEE Trans. Med. Imag.*, vol. 35, no. 2, pp. 665-673, Feb. 2016.

[4] D. Colton and R. Kress, *Inverse Acoustic and Electromagnetic Scattering Theory*. Berlin: Springer-Verlag, 1992.

[5] W. Zhang and Q. H. Liu, "Three-dimensional scattering and inverse scattering from objects with simultaneous permittivity and permeability contrasts," *IEEE Trans. Geosci. Remote Sens.*, vol. 53, no. 1, pp. 429-439, Jan. 2015.

[6] T. G. Papadopoulos and I. T. Rekanos, "Time-domain microwave imaging of inhomogeneous Debye dispersive scatterers," *IEEE Trans. Antennas Propagat.*, vol. 60, no. 2, pp. 1197-1202, Feb. 2012.

[7] I. T. Rekanos and A. Räisänen, "Microwave imaging in the time domain of buried multiple scatterers by using an FDTD-based optimization technique," *IEEE Trans. Magn.*, vol. 39, no. 3, pp. 1381-1384, May 2003.

[8] T. Takenaka, H. Jia, and T. Tanaka, "Microwave imaging of electrical property distributions by a forward-backward time-stepping method," *J. Electromagn. Waves Appl.*, vol. 14, no. 12, pp. 1609-1626, 2000.

[9] I. T. Rekanos, "Time-domain inverse scattering using Lagrange multipliers: An iterative FDTD-based optimization technique," *J. Electromagn. Waves Appl.*, vol. 17, no. 2, pp. 271-289, 2003.

[10] S. Gabriel, R. W. Lau, and C. Gabriel, "The dielectric properties of biological tissues. III. Parametric models for the dielectric spectrum of tissues," *Phys. Med. Biol.*, vol. 41, no. 11, pp. 2271-2293, Nov. 1996.

[11] D. W. Winters, E. J. Bond, B. D. V. Veen, and S. C. Hagness, "Estimation of frequency-dependent average dielectric properties of breast tissue using a time-domain inverse scattering technique," *IEEE Trans. Antennas Propag.*, vol. 54, no. 11, pp. 3517-3528, Nov. 2006.

[12] I. T. Rekanos and T. G. Papadopoulos, "An

auxiliary differential equation method for FDTD modeling of wave propagation in Cole-Cole dispersive media," *IEEE Trans. Antennas Propag.*, vol. 58, no. 11, pp. 3666-3674, Nov. 2010.

[13] I. T. Rekanos and T. V. Yioultsis, "Approximation of Grünwald-Letnikov fractional derivative for FDTD modeling of Cole-Cole media," *IEEE Trans. Magn.*, vol. 50, no. 2, pp. 7004304, Feb. 2014.

[14] H. Sagan, *Introduction to the Calculus of Variations*. New York, NY: McGraw-Hill, 1969.

[15] M. Dalir and M. Bashour, "Applications of fractional calculus," *Applied Mathematical Sciences*, vol. 4, no. 21, pp. 1021-1032, 2010.

[16] Y. H. Dai, "A family of hybrid conjugate gradient methods for unconstrained optimization," *Math. Comput.*, vol. 72, no. 243, pp. 1317-1328, Feb. 2003.

[17] J. A. Roden and S. D. Gedney, "Convolution PML (CPML): An efficient FDTD implementation of the CFS-PML for arbitrary media," *Microw. Opt. Technol. Lett.*, vol. 27, no. 5, pp. 334-339, Dec. 2000.

[18] W. C. Chew and J. H. Lin, "A frequency-hopping approach for microwave imaging of large inhomogeneous bodies," *IEEE Microw. Guided Wave Lett.*, vol. 5, no. 12, pp. 439-441, Dec. 1995.

[19] Q. Fang, P. M. Meaney, and K. D. Paulsen, "Microwave image reconstruction of tissue property dispersion characteristics utilizing multiple-frequency information," *IEEE Trans. Microw. Theory Tech.*, vol. 52, no. 8, pp. 1866-1875, Aug. 2004.

[20] P. R. Johnston and R. M. Gulrajani, "Selecting the corner in the L-curve approach to Tikhonov regularization," *IEEE Trans. Biomed. Eng.*, vol. 47, no. 9, pp. 1293-1296, Sep. 2000.

[21] L. Hao and L. Xu, "Joint L^1 and total variation regularization for magnetic detection electrical impedance tomography," *ACES Journal*, vol. 31, no. 6, June 2016.

Guangdong Liu was born in Jiangsu, China, in 1972. He received the Dr. Eng. Degree in Electromagnetic Field and Microwave Technology, from the College of Electronic Science and Engineering, Nanjing University of Posts and Telecommunications, in 2011. Currently, he is an Associate Professor of the School of Physics and Electronic Engineering, Fuyang Normal University, China. His research interests are in electromagnetic inverse scattering theory and its applications.

Novel Extraction Method of Inductance Parameter for Nonuniform Transmission Line in Anisotropic Dielectric

Yaxiu Sun and Xiaomeng Wang

College of Information and Communication Engineering
Harbin Engineering University, Harbin, 150001, China
sunyaxiu@hrbeu.edu.cn, wangxiaomeng@hrbeu.edu.cn

Abstract ─ Since the parameters of transmission line can affect the signal integrity and electromagnetic compatibility directly in high frequency circuit, and there is lack of researches in the field of solving the inductance parameter of nonuniform transmission line in anisotropic dielectric, a novel method has been proposed in this paper to solve this problem. The new method uses filament division to establish the dispersion model of nonuniform transmission line, and formulates the filament division principle based on Biot-Savart Law and skin effect. Then it develops the Ampere loop integral dyadic equations and the closed circuit dyadic impedance matrix equation with direction factor in frequency domain based on electromagnetic quasi-static (EMQS). To obtain the corresponding magnetic field direction factor, the relative position of filaments in geometric space is analyzed. Finally, the inductance parameters are obtained by the impedance matrix equation. The correctness of proposed method is verified by applying to uniform transmission line model. Then the new method is applied to the calculation of two nonuniform transmission line models which filled in free space and anisotropic dielectric respectively. The inductance parameters and frequency dependency solved by different methods are compared, showing accuracy and validity of the proposed method. Besides, the new method can be applied to various transmission line structures and different anisotropic dielectric.

Index Terms ─ Anisotropic dielectric, inductance parameter, nonuniform transmission line, tensor dielectric constant.

I. INTRODUCTION

Nonuniform transmission line has been widely used in high speed circuit systems and affected the circuit performance and reliability [1-4]. So the extraction of distributed parameter for nonuniform transmission line is particularly important. Many electromagnetic numerical methods have been extensively used to solve this problem, such as finite-difference time-domain (FDTD) and moment of method (MOM) [5-9]. Afrooz and his fellows have used FDTD to analyze the electromagnetic field and extract the inductance parameter from the time-domain difference transmission line equations [5]. However, it cannot take the skin effect into consideration when current is in high frequency, so that the parameter value is inaccurate. Paul extracted the capacitance matrix by using MoM, and then the inductance matrix can be obtained from it [8]. Although this method can effectively solve the inductance matrix of transmission line, the analysis process is complex and needs to be solved many times. For this problem, the researchers of MIT have developed a FastHenry software to extract the parameters of integrated circuit based on the network analysis method. This software can solve the parameter fast, exactly, and universally. However, this software can be invalidated when the circuits are under the condition of electromagnetic quasi-static (EMQS) [10]. Besides, with the development of engineering technology, the performance of the circuit filled in general medium can no longer meet the demand of circuit design. So anisotropic dielectric has been more widely used because of the special electromagnetic characteristics [11-13]. For the research of anisotropic dielectric, many achievements focus on the influence of electromagnetic wave radiation, while few researches focus on inductance extraction of nonuniform transmission line in anisotropic dielectric [14-15].

In this paper, a novel extraction method of inductance parameters for nonuniform transmission line in anisotropic dielectric is proposed. It establishes the filament physical model according to Biot-Savart Law and skin effect, and derives the Ampere circuit dyadic integral equations and closed circuit dyadic impedance matrix equation with direction factor in frequency domain. Finally, the inductance parameter can be solved. The new method can be applied to various complex nonuniform transmission line structures and has some theoretical significance and engineering value.

This paper is organized as follows. In Section II, the filament dispersion of nonuniform transmission line is introduced and Ampere loop integral dyadic equations are summarized. The closed circuit dyadic impedance

Submitted On: March 31, 2016
Accepted On: November 17, 2016

matrix equation with direction factor is obtained in Section III. The proposed method is finally verified by numerical examples in Section IV, showing the correctness, accuracy and validity. The conclusions are given in Section V.

II. NONUNIFORM TRANSMISSION LINE MODELING

A. Filament division of nonuniform transmission line model

A physical structure is established and shown in Fig. 1 to solve the inductance parameter of nonuniform transmission line. It consists of a lossy nonuniform signal line and a ground plate. The direction of signal line is Z. Its section radius is $r(z)$.

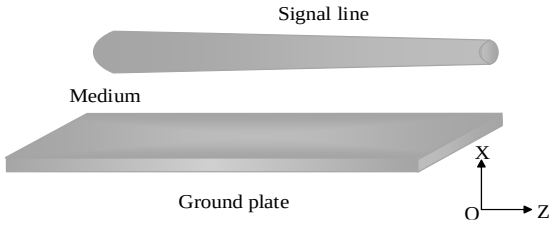

Fig. 1. The nonuniform transmission line model.

The structure in Fig. 1 can be discretized into some filaments with an approximate cross section. The number of filaments can be determined based on skin effect and the filament condition of Biot-Savart Law. So the side length of filament section g should meet the condition:

$$g \le \frac{1}{5}\delta, \tag{1}$$

where skin depth δ can be described as $\delta = 1/\sqrt{\pi f \mu\sigma}$. f is frequency, μ is permeability, σ is conductivity. So filament number N should meet the condition:

$$N \ge \frac{s(z)}{g^2}, \tag{2}$$

where $s(z)$ is the effective section which is described as:

$$s(z) = \pi\left[r(z)^2 - \left[r(z)-\delta\right]^2\right] = \pi\delta^2 + 2\pi r(z)\delta, \delta < r(z). \tag{3}$$

When the frequency is enough high, $s(z)$ can be approximately described as:

$$s(z) = 2\pi r(z)\delta = 2r(z)\cdot\sqrt{\pi / f\mu\sigma}, \delta << r(z). \tag{4}$$

The final update equation can be written as:

$$N \ge 50\pi r(z)\sqrt{f\mu\sigma}. \tag{5}$$

Equation (5) is the condition of the filament division.

According to the condition of filament division, the model in Fig. 1 is discretized as Fig. 2. The filament numbers of signal line and ground plate are N_C and N_D. The total filament number is N_{tot}. When the section of filament is small enough, it can be considered that the current here is evenly distributed. So the current of filament n at z point can be expressed as $i_n(z) = J_n(z)S_0$, where $J_n(z)$ is the current density of filament n at z point, S_0 is the area of filament section.

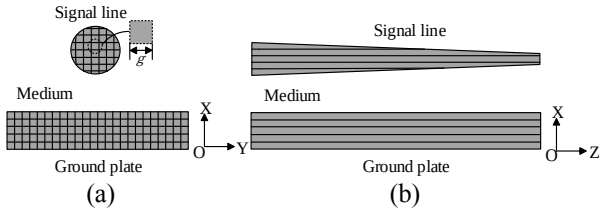

Fig. 2. Filament division of nonuniform transmission line: (a) XOY plane and (b) XOZ plane.

B. Filaments circuit modeling

Figure 3 is the instruction of filaments circuit $a \to b \to c \to d \to a$, in which the filaments k and s are chosen any from the filaments of signal line and ground plate. The length of filament is Δz. The circuit is in Electromagnetic quasi-static (EMQS).

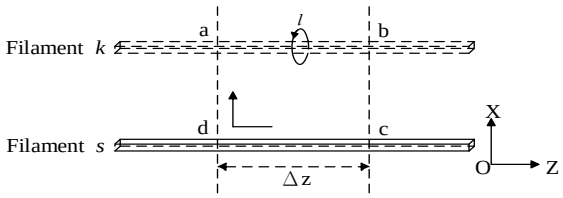

Fig. 3. The instruction of filaments circuit.

According to Faraday electromagnetic law, the closed circuit integral equation in frequency domain can be written as:

$$\begin{aligned}&\int_a^b \boldsymbol{E}_k(x,y,z)\mathrm{d}z + \int_b^c \boldsymbol{E}(x,y,z+\Delta z)\mathrm{d}x \\ &+\int_c^d \boldsymbol{E}_s(x,y,z)\mathrm{d}z + \int_d^a \boldsymbol{E}(x,y,z)\mathrm{d}x \\ &= -j\omega\mu\int_s^k\int_z^{z+\Delta z} \boldsymbol{H}_\perp(x,y,z)\mathrm{d}z\mathrm{d}x.\end{aligned} \tag{6}$$

The left part of (6) can be expressed as:

$$\int_a^b \boldsymbol{E}_k(x,y,z)\mathrm{d}z = i_k(z)R_k\Delta z, \tag{7}$$

$$\int_b^c \boldsymbol{E}(x,y,z+\Delta z)\mathrm{d}x = v_k(z+\Delta z) - v_s(z+\Delta z), \tag{8}$$

$$\int_c^d \boldsymbol{E}_s(x,y,z)\mathrm{d}z = -i_s(z)R_s\Delta z, \tag{9}$$

$$\int_d^a \boldsymbol{E}(x,y,z)\mathrm{d}x = v_s(z) - v_k(z), \tag{10}$$

where $\boldsymbol{E}(x,y,z)$ is spatial electric field strength; $\boldsymbol{E}_k(x,y,z)$ and $\boldsymbol{E}_s(x,y,z)$ are electric field strength of filaments k and s respectively; $v_k(z)$ and $v_s(z)$ are the voltage of filaments k and s at point z; R_k and R_s are the unit resistance of filaments k and s.

The right part of (6) can be described as follows:

$$\mu\int_s^k\int_z^{z+\Delta z}\boldsymbol{H}_\perp(x,y,z)\mathrm{d}z\mathrm{d}x=\mu\sum_{n=1}^{N_{tot}}\int_s^k\int_z^{z+\Delta z}\boldsymbol{H}_{n\perp}(x,y,z)\mathrm{d}z\mathrm{d}x, \quad (11)$$

where $\boldsymbol{H}_{n\perp}(x,y,z)$ is the magnetic field component of filament n which vertically through the area of $\mathrm{a}\to\mathrm{b}\to\mathrm{c}\to\mathrm{d}\to\mathrm{a}$.

So the Equation (6) can be updated as:

$$\begin{aligned}&v_k(z+\Delta z)-v_k(z)-v_s(z+\Delta z)\\&+v_s(z)+i_k(z)R_k\Delta z-i_s(z)R_s\Delta z\\&=-j\omega\mu\sum_{n=1}^{N_{tot}}\int_s^k\int_z^{z+\Delta z}\boldsymbol{H}_{n\perp}(x,y,z)\mathrm{d}z\mathrm{d}x.\end{aligned} \quad (12)$$

Taking the filament k as an example, the Ampere loop integral equation can be written as:

$$\oint_1\boldsymbol{H}_k\cdot\mathrm{d}\boldsymbol{l}=\int_s\boldsymbol{J}_k\cdot\mathrm{d}\boldsymbol{s}+j\omega\int_s\boldsymbol{D}_k\cdot\mathrm{d}\boldsymbol{s}, \quad (13)$$

where $\boldsymbol{H}_k$ is total magnetic field strength of filament k through the area of $\mathrm{a}\to\mathrm{b}\to\mathrm{c}\to\mathrm{d}\to\mathrm{a}$, $\boldsymbol{J}_k$ and $\boldsymbol{D}_k$ are the conduction current density and electric displacement vector respectively, where $\boldsymbol{J}_k$ can be expressed as $\boldsymbol{J}_k=\sigma\boldsymbol{E}$.

C. Ampere loop integral dyadic equations

The constitutive relation of isotropic medium is only simple one dimension relationship which can be represented as $\boldsymbol{D}=\varepsilon\boldsymbol{E}$. However, it usually takes anisotropic dielectric as medium in application. The dielectric constant ε of anisotropic dielectric shows a form of tensor, and it can be described as a matrix:

$$[\varepsilon_{ki}]=\begin{bmatrix}\varepsilon_{11}&\varepsilon_{12}&\varepsilon_{13}\\\varepsilon_{21}&\varepsilon_{22}&\varepsilon_{23}\\\varepsilon_{31}&\varepsilon_{32}&\varepsilon_{33}\end{bmatrix}. \quad (14)$$

So the constitutive relations of anisotropic dielectric can be written as follows:

$$D_k=\sum_{i=1}^{3}\varepsilon_{ki}E_i\quad(k=1,2,3), \quad (15)$$

and it can also be represented in dyadic form as:

$$\boldsymbol{D}=\overline{\overline{\varepsilon}}\boldsymbol{E}, \quad (16)$$

where $\overline{\overline{\varepsilon}}$ is the dielectric constant tensor.

In this paper, the electric anisotropic dielectric is taken as the example, whose three principal axes coincide with the coordinate axes and the dielectric constant tensor is symmetric. So the dielectric constant tensor can be written as:

$$\overline{\overline{\varepsilon}}=\begin{bmatrix}\varepsilon_{11}&0&0\\0&\varepsilon_{22}&0\\0&0&\varepsilon_{33}\end{bmatrix}. \quad (17)$$

By applying the new constitutive relations to (13), the following expression can be obtained as:

$$\int_s\boldsymbol{J}_k\cdot\mathrm{d}\boldsymbol{s}+j\omega\int_s\boldsymbol{D}_k\cdot\mathrm{d}\boldsymbol{s}=\int_s\sigma\boldsymbol{E}_k\cdot\mathrm{d}\boldsymbol{s}+j\omega\int_s(\overline{\overline{\varepsilon}}\cdot\boldsymbol{E}_k)\cdot\mathrm{d}\boldsymbol{s}, \quad (18)$$

which leads to:

$$\int_s\boldsymbol{J}_k\cdot\mathrm{d}\boldsymbol{s}+j\omega\int_s\boldsymbol{D}_k\cdot\mathrm{d}\boldsymbol{s}=j\omega\int_s(\frac{\sigma\overline{\overline{\mathrm{A}}}}{j\omega}+\overline{\overline{\varepsilon}})\cdot\mathrm{d}\boldsymbol{s}, \quad (19)$$

where $\overline{\overline{\mathrm{A}}}$ is the unit matrix. So the right part of (19) can be further derived as:

$$j\omega\int_s(\frac{\sigma\overline{\overline{\mathrm{A}}}}{j\omega}+\overline{\overline{\varepsilon}})\boldsymbol{E}_k\cdot\mathrm{d}\boldsymbol{s}=j\omega\int_s\overline{\overline{\zeta}}\boldsymbol{E}_k\cdot\mathrm{d}\boldsymbol{s}, \quad (20)$$

in which $\overline{\overline{\zeta}}=\frac{\sigma\overline{\overline{\mathrm{A}}}}{j\omega}+\overline{\overline{\varepsilon}}$. Then the Ampere loop integral dyadic equation in frequency domain can be written as:

$$\oint_c\boldsymbol{H}_k\cdot\mathrm{d}\boldsymbol{l}=j\omega\int_s\overline{\overline{\zeta}}\boldsymbol{E}_k\cdot\mathrm{d}\boldsymbol{s}. \quad (21)$$

Therefore, $\boldsymbol{H}_k$ can be solved by this equation. The magnetic field strengths $\boldsymbol{H}_n$ produced by the other filaments can also be obtained by this equation. To obtain $\boldsymbol{H}_{n\perp}$, a new parameter has been defined here, that is the direction factor β. It shows the relationship between effective magnetic $\boldsymbol{H}_{n\perp}$ and total magnetic $\boldsymbol{H}_n$ through the particular rectangular loop. And this relationship cannot be expressed in simple mathematical expressions. The expression and usage of direction factor will be described in next section.

III. FORMULATION OF CLOSED CIRCUIT DYADIC IMPEDENCE MATRIX EQUATION

A. Expression of direction factor

Direction factor β can be solved according to the relative geometric position of filaments and rectangular loop. To solve the corresponding direction factor of $\boldsymbol{H}_{n\perp}$, the rectangular loop of filament k and s is taken as the example.

The section center point coordinates of filament k, s, and n are (x_k,y_k), (x_s,y_s), and (x_n,y_n). The right part of (12) can be represented as:

$$\begin{aligned}&\mu\sum_{n=1}^{N_{tot}}\int_s^k\int_z^{z+\Delta z}\boldsymbol{H}_{n\perp}\mathrm{d}z\mathrm{d}x=\\&\mu\int_s^k\int_z^{z+\Delta z}\boldsymbol{H}_{k\perp}\mathrm{d}z\mathrm{d}x+\mu\int_s^k\int_z^{z+\Delta z}\boldsymbol{H}_{s\perp}\mathrm{d}z\mathrm{d}x+\mu\sum_{\substack{n=1\\n\neq k\,n\neq s}}^{N_{tot}}\int_s^k\int_z^{z+\Delta z}\boldsymbol{H}_{n\perp}\mathrm{d}z\mathrm{d}x,\end{aligned} \quad (22)$$

where $\mu\int_s^k\int_z^{z+\Delta z}\boldsymbol{H}_{k\perp}\mathrm{d}z\mathrm{d}x$ and $\mu\int_s^k\int_z^{z+\Delta z}\boldsymbol{H}_{s\perp}\mathrm{d}z\mathrm{d}x$ are the magnetic flux induced by the current of filaments k and s. Then they can be further derived as:

$$\begin{aligned}\int_s^k\int_z^{z+\Delta z}\boldsymbol{H}_{k\perp}\mathrm{d}z\mathrm{d}x&=-\frac{1}{8\pi}\frac{j\omega\overline{\overline{\zeta}}}{\sigma}i_k\Delta z-\int_0^{(x_k-x_s)^2+(y_k-y_s)^2}\int_{\mathrm{b}}^{\mathrm{c}}\boldsymbol{H}_{k\perp}\mathrm{d}z\mathrm{d}x\\&=-\frac{1}{8\pi}\frac{j\omega\overline{\overline{\zeta}}}{\sigma}i_k\Delta z-\frac{1}{2\pi}\frac{j\omega\overline{\overline{\zeta}}}{\sigma}i_k\Delta z\ln\frac{\sqrt{(x_k-x_s)^2+(y_k-y_s)^2}-g}{g},\end{aligned} \quad (23)$$

$$\int_s^k \int_z^{z+\Delta z} \mathbf{H}_{s\perp} dz dx = \frac{1}{8\pi} \frac{j\omega \overline{\overline{\zeta}}}{\sigma} i_s \Delta z + \frac{1}{2\pi} \frac{j\omega \overline{\overline{\zeta}}}{\sigma} i_s \Delta z \ln \frac{\sqrt{(x_k - x_s)^2 + (y_k - y_s)^2} - g}{g}. \tag{24}$$

The third part of (22) is the magnetic flux induced by the current of filaments except *k* and *s*, and can be written as:

$$\sum_{\substack{n=1 \\ n\neq k, n\neq s}}^{N_{tot}} \int_s^k \int_z^{z+\Delta z} \mathbf{H}_{\mathbf{n}\perp} dz dx = \sum_{\substack{n=1 \\ n\neq k, n\neq s}}^{N_{tot}} \int_s^k \int_z^{z+\Delta z} \mathbf{H}_{\mathbf{n}} \cdot \beta dz dx = \sum_{\substack{n=1 \\ n\neq k, n\neq s}}^{N_{tot}} \int_0^{(x_k - x_s)^2 + (y_k - y_s)^2} \int_z^{z+\Delta z} \mathbf{H}_n \cos\alpha dz dx, \tag{25}$$

where α is the angle between magnetic flux and rectangular loop of filaments *k* and *s*. Based on the multiple relative position among filaments *k*, *s* and *n*, Equation (25) are final updated as:

$$\sum_{\substack{n=1 \\ n\neq k, n\neq s}}^{N_{tot}} \int_s^k \int_z^{z+\Delta z} \mathbf{H}_{\mathbf{n}\perp} dz dx = \sum_{\substack{n=1 \\ n\neq k, n\neq s}}^{N_{tot}} \frac{1}{4\pi} \frac{j\omega \overline{\overline{\zeta}}}{\sigma} i_n \Delta z \ln \frac{(u\cos\theta - v)^2 + (u\sin\theta)^2}{(u\cos\theta + v)^2 + (u\sin\theta)^2}, \tag{26}$$

where

$$u = \sqrt{(x_n - \frac{x_k + x_s}{2})^2 + (y_n - \frac{y_k + y_s}{2})^2},$$
$$v = \frac{\sqrt{(x_k - x_s)^2 + (y_k - y_s)^2}}{2},$$
$$w = \sqrt{(x_k - x_n)^2 + (y_k - y_n)^2},$$
$$\cos\theta = \frac{u^2 + v^2 - w^2}{2uv}.$$

Therefore, the corresponding direction factor β of $\boldsymbol{H}_{n\perp}$ has been simplified as a relationship between the filament section center point coordinates and angle α. These variables can be obtained directly. So the corresponding direction factor can be represented as a relationship:

$$\beta = \frac{\sum_{\substack{n=1 \\ n\neq k, n\neq s}}^{N_{tot}} \int_s^k \int_z^{z+\Delta z} \mathbf{H}_{n\perp} dz dx}{\sum_{\substack{n=1 \\ n\neq k, n\neq s}}^{N_{tot}} \int_s^k \int_z^{z+\Delta z} \mathbf{H}_n dz dx}. \tag{27}$$

The direction factor of other filaments can also be obtained based on above process.

B. Closed circuit dyadic equations with direction factor

The total number of filament circuits is $C_{N_{tot}}^2$. They are similar to the filaments circuit of *k* and *s*. Taking the convenience and realization for calculation into account, the closed circuits which constituted by all signal line filaments with the first filament (namely N_C+1) of ground plate are selected. Moreover, the closed circuits constituted by all ground plate filaments with the longest one (namely filament *k*) of signal line are selected too. So the closed circuit dyadic equations with direction factor can be concluded as follows:

when $1 \le m \le N_C$,

$$\frac{v_m(z+\Delta z) - v_m(z)}{\Delta z} = -\lambda'(i_m - i_{N_C+1}) + \frac{\omega^2 \mu}{\sigma} \overline{\overline{\zeta}} \sum_{\substack{n=1 \\ n\neq m, n\neq N_C+1}}^{N_{tot}} \frac{i_n}{4\pi} \ln \frac{(u'\cos\theta' - v')^2 + (u'\sin\theta')^2}{(u'\cos\theta' + v')^2 + (u'\sin\theta')^2}, \tag{28}$$

where

$$\lambda' = \frac{1}{4\sigma g^2} \overline{\overline{A}} - \frac{\omega^2 \mu}{\sigma} \overline{\overline{\zeta}} \left[\frac{1}{8\pi} + \frac{1}{2\pi} \ln \frac{\sqrt{(x_m - x_{N_C+1})^2 + (y_m - y_{N_C+1})^2} - g}{g} \right],$$
$$u' = \sqrt{(x_n - \frac{x_m + x_{N_C+1}}{2})^2 + (y_n - \frac{y_m + y_{N_C+1}}{2})^2},$$
$$v' = \frac{\sqrt{(x_m - x_{N_C+1})^2 + (y_m - y_{N_C+1})^2}}{2},$$
$$w' = \sqrt{(x_m - x_n)^2 + (y_m - y_n)^2},$$
$$\cos\theta' = \frac{u'^2 + v'^2 - w'^2}{2u'v'},$$

when $N_C + 1 \le m \le N_{tot}$,

$$\frac{v_{N_k}(z+\Delta z) - v_{N_k}(z)}{\Delta z} = -\lambda''(i_{N_k} - i_m) + \frac{\omega^2 \mu}{\sigma} \overline{\overline{\zeta}} \sum_{\substack{n=1 \\ n\neq m, n\neq N_k}}^{N_{tot}} \frac{i_n}{4\pi} \ln \frac{(u''\cos\theta'' + v'')^2 + (u''\sin\theta'')^2}{(u''\cos\theta'' - v'')^2 + (u''\sin\theta'')^2}, \tag{29}$$

where

$$\lambda'' = \frac{1}{4\sigma g^2} \overline{\overline{A}} - \frac{\omega^2 \mu}{\sigma} \overline{\overline{\zeta}} \left[\frac{1}{8\pi} + \frac{1}{2\pi} \ln \frac{\sqrt{(x_m - x_{N_k})^2 + (y_m - y_{N_k})^2} - g}{g} \right],$$
$$u'' = \sqrt{(x_n - \frac{x_m + x_{N_k}}{2})^2 + (y_n - \frac{y_m + y_{N_k}}{2})^2},$$
$$v'' = \frac{\sqrt{(x_m - x_{N_k})^2 + (y_m - y_{N_k})^2}}{2},$$
$$w'' = \sqrt{(x_{N_k} - x_n)^2 + (y_{N_k} - y_n)^2},$$
$$\cos\theta'' = \frac{u''^2 + v''^2 - w''^2}{2u''v''}.$$

There is a duplicate closed circuit dyadic equation in above equations. So we should remove it and add the

current conservation equation which can be written as:

$$\sum_{n=1}^{N_{tot}} i_n = 0. \tag{30}$$

Therefore, there are N_{tot} equations totally.

C. Matrix form of closed circuit dyadic equations

The voltage and current of signal line is $V(z)$ and $I(z)$. The potential of ground plate is zero. When $\Delta z \to 0$, the closed circuit dyadic equations can be written in matrix form, and the current conservation equation can be added in the N_C+1 row of the matrix. N_C can be obtained based on Equation (5). So the matrix form of the closed circuit equations is:

$$\boldsymbol{FD} = -\boldsymbol{SM} \tag{31}$$

where $\boldsymbol{F}(m,1) = \begin{cases} 0, & m = N_C+1 \\ 1, & \text{others} \end{cases}$, $\boldsymbol{D} = \dfrac{\mathrm{d}V(z)}{\mathrm{d}z}$. $\boldsymbol{S}$ is $N_{tot}\times N_{tot}$ coefficient matrix which can be obtained by the closed circuit equations and written as:

$$\boldsymbol{S}(m,n) = \begin{cases} \lambda', & 1 \le m \le N_C, 1 \le n \le N_{tot}, m = n \\ -\lambda', & 1 \le m \le N_C, n = N_C+1 \\ -\dfrac{\omega^2 \mu \bar{\bar{\zeta}}}{4\pi\sigma} \ln \dfrac{(u'\cos\theta' - v')^2 + (u'\sin\theta')^2}{(u'\cos\theta' + v')^2 + (u'\sin\theta')^2}, & 1 \le m \le N_C, 1 \le n \le N_{tot}, m \ne n \\ 1, & m = N_C+1, 1 \le n \le N_{tot} \\ -\lambda'', & N_C+2 \le m \le N_{tot}, 1 \le n \le N_{tot}, m = n \\ \lambda'', & N_C+2 \le m \le N_{tot}, n = N_k \\ -\dfrac{\omega^2 \mu \bar{\bar{\zeta}}}{4\pi\sigma} \ln \dfrac{(u''\cos\theta'' + v'')^2 + (u''\sin\theta'')^2}{(u''\cos\theta'' - v'')^2 + (u''\sin\theta'')^2}, & N_C+2 \le m \le N_{tot}, 1 \le n \le N_{tot}, m \ne n \end{cases}$$

M is $N_{tot}\times 1$ current matrix:

$$\boldsymbol{M} = (i_1 \;\; i_2 \;\; \cdots \;\; i_C \;\; i_C{+}1 \;\; i_C{+}2 \;\; \cdots \;\; i_{tot})^{\mathrm{T}}.$$

Another relationship can be concluded as:

$$\boldsymbol{I}(z) = \boldsymbol{QM} \tag{32}$$

where $\boldsymbol{Q}(1,m) = \begin{cases} 1, & 1 \le m \le N_C \\ 0, & \text{others} \end{cases}$.

By applying the matrix transformation, the updated relationship can be written as:

$$\boldsymbol{D} = -(\boldsymbol{QS}^{-1}\boldsymbol{F})^{-1}\boldsymbol{I}(z) \tag{33}$$

This equation is the closed circuit impedance dyadic matrix equation with direction factor. Thus, the impedance matrix can be expressed as:

$$\boldsymbol{Z} = (\boldsymbol{QS}^{-1}\boldsymbol{F})^{-1} \tag{34}$$

According to the transmission line impedance equation $\boldsymbol{Z}=\boldsymbol{R}+j\omega\boldsymbol{L}$, the resistive parameter can be obtained form the real part of Equation (34), and the inductance matrix can also be concluded from the imaginary part as:

$$\boldsymbol{L}(z) = \frac{\mathrm{Im}[\boldsymbol{Z}]}{2\pi f} = \frac{\mathrm{Im}\left[(\boldsymbol{QS}^{-1}\boldsymbol{F})^{-1}\right]}{2\pi f} \tag{35}$$

IV. NUMERICAL RESULTS

A. Uniform transmission line model in free space

In this section, the uniform transmission line model shown in Fig. 4 is considered to verify the validity and correctness of the new method. The two kind of different radius of signal line we used here are $r1$=0.5 mm and $r2$=0.4 mm. The size of cross section of ground plate is 3 mm×1 mm. The nearest distance between signal line and ground plate is 1 mm. The conductivity of transmission line is σ=5.98×10^{7}S/m. The magnetic permeability is $\mu = \mu_0$. New method and traditional method are used to solve the inductance parameter of this model.

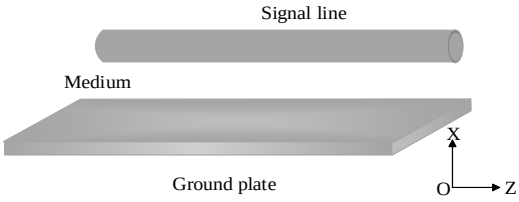

Fig. 4. The uniform transmission line model.

To verify the correctness of proposed method, the per unit length inductance of uniform transmission line has been obtained by three different methods: proposed method, traditional method and measurement. In traditional method, the skin effect of transmission line in high frequency has been neglected, which can decrease the area of effective cross section and affect the value of inductance parameter [16]. While the new method can take it into consideration. Besides, the measurement has also been used to prove the validity of proposed method. The schematic of measurement is shown in Fig. 5. It uses the vector network analyzer to measure the impedance of equipment under test (EUT), namely, the transmission line, and the inductance parameter can be obtained from it.

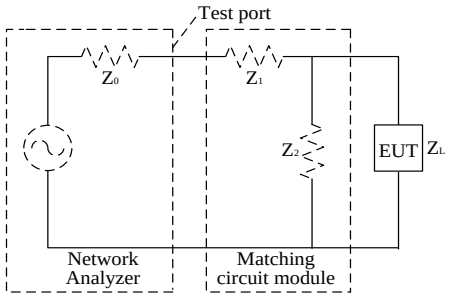

Fig. 5. Measurement setup schematic.

Table 1 shows the filament numbers and computing time of new method to calculate the inductance parameter in various frequency.

Figure 6 shows the inductance distribution of uniform transmission line in free space and 100 MHz frequency. As shown in the figure, we can conclude that the per unit length inductance does not change with the coordinate z. Moreover, the inductance values of the line

with different radius are different, and they increase with the decrease of radius when the frequency of current is constant. Compare the traditional method and the proposed method, the changing trend of the new method is more close to the measurement one. So the correctness of proposed method has been verified, and it is more accurate than traditional one.

The frequency dependency of inductance parameter for uniform transmission line is shown in Fig. 7, which indicates the inductance calculated by new method and the measurement are vary with frequency, while the traditional method does not. Because traditional method cannot consider the skin effect in high frequency. Besides, comparing the results with measurement, the error between new method and measurement is less than 5%, namely 15nH. So the validity and correctness of new method can be verified, and it has a high precision.

Table 1: Filament numbers and computing time in various frequency

f/MHz	N_C	N_D	N_{tot}	t/s
10	381	871	1252	0.52
100	1206	2972	4178	2.6
1000	3815	9615	13430	30.45

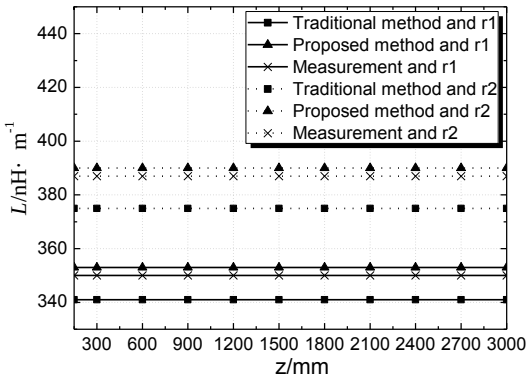

Fig. 6. Inductance distribution of uniform transmission line in free space.

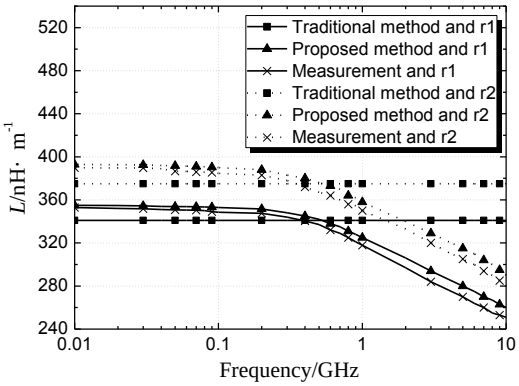

Fig. 7. Frequency dependency of inductance parameter for uniform transmission line.

In order to further illustrate the influence that the skin effect bring to the calculation of inductance parameter in high frequency, Fig. 8 shows the frequency dependency for unit inductance parameters expressed by the ratio of radius to skin depth. When the radius of conductor is less than twice the skin depth, the unit inductance parameter of new method is approximately equal to the value of traditional method (341nH/m). The reason is that the current can be considered as uniform distributed in low frequency. However, the radius of conductor is twice larger than skin depth, the unit inductance parameter is gradually decreased with the increased frequency. So the skin effect in high frequency cannot be ignored.

Figure 9 shows the current distribution within the cross section of the uniform transmission line at different frequency. It shows the variation of current density along the radial direction at 1 MHz, 10 MHz and 100 MHz frequency respectively. Compare the curves, we can further validate the effect of skin effect and get the conclusion; as the frequency increases, the skin depth of the wire decreases, and the smaller the effective area of the current along the wire. Thus, the greater the resistance loss of the wire.

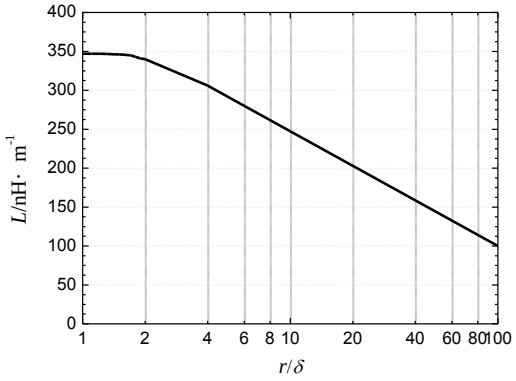

Fig. 8. Frequency dependency of inductance parameter expressed by the ratio of radius to skin depth.

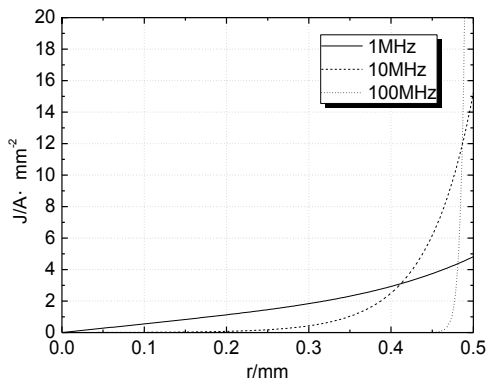

Fig. 9. Current distribution within the cross section of uniform transmission line at different frequency.

B. Nonuniform transmission line model in free space

For better investigation of accuracy and availability of proposed method, the nonuniform transmission line model introduced in Fig. 1 is used in this section. The medium is free space. The two kind of different radius of signal line we used here are $r3$=0.5-0.1(z/l) mm and $r4$=0.5-0.05(z/l). The size of ground plate and distance between signal line and ground plate are the same to Fig. 4. The length of signal line is 3000 mm, namely that coordinate z is from 0 to 3000 mm. New method and traditional method are used to solve the inductance parameter of this model.

Table 2 shows the filament numbers and computing time of the new method to calculate the inductance parameter in various frequency.

Table 2: Filament numbers and computing time in various frequency

f/MHz	N_C	N_D	N_{tot}	t/s
10	419	871	1290	0.6
100	1327	2972	4299	2.71
1000	4196	9615	13811	31.72

Figure 10 shows the inductance distribution of nonuniform transmission line in free space and 100 MHz frequency, which indicates that the unit inductance parameter is gradually increased with the increased coordinate z. So we can conclude that the unit inductance parameter of nonuniform transmission line in free space is increased with the decreased radius when the frequency of current is constant. Moreover, the traditional method has been used to prove the validity of the proposed method [17]. In the traditional method, the nonuniform transmission lines are considered to be equivalent to a cascaded chain of many multiport subnetworks which are made of short sections of uniform lines. Compare the two methods, the changing trend of the new method is more pronounced than the traditional one.

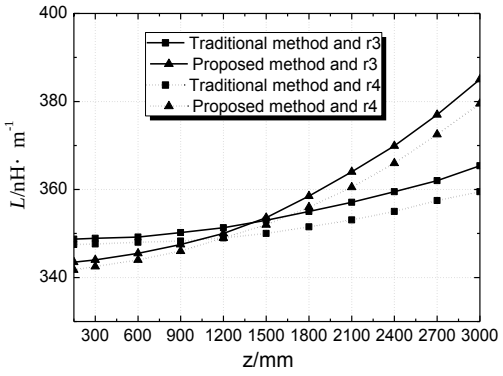

Fig. 10. Inductance distribution of nonuniform transmission line in free space.

For analysis of frequency dependency of unit inductance parameter of nonuniform transmission line in free space, the unit line in z=150 mm is calculated. The result is shown in Fig. 11, which indicates the unit inductance parameter is decreased with the increased frequency. It is caused by skin effect, which makes the current distribute near the surface of line so that the effective section can be decreased. Besides, when the frequency is 0.1 GHz, the inductance value in Fig. 10 is 344nH/m, which also is the value corresponding to z=150 mm in Fig. 10.

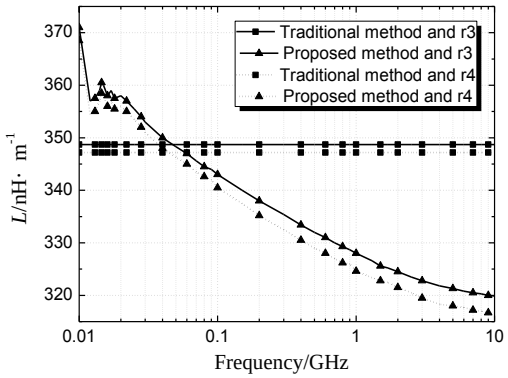

Fig. 11. Frequency dependency of inductance parameter for nonuniform transmission line in free space.

C. Nonuniform transmission line model in anisotropic dielectric

Because the traditional method cannot solve the inductance parameter of nonuniform transmission line in anisotropic dielectric, in this section, the new method is applied to calculating the model of Fig. 1. The anisotropic dielectric we choose here is the uniaxial anisotropic medium, which is widely used in the microwave field of aviation industry. In this paper, we take the two kind of anisotropic dielectric as the example to analyze the influence of anisotropic dielectric on the inductance parameters. The tensor dielectric constant of anisotropic dielectric 1 is ε_{11}=1.44ε_0, ε_{22}=1.12ε_0, ε_{33}=1.44ε_0, and the tensor dielectric constant of anisotropic dielectric 2 is ε_{11}=2.88ε_0, ε_{22}=2.24ε_0, ε_{33}=2.88ε_0.

Table 3 shows the filament numbers and computing time of the new method to calculate inductance parameter in various frequency. Comparing the data in Table 3 with Table 2, we can conclude that the computing time of the model in anisotropic dielectric is longer than in free space. That is caused by the tensor dielectric constant with three-degree matrix, which leads to a more complex matrix processing process and increased computing time.

Table 3: Filament numbers and computing time in various frequency

f/MHz	N_C	N_D	N_{tot}	t/s
10	419	871	1290	0.9
100	1327	2972	4299	3.12
1000	4196	9615	13811	39.72

Figure 12 is the inductance distribution of nonuniform transmission line in different medium and 100 MHz frequency. The figure shows the inductance parameter increases with the decrease of transmission line's radius. Compared with Fig. 10, the value in Fig. 12 is bigger than in Fig. 10, which is caused by the principal axis of tensor dielectric constant. Besides, the isotropic dielectric of ε=1.44ε_0 is compared with the anisotropic medium. It shows the inductance parameter is reduced in anisotropic dielectric when other conditions are the same. Because both the real part and the imaginary part of the magnetic field intensity are reduced in anisotropic dielectric. And it can decrease with the increase of coefficient of tensor dielectric constant.

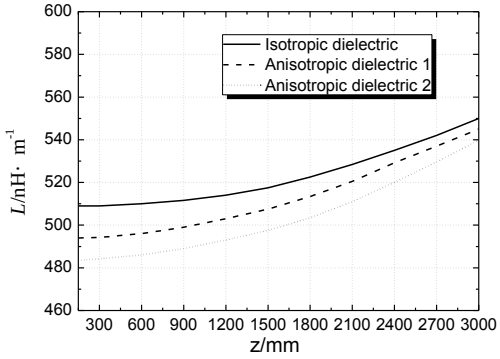

Fig. 12. Inductance distribution of nonuniform transmission line in different medium and 100 MHz.

For better analysis of new method, the frequency dependency of unit inductance parameter for nonuniform transmission line model in anisotropic dielectric is solved. The process of simulation is the same to Fig. 11 and shown in Fig. 13. It indicates that the inductance parameter is decreased with frequency. And when frequency is more than 1 GHz, the unit inductance parameter is decreased in exponential form. Therefore, anisotropic dielectric has a great influence on inductance parameter, and it should not be ignored in solving electric parameter of transmission line.

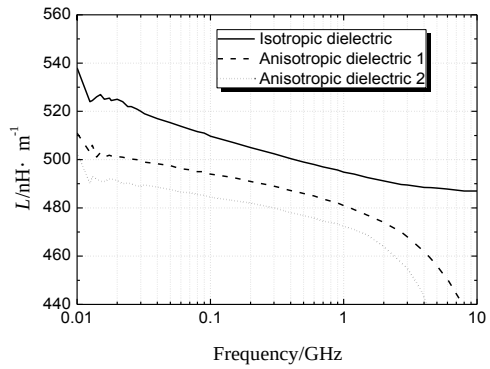

Fig. 13. Frequency dependency of inductance parameter for nonuniform transmission line in different dielectric.

V. CONCLUSION

A novel method has been proposed for extracting inductance parameter of nonuniform transmission line in anisotropic dielectric. The proposed method can take the nonuniform distributed resistance and current caused by skin effect in high frequency and complex form of tensor dielectric constant into consideration. The correctness, validation, and accuracy of proposed method are demonstrated by several examples. The results show that the new method can be applied to solving inductance parameter when the model medium is anisotropic dielectric and transmission line is nonuniform. Moreover, it can be applied to solving various nonuniform transmission line structures and different anisotropic dielectric conditions.

ACKNOWLEDGMENT

This project was supported by the National Natural Science Foundation of China (Grant No. 51209055), the China Postdoctoral Special Foundation (Grant No. 2015T80324), and the Natural Science Foundation of Heilongjiang, China (Grant No. F2015028).

REFERENCES

[1] D. Lei and D. Jiao, "Sensitivity analysis of lossy nonuniform transmission lines with nonlinear terminations," *IEEE Trans. Adv. Packag.*, vol. 33, no. 2, pp. 492-497, May 2010.

[2] T. Takahiro, S. Tadatoshi, and A. Hideki, "Fast transient analysis of nonuniform multiconductor transmission lines using HIE-Block-LIM," *IEEE Microw. Wirel. Co.*, vol. 23, no. 10, pp. 512-514, Oct. 2013.

[3] L. Jacek, "Equivalent circuits for nonuniform transmission line simulation," *Applied Comput. Electromagn. Society J.*, vol. 25, no. 9, pp. 764-779, Sep. 2010.

[4] Q. Xu and P. Mazumder, "Accurate modeling of lossy nonuniform transmission lines by using differential quadrature methods," *IEEE Trans. Microw. Theory Tech.*, vol. 50, no. 10, pp. 2233-2246, Oct. 2002.

[5] K. Afrooz and A. Abdipour, "Efficient method for time-domain analysis of lossy nonuniform multiconductor transmission line driven by a modulated signal using FDTD technique," *IEEE Trans. Electromagn. Compat.*, vol. 54, no. 2, pp. 482-494, Apr. 2012.

[6] V. Nayyeri, M. Soleimani, and O. M. Ramahi, "A method to model thin conductive layers in the Finite-Difference Time-Domain method," *IEEE Trans. Electromagn. Compat.*, vol. 56, no. 2, pp. 385-392, Apr. 2014.

[7] Y. Liu, J. Hong, and K. K. Mei, "Analysis of a double step microstrip discontinuity using generalized transmission line equations," *IEEE*

Trans. Adv. Packag., vol. 26, no. 4, pp. 368-374, Nov. 2003.

[8] C. R. Paul and A. E. Feather, "Computation of the transmission line inductance and capacitance matrices from the generalized capacitance matrix," *IEEE Trans. Electromagn. Compat*., vol. 18, no. 4, pp. 175-183, Dec. 1976.

[9] Y. Altuncu, "A numerical method for electro-magnetic scattering by 3-D dielectric objects buried under 2-D locally rough surfaces," *IEEE Trans. Antennas Propagat.*, vol. 63, no. 8, pp. 3634-3643, Aug. 2015.

[10] M. Kamon, M. J. Tsuk, and J. White, "FastHenry: A multipole-accelerated 3-D inductance extraction program," *IEEE Trans. Microw. Theory Tech.*, vol. 42, no. 9, pp. 1750-1758, Sep. 1994.

[11] Y. Li, J. Li, and M. Wang, "Internal and external electric field for an anisotropic dielectric particle in electromagnetic beams," *IEEE Trans. Antennas Propagat.*, vol. 61, no. 9, pp. 4754-4759, 2013.

[12] K. Agarwal, P. Li, and X. Chen, "Subspace-based optimization method for reconstruction of 2-D complex anisotropic dielectric objects," *IEEE Trans. Microw. Theory Tech.*, vol. 58, no. 4, pp. 1065-1074, Apr. 2010.

[13] B. Carl, W. Gregory, and C. John, "A second-order 2D electromagnetics algorithm for curved interfaces between anisotropic dielectrics on a Yee mesh," *J. Comput. Phys.*, no. 230, pp. 2060-2075, 2011.

[14] S. N. Dudorov, D. V. Lioubtchenko, and A. V. Raisanen, "Modification of marcatili's method for the calculation of anisotropic dielectric waveguides," *IEEE Trans. Microw. Theory Tech.*, vol. 50, no. 6, pp. 1640-1642, June 2002.

[15] B. Benjamin, R. David, and N. Robert, "Multi-conductor spectral domain analysis of the mutual coupling between printed dipoles embedded in stratified uniaxial anisotropic dielectrics," *IEEE Trans. Antennas Propagat.*, vol. 60, no. 4, pp. 1886-1898, Apr. 2012.

[16] C. R. Paul and A. E. Feather, "Computation of the transmission line inductance and capacitance matrices from the generalized capacitance matrix," *IEEE Trans. Electromagn. Compat*., vol. 18, no. 4, pp. 175-183, 1976.

[17] J. Mao and Z. Li, "Analysis of the time response of nonuniform multiconductor transmission lines with a method of equivalent cascaded network chain," *IEEE Trans. Microw. Theory Tech.*, vol. 40, no. 5, pp. 948-954, May 1992.

The Investigation of Substrate's Dielectric Properties for Improving the Performance of Witricity Devices

Mohd H. M. Salleh [1], Norhudah Seman [1], and Raimi Dewan [2]

[1] Wireless Communication Centre
University Teknologi Malaysia, 81310 UTM Johor Bahru, Johor, Malaysia
eday_89@yahoo.com.my, huda@fke.utm.my

[2] Faculty of Electrical Engineering
University Teknologi Malaysia, 81310 UTM Johor Bahru, Johor, Malaysia
raimidewan@gmail.com

Abstract **—** In designing a better Witricy device, there are several parameters that contribute to the improvement of efficiency. In this article, the substrate characteristics, which gaining less attention despite their potential for the improvement of Witricity performance are thoroughly studied. The characteristics such permittivity and loss tangent that very common in microwave design are investigated. The investigation has proven that RO 3010 substrate composed of ceramic-filled Polytetrafluoroethylene (PTFE) composites is the best material for the optimal Witricity performance, independent of the spiral coil's number of turns. This is due to its high-energy storage capacity obtained from the real permittivity, and roughly low loss factor and tangent loss. Hence, the Rogers RO 3010 substrate is proposed in this study as it performs reliable 50% to 74% coupling efficiency with the varied number of spiral coil turns.

Index Terms **—** Inductive power transfer, strongly coupled magnetic resonance, substrate, wireless power transfer, Witricity.

I. INTRODUCTION

The first experiment on wireless electrical transmission has been conducted by Nikola Tesla since 1890's [1]. However, the work on this wireless power transfer (WPT) was not taken up by scientific community except for some significant experiments [2], such studying a variation of electric potential and its casual fluctuation on a transformer [3]. Then, a more significant and modern experiment has been initiated by a group of researchers in Massachusets Institute of Technology (MIT), by introducing the name of 'Witricity' as a method of WPT that focuses on non-radiative mid-range power transmission. Witricity, which based on reliable and strongly coupled magnetic resonance technique is efficiently lighting up 60 watts light bulbs using 50 cm diameter coils over 2 meter distance in 2007 [4], has gained interests from worldwide researchers. In addition, Intel has also proven the method by an experiment at 60 cm distance with 75% efficiency [5]. Besides Witricity, there are several other methods of wireless power transfer (WPT) including energy harvesting, inductive coupling and capacitive coupling.

A few parameters such as impedance matching [6], coupling [7] and Q-factors [8] are reported to improve WPT efficiency. Study of the substrate thickness, the dimension of the capacitors and the number of turns of the coils is demonstrated in [9] to align the design with a given resonance frequency. However, this work is merely focused on the changing of the substrate thickness of the device concerning only Flame Retarded 4 (FR-4). In addition to thickness, permittivity is one of the important substrate characteristics to be considered in determining the best material that could contribute to the performance improvement of Witricity devices. Therefore, this characteristic needs to be carefully studied and thoroughly discussed. Referring to [10], varying the substrate dielectric property is expected useful in characterizing the resonance frequency of the Witricity device; whereby the lower values of permittivity correspond to higher resonance frequency and vice versa. Furthermore, a study in [11] proves that the increases of the material permittivity result in the increases of the antenna gain for a given resonance frequency. As the gain of antenna related to its efficiency, thus, it is interesting to apply this concept to the Witricity design by studying the effect of the parameter towards its performance, especially in coupling efficiency.

Furthermore, capacitance, C is one of the factors in designing Witricity device as it provides electrical energy storage [9]. The electrostatic energy stored in a parallel plate capacitor measured in the unit of Joules as given by $W = 1/2CV^2$; where V is the voltage difference between two parallel plates. However, the value

Submitted On: February 28, 2016
Accepted On: October 31, 2016

of capacitance strictly depends on the substrate permittivity, ε, the thickness of substrate, d and the area of parallel plates, A as $C = \varepsilon A/d$. Therefore, a significant increase in energy density can be made by either increasing the permittivity, ε of the substrate or the applied field strength, E [12].

In this article, the substrate's dielectric properties are investigated for improving Witricity device performance. A few types of substrates with different permittivity, including Flame Retardant 4 (FR-4), RO4003C, TMM-4 and RO3010 have been measured and compared to CST simulated data. Then, a similar Witricity device design is applied on each substrate to study the permittivity effect towards Witricity performance. The best material is chosen, and the proposed prototype is verified practically.

II. WITRICITY DESIGN AND THEORETICAL CONCEPT

The proposed Witricity device consists of a transmitter and a receiver, which resonates at similar frequencies. Figure 1 depicts a transmission scheme from the first port to the second port. While, Fig. 2 shows the CST generated layout of the proposed Witricity device and the arrangement in the three-dimensional (3D) simulation tool of CST Microwave Design Studio.

In Figs. 1 and 2, each transmitter and receiver consist of two conducting layers: top and bottom are separated by the air gap. The top layer consists of a rectangular spiral coil inductor (Tx and Rx coil), while the bottom layer has two slotted capacitor plates that are arranged and attached to a single turn coil (Tx and Rx loop). To achieve a simple design workflow, an identical design is implemented in both transmitter and receiver to ensure both devices are always resonating at the same frequency.

The device is designed accordingly to meet the best coupling efficiency, η and impedance matching. Each transmitter and receiver design consists of a substrate with a thickness of 0.635 mm and copper layers on top and bottom layer. On the top layer, a spiral coil of conductive copper, which consists of several numbers of loops that is varied from 10 to 30 turns. The limit of the number of turns is fixed to 30 due to a further increase of turns will lead to a more complicated design and may compromise the precision of the design in fabrication stage. According to the Biot-Savart law in [14], the amount of the induced magnetic field at receiver, H_{Rx} is proportional to the spiral coil's number of turns, n as (1):

$$H_{Rx} = \frac{I \cdot n}{4\pi} \oint \frac{\vec{dl} \times \vec{r}}{r^3}, \tag{1}$$

where, I, n and r are the respective input current, number of turns and distance between the transmitter coil to the receiver. Whilst, dl is the tangential vector around a single loop coil. Accordingly, the spiral coil's number of turns, n is directly influencing the inductance, L value as shown by the modified Wheeler formula in (2) [18]:

$$L = \frac{K_1 \mu_0 n^2 D_{avg}}{1 + K_2 \rho}, \tag{2}$$

where, K_1 and K_2 are the spiral shape dependent coefficients, which equal to 2.34 and 2.75 respectively. Meanwhile, D_{avg} is the average diameter of the rectangular spiral; and ρ is the fill ratio, which defined to 1 for the design. Thus, by varying the spiral coil's number of turns, n will proportionally affect the inductance, L, which then alter the induced magnetic field, H_{Rx} analogously at the receiver. Consequently, the unloaded quality factor, Q of the spiral coil that analogous to $\omega L/R$ will change accordingly.

The overall coupling efficiency of the Witricity device, η can be written as the following Equation (3) [15-16]:

$$\eta = \frac{k^2 Q_1 Q_2}{\left[1 + \left(1 + k^2 Q_1 Q_2\right)^{1/2}\right]^2}, \tag{3}$$

where, Q_1 and Q_2 are unloaded quality factors of the transmitter and receiver coils, respectively, which are equal to $\omega L/R$. While, k is the mutual coupling constant, which has a value ranging from 0 to 1, that closely depending on the distance between transmitter and receiver. Therefore, it is proven in the Equations (1), (2) and (3) that by increasing the spiral coil's number of turns upsurges in the induced magnetic field at the receiver, H_{Rx}, the inductance value of L as well as the overall efficiency of the Witricity device.

As presented in Fig. 2 (b), the bottom layer of the designed Witricity device consists of a single source/load loop is linked to the two 14 x 8 mm^2 slotted rectangular capacitors, which stores electrical charges supplied to the device. The advantages of slotted capacitors over traditional capacitors are the improvement in reflection coefficient and bandwidth [13]. The used substrates in the proposed Witricity are changed to observe the effect of different substrates of FR-4, RO4003C, TMM4, RO3006 and RO3010 that having the relative permittivity in the range of 4 to 11 towards its performance. The information on substrates' properties obtained from the data sheet is listed in Table 1. Table 1 shows the properties of several substrates obtained from the data sheet together with simulated and measured relative permittivity.

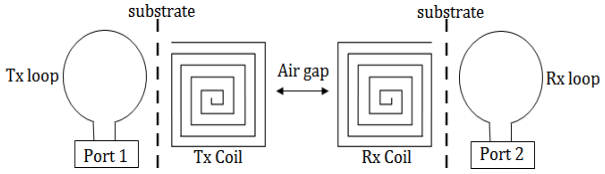

Fig. 1. Witricity device transmission scheme.

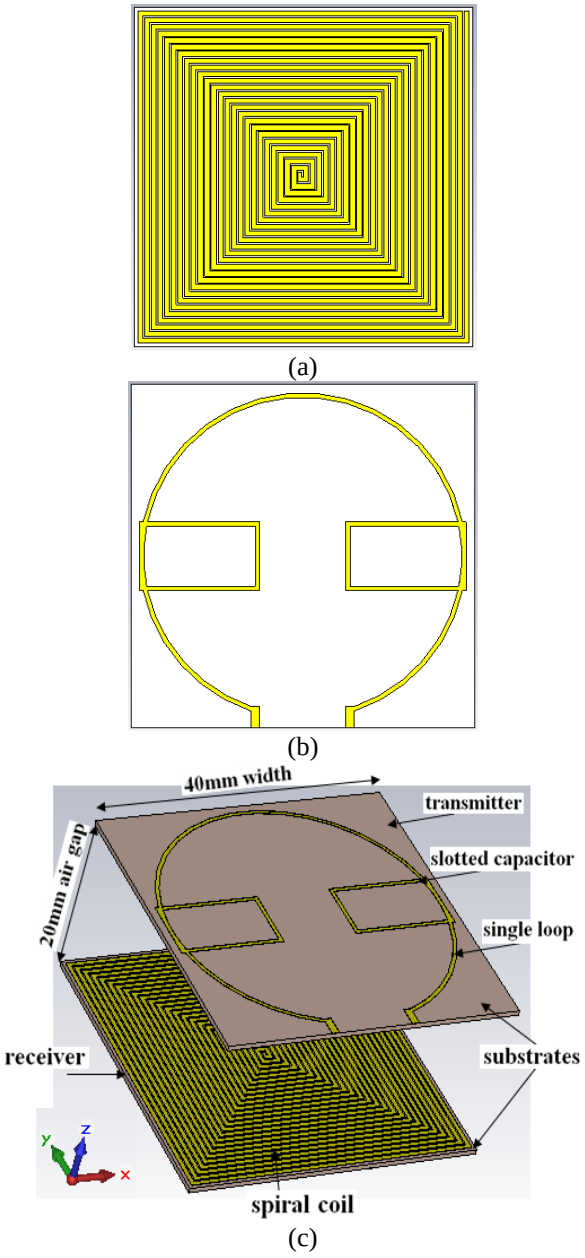

Fig. 2. (a) The top, (b) bottom, and (c) full 3D CST generated layout of Witricity device.

III. RESULTS AND DISCUSSION

The simulation and experimental results, and discussion are divided into two parts; A and B. Section A discusses the respective results obtained related to complex permittivity. Meanwhile, Section B presents the effect of permittivity towards coupling efficiency and the verification of Witricity design with the best substrate.

A. Complex permittivity

The dielectric property is derived from the effective complex permittivity, ε^* of the substrate, which determines its electromagnetic (EM) ability such as the polarization, dielectric losses and conductivity. Compared to ε^*, its complex relative permittivity, ε_r^* as expressed in (4) is used more often as the value is dimensionless and simpler [16]:

$$\varepsilon_r^* = \frac{\varepsilon^*}{\varepsilon_0} = \frac{\varepsilon^{'} - j\varepsilon^{''}}{\varepsilon_0} = \varepsilon_r^{'} - j\varepsilon_r^{''}, \tag{4}$$

where, ε_0, ε_r' and ε_r'' are the permittivity of free space (8.85 x 10^{-12} F/m), the real and imaginary part of the complex relative permittivity, accordingly. The real part of ε^*, which is ε' that denotes the ability of a material to store the incident EM energy through the wave propagation. Whilst, the imaginary part of ε^* noted by ε'' represents the degree of EM energy losses in the material. Thus, the respective ε_r' and ε_r'' are also known as the dielectric constant and loss factor. The real and imaginary relative permittivity values of four different types of dielectric materials; RO 4003, FR-4, TMM-4 and RO 3010 are depicted in Table 1.

As shown in Table 1, the measured data of real relative permittivity between the dielectric materials have no significant differences with either simulated data obtained from CST and data sheet. Thus, it can be drawn that the Rogers RO4003 has the lowest ε_r' comparative to FR-4, TMM-4 and RO 3010. The FR-4 ε_r' is slightly higher than RO 4003 but almost similar to TMM-4 followed by RO 3010 that has the highest ε_r' with more than two-time values of the others. Considering from this aspect only, thus, the lowest energy transfer efficiency is expected from RO 4003 due to the less EM energy storage ability that related to lowering real permittivity and followed by FR-4, TMM-4 and RO 3010.

N onetheless, there is another factor that contributes to the efficient energy transfer, which is substrate's loss tangent, tan δ can be expressed as (5) [17]:

$$\tan\delta = \frac{\omega\varepsilon_r^{''} + \sigma}{\omega\varepsilon_r^{'}}, \tag{5}$$

where, ω and σ are angular frequency and conductivity loss, respectively in conditions of $\varepsilon_r'' \geq 0$ and $\varepsilon_r' \gg \varepsilon_r''$. At high frequency as considered in this proposed work, the substrate's loss tangent, tan δ can be simplified to $\varepsilon_r''/\varepsilon_r'$. It is also known as the dissipation factor that describes the angle difference between capacitance current and voltage. As noted from Table 1, the highest value of the loss tangent belongs to FR-4, followed by RO 3010, RO 4003, and the lowest belongs to TMM-4. Thus, concludes the FR-4 and TMM-4 have the respective highest and lowest loss.

By having the information of the loss tangent, the imaginary relative permittivity, ε_r'' in Table 1 is obtained by multiplying the real relative permittivity, ε_r' and the loss tangent. The imaginary relative permittivity, ε_r'' presents the loss factor that portraying the efficiency of energy transfer. Therefore, higher loss factor (imaginary

relative permittivity, ε_r'') leads to the least efficient energy transfer. The results show a significant difference between FR-4 and other substrates. It can be deduced that FR-4 have the largest loss factor with almost three-time values of RO 3010 and more than six-time of the other substrates. However, RO 4003 that has the lowest $\varepsilon_r^{"}$ will have the smallest loss factor that expected to contribute for better energy transfer.

By considering both real and imaginary relative permittivity, it can be deduced that a substrate must have small loss factor (imaginary relative permittivity) and large real relative permittivity to store more energy from incident EM wave. As a result from both real and imaginary relative permittivity, the smaller value of loss tangent is important in determining the best material for Witricity device.

Table 1: The substrate properties obtained from the data sheet, CST and measured relative permittivity

Substrate	Data Sheet			CST	Measurement	Calculated
	Material Composition	Real Relative Permittivity (ε_r')	Loss Tangent	Real Relative Permittivity (ε_r')	Real Relative Permittivity (ε_r')	Imaginary Relative Permittivity (ε_r'')
FR-4	Epoxy resin	4.4-4.7	0.014-0.017	4.41	4.30	0.06-0.07
RO4003C	Glass reinforced ceramics	3.55	0.0021	3.56	3.55	0.0075
TMM-4	Ceramic thermoset	4.70	0.002	4.51	4.50	0.0090
RO3010	Ceramic-filled PTFE	11.20	0.0022	10.22	10.20	0.0224

B. Coupling efficiency

The concerned coupling efficiency of the Witricity device, η expressed in (3) is analogous to $|S_{21}|^2$. The comparison of the proposed Witricity device's coupling efficiency performance that designed using different dielectric materials, including FR-4, RO 4003, TMM 4, and RO 3010 are obtained via CST Microwave Studio simulation. It is to study the relationship between the complex permittivity and loss tangent toward coupling efficiency performance. The effect of varying the spiral coil's number of turns in the Witricity design for the different dielectric materials is shown in Fig. 3, while the corresponding coupling efficiency of their optimal design is shown in Fig. 6.

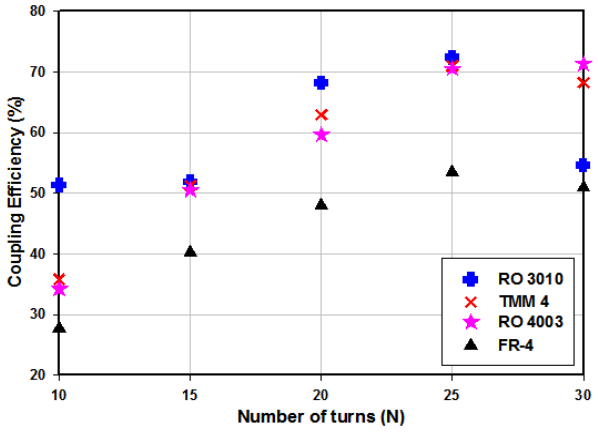

Fig. 3. Coupling efficiency of Witricity device with diferent substrates and varied number of spiral coil turns between 10 and 30.

Based on Fig. 3, at the low number of turns, there are significant results shown between each material with RO 3010 has the best coupling with approximately 50% followed by TMM 4, RO 4003 and FR-4. The result complies with the sequence of ε_r' from the highest to the lowest as shown in Table 1, except for FR-4, which has greater ε_r' compared to RO 4003 but has lower coupling efficiency performance. This result deduces that the real part of complex relative permittivity is important in achieving high capacitance value of the Witricity device, which enabling high-energy storage at the transmitter and receiver. Likewise, the imaginary part of the complex relative permittivity is also an important factor as it represents the energy loss in the material. The lower value reflects a low-energy loss due to absorption of the material. Therefore, the performance of FR-4 is the worst among all the substrates as it has low real relative permittivity, but highest imaginary, which results in lower coupling efficiency. At the highest number of turns, most of the substrates show a significant drawback, especially by RO 3010 yet better than FR-4, which has the largest imaginary relative permittivity and tangent loss. However, RO 4003 performs almost similar result with 25 turns even at higher turns as it has the lowest loss factor. Both phenomena prove a stronger dependency of imaginary permittivity compared to the real permittivity for the number of turns higher the optimal 25. This is, on the contrary, for a number of turns that less than optimal 25, which shows stronger dependency on the real permittivity compared to the imaginary.

Referring to the obtained results, Witricity device with RO 3010 substrate and optimal 25 number of turns is fabricated. The fabricated prototype is shown in Fig. 4. The 25 number of turns is chosen as an optimum as most of the substrates show best coupling at this number.

The measurement setup used to validate the performance of this proposed Witricity device is shown in Fig. 5. The results of the coupling efficiency of their optimal design are shown in Fig. 6.

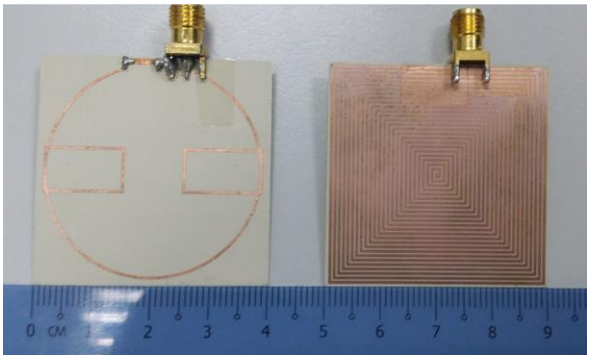

Fig. 4. Prototype of Witricity device with optimal 25 number of spiral coil turns using RO3010 substrate.

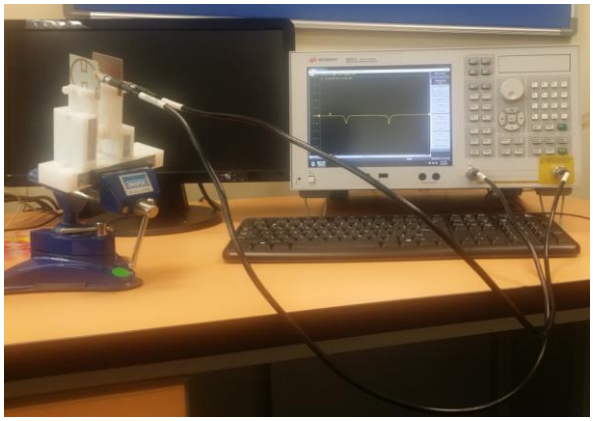

Fig. 5. Measurement setup using Keysight Vector Network Analyzer (VNA).

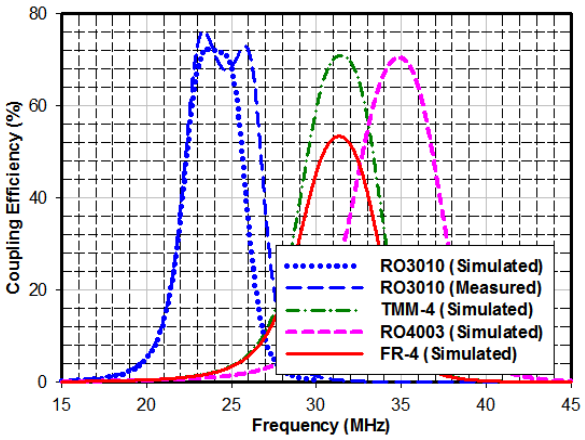

Fig. 6. Coupling efficiency results Witricity device using different materials having optimal 25 number of spiral coil turns.

At the optimal 25 number of turns, the coupling efficiency results in Fig. 6 show the lead taking by the design using RO 3010 with comparable simulated and measured performance of 72.3% and 76.2%, respectively at approximately 24 MHz. While, the design using FR-4 has performed worse coupling efficiency with 53.4% at a higher frequency of 31.5 MHz. However, other materials perform at the almost similar level between 70.5% to 71.0% due to the nearly close loss tangent about 0.002-0.0022, which is about eight times lower than FR-4 of 0.014-0.017.

By considering different substrates of various real relative permittivities, the distinct values of capacitances are expected in each design as the number of spiral coil turns are kept at a constant of 25 turns. This has led to different operating frequency for each design, where the lowest frequency obtained by the highest real relative permittivity substrate. This contrasts to the design with the lowest real relative permittivity material that has the highest operating frequency. Consequently, the operating frequency of the designed Witricity device is inversely proportional to capacitance and real relative permittivity of the chosen substrate.

IV. CONCLUSION

The performance of the Witricity device can be improved by selecting an appropriate dielectric material or known as a substrate in the design process. The dielectric properties of substrate involve in designing Witricity device is shown by investigating the effect of complex permittivity to the device performance. The study shows that the high real relative permittivity, which also branded as dielectric constant results in great coupling performance, especially for the spiral coil's number of turns from 10 to 25. RO 3010 has the widest range of the tunable number of coil turns as it has been greater than 50% efficiency for 10-30 turns, followed by TMM-4 and RO 4003 that achieve more than 50% efficiency at 15-30 turns. Meanwhile, FR-4 needs at least 25 turns to perform well. The study also has shown a great performance of Witricity device with a high real relative permittivity substrate from a low number of coil turns up to the optimal of 25. Afterward, the performance has strongly affected by the value of imaginary permittivity as been noted by the design using RO 3010 substrate compared to others at 30 number turns.

ACKNOWLEDGMENT

This work is carried out with the financial support from the Malaysian Ministry of Higher Education (MOHE) via MyPhD program and Universiti Teknologi Malaysia (UTM) via GUP, Flagship and HiCoE Grant with the respective vote number of 05H43, 03G41 and 4J212.

REFERENCES

[1] N. Tesla, *Colorado Springs Notes*. Nolit, Beograd,

1978.
[2] C. A. Tucker, K. Warwick, and W. Holderbaum, "A contribution to the wireless transmission of power," *Int. J. Electr. Power Energy Syst.*, vol. 47, pp. 235-242, May 2013.
[3] N. Tesla, "The transmission of electrical energy without wires," *Twenty First Century Books*, 1904.
[4] A. Kurs, A. Karalis, R. Moffatt, J. Joannopoulos, P. Fisher, and M. Soljačić, "Wireless power transfer via strongly coupled magnetic resonances," *Science*, vol. 317, pp. 83-86, July 2007.
[5] N. Borges Carvalho, A. Georgiadis, A. Costanzo, H. Rogier, A. Collado, J. A. García, S. Lucyszyn, P. Mezzanotte, J. Kracek, D. Masotti, A. J. S. Boaventura, M. de las Nieves Ruíz Lavin, M. Pinuela, D. C. Yates, P. D. Mitcheson, M. Mazanek and V. Pankrac, "Wireless power transmission: R&D activities within europe," *IEEE Trans. Microw. Theory Tech.*, vol. 62, no. 4, pp. 1031-1045, Apr. 2014.
[6] M. Pinuela, D. C. Yates, S. Lucyszyn, and P. D. Mitcheson, "Maximizing DC-to-load efficiency for inductive power transfer," *IEEE Trans. Power Electron.*, vol. 28, no. 5, pp. 2437-2447, May 2013.
[7] R. Bosshard, J. Muhlethaler, J. W. Kolar, and I. Stevanovic, "Optimized magnetic design for inductive power transfer coils," *In Proceedings of 2013 Twenty-Eighth Annual IEEE Applied Power Electronics Conference and Exposition (APEC)*, pp. 1812-1819, 2013.
[8] C. M. Zierhofer and E. S. Hochmair, "Geometric approach for coupling enhancement of magnetically coupled coils," *IEEE Trans. Biomed. Eng.*, vol. 43, no. 7, pp. 708-714, July 1996.
[9] M. H. Salleh, N. Seman, and R. Dewan, "Reduced-size witricity charger design and its parametric study," *In Proceedings of 2013 IEEE International RF and Microwave Conference (RFM)*, pp. 387-390, 2013
[10] Z. Sheng and V. V. Varadan, "Effect of substrate dielectric properties and tunable metamaterials," *In Proceedings of IEEE Antennas and Propagation Society International Symposium 2006*, pp. 4497-4500, 2006.
[11] V. Rathi, S. Rawat, and H.S. Pokhariya, "Study the effect of substrate thickness and permittivity on patch antenna," *In Proceedings of 2011 IEEE International Conference on Signal Processing, Communications and Computing (ICSPCC)*, pp. 1-4, 2011.
[12] J. R. Laghari and W. J. Sarjeant, "Energy-storage pulsed-power capacitor technology," *IEEE Trans. Power Electron.*, vol. 7, no. 1, pp. 251-257, Jan. 1992.
[13] M. H. M. Salleh, N. Seman, and D. N. A. Zaidel, "Design of a compact planar Witricity device with good efficiency for wireless applications," *In Proceedings of 2014 Asia-Pacific Microwave Conference (APMC)*, pp. 1369-1371, 2014.
[14] W. Junhua, S. L. Ho, W. N. Fu, and S. Mingui, "Analytical design study of a novel Witricity charger with lateral and angular misalignments for efficient wireless energy transmission," *IEEE Trans. Magn.*, vol. 47, pp. 2616-2619, Oct. 2011.
[15] A. Islam, S. Islam, and F. Tulip, "Design and optimization of printed circuit board inductors for wireless power transfer system," *Circuits and Systems*, vol. 4, no. 2, pp. 237-244, Apr. 2013.
[16] O. Büyüköztürk, T. Y. Yu, and J. A. Ortega, "A methodology for determining complex permittivity of construction materials based on transmission-only coherent, wide-bandwidth free-space measurements," *Cem. Concr. Compos.*, vol. 28, no. 4, pp. 349-359, Apr. 2006.
[17] D. M. Pozar, *Microwave Engineering*. 4th Edition, Wiley, New Jersey, 2012.
[18] S. S. Mohan, M. M. Hershenson, S. P. Boyd, and T. H. Lee, "Simple accurate expressions for planar spiral inductances," *IEEE J. Solid-State Circuit*, vol. 34, no. 10, pp. 1419-1424, Oct. 1999.

Mohd Hidir Mohd Salleh obtained his first degree from Universiti Teknologi Malaysia (UTM) in Electrical Engineering (Telecommunication) in 2012 with first class honour. He currently pursues his Ph.D. in Electrical Engineering at UTM since 2012 under a fast-track programme. His research topic focusing on wireless power transfer using strongly magnetic resonance and inductive coupling.

Norhudah Seman received the B.Eng. in Electrical Engineering (Telecommunications) degree from the Universiti Teknologi Malaysia, Johor, Malaysia, in 2003 and M.Eng. degree in RF/Microwave Communications from The University of Queensland, Brisbane, St. Lucia, Qld., Australia, in 2005. In September 2009, she completed her Ph.D. degree at The University of Queensland. In 2003, she was an Engineer with Motorola Technology, Penang, Malaysia, where she was involved with the RF and microwave components design and testing. Currently, she is a Senior Lecturer in Wireless Communication Centre (WCC), Universiti Teknologi Malaysia. Her research interests concern the design

of microwave circuits for biomedical and industrial applications, specific absorption rate (SAR), UWB technologies, and mobile communications.

Raimi Dewan received his Bachelor Degree in Engineering (Electrical-Telecommunication) and Master Degree of Engineering (Electrical) from Universiti Teknologi Malaysia (UTM) in 2010 and 2013 respectively. He recently pursues his Ph.D. at the same university. His research interests include antenna design, metamaterial, Radio Frequency (RF) and microwave devices.

Assessment of Kapton-based Flexible Antenna for Near Field Wireless Energy Transfer

Mohamad Harris Misran [1,3], Sharul Kamal Abdul Rahim [1], Akaa Agbaeze Eteng [1], and Guy A. E. Vandenbosch [2]

[1] Wireless Communication Centre (WCC), Faculty of Electrical Engineering
Universiti Teknologi Malaysia, 81310 UTM Skudai Johor, Malaysia
harris@utem.edu.my, sharulkamal@fke.utm.my, aeakaa2@live.utm.my

[2] Department of Electrical Engineering
Antenna Design University, KU Leuven, Belgium
guy.vandenbosch@esat.kuleuven.be

[3] Fakulti Kejuruteraan Elektrik dan Kejuruteraan Komputer
Universiti Teknikal Malaysia Melaka, Hang Tuah Jaya, 76100 Durian Tunggal, Melaka, Malaysia
harris@utem.edu.my

Abstract ─ This letter presents the design of a flexible highly efficient antenna for Wireless Energy Transfer (WET) at 13.56 MHz. The proposed antenna uses very thin kapton, with a thickness of 25 μm as a substrate, and an 18 μm layer of copper as the conductive material. The 40 mm x 40 mm 6 loop antenna produces almost 90% ETE (energy transfer efficiency) and a bandwidth (BW) of almost 4 MHz for inductive wireless communications. This flexible antenna is suitable for use in small mobile devices, for wireless charging and communication purposes at the NFC operating frequency. In addition, kapton offers very high durability, high mechanical strength, and unique distortional resistance to harsh environments and corrosive aqueous etchants, in this way increasing the reliability of the antenna.

Index Terms ─ Flexible antenna, high efficiency, kapton, Near Field Communication (NFC), Wireless Energy Transfer (WET).

I. INTRODUCTION

Near Field Communication (NFC) enables data transfer between devices. Since it is facilitated through inductive coupling, NFC can also be used to enable the transfer of energy between these devices. Due to NFC's unique ability, many high- and mid-end smartphones come with embedded NFC features. However, with the current technology, NFC antennas embedded in smartphones are only used for data transfer, rather than wireless charging.

Various substrate materials have been investigated for use in energy transfer applications. Some studies have achieved insensitivity to distance and strong magnetic coupling using low-cost glass reinforced epoxy laminated boards (FR 4) [1-3]. A Nickel-Zinc-based ferrite substrate has also been used to implement near-field antennas with high efficiency at 13.56 MHz [8]. However, the growing demand for flexible electronic devices necessitates further research into the implementation of antennas on flexible substrates. Some of the more popular flexible substrates found in literature include kapton polyimide film, polydimethylsiloxane (PDMS) and polyethylene (PET). Yu has proposed a multi-layer spiral antenna for wireless power transfer at 300 kHz using copper coils separated by kapton films [4]. The author manages to transfer 5 Watts of power over a distance of two times the coil diameter. Choo has designed a flexible antenna for near-field communication at the UHF frequency of 912 MHz [5]. The author used printed copper strip line on flexible polyethylene (PET) to couple a reader and a microchip, solely for wireless communication [5]. However, except for a few examples of the application of flexible PDMS substrates in telemetry systems [6], not much research has been carried out on flexible antenna substrates for wireless energy transfer.

To the best of our knowledge, there are no papers on the study and design of flexible antennas for simultaneous wireless communication and energy transfer at 13.56 MHz. Therefore, this research proposes a design of a flexible antenna for wireless energy transfer, which supports wireless data transfer as well. A frequency of 13.56 MHz is chosen to fit the standard operation frequency of NFC. Kapton is assessed as the substrate because of its

Submitted On: May 19, 2016
Accepted On: October 31, 2016

flexibility, the possibility to use very thin layers (in contrast to PDMS), the rather low cost (in comparison with graphene), and the very high durability and mechanical strength.

II. ANTENNA GEOMETRY

In order to fit into a smartphone, the antenna is sized at 40 mm x 40 mm. The antenna topology is shown in Fig. 1 and its dimensions are given in Table 1. For a perfect circular loop, the best operation distance with the strongest magnetic field flux is $r = d\sqrt{2}$ [7], where d is the operating distance and r is the antenna's radius. Assuming that changing the shape to a square will not change this characteristic drastically, the operating distance for the wireless energy transfer link is set at 14.14 mm.

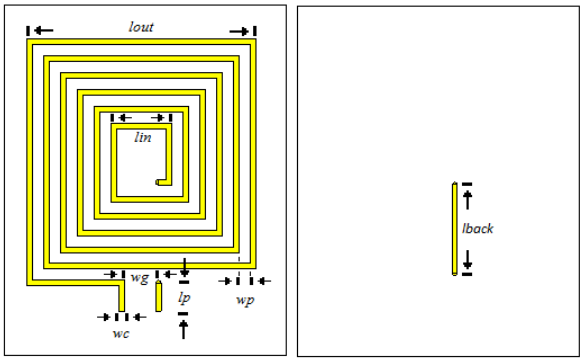

(a) (b)

Fig. 1. Antenna topology: (a) front view and (b) back view, connected by vias.

Table 1: Antenna dimensions

Parameter	Value
Outer loop length, l_{out}	41 mm
Inner loop length, l_{in}	4 mm
Strip width, w_c	1 mm
Gap width, w_g	2 mm

The transfer efficiency of a pair of antennas in an energy transfer link is calculated by [8]:

$$\eta = \frac{k^2 Q_1 Q_2}{\left(1+\sqrt{1+k^2 Q_1 Q_2}\right)^2}, \quad (1)$$

where Q_1 and Q_2 are the quality factors of the transmitting and receiving antenna respectively:

$$Q_1 = \frac{\omega L_1}{R_1}, \quad (2)$$

$$Q_2 = \frac{\omega L_2}{R_2}, \quad (3)$$

$$\omega = 2\pi f, \quad (4)$$

k is the coupling coefficient between both antennas and can be determined using:

$$k = \frac{M}{\sqrt{L_1 L_2}}. \quad (5)$$

Since the kapton layer is extremely thin, the inductance of each antenna can be computed as [9]:

$$L_{1,2} = 0.635\mu l_{avg}\left[\ln\left(\frac{2.07}{l_p}\right) + 0.18 l_p + 0.13 {l_p}^2\right], \quad (6)$$

where μ is the permeability of the background medium and,

$$l_p = \frac{l_{out} - l_{in}}{l_{out} + l_{in}}, \quad (7)$$

$$l_{avg} = \frac{l_{out} + l_{in}}{2}. \quad (8)$$

The mutual inductance between both antennas, M can be obtained using [10]:

$$M = \left(\frac{4}{\pi}\right)^2 2\sum_{i=1}^{i=N} M_i \quad \text{and}$$

$$M_i = \frac{\mu_o \pi a_i^4}{2(2a_i^4 + d^2)^{\frac{3}{2}}}\left(1 + \frac{15}{32}\gamma^2 + \frac{315}{1024}\gamma^4\right), \quad (9)$$

$$\gamma = \frac{2a_i^2}{2a_i^2 + d^2}, \quad (10)$$

where N is the number of turns and $a_i = l_{out} - (N-1)(w_c + w_g) - w_c/2$. The skin depth, δ and the resistance of each antenna are determined by using:

$$R_{DC} = \frac{\rho l}{A}, \quad \delta = \frac{\sqrt{\rho}}{\sqrt{\pi f \mu_o}}, \quad (11)$$

$$R = \frac{R_{DC}}{4\delta}\left(\frac{t_c}{1 - e^{-\frac{t_c}{\delta}}}\right), \quad (12)$$

where ρ is the resistivity of copper (1.7×10^{-8} Wm), A is the cross-sectional area of the strip, and t_c is the thickness of the copper conductor.

With reference to Fig. 1, l and A can be defined as:

$$l = 6(w_p + w_c) + l_{back} + \frac{l_{out} + w_p - w_g}{2} + l_{out} + w_p + 2(l_{out} - w_c) + 2\sum_{i=1}^{i=2N-1}(l_{out} - (i-1)\, w_p - i w_c), \quad (13)$$

$$A = w_c \; t_c. \quad (14)$$

The bandwidth of the antenna is defined as the frequency interval in between the two -3 dB points with respect to the value at the resonant frequency.

III. RESULTS AND DISCUSSION

Using described model in previous section, transfer efficiency of the antennas is calculated using Matlab. Based on the mathematical model, transfer efficiency obtained is 81.28%. However, this computation does not take the dielectric effects into consideration. Hence, full-wave simulations are employed to examine the transfer efficiencies obtained using different dielectric substrates.

There are various kapton substrates in the market, as given in Table 2. Since the kapton itself is extremely thin, it will have a negligible effect on the energy transfer

link. The copper thickness does have an effect on the efficiency of this transfer link, but it will be shown that a thickness of 18 µm already yields efficiencies near 90%. The energy transfer system uses identical antennas for transmitter and receiver at an operating distance of 14.14 mm, as shown in Fig. 2.

Table 2: Kapton with different thicknesses of substrate and copper, as available from Shengyi Technology Co, Ltd

Substrate	Dielectric Constant (μ)	Loss Tangent	Substrate Thickness	Copper Thickness
Kapton	3.6	0.031	12.5 µm	18 µm
Kapton	3.5	0.030	25 µm	18 µm
Kapton	3.5	0.030	25 µm	35 µm
Kapton	3.5	0.030	75 µm	35 µm

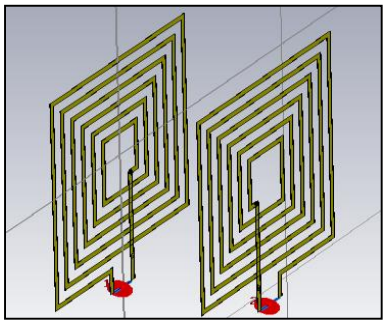

Fig. 2. Energy transfer topology.

Both antennas have been matched using the lumped element technique, see Fig. 3. Based on a compromise between efficiency, flexibility, and mechanical strength, the kapton is chosen 25 µm thick and the copper is chosen 18 µm thick. The resulting efficiency is given in Fig. 4. All simulations were done with CST Microwave Studio.

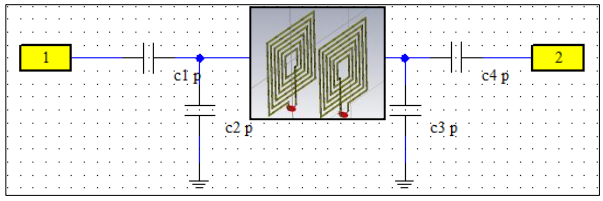

Fig. 3. Wireless link with matching networks for both antennas.

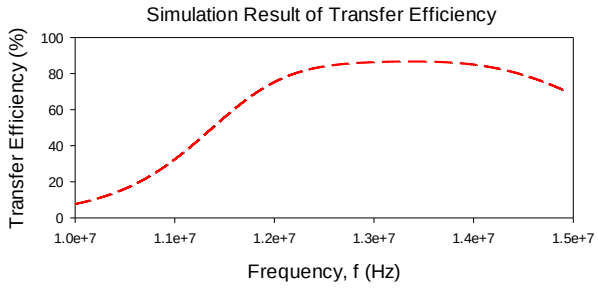

Fig. 4. Efficiency of the antenna using 25 µm kapton and 18 µm copper thickness.

The antenna was fabricated and measured, see Fig. 5. S-parameters were recorded and analyzed, and both antennas were impedance matched using lumped elements. The capacitor values available in the market nearest to the optimal values were selected, see Table 3.

It is easily shown that the efficiency of the energy transfer link $P_{received}/P_{transmitted}$ is given by $|S_{21}|^2$. This parameter is shown in Fig. 6.

Table 3: Capacitor values used in the impedance matching

	C_1 (pF)	C_2 (pF)	C_3 (pF)	C_4 (pF)
Simulation	100	60	62	100
Actual	98.61	58.89	61.23	95.71

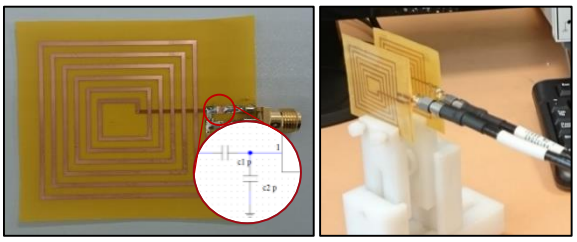

Fig. 5. Fabricated antenna and measurement setup.

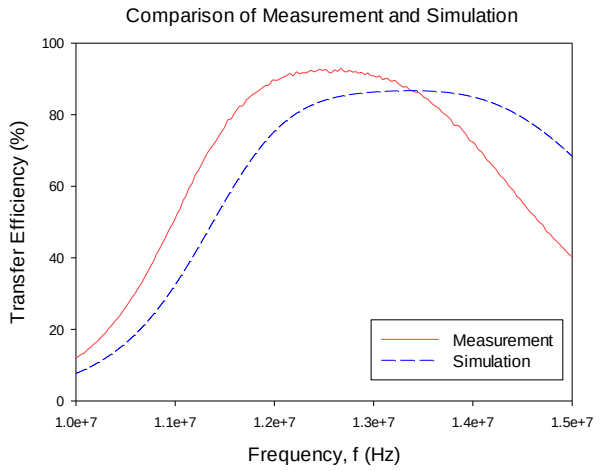

Fig. 6. Realized transfer efficiency.

At a distance of 14.14 mm, the energy transfer

efficiency achieved is as high as 86.61% and 83.82% in simulations and measurements, respectively. The difference of 2.79% with the simulated value is caused by the tolerances on the etching process, and slightly deviating distance from the simulated distance in real life.

Based on this result, it can be clearly concluded that kapton is a suitable material to be used for wireless energy transfer. Kapton can offer transfer efficiencies as high as rigid materials like FR4, with the huge advantage of adding flexibility.

Figure 7 shows that the optimal frequency of the transfer system decreases slightly when the operating distance is increased. This happens because changing the distance will alter the mutual inductance between transmitter and receiver antenna. Hence, both antennas will not be perfectly matched anymore. Therefore, at the NFC frequency, the efficiency of the wireless energy transfer is significantly changed, see Fig. 8.

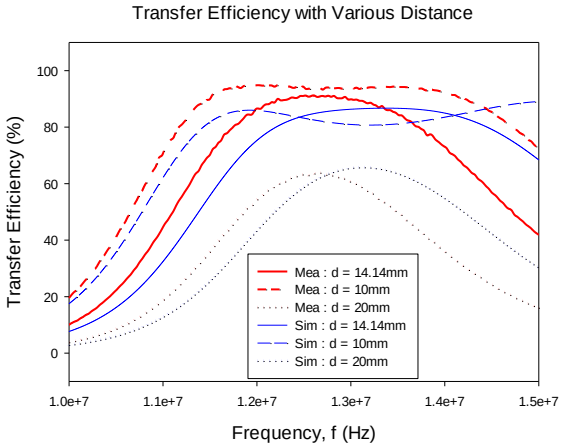

Fig. 7. Transfer efficiency as a function of frequency, simulation (Sim) and measurement (Mea) for several distances, *d*.

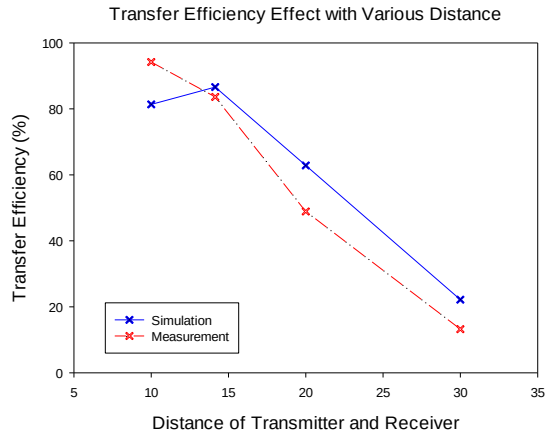

Fig. 8. Change in measurement of transfer efficiency with varying distance between antennas.

When the distance between both antennas is smaller than the optimum distance, a multi-resonance appears, as shown in Fig. 7. Multi-resonance condition will result two maximum transfer efficiencies at two different frequencies. This phenomenon is caused by an over-coupling condition, which occurs when the transmitter is too close to the receiver and creates frequency splitting phenomenon. As a result, the transfer efficiency at operating frequency will reduce significantly. The discrepancy in the trend of the change of transfer efficiency with distance between antennas for measurement and simulation is recorded. The different is contributed by the non-exist exact capacitor value for matching circuit in market. The 5% capacitors tolerance also causes the difference between measurement result and simulation result

Since we are considering a flexible substrate, bending may be an issue, since it may occur, accidentally or on purpose, in practical situations. The bending situation studied is given in Fig. 9. One of the two antennas is bent with a radius of 20 mm. Results for bending are given in Fig. 10. It is shown that bending the antenna will slightly reduce its efficiency. However, the drop of 4.5% in efficiency (from 83.6%) is acceptable.

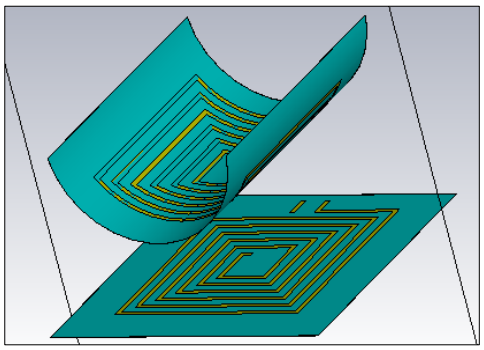

Fig. 9. Bending situation with bending radius r = 20 mm.

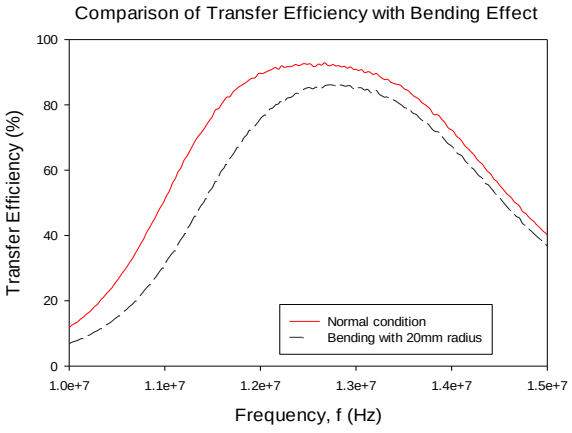

Fig. 10. Measurement for effect of bending on transfer efficiency.

Figure 11 shows that the antenna has a large bandwidth of 3.86 MHz around the operating frequency of 13.56 MHz at matching distance, 14.14 mm. This is sufficient for inductive signal transmission. This proves that antennas using kapton substrates are suitable for wireless communications as well.

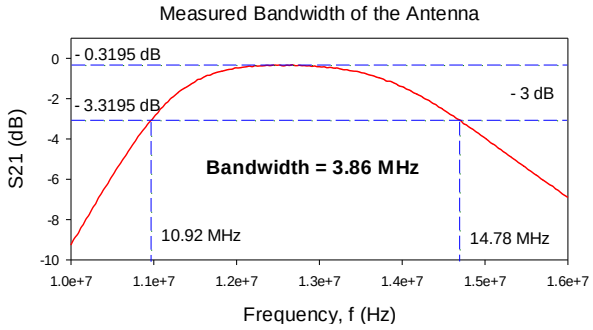

Fig. 11. Measured bandwidth of the antenna.

IV. CONCLUSION

It is shown that kapton is suitable to be used as an antenna substrate for WET purposes. Results show that this flexible material can produce high performance in terms of ETE and bandwidths, comparable to rigid substrates such as FR4. In addition, kapton is flexible, and that can increase the robustness of the antenna by enabling it to fit with any device shape.

ACKNOWLEDGMENT

This research was supported by the Ministry of Higher Education, Universiti Teknikal Malaysia Melaka and Universiti Teknologi Malaysia.

REFERENCES

[1] F. Jolani, Y. Yu, and Z. Chen, "A novel planar wireless power transfer system with strong coupled magnetic resonances," *2014 IEEE International Wireless Symposium (IWS)*, pp. 1-4, 2014.

[2] K. Mori, H. Lim, S. Iguchi, K. Ishida, M. Takamiya, and T. Sakurai, "Positioning-free resonant wireless power transmission sheet with staggered repeater coil array (SRCA)," *IEEE Antennas and Wireless Propagation Letters*, vol. 11, pp. 1710-1713, 2013.

[3] W. Lee, K. Oh, and J. Yu, "Distance-insensitive wireless power transfer and near-field communication using a current-controlled loop with a loaded capacitance," *IEEE Transactions on Antennas and Propagation*, vol. 62, no. 2, pp. 936-940, 2014.

[4] X. Yu, F. Herrault, C.-H. Ji, S.-H. Kim, M. G. Allen, G. Lisi, L. Nguyen, and D. I. Anderson, "Watt-level wireless power transfer based on stacked flex circuit technology," *2011 IEEE 61st Electronic Components and Technology Conference (ECTC)*, pp. 2185-2191, 2011.

[5] J. Choo, J. Ryoo, I. Park, J. Hong, et al., "A novel multi-loop tag for near field communication in UHF band," *APMC 2007 Asia-Pacific Microwave Conference*, pp. 1-4, 2007.

[6] A. Qusba, A. K. RamRakhyani, J.-H. So, and G. J. Hayes, "On the design of microfluidic implant coil for flexible telemetry system," *IEEE Sensors Journal*, vol. 14, no. 4, pp. 1074-1080, 2014.

[7] W. Aerts, E. De Mulder, B. Preneel, G. A. E. Vandenbosch, and I. Verbauwhede, "Dependence of RFID reader antenna design on read out distance," *IEEE Transactions on Antennas and Propagation*, vol. 56, no. 12, pp. 3829-3837, 2008.

[8] E. Strommer, M. Jurvansuu, T. Tuikka, A. Ylisaukko-oja, H. Rapakko, and J. Vesterinen, "NFC-enabled wireless charging," *2012 4th International Workshop on Near Field Communication (NFC)*, pp. 36-41, 2012.

[9] S. S. Mohan, M. Del Mar Hershenson, S. P. Boyd, and T. H. Lee, "Simple accurate expressions for planar spiral inductances," *IEEE Journal of Solid-State Circuits*, vol. 34, no. 10, pp. 1419-1420, 1999.

[10] S. Raju, R. Wu, M. Chan, and C. P. Yue, "Modeling of mutual coupling between planar inductors in wireless power applications," *IEEE Transactions on Power Electronics*, vol. 29, no. 1, pp. 481-490, 2013.

Mohamad Harris Misran was born in Johor, Malaysia He obtained his degree in B.Eng. in Electronics Engineering (Telecommunication) from University of Surrey, UK in 2006 and M.Eng. in Master of Engineering (Telecommunication) in 2008 from University of Wollongong, Ausralia. He is currently a full-time Ph.D. Research Student at the Wireless Communication Centre (WCC), Faculty of Electrical Engineering, Universiti Teknologi Malaysia (UTM), Johor, Malaysia.

Sharul Kamal Abdul Rahim received his first degree from University of Tennessee, USA majoring in Electrical Engineering, graduating in 1996, M.Sc. in Engineering (Communication Engineering) from Universiti Teknologi Malaysia (UTM) in 2001, and PhD. in Wireless Communication System from University of

Birmingham, UK in 2007. Currently, he is an Associate Professor at Wireless Communication Centre, Faculty of Electrical Engineering, UTM. His research interest is Smart Antenna on Communication System.

Akaa Agbaeze Eteng received the B.Eng. degree in Electrical/Electronic Engineering from the Federal University of Technology Owerri, Nigeria, in 2002. He obtained an M.Eng. degree in Telecommunications and Electronics from the University of Port Harcourt, Nigeria in 2008. Currently, he is working towards a Ph.D degree in Electrical Engineering at the Universiti Teknologi Malaysia.

Guy A. E. Vandenbosch received the M.S. and Ph.D. degrees in Electrical Engineering from the Katholieke Universiteit Leuven, Leuven, Belgium, in 1985 and 1991, respectively. From 1991 to 1993, he held a Postdoctoral Research position at the Katholieke Universiteit Leuven. Since 1993, he has been a Lecturer, and since 2005, a Full Professor at the same university. In the period 1999-2004, he was Vice-Chairman, and in the period 2005-2009 Secretary of the IEEE Benelux Chapter on Antennas and Propagation. Currently he holds the position of Chairman of this Chapter. In the period 2002-2004 he was Secretary of the IEEE Benelux Chapter on EMC.

Determination of Reverse-Current Coil Turns Layout to Mitigate Over-Coupling in Resonant Inductive Power Transfer Links

Akaa A. Eteng [1], Sharul K. A. Rahim [1], Chee Y. Leow [1], Beng W. Chew [2], and Guy A. E. Vandenbosch [3]

[1] Wireless Communication Centre
Universiti Teknologi Malaysia, Skudai, 81310, Johor, Malaysia
aeakaa2@live.utm.my, sharulkamal@fke.utm.my, bruceleow@fke.utm.my

[2] Intel Microelectronics
Halaman Kampung Jawa, 11900 Penang, Malaysia
beng.wah.chew@intel.com

[3] Department of Electrical Engineering
Katholieke Universiteit Leuven, Leuven, Belgium
guy.vandenbosch@kuleuven.be

Abstract ─ The transfer efficiency of two-coil resonant inductive power transfer links is known to significantly degrade with a reduction of the coil distance, due to an over-coupling at shorter distances. In this work, a simple technique is introduced to determine the spatial layout of reverse-current coil turns, which suppresses the over-coupling-induced transfer efficiency drop. By employing the spatial layout of reverse-current turns as a design parameter, the proposed method provides more generality in its implementation compared to other reverse-current turn methods. Simulation and experimental results validate the method, suggesting a potential for distance-insensitive implementations.

Index Terms ─ Inductive power transfer, mutual inductance, over-coupling.

I. INTRODUCTION

Two-coil resonant inductive power transfer links have been widely studied in recent times as wireless power transfer implementations [1]. These links typically operate within the low- and high-frequency spectral ranges, with 13.56 MHz being one of the more popular frequencies. Energy is transferred from transmitting to receiving terminals through inductive coupling. Consequently, tuned coil structures are used at the transmitter and receiver terminals to facilitate wireless power transfer. Typical applications of inductive power transfer include wireless chargers for portable household devices, power delivery to biomedical implants, in addition to numerous industrial applications [2].

Inductive coupling-based wireless power transfer links are sensitive to variations in coil positioning [3, 4]. Specifically, bringing a pair of coupled resonant coil terminals closer is known to lead to over-coupling, which is characterized by a drop in the transfer efficiency at the original link frequency, and the appearance of split resonance frequencies [4-7].

High transfer efficiency levels in the over-coupled regime may be maintained through an arrangement to track the new split-resonance frequencies [5, 6], which unfortunately increases link complexity. Alternatively, coil terminals themselves could be designed to mitigate over-coupling. Over-coupling can be controlled by introducing reverse-current turns in the coil structures, thereby providing a reverse mutual inductance to limit the increase in mutual inductance associated with the over-coupled regime [8, 9]. In [8], the required reverse mutual inductance is generated through an appropriate ratio of forward- and reverse-current turns. Nonetheless, this approach requires a rational turns-ratio in order to be physically implementable. Alternatively, the approach in [9] employs one each of forward- and reverse-current turns in a transmit coil, with a lumped capacitance controlling the ratio of currents through these turns. However, the practical performance of the realized energy transfer link using this technique may be constrained by the availability of commercial off-the-shelf (COTS) capacitors with the level of precision determined by the design process. The limitations of these reverse-current turn methods can be surmounted by a more general approach, which uses the spatial layout of reverse-current turns as the over-coupling mitigating parameter.

Consequently, this paper proposes a simple method

Submitted On: May 29, 2016
Accepted On: October 25, 2016

for determining a spatial layout of reverse-current turns to be included in a transmit coil to mitigate over-coupling. The rest of the paper is organized as follows. Section II describes the design method, while results obtained from applying the proposed method to a test scenario are discussed in Section III. The paper is concluded in Section IV.

II. DESIGN METHOD

A key aspect of the proposed method to mitigate over-coupling is the determination of mutual inductances between coupled coils. The mutual inductance between a pair of multi-turn circular transmit and receive coils separated by a distance z can be calculated using [10]:

$$M=\sum_{i=1}^{i=n_{tx}}\sum_{j=1}^{j=n_{rx}}\frac{\mu_0\pi a_i^2 b_j^2}{2\left(a_i^2+b_j^2+z^2\right)^{3/2}}\left(1+\frac{15}{32}\gamma_{ij}^2+\frac{315}{1024}\gamma_{ij}^4\right), \quad (1)$$

$$\gamma_{ij}=\frac{2a_i b_j}{a_i^2+b_j^2+z^2}, \quad (2)$$

where a_i and b_j are the radii of the *i*-th and *j*-th turns of the n_{tx}-turn transmit and n_{rx}-turn receive coils, respectively. Equations (1) and (2) can be rewritten by replacing the n_{tx} and n_{rx} turn-radii in the transmit and receive coils by average radii, such that,

$$\sum_{i=1}^{i=n_{tx}} a_i = n_{tx}a^{(a)}, \quad (3)$$

$$\sum_{j=1}^{j=n_{rx}} b_j = n_{rx}b^{(a)}, \quad (4)$$

where the superscript (a) denotes an average. Consequently, Equation (1) and Equation (2) become:

$$M=\frac{n_{tx}n_{rx}\mu_0\pi a^{(a)2}b^{(a)2}}{2\left(a^{(a)2}+b^{(a)2}+z^2\right)^{3/2}}\left(1+\frac{15}{32}\gamma^2+\frac{315}{1024}\gamma^4\right), \quad (5)$$

$$\gamma=\frac{2a^{(a)}b^{(a)}}{a^{(a)2}+b^{(a)2}+z^2}. \quad (6)$$

The transfer efficiency of the inductive link realized by coupling the transmit and receive coils can be characterized using the s-parameter transmission coefficient as [4, 11]:

$$\eta(\%)=100\times|s_{21}|^2. \quad (7)$$

For a given configuration of the receive coil, the first step in the proposed design method is to determine an appropriate transmit coil to realize an adequate transfer efficiency at the operating distance from the transmit coil z_1. Bi-conjugate matching of the coupled coils at this distance imposes a critical coupling condition on the link [3, 5]. The next step is to assume an envisaged shortest separation distance between the pair of coupled coils when put into operation, and designate this as z_3. Over-coupling between a pair of coils increases the mutual inductance. Consequently, the mitigation of over-coupling requires the introduction of a reverse mutual inductance to counteract the increase in mutual inductance for shorter separation distances [8, 9].

With the incorporation of reverse-current turns, the mutual inductance at the critical coupling distance z_1 is a superposition of forward (M_{f_1}) and reverse (M_{r_1}) mutual inductances, namely,

$$M_1 = M_{f_1} - M_{r_1}. \quad (8)$$

M_{f_1} and M_{r_1} can be calculated with Equations (5) and (6), using the appropriate average radii in the expressions, namely $a_f^{(a)}$ for the forward turns and $a_r^{(a)}$ for the reverse turns. Similarly, at the envisaged shortest distance z_3 and a chosen intermediate distance z_2, the mutual inductances are:

$$M_3 = M_{f_3} - M_{r_3}, \quad (9)$$

$$M_2 = M_{f_2} - M_{r_2}. \quad (10)$$

To mitigate over-coupling, the average radius of reverse-current turns $a_r^{(a)}$ is determined, such that the function,

$$f\left(a_r^{(a)}\right)=\left(M_2-M_1\right)-\left(M_3-M_2\right)=0, \quad (11)$$

while using the same number of reverse-current turns as there are forward-current turns in the transmit coil. The value of $a_r^{(a)}$ which satisfies Equation (11) is determined by substituting Equations (5)-(6) and (8)-(10) in Equation (11).

A good choice of intermediate distance z_2 provides a value of $a_r^{(a)}$ small enough such that the inner diameter of the receive coil just overlaps the inner diameter of the reverse-current turns of the transmit coil. This ensures that the receive coil is always under the influence of a superposition of mutual inductances from the forward- and reverse-current turns throughout the envisaged range of operating distances.

Although the widths and spacings of the reverse-current turns are not used in the approximate expressions given above, they have an impact on the coil quality factor, and thus on the transfer efficiency. A significant spacing between the additional reverse-current turns and the existing forward-current turns conceptually leads to a distributed turns coil, which may lead to a lower coil quality factor [12, 13]. Hence, it may be necessary in a second stage to adjust the spacing and width of the reverse-current turns in a full-wave electromagnetic (EM) solver in order to maintain high transfer efficiency levels. Furthermore, less variation in the transfer efficiency over the range of operating distances can be realized by slightly detuning the link at the critical coupling distance, such that the impedance match

conditions are realized at a slightly shorter distance than the critical coupling distance.

III. RESULTS AND DISCUSSION

To test the proposed design method, an initial configuration of a square transmit printed spiral coil (PSC) was modelled in CST Microwave Studio to provide a transfer efficiency above 80% at 13.56 MHz, when coupled to a square receive PSC at an axial distance of 35 mm. The PSCs were designed on low-cost FR4 substrate boards, with a dielectric constant of 4.7, and copper conductor thickness of 0.035 mm. The design parameters are described in Table 1. Note that both coils are square, which makes this a more stringent test for the technique proposed.

Figure 1 shows the full-wave EM simulation results. As the paired coils were brought closer together, the 13.56 MHz transfer efficiency of 82.63% at a 35 mm separation dropped to 25.32% at 1 mm, due to the over-coupling. The resulting percentage variation $(\eta_{\max} - \eta_{\min})/\eta_{\max}$ is 69.36%. Also, splitting of the resonance frequency is observed in the transfer efficiency profiles at distances less than 35 mm, with an increase in the gap between resonance frequencies as the coils are brought closer together.

To mitigate over-coupling the square coils were conceptually substituted with theoretically equivalent circular coils with the same enclosed area, with $b^{(a)}$ and $a_f^{(a)}$ being the average radii of the equivalent circular receive and transmit coils, respectively. An appropriate value of the average radius of reverse-current turns $a_r^{(a)}$ was then determined using Equations (5)-(6), and (8)-(11).

Table 1: Coil parameters

Parameter	Value
Transmit PSC equivalent average radius $a_f^{(a)}$	36.95 mm
Receive PSC equivalent average radius $b^{(a)}$	19.30 mm
Width of transmit PSC forward-current turns w_f	4 mm
Width of receive PSC turns w_{rx}	0.9 mm
Transmit PSC forward-current turn-spacing S_f	0.5 mm
Receive PSC turn-spacing S_{rx}	0.5 mm
Number of forward-current turns in transmit PSC n_a	2
Number of turns in receive PSC n_b	10
Operating distance z_1	35 mm
Closest distance z_3	1 mm

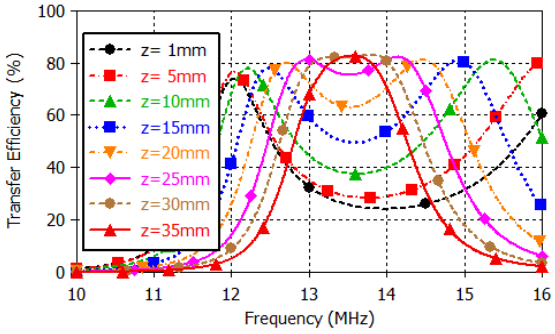

Fig. 1. Link transfer efficiency profiles using initial square transmit coil.

Figure 2 is a study of Equation (11), showing the variation of the function $f\left(a_r^{(a)}\right)$ with the average reverse-current turn radius $a_r^{(a)}$, at various values of intermediate distance z_2. It is observed that with $z_2 = 2$ mm, Equation (11) is satisfied with an average reverse-current radius of $a_r^{(a)} = 12.46$ mm. This is small enough to ensure that, using the same spacing as the forward-current turns, the inner diameter of the reverse-current turns is slightly overlapped by the inner side-length of the receive coil.

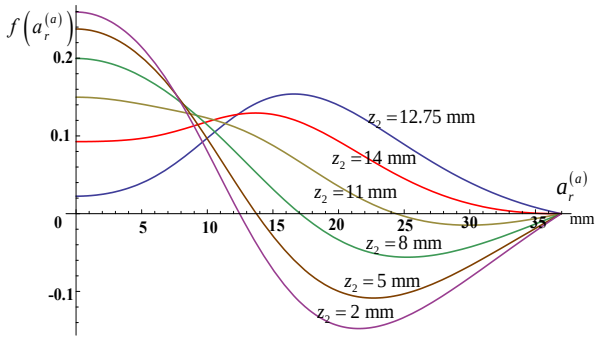

Fig. 2. Study of design Equation (11) for various values of z_2, using the coil parameters in Table 1.

For demonstration purposes, $a_r^{(a)}$ was directly used to model circular reverse-current turns in the transmit coil in CST Microwave Studio for full-wave EM simulations. In order to maintain high-transfer efficiency at the critical coupling distance of 35 mm, the width and spacing of the reverse-current turns were then adjusted to achieve a convenient threshold transfer efficiency of 77%, without altering the calculated average radius. The final designed transmit coil, hence consisted of square forward-current turns and circular reverse-current turns, as illustrated in Fig. 3.

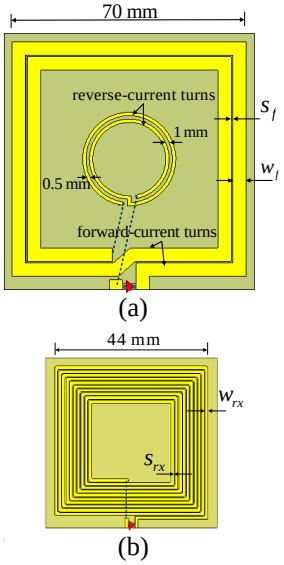

Fig. 3. Physical models of the: (a) transmit and (b) receive coils. The dotted lines show the connection between coil turns behind the substrate board.

Figure 4 shows results of a full-wave EM simulation of the designed transmit coil coupled to the receive coil in CST Microwave Studio. The link resonance condition was realized by bi-conjugate matching the coupled coils using capacitive L-match circuits, as illustrated in Fig. 5. The capacitance values are listed in Table 2. As compared to Fig. 1, the results in Fig. 4 show a marked improvement. Although some frequency splitting can still be observed at distances between 5 mm and 30 mm, the depth of the trough is significantly less than in Fig. 1. The best 13.56 MHz transfer efficiency value of 78.35% occurs at an axial distance of 30 mm, while the lowest value of 52.73% occurs at a distance of 10 mm, implying an improved percentage variation in transfer efficiency of 32.70%. The mitigation of over-coupling has, however, been achieved with a trade-off in the transfer efficiency at the original critical coupling distance of 35 mm. The initial 13.56 MHz transfer efficiency of 82.63% has dropped to 77.29%.

The over-coupling mitigation obtained in Fig. 4 was further improved by slightly detuning the link at the critical coupling distance of 35 mm. As shown in Fig. 6, this adjustment further reduces percentage variation in link transfer efficiency to 20.67%.

To experimentally validate the over-coupling mitigation arising from the inclusion of the analytically determined reverse-current turns in the transmit PSC, s-parameters were measured at different separation distances of the fabricated PSCs using a vector network analyzer, as shown in Fig. 7. The measured s-parameters were used to determine the link transfer efficiency using Equation (7). Due to measurement constraints the shortest measured distance was 5 mm.

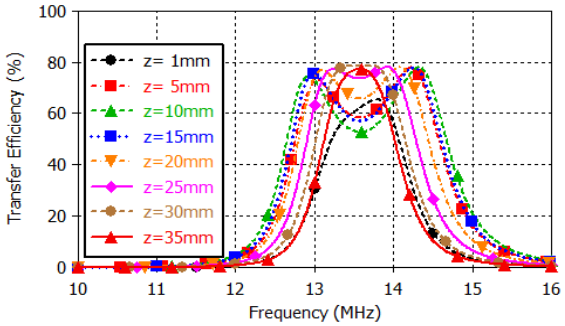

Fig. 4. Link transfer efficiency profile using modified transmit coil.

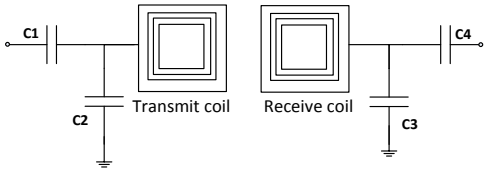

Fig. 5. Schematic representation of impedance match arrangement.

Table 2: Impedance matching capacitance values

Capacitance	Value (pF)
C1	57
C2	167
C3	22
C4	2

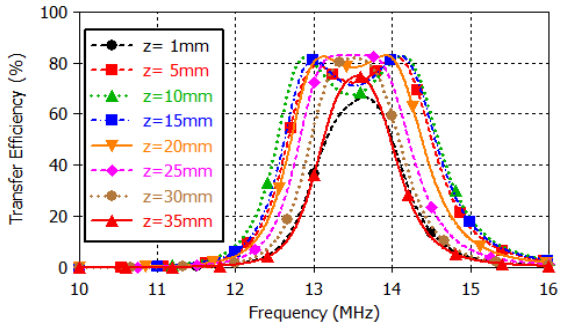

Fig. 6. Link transfer efficiency with adjustment of the critical coupling distance.

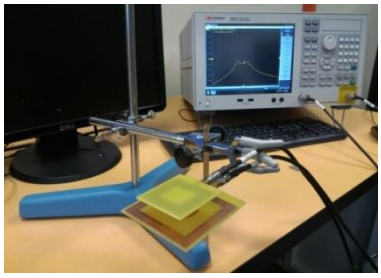

Fig. 7. Measurement set-up.

In Fig. 8, the measured 13.56 MHz transfer efficiency values are compared with the simulated results shown in Fig. 1 and Fig. 6. Trends in measured transfer efficiency using forward and reverse-current turns are in good agreement with the predicted over-coupling mitigation demonstrated by the simulation results. However, the measured transfer efficiency values at each distance were lower than the simulated values, mainly due to losses arising from fabrication inaccuracies.

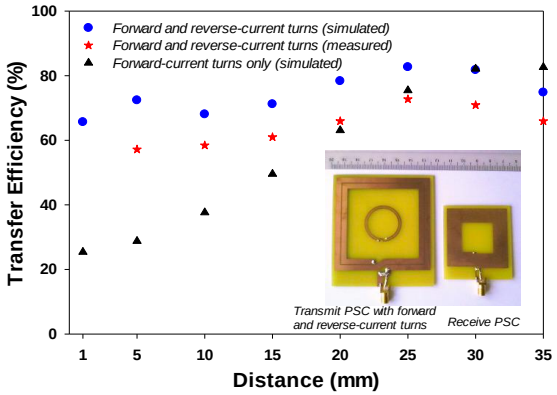

Fig. 8. Comparison of 13.56 MHz transfer efficiencies using transmit coil with forward-current turns only, and transmit coil with forward and reverse-current turns.

IV. CONCLUSION

This paper has discussed a method to suppress the over-coupling that occurs as the distance between coupled coils in a resonant inductive power transfer link reduces. The simulation and experimental results clearly show that the incorporation of reverse-current turns mitigates over-coupling effects in a resonant inductive power transfer link. The central issue addressed in this paper is the determination of the appropriate coil-turn configuration to provide adequate suppression of over-coupling. By employing the spatial layout of turns as the design parameter, the method proposed in this paper provides more generality than other contemporary reverse-current turn methods, which are either dependent on rational turns-ratios or realizable capacitive current-control.

ACKNOWLEDGMENT

This work was supported in part by the Collaborative Research in Engineering, Science and Technology (CREST) fund, Malaysia, and Universiti Teknologi Malaysia under Grant Numbers 4B151, 05H39 and 4F617.

REFERENCES

[1] S. Y. R. Hui, W. Zhong, and C. K. Lee, "A critical review of recent progress in mid-range wireless power transfer," *IEEE Trans. Power Electron.*, vol. 29, no. 9, pp. 4500-4511, Sep. 2014.

[2] X. Lu, D. Niyato, P. Wang, D. I. Kim, and H. Zhu, "Wireless charger networking for mobile devices: Fundamentals, standards, and applications," *IEEE Wirel. Commun.*, vol. 22, no. 2, pp. 126-135, 2015.

[3] W.-Q. Niu, J.-X. Chu, W. Gu, and A.-D. Shen, "Exact analysis of frequency splitting phenomena of contactless power transfer systems," *IEEE Trans. Circuits Syst. I Regul. Pap.*, vol. 60, no. 6, pp. 1670-1677, June 2013.

[4] N. Inagaki, "Theory of image impedance matching for inductively coupled power transfer systems," *IEEE Trans. Microw. Theory Tech.*, vol. 62, no. 4, pp. 901-908, 2014.

[5] A. P. Sample, D. A. Meyer, and J. R. Smith, "Analysis, experimental results, and range adaptation of magnetically coupled resonators for wireless power transfer," *Ind. Electron. IEEE Trans.*, vol. 58, no. 2, pp. 544-554, 2011.

[6] A. P. Sample, B. H. Waters, S. T. Wisdom, and J. R. Smith, "Enabling seamless wireless power delivery in dynamic environments," *Proc. IEEE*, vol. 101, no. 6, pp. 1343-1358, 2013.

[7] X. Shi, C. Qi, M. Qu, S. Ye, and G. Wang, "Effects of coil locations on wireless power transfer via magnetic resonance coupling," *Appl. Comput. Electromagn. J.*, vol. 31, no. 3, pp. 270-278, July 2016.

[8] W.-S. Lee, W.-I. Son, K.-S. Oh, and J.-W. Yu, "Contactless energy transfer systems using antiparallel resonant loops," *IEEE Trans. Ind. Electron.*, vol. 60, no. 1, pp. 350-359, Jan. 2013.

[9] W. Lee, K. Oh, and J. Yu, "Distance-insensitive wireless power transfer and near-field communication using a current-controlled loop with a loaded capacitance," *IEEE Trans. Antennas Propag.*, vol. 62, no. 2, pp. 936-940, Feb. 2014.

[10] S. Raju, R. Wu, M. Chan, and C. P. Yue, "Modeling of mutual coupling between planar inductors in wireless power applications," *IEEE Trans. Power Electron.*, vol. 29, no. 1, pp. 481-490, Jan. 2014.

[11] T. Imura and Y. Hori, "Maximizing air gap and efficiency of magnetic resonant coupling for wireless power transfer using equivalent circuit and Neumann formula," *Ind. Electron. IEEE Trans.*, vol. 58, no. 10, pp. 4746-4752, 2011.

[12] C. M. Zierhofer and E. S. Hochmair, "Geometric approach for coupling enhancement of magnetically coupled coils," *IEEE Trans. Biomed. Eng.*, vol. 43, no. 7, pp. 708-14, July 1996.

[13] A. Sharma, I. J. G. Zuazola, A. Gupta, A. Perallos, and J. C. Batchelor, "Non-uniformly distributed-turns coil antenna for enhanced H-field in HF-RFID," *IEEE Trans. Antennas Propag.*, vol. 61,

no. 10, pp. 4900-4907, Oct. 2013.

Akaa A. Eteng obtained the B.Eng. degree in Electrical/Electronic Engineering from the Federal University of Technology, Owerri, Nigeria, in 2002, and the M.Eng. in Telecommunications and Electronics from the University of Port Harcourt, Nigeria in 2008. He is currently studying for a Ph.D. degree at the Wireless Communication Centre (WCC), Universiti Teknologi Malaysia (UTM).

Sharul K. A. Rahim obtained his first degree from University of Tennessee, USA majoring in Electrical Engineering, graduating in 1996, M.Sc. in Engineering (Communication Engineering) from Universiti Teknologi Malaysia (UTM) in 2001 and Ph.D. in Wireless Communication System from University of Birmingham, UK in 2007.

Currently, Rahim is an Associate Professor at the Wireless Communication Centre, Faculty of Electrical Engineering, UTM Skudai. His research interests include antenna design, RF and microwave systems, reconfigurable antennas, beamforming networks, smart antenna systems and antennas for wireless energy transfer. He is also a Senior Member of IEEE Malaysia Section, Member of Institute of Engineer Malaysia (MIEM), Member of the Institute of Electronics, Information and Communication Engineers (IEICE) and Eta Kappa Nu Chapter (International Electrical Engineering Honour Society, University of Tennessee).

He has published a number of technical papers including journals articles, book chapters, and conference papers.

Chee Y. Leow obtained his B.Eng. degree in Computer Engineering from Universiti Teknologi Malaysia (UTM) in 2007. Since July 2007, he has been an Academic Staff in the Faculty of Electrical Engineering, UTM. In 2011, he obtained a Ph.D. degree from Imperial College London. He is currently a Senior Lecturer in the faculty and a Member of the Wireless Communication Centre (WCC), UTM. His research interest includes but not limited to wireless relaying, MIMO, physical layer security, convex optimization, communications theory, near field wireless charging and 5G.

Beng W. Chew obtained the B.Sc. degree in Electrical Engineering from University of Malaya, Kuala Lumpur, Malaysia, in 1999, and the M.Sc. degree in Microelectronics Engineering from the Multimedia University, Cyberjaya, Malaysia, in 2004. He is currently a Staff Design Engineer at Intel Microelectronics, Penang, Malaysia.

Guy A. E. Vandenbosch is a Full Professor at KU Leuven. His interests are in the area of electromagnetic theory, computational electromagnetics, planar antennas and circuits, nano-electromagnetics, EM radiation, EMC, and bio-electromagnetics. His work has been published in ca. 225 papers in international journals and has led to ca. 330 presentations at international conferences. Currently, he leads the Working Group on Software within EuRAAP, and he holds the position of Chairman of the IEEE AP/MTT Benelux Chapter. Vandenbosch is a Fellow of the IEEE since January 2013.

A Data Collection Method Based on the Region Division in Opportunistic Networks

Yaqing Ma [1], Shukui Zhang [1,2], Chengkuan Lin [1], and Lingzhi Li [1]

[1] School of Computer Science and Technology
Soochow University, Suzhou, Jiangsu 215006, China
yqma@stu.suda.edu.cn, zhangsk2000@163.com

[2] Jiangsu High Technology Research Key Laboratory for Wireless Sensor Networks
Nanjing, Jiangsu 210003, China

Abstract ─ The popularity of wearable devices and smart phones provide a great convenience for large-scale data collection. Owing to the non-uniform distribution of mobile sensors, the data quantity collected from different regions has a wide variation. So we design the region division algorithm that divides area into different density grades and sets appropriate sampling frequency on different regions. Furthermore, we propose Circle of Time Slice (CoTS) and Cardinal Number Timing Method (CNTM) to solve the sampling error when nodes move from one area to another. On this basis, we propose the Data Collection Algorithm Based on the Sampling Frequency (DC-BSF) to reduce the data redundancy. Simulations demonstrate that the method proposed in this paper can reduce data redundancy under the condition of achieving high coverage.

Index Terms ─ Data collection, region division, sampling frequency, time slice cycle.

I. INTRODUCTION

With the rapid development of mobile communication and sensing technology, a number of innovative applications and services have emerged. In particular, the popularity of portable devices (e.g., smart phones, wearable devices, etc.) and vehicle sensors (e.g., GPS), provide efficient ways to sense physical objects and environmental conditions on a large scale. It greatly expanded the dimensions of human perception and changed the way people perceive the world [1].

Mobile Crowd Sensing (MCS), where individuals with sensing and computing devices collectively share data and extract information to measure phenomena of common interest [2]. Sensor nodes collect data adaptively in the mobile process. It forms a Mobile Opportunistic Networks (MONs) when data is transferred between sensor nodes [3]. The data transmission depends on the cooperation of nodes to fulfill a "store – carry – process – forward" mode.

Sensors are embedded in a taxi and collect data periodically. Since different taxis always have heterogeneous mobility regions with some randomness, they could make different contributions to the coverage. The mobile trajectory is more intensive in hot regions, like shopping malls, stations and so on. So there are a large number of sensors in these regions. If they collect data at the same sampling frequency as sensors in sparse region, it may lead to serious data redundancy. On the contrary, the mobile trajectory is relatively sparse in remote areas. The data coverage is low in the sparse area. Sensors in these regions need to be set a higher sampling frequency. So we divide the region according to the density of taxi trajectory. Then we set the sampling frequency of sensors in regions of different density. At last, we propose an effective sensing mechanism that can reduce data redundancy in the premise of high coverage. The main contributions of this paper are shown as follows.

1) We design the Region Division algorithm (D-RG) to divide the entire area into regions of different grades, according to density of nodes' trajectory.
2) We propose the Circle of Time Slice and Cardinal Number Timing Method to solve the sampling error resulted from nodes moving from one region to another.
3) We propose the Data Collection Algorithm Based on the Sampling Frequency that can reduce data redundancy in the premise of high coverage.

The remainder of this paper is organized as follows. Section 2 reviews the related work. Section 3 describes the system model and two algorithms. In Section 4, we evaluate the performance of our model by real mobile traces. Finally, we conclude the paper in Section 5.

II. RELATED WORK

Recently the concept of mobile crowd sensing has

Submitted On: September 27, 2016
Accepted On: December 4, 2016

attracted the attention of many researchers. Challenges in this research include localized analytics, resource limitation, privacy, security, data integrity, architecture and so on [1]. The 4W1H characterize the major research issues in the MCS life cycle [4]. The noise-mapping system can intuitively present the urban noise level by encoding levels with colors [5]. COUPON is a cooperative framework for building sensing maps in mobile opportunistic network [6]. The CarTel is a distributed mobile sensor computing system [7].

As more and more sensors are integrated on mobile devices, the application field of mobile crowd sensing is constantly expanding [8]. In the paper [9], smart parking was used as a case study to investigate features of crowdsourcing that may apply to other mobile applications. Participatory sensing can be applied in environmental monitoring [10]. The Intelligent Traffic System (ITS) is based on mobile crowd sensing [11]. Smart P2P model can optimize the search process [12].

Due to the different scenarios and purposes, the type of data needed is different. So many scholars have studied the methods of data collection. ITAMP is a new sparsely adaptive algorithm with high recovery rate and fast reconstructing speed [13]. In paper [14], the data collection method of wireless sensor networks in gateway was proposed. Another data acquisition method was proposed in paper [15], heterogeneous multi-source multi-mode sensory based on data quality.

The data sensing mechanism is the key to obtaining valid data in the process of data collection. Researchers have proposed some sensing mechanisms. Researchers designed two cooperative schemes to optimize the system performances in terms of sensing quality, delivery delay and energy consumption [16]. Researchers proposed a city hot spot event sensing method based on mobile crowd sensing. This method can discover and classify hot spots [2]. Previous studies have considered the characteristics of nodes mobility and the spatial-temporal correlation among sensory data. But they ignored the moving speed of sensors, residence time in each area and the sampling error resulted from nodes moving from one region to another. In view of the above problems, we propose a new data collection algorithm. It can reduce data redundancy under the condition of achieving high coverage.

III. PERCEPTION PROCESS

In this part, we divide the entire sensing area into different grades according to the data of pre-sampling firstly. Furthermore, we propose the Circle of Time Slice and Cardinal Number Timing Method to solve the sampling error resulting from nodes moving from one region to another. Finally, we propose the Data Collection Algorithm Based on the Sampling Frequency (DC-BSF).

A. Division of sensing area

Although the movement trajectory possesses some randomness, it has characteristics of dense or sparse. The data of taxi movement trajectory is provided by Korea Advanced Institute of Science and Technology (KAIST) [17]. The graph of movement trajectory is shown in Fig. 1.

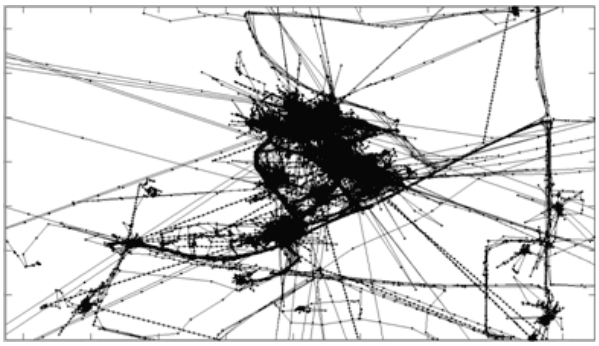

Fig. 1. The graph of taxi movement trajectory.

In order to further analyze the characteristics of the trajectory of sensors, we divide the entire sensing area into the same size grid cells $G=\{g_1,g_2\cdots,g_m\}$, and sensors $(s_1,s_2\cdots,s_n)$ are embedded in mobile vehicles [7], as illustrated in Fig. 2.

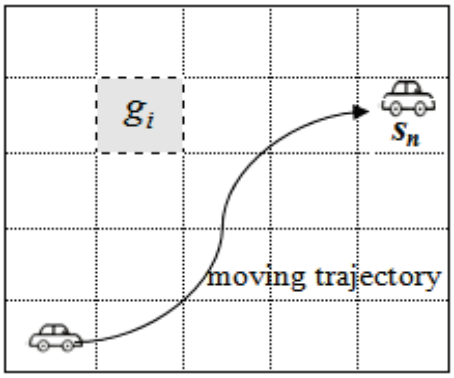

Fig. 2. The sensing area with same size grid cell.

The cell-grid (g_i) shown in Fig. 2 is the smallest unit of region division. In order to divide the sensing area according to the density of the vehicle trajectory, we need to calculate the density of trajectory firstly. The statistical method is shown in Algorithm 1. It counts the number of trajectories in each grid cell according to the data of pre-sampling.

Statistical results are stored in a table like Table 1. The a_i in the *i*-th row represents the number of trajectory in a grid cell. The u_i in *i*-th row represents the total number of grids that include a_i trajectories.

Algorithm 1: Statistical method of sampling times

```
Input:
    vecData;  // Pre sampled data
    tabsize; // Grid size
    Xnum; // the number of grid on the X axis
    Ynum; // the number of grid on the Y axis
Output:
    vecTabData; // Sampling times
    mapSumData; //the number of grid sampled n times
Initialize vecTabData is NULL;
for i ← 0 to vecData.size do
    index_x ← floor(vecData[i].x / tabsize) + 1;
    index_y ← floor(vecData[i].y / tabsize) + 1;
    // floor() is a Integral Formula.
    vecTabData[index_x][index_y]
    ←vecTabData[index_x][index_y] + 1;
repeat
for i ← 0 to vecTabData.size do
  for j ← 0 to vecTabData[i].size do
    if (mapSumData.find( vecTabData[i][j] ))
      then  mapSumData(vecTabData[i][j])
          ←mapSumData(vecTabData[i][j]) + 1;
    else
      mapSumData(vecTabData[i][j]) ← 1;
    endif
  repeat
repeat
```

Table 1: Statistical table

Number of tracks (a_i)	Number of grids (u_i)
$a_0 = 0$	u_0
$a_1 = 1$	u_1
⋮	⋮
$a_n = n$	u_n

We set a information table stored at each node and the table is dynamic. The information table includes the current time, data (collected and transmitted), sampling frequency ($f(l_k)$) and current location, as illustrated in Table 2. Current location is stored in a two-dimensional array. tab[i][j] represents that the location of a cell-grid is the i-th row and j-th column of the area. *level_k* represents that the grade of the grid is *k*. The formula *level_k* = f (l_k) in Table 1 means that the sampling frequency of sensors located in *level_k* is f (l_k).

Table 2: Storage table in sensors

Current Location	Frequency	Data	
$tab[i][j] = level\_k$	$level\_k = f(l_k)$	*Collect*	*Transmit*

The traditional K-means algorithm [18] is a typical distance-based clustering algorithm. Distance between the surrounding sensors and the center sensor was used as the evaluation index of similarity. Therefore, we propose a method based on the number of trajectory in each cell-grid to divide sensing area. We divide the entire area into three levels according to the data of Table 1. The steps are shown bellow, and the algorithm is shown in Algorithm 2;

$$sum = \frac{1}{3} \times \sum_{i=0}^{n} (a_i \times u_i), \tag{1}$$

where *sum* represents one-third of the total number of trajectory in all grids. There is a constant p that satisfies the Equation (2):

$$\begin{cases} a_0 + a_1 + \cdots + a_p \le sum \\ a_0 + a_1 + \cdots + a_p + a_{p+1} > sum \end{cases}, \ p \in [0, n). \tag{2}$$

We divide the grids that satisfy the above conditions into the region of low sampling frequency (*level_1*). As shown in Fig. 3, the different textures represent different region grades. Similarly, there is a constant q that satisfies the Equation (3):

$$\begin{cases} a_{p+1} + a_{p+2} + \cdots + a_q \le sum \\ a_{p+1} + a_{p+2} + \cdots + a_{q+1} > sum \end{cases}, \ q \in [p+1, n). \tag{3}$$

We divide the grids satisfying the above conditions into the region of intermediate sampling frequency (*level_2*), as shown in Fig. 3. The rest of the grids are divided into the region of high sampling frequency (*level_3*).

Algorithm 2: D-RG algorithm

```
Input: a_i , u_i
Output: a_p , a_q
Initialize s ← 0;
for i ← 0 to n do
    s ← s + a_i × u_i ;
    //Determine the boundary value of the level region.
    if( s >= sum ) then
        Get a boundary value: a_i ;
        s ← 0; // get the next boundary value.
    end if
repeat
```

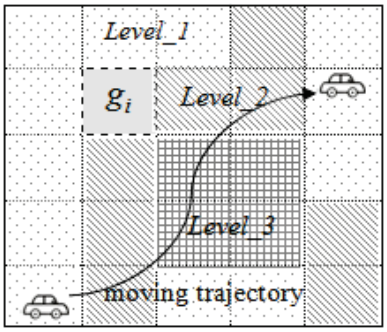

Fig. 3. The graph of region grades represented by different textures.

B. The algorithm of data collection

The sensor performs the sampling task, when the sampling time is reached and the sensor does not contain the data of the current grid. Due to the limited transmission range of sensors, the transmission delay is relatively serious. So we set different sampling frequency for sensors in different regions. Sensors can collect data according to their own sampling frequency, rather than entirely relying on collaboration with other sensors. Therefore, it can reduce the interdependence between sensors.

In the pre-sampling process, sampling period is T_1 (30 seconds). Considering the number of grids that are over-sampled and the region grade, we set the different sampling frequency for sensors in different grade regions. The time interval of sampling in *level_k* is shown bellow:

$$T_{l_k} = 2^k \times T_1 \times \frac{\sum(a_i \times u_i)}{\sum u_i},$$
$$i \in [0, p) \ or \ [p+1, q) \ or \ i \in [q+1, n], \ k = 1, 2, 3. \quad (4)$$

So the sampling frequency in *level_k* is shown below:

$$f(l_k) = \lambda \times \frac{1}{T_{l_k}}, \ (k = 1, 2, 3; \lambda \ is \ a \ constant). \quad (5)$$

In the sensing process, sensors may move from one region to another. However, the sampling frequency of sensors in these regions is different. If sensors stay in one region for a short time, it may miss some data. From the trajectory of the sensor in Fig. 4, we can see that the sensor moves to the *level_2* region and then leaves here. Under the condition of the same speed, the sensor stays in the *level_2* region for a short time. If the dwell time is much shorter than the sampling interval of the sensor, the data in that region may be missed.

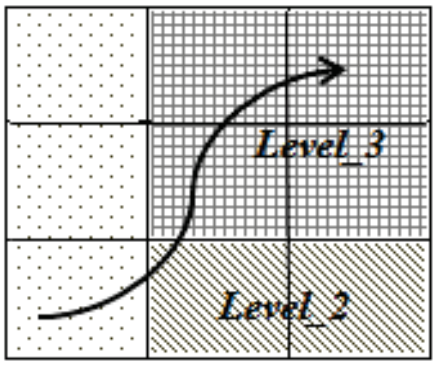

Fig. 4. Moving trajectory in different grade regions.

So we propose the Circle of Time Slice (CoTS) and Cardinal Number Timing Method (CNTM) to solve the sampling error resulted from sensors moving from one area to another. The Time Slice aims to divide the time axis into many short time periods. The sampling interval is much longer than the time slice. CoTS means that sensors check information at the beginning of each time slice. The sensor requires checking its current location, whether it contains the data of current grid and whether it has reached the sampling time. CNTM is a method of calculating time length, as shown in Equation (6):

$$cur\_time = cur\_time - \frac{const\_init\_time}{time\_k}, \quad (6)$$

where *cur_time* indicates how long it takes to reach the sampling instants. The *time_k* represents the sampling interval in *level_k* region. The *const_init_time* is the lowest common multiple of *time_k* (k = 1, 2, 3). After a time slice, the *cur_time* is shortened by *const_init_time*/ *time_k*. This also ensures that the longer the sampling interval, the more times that sensors check information during the sampling interval. The data collection algorithm based on the sampling frequency is shown as follows.

Algorithm 3: DC-BSF

Input: *time_k*, *const_init_time*, *transimit_length*
Output: the data required;
Initialize *cur_time* ← *const_init_time*;
while(during the sampling time **) do**
  if(current location is included in level_k **) then**
    cur_time = *cur_time*−*const_init_time* / *time_k*;
    // the circle of time slice
  end if
  for i ← 0 **to** n **do**
    Traverse all nodes;
    if(*dis* <= *transimit_length* **) then**
      // *dis* is the distance between two nodes.
      Process and forward the collected data;
    end if
  repeat
  if(*cur_time* <= 0 &&
    Data of current grid is not included in the node.**)**
  then Perform sampling task;
  end if
repeat

C. Analysis of algorithm

In algorithm DC-BSF, T, $x * y$, n and m respectively represent the sampling period, the number of grids in the entire area, sensors and grids that have been sampled. The algorithm is mainly completed in a while circulation and the total number of circulation is t. The following three steps are performed in each cycle.

1) Sensors check the grade of the region that the sensor is located and the sampling interval in this grade. So the time complexity in this part is

$\Theta\left((\log_2 x)\times\log_2 y\right)$.

2) Sensor nodes transmit data between each other. The time complexity in this part is $\Theta\left(n\times x\times y\times(\log_2 x)\times\log_2 y\right)$.

3) Sensor nodes check whether it contains the data of current grid. The time complexity in this part is $\Theta\left((\log_2 x)\times\log_2 y\right)$.

So the time complexity of algorithm DC-BSF is $\Theta\left(t\times n\times x\times y\times(\log_2 x)\times\log_2 y\right)$.

IV. PERFORMANCE EVALUATION

In order to verify the feasibility and superiority of DC-BSF, we carry out the following evaluation based on the real mobility traces provided by Korea Advanced Institute of Science and Technology [17]. The simulation platform we used is Opportunistic Network Environment (ONE) [19]. ONE is a free simulation platform developed in Java language. It can be used to simulate Opportunistic Network and Delay Tolerant Network. The simulation parameter is shown in Table 3.

Table 3: Simulation parameter

Parameter	Value
Time	35ks (about 10 hours)
Area	30km×30km
The number of nodes	92
Communication range	100m
Size of level_k	500m
λ	0.5; 0.8; 1; 1.5; 2; 5
Size of grid	100; 200… ; 900; 1000m

We evaluate the feasibility of DC-BSF algorithm in terms of coverage and data redundancy as follows.

In Fig. 5, we compare the coverage with various values of λ by ten sizes of grid from 100 to 1000 m. The legend in this figure represents different grid size. We can obviously find that the coverage rate increases with the increase of λ regardless of the size of grid. When the coefficient of sampling frequency (λ) increases from 0.2 to 0.8 the coverage rate increase greatly, but the coverage level is low. When λ > 0.8, the coverage rate reaches a high level and keeps stable. So the optimum range of λ is from 0.8 to infinity considering the coverage rate only.

Data redundancy is an inevitable problem under the condition of high coverage rate. In order to reach the best compromise between coverage rate and data redundancy, we compare the data redundancy with various values of λ by ten sizes of grid from 100 to 1000 m. And the simulation parameter is shown in Table 3. From Fig. 6, we can see that the DC-BSF can achieve a lower data redundancy and the data redundancy increases slowly when λ is less than 2. On the contrary, the data redundancy is large and increases rapidly when λ > 2. So the optimum range of λ is from negative infinity to 2 considering the data redundancy only.

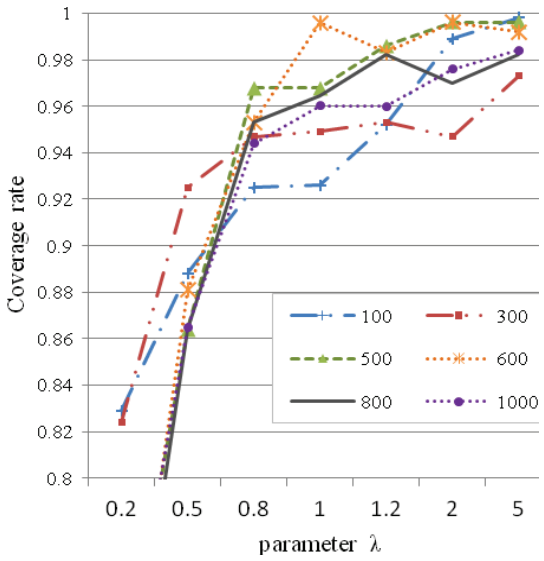

Fig. 5. Coverage rate with various values of λ.

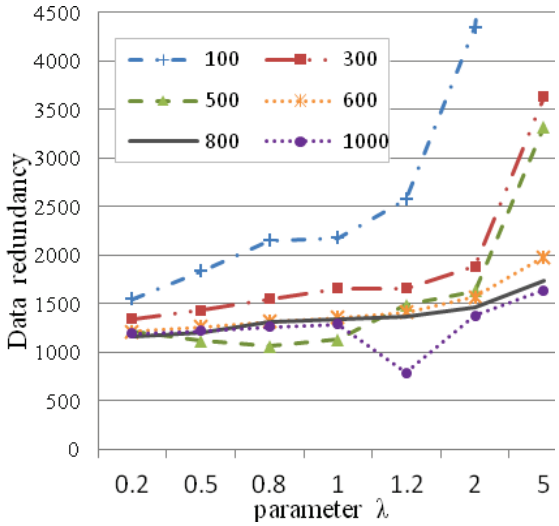

Fig. 6. Data redundancy with various values of λ.

Therefore, considering the best compromise between coverage rate and data redundancy, we take the intersection of the two parts. From the two sets of simulation above, we can get a conclusion that the optimum range of λ is from 0.8 to 2. It means that the data collection method based on the sampling frequency can reduce data redundancy in the condition of achieving

high coverage when the range of λ is from 0.8 to 2.

The simulation results above verified the feasibility of the method we proposed. In order to verify the efficiency of DC-BSF proposed in this paper, we compare it with Cooperative Sensing (CS) [6] in terms of coverage and redundancy. The Cooperative Sensing method is based on spatial-temporal correlation among sensory data.

We have $\lambda = 1$ in our DC-BSF and set the parameter k=1 in CS. Other parameters in the simulation are the same as in Table 2. As shown in Fig. 7, we compare the DC-BSF with CS about the coverage rate by using ten kinds of grid size. These two methods both get a high coverage rate and the gap between them is small. And then from Fig. 8, we can see that compared to the data redundancy of CS, it is significantly less of DC-BSF. So the method we proposed in this paper outperforms the CS relatively, although the DC-BSF does not achieve its best performance.

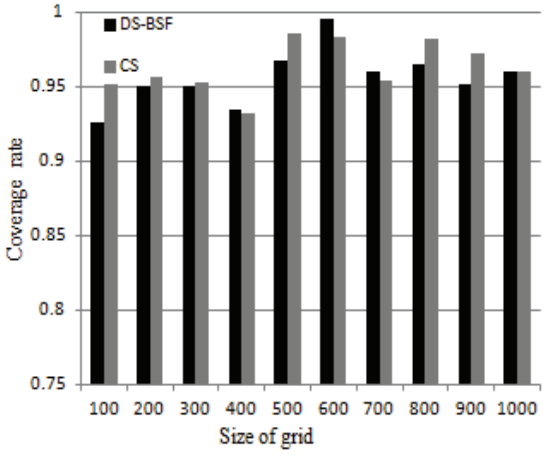

Fig. 7. Coverage rate of two kinds of sampling mechanisms in different grids.

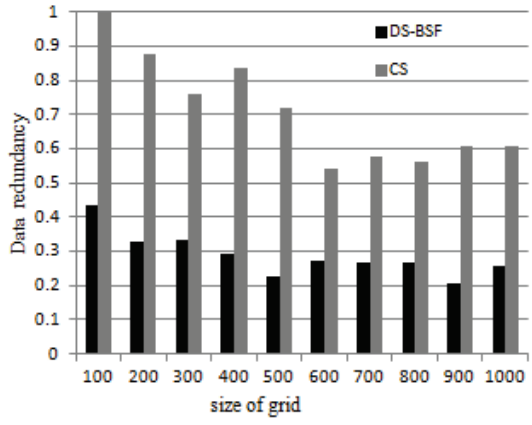

Fig. 8. Data redundancy of two kinds of sampling mechanisms in different grids.

V. CONCLUSION AND FUTURE WORK

In this paper, we propose the Division of Region Grade algorithm to divide the entire area into three regions of different grades. Furthermore, we put forward two concepts: CoTS and CNTM. These two methods can solve the sampling error resulting from nodes moving from one area to another. Last but not least, we proposed the Data Collection Algorithm Based on the Sampling Frequency that can reduce data redundancy in the premise of high coverage.

The model proposed in this paper has strict constraints. In the future, we plan to further study and improve it.

ACKNOWLEDGMENT

This work is supported by National Natural Science Foundation of China under Grants No. 61070169, 61201212, 61572340 and Natural Science Foundation of Jiangsu Province under Grant No. BK2011376 and Production-Teaching-Research Prospective of Jiangsu Province No. BY2012114 and Suzhou Key Laboratory of Converged Communication No SKLCC2013XX, SZS0805 and Application Foundation Research of Suzhou of China No. SYG201239 and "Six Talent Peak" high-level personnel selection and training foundation of Jiangsu Province under Grant No. 2014-WLW-010.

REFERENCES

[1] R. K. Ganti, F. Ye, and H. Lei, "Mobile crowd sensing: Current state and future challenges," *IEEE Communications Magazine*, vol. 49, no. 2, pp. 32-39, 2011.

[2] B. Guo, Z. Yu, X. Zhou, et al., "From participatory sensing to mobile crowd sensing," *IEEE International Conference*, pp. 593-598, 2014.

[3] P. Luciana, P. Andrea, and C. Marco, "Opportunistic networking: Data forwarding in disconnected mobile ad hoc networks," *IEEE Communications Magazine*, vol. 44, no. 11, pp. 134-141, 2006.

[4] D. Zhang, L. Wang, H. Xiong, et al., "4W1H in mobile crowd sensing," *IEEE Communications Magazine*, vol. 52, no. 8, pp. 42-48, 2014.

[5] W. Wu, B. Guo, and Z. Yu, "Crowd sensing based urban noise map and temporal-spatial future analysis," *Journal of Computer-Aided Design & Computer Graphics*, vol. 26, no. 4, pp. 638-643, 2014.

[6] D. Zhao, H. Ma, S. Tang, et al., "COUPON: A cooperative framework for building sensing maps in mobile opportunistic networks," *IEEE Transactions on*, vol. 26, no. 2, pp. 392-402, 2014.

[7] B. Hull, V. Bychkovsky, Y. Zhang, et al., "CarTel: A distributed mobile sensor computing system," *ACM*, pp. 125-138, 2006.

[8] H. Huang, Q. Ding, and L. Li, "Research on mobile terminal crowdsourcing," *Computer and*

Development, vol. 24, no. 6, pp. 6-9, 2014.
[9] X. Chen, N. E. Santos, and M. Ripeanu, "Crowdsourcing for on street smart parking," *New York, NY, USA: ACM*, pp. 1-8, 2012.
[10] V. Kotovirta, T. Toivanen, R. Tergujeff, et al., "Participatory sensing in environmental monitoring experiences," *Proc of 2012 Sixth International Conferences on IMIS*, Palermo: [s. n.], pp. 155-162, 2012.
[11] K. Ali, D. Al Yaseen, A. Ejaz, et al., "CrowdITS: Crowdsourcing in intelligent transportation systems," *IEEE Conferences on WCNC*, pp. 3307-3311, 2012.
[12] G. Chatzimilioudis, A. Konstantinidis, C. Laoudias, et al., "Crowd sourcing with smart phones," *IEEE Internet Computing*, vol. 16, no. 5, pp. 36-44, 2012.
[13] L. Lv, "Research on data acquisition and reconstruction algorithm of Internet of things sensor based on compressed sensing theory," *Nankai University*, pp. 1-95, 2011.
[14] L. Yao, Z. Zhao, N. An, and W. Wen, "Data acquisition and processing of wireless sensor networks in gateway," *Chinese Journal of Scientific Instrument*, pp. 1577-1578, 2008.
[15] Q. Ma, Y. Gu, T. Zhang, and G. Yu, "A heterogeneous multi-source multi-mode sensory data acquisition method based on data quality," *Chinese Journal of Computers*, vol. 36, no. 10, pp. 2120-2131, 2013.
[16] D. Zhao, "Research on data collection and incentive mechanisms in mobile crowd sensing network," *Beijing University of Posts and Tele-communications*, 2014.
[17] H. Xia, J. Chen, M. Marathe, et al., "Synthesis and refinement of detailed subnetworks in a social contact network for epidemic simulations," *4th International Conference on Social Computing, Behavioral-cultural Modeling and Prediction*, pp. 366-373, 2011.
[18] J. Liu, *Introduction to Social Network Analysis [M]*. Social Science Academic Press, 2004.
[19] J. Sun, *Opportunistic Network Routing Algorithm*. Post & Telecom Press, 2013.

Yaqing Ma is a student in the school of Computer Science and Technology, Soochow University, Suzhou, China. Her research interests include Wireless Sensor Networks, mobile computing and Mobile crowd sensing.

Shukui Zhang received his Ph.D. degree in Computer Science from the University of Science and Technology of China. Currently, he is a Professor and Doctoral Supervisor in the School of Computer Science and Technology at the Soochow University. His main research interest is ad hoc and wireless sensor networks, mobile computing, distributing computing, intelligent information processing, parallel and distributed systems etc. School of Computer Science and Technology, Soochow University, Suzhou, 215006, P.R. China.

Cheng-Kuan Lin received his B.S. degrees in Science Applied Mathematics from the Chinese Culture University in 2000; and received his M.S. degrees in Mathematic from the National Central University in 2002. He obtained his Ph.D. in Computer Science from the National Chiao Tung University in 2011.

His research interests include graph theory, design and analysis of algorithms, discrete mathematics, wireless sensor networks, mobile computing, wireless communication, wireless applications, and parallel and distributed computing.

Lingzhi Li received the Ph.D. degree in Computer Application from Nanjing University of Aeronautics and Astronautics in 2006. He is working as an Associate Professor in School of Computer Science & Technology, Soochow University, Suzhou, China. His research interests include network coding, vehicular network and wireless networks.

Design of Parabolic Reflector Antenna with Two Directional Cosecant-Squared Pattern Using Curve-Deformation Equations

Ki-Bok Kong

Kukdong Telecom
78-43 Beagilheon-Ro, Bujeok-Myun, Nonsan-City, Chungnam, 320-862 Republic of Korea
kbkong@kaist.ac.kr

Abstract ─ A Ka-band doubly curved reflector antenna for a warning radar system for the road was designed based on the curve-deformation equations. This antenna requires a cosecant-squared radiation pattern in the vertical and horizontal planes. Using curve-deformation equations, the shaped reflector antenna was designed to satisfy the desired beam pattern. The curve-deformation equations include the parameters which determine the shape of the curve, and these parameters are obtained by the optimization process. The simulated result shows the designed antenna satisfies the specifications of the antenna for the road radar system.

Index Terms ─ Cosecant squared pattern, parabolic antenna.

I. INTRODUCTION

Radar is widely used to detect the obstacles and to avoid collisions on the road and airport surfaces [1]-[2]. In order to survey a wide range, the power received from the reflector antenna needs to be uniform for a fixed height. The relationship between the uniform received power and the distance between the object and the antenna can be defined by the cosecant-squared function [3]. The cosecant-squared pattern can be achieved by displacing the reflector surface from the original parabolic shape [4]-[7]. Recently, the analytical regularization method (ARM) [5] was used to produce the cosecant square pattern in the vertical plane. This method solves a two-dimensional integral equation with Dirichlet boundary condition corresponding to the reflector's surface. The geometry of a reflector is generated by continuous segments that are defined using parameterization of different length and bending angles. This contour is a two-dimensional closed curve, from which the cosecant-squared pattern is obtained in the vertical plane. In this paper, the equations of the cosecant-squared patterns in the horizontal and vertical plane will be derived using the ARM's parameterization process. Instead of solving differential equations, the parameter optimization method is used to synthesize the desired reflector. Invasive weed optimization is one method that determines the optimum values of the coefficients of a distribution polynomial using the optimization process [2]. In this optimization process, if the coefficients of the distribution polynomial are given, then the radiation pattern can be obtained using commercial software, and this pattern is compared to the cosecant-squared pattern. This procedure continues until the desired pattern is obtained. Here, the optimization process will be used to acquire the optimum values of the parameters corresponding to the bending angle and length of a curve. These parameters determine the curvature in the direction of the vertical and horizontal planes.

II. DESIGN OF ANTENNA

A. Curve-deformation equations

The formula is based on the parameterization equations of ARM [5]. In order to define the formula concerning the geometry of a cosecant-squared pattern reflector, each interval of the geometrical curve is divided as follows:

$$\frac{2L_k\pi}{L} - \pi \le \theta < \frac{2L_{k+1}\pi}{L} - \pi, \tag{1}$$

where $L_0 = 0$, $L_1 = 2\,a\tan(\alpha/2)$, $\alpha = \alpha_2 - \alpha_1$, $L_{k+1} = L_k + r_k$, $r_0 = r_1 = 0$, $k = 0, \dots, N_{max}$, and $L = \sum_1^{N_{max}} L_k$.

As shown in Fig. 1, α_1 and α_2 are the angles between the *x*-axis and the end points of the non-shaped section, and a is the focal length of the parabolic reflector. In (1), N_{max} indicates the number of splitting of $[-\pi, \pi]$ and a parameter r_k determines the length of the k-th section. The non-shaped section is defined as the function of a parameter θ and is as follows:

$$x_1(\theta) = -\frac{2a\cos(\psi)}{1+\cos(\psi)}, \tag{2}$$

$$y_1(\theta) = \frac{2\,\mathrm{asin}(\psi)}{1+\cos(\psi)}, \tag{3}$$

where $\psi = \psi(\theta) = \alpha_2 - \alpha(\theta + \pi)L/(4\pi a\tan(\alpha/2))$, and $\theta \in [-\pi,\ 2L_1\pi/L - \pi]$. Note that, if ψ is cancelled

Submitted On: March 9, 2016
Accepted On: November 17, 2016

from (2) and (3), then we have the original parabolic equation with respect to parameters *x*, *y*:

$$x = \frac{y^2}{4a} - a. \tag{4}$$

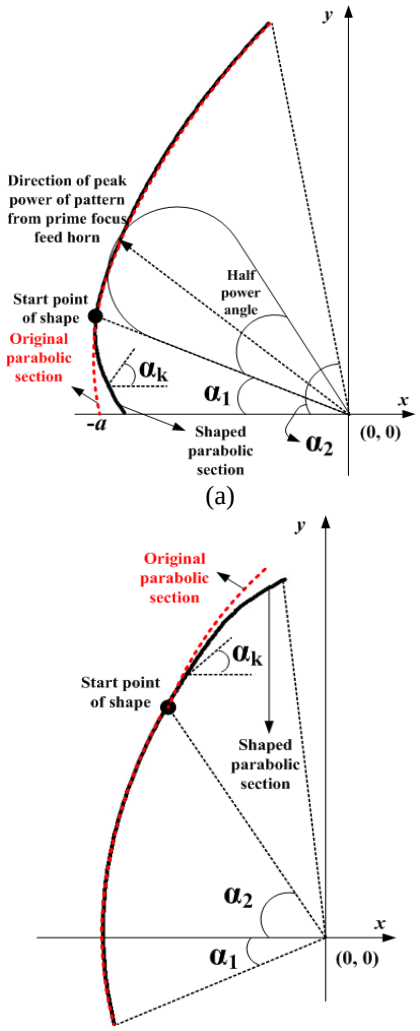

Fig. 1. (a) Geometry of the shaped reflector with the cosecant-squared pattern directed at a positive angle, and (b) at a negative angle.

The graph of Equation (4) is plotted as indicated by the red dotted line in Fig. 1. The k-th section of the shaped curve of an antenna with cosecant-squared pattern can be represented by a function of parameter ϕ, which is defined on the interval $\phi \in [2L_{k-1}\pi/L - \pi, 2L_k\pi/L - \pi]$, and the line when ϕ is varying is as follows:

$$x_k(\phi) = -2\,\mathrm{acos}(\alpha_1)/(1+\cos(\alpha_1)) + \left(\frac{(\phi+\pi)L}{2\pi} - L_{k-1}\right)\cos(\alpha_k) + \sum_{i=3}^{k} r_i \cos(\alpha_i), \tag{5}$$

$$y_k(\phi) = 2\,\mathrm{asin}(\alpha_1)/(1+\cos(\alpha_1)) - \left((\phi+\pi)L/2\pi - L_{k-1}\right)\cos(\alpha_k) - \sum_{i=3}^{k} r_i \sin(\alpha_i), \tag{6}$$

where $\alpha_k > 0, k = 2, 3, \ldots, N_{max}$, and the last summation $\sum_{i=3}^{k} *$ is zero when $k = 2$.

In Equations (5) and (6), α_k is the bending angle of the k-th section. Using Equations (2) to (6), the shaped reflector of the cosecant-squared pattern in the vertical plane can be obtained by determining α_i and r_i. As shown in Fig. 1 (a), the sections of the shaped parabolic curve are located on the lower part of the non-shaped section. Thus, the cosecant-squared pattern appears at positive angle. However, in order to detect an object on the road, the cosecant beam should be directed at a negative angle. For this purpose, modifications of (5) and (6) are needed. First, the parameters for the translation are defined as:

$$x_{max1} = \max\{x_1(\phi) | \phi \in [-\pi,\ 2L_1\pi/L - \pi], y_1(\phi) \geq 0\},$$
$$x_{max2} = \max\{x_1(\phi) | \phi \in [-\pi,\ 2L_1\pi/L - \pi], y_1(\phi) < 0\},$$
$$y_{max} = \max\{y_1(\phi) \mid \phi \in [-\pi,\ 2L_1\pi/L - \pi]\},$$
$$y_{min} = \min\{y_1(\phi) \mid \phi \in [-\pi,\ 2L_1\pi/L - \pi]\},$$

and

$$x_{move} = \begin{cases} x_{max1} & \text{if } \alpha_1 \geq 0 \\ x_{max1} - x_{max2} & \text{if } \alpha_1 < 0' \end{cases}$$
$$y_{move} = y_{max} - y_{min}.$$

The function that determines the curve of the reflector with the cosecant-squared pattern directed at a negative angle can be expressed as:

$$x'_k(\phi) = x_2(\phi) + \sum_{i=3}^{k} r_i \cos(\alpha_i) + x_{move}, \tag{7}$$

$$y'_k(\phi) = y_2(\phi) + \sum_{i=3}^{k} r_i \sin(\alpha_i) + y_{move}. \tag{8}$$

Using (7)-(8), the geometry of an elevation direction of reflector can be obtained. The deformation process of an azimuth direction of reflector is carried out on each fraction of partition of the z range. For a fixed point (x_0, y_0) of the shaped curve shown in Fig. 1, the right side of a curve on the transverse section of a $x-z$ plane through y_0 is expressed as a coordinate system (x, z):

$$\text{For } z \in [z_{j-1}, z_j] \subset [0, z_{max}],$$
$$x = c_j \frac{z^2}{4a} + x_0, \tag{9}$$

where a parameter c_j determines the deformation level of the j-th section, and is less than 1. The left section of the curve can be symmetrically obtained from the right section.

B. Design of reflector using curve-deformation equations

The antenna for the detection radar system requires the specifications presented in Table 1. As shown in Fig. 2, this antenna was installed at a height of 6 m, and was

designed to detect within a band of road 20 m wide.

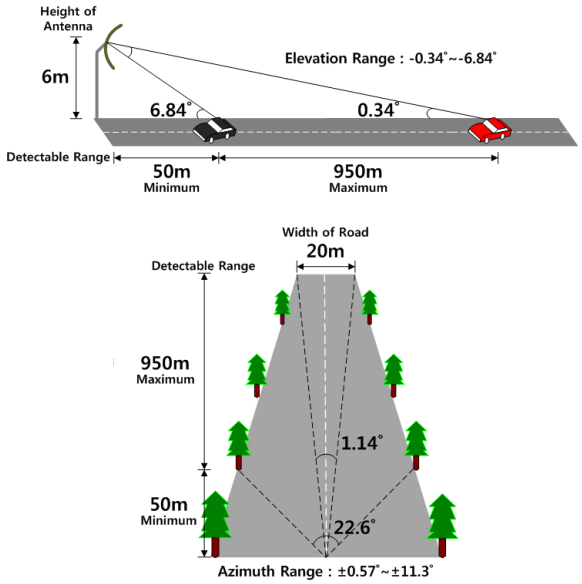

Fig. 2. Range of the detection by the radar system.

Table 1: Specifications of antenna

Parameter	Horizontal	Vertical
Frequency	34.5 GHz	34.5 GHz
Maximum gain	32 dBi	32 dBi
Cosecant-squared region	1.14°~7.62°	0.34°~2.29°
Size of antenna	0.20×0.217 m^2	

The measurable distance from the antenna to the target by this radar system is between 150 and 1000 m. In order to obtain the desired cosecant-squared pattern, the values of α_i, r_i, and c_j have to be determined. The first step of the process is to determine the region of the curve that is deformed. Considering the half-power of the radiation pattern of the feed horn, the outside of the half-power angle of the feed pattern was selected as the area of deformation, as shown in Fig. 1.

The shaped curve is approximated by N_{max} sections. In this paper, N_{max} was set to 8. The next step was to select the initial parameters (α_i, r_i, and c_j) randomly. These parameters were inserted into the deformation Equations (7)-(9), and the three-dimensional geometric data was obtained. These data were imported into CATIA (commercial software), and the surface of the reflector was designed and saved as a CATIA file. This surface file was imported into CST (commercial software), and the radiation pattern of the reflector was obtained using CST. Then, this pattern was compared to the desired cosecant-squared pattern. If the difference error between the simulated pattern and the desired pattern is greater than the tolerance limit, then the parameters have to be corrected. The tolerance limit means the acceptable difference error between the desired pattern and the selected pattern. The tolerance limit function can be defined in the same way as introduced in [2]. This process continues until the pattern is well fitted to the desired patterns. Figure 3 (a) shows the geometry of the designed reflector antenna. The focal length was 0.15 m and the offset angle was 35°. The size of the reflector was 0.20×0.217 m^2. Because the cosecant deformation of a reflector is performed in the azimuth and elevation directions, the upper edge of the reflector is inclined toward the aperture along the vertical direction, and the lower edge is bent back along the azimuthal direction, as shown in Figure 3 (b). Table 2 shows the optimized values of the parameter in the curve-deformation equations. The parameter r_i determines the length of shaped curve and, we set the parameter r_i as the same value 0.0189 for all $i > 1$.

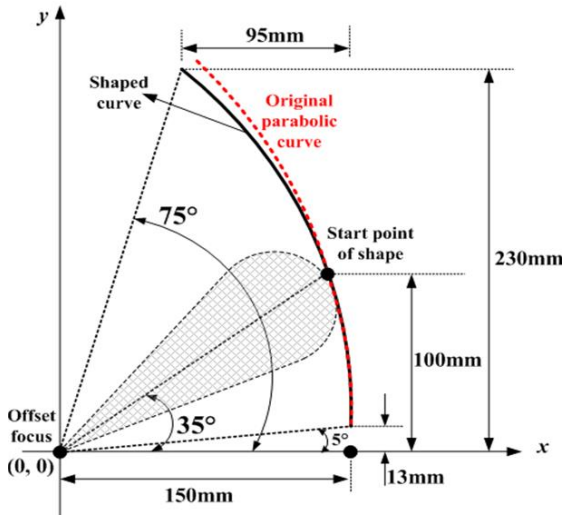

(a) Geometry of the shaped parabolic reflector

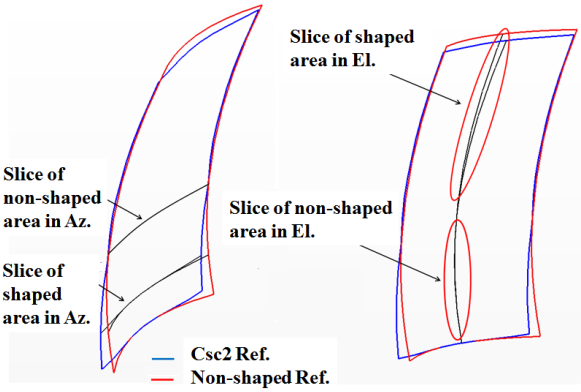

(b) Comparison with the non-shaped parabolic reflector depicted by CST

Fig. 3. Shaped reflector antenna and comparison with the non-shaped parabolic reflector.

Table 2: Parameters of curve-deformation equations

Parameter	Value [degree]	Parameter	Parameter
α_1	5	c_1	1.0
α_2	37	c_2	0.96
α_3	71	c_3	0.92
α_4	65	c_4	0.88
α_5	62	c_5	0.84
α_6	60	c_6	0.8
α_7	57.5	c_7	0.72
α_8	54.5	c_8	0.64
α_9	53.5	c_9	0.56
α_{10}	51.5	c_{10}	0.48

III. RESULTS OF SIMULATION

A. Measurement of radar system

The newly designed antenna was simulated by CST in order to obtain the radiation patterns. To be agreed with the cosecant-squared pattern using the curve-deformation equations, designing a cosecant antenna is performed in the early stage of the optimization. The results of the radiation patterns of the main beam are displayed at Fig. 4. The beamwidths of the radiation patterns are 2.1° and 4.2° in the azimuthal and elevation directions respectively and the gain is 33.2 dBi. To achieve the desired pattern of Fig. 4, around five to eight optimization procedures are enough. We calculated errors between the desired pattern and the designed pattern using CST. The parameters of the deformation Equations (7)-(9) are corrected to optimized values. But in this case, only the pattern at zero angle was obtained, and in order to get the broad beam, the beamwidth, gain and patterns at each angle must be considered. Moreover, the monopulse beam pattern at each angle also have to be considered because it is used to detect the exact location of the debris on the road. The optimization process have to continue until the desired gain distribution at the detection area as shown at Fig. 5 are obtained, and 8~10 optimization steps were carried out.

The gain of Fig. 5 was obtained proportional to the square of the distance, which means the gain loss of the antenna.

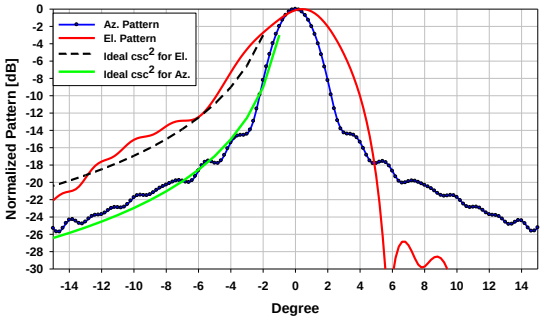

Fig. 4. Radiation pattern obtained from the first optimization step.

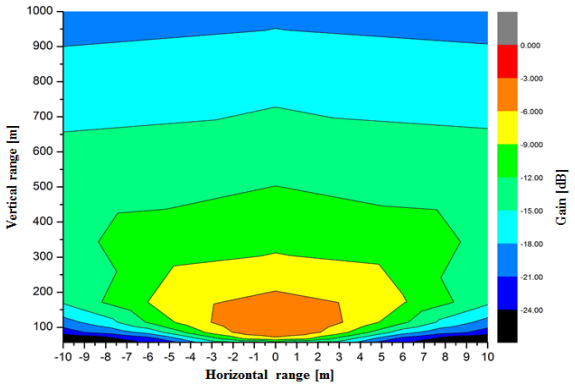

Fig. 5. Gain distribution on the detection area.

Figure 5 shows that the designed antenna has a wide broad cosecant beam directed in a downward direction, which is suitable for detecting objects on the road. Figure 6 displays the power distributions of a sum and a delta pattern of the final designed cosecant antenna. In Fig. 7, these patterns are compared with the desired cosecant-squared patterns. The dual-mode horn antenna for a monopulse feed system was used to obtain the sum and difference beams. The beamwidth used as the edge taper was 14 dB and 18 dB, in the azimuth and elevation planes, respectively. Because the range of the degree satisfying the cosecant-squared pattern is very narrow, the shaped curve was designed to have a wide beamwidth in order to achieve the cosecant-squared pattern. Even though the pattern did not agree well with the cosecant-squared curve, the antenna had higher gain, and the difference monopulse pattern had wider beamwidth, than would an antenna with a pattern well-fitted to the cosecant-squared region over the wide region. As shown in Table 1, the cosecant regions of horizontal and vertical directions were 1.14°~7.62° (=±3.81°) and 0.34°~2.29°, and the radiation patterns of the main beam presented in Fig. 7 satisfied the desired cosecant-squared level. Figure 8 shows the horizontal sections of the radiation pattern of the reflector antenna when the elevation angles varied from 0° to −5°. In the case of the sum patterns, the maximum gain of the main horizontal section was 32 dBi, and the beam peak decreased according to the main vertical section of the pattern. The difference between the maximum gain of 0° sum pattern and that of a 4° sum pattern was only 3 dBi. The sum patterns also maintained the shape and the beamwidth, and satisfied the desired cosecant-squared level. This means that the antenna is designed to be suitable for detecting the debris all over the surface. The difference pattern can be used to determine accurately the angular location of the target. The gap between the null point and the peak point of the difference pattern was almost 5°, and it is sufficient to determine the angular location of the target because the maximum angle in the azimuthal direction within the detection area

is ±3.81°.

Figure 9 shows the monopulse curve that represents the difference between the gain of the sum pattern and the gain of the difference pattern.

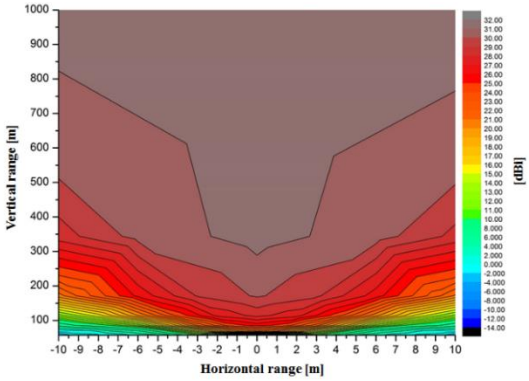

(a) Distribution of sum signals of monopulse antenna along the range

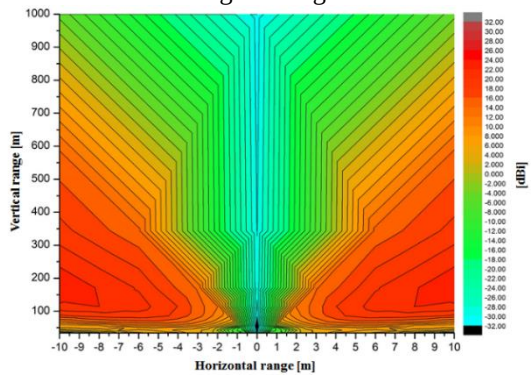

(b) Distribution of delta (or difference) signals of monopulse antenna along the range

Fig. 6. Power distribution of the final designed cosecant antenna along the range of detection.

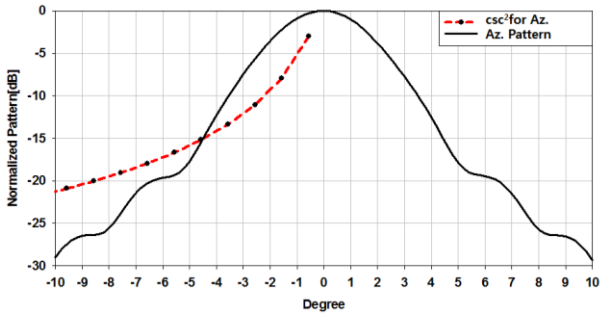

(a) Azimuth radiation pattern

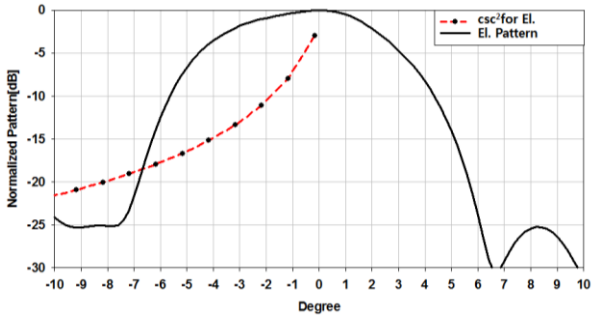

(b) Elevation radiation pattern

Fig. 7. Comparison of a designed pattern with an ideal csc^2 pattern.

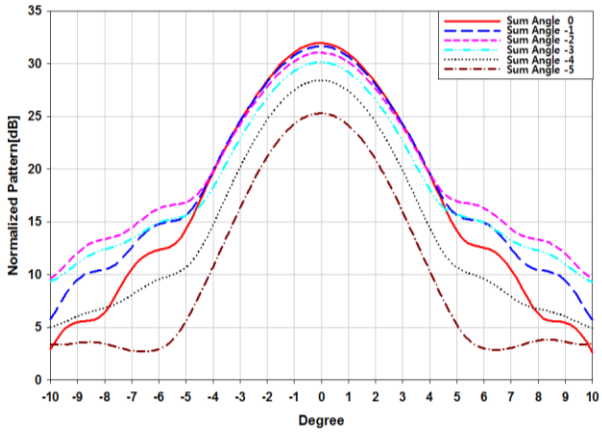

(a) Monopulse sum pattern

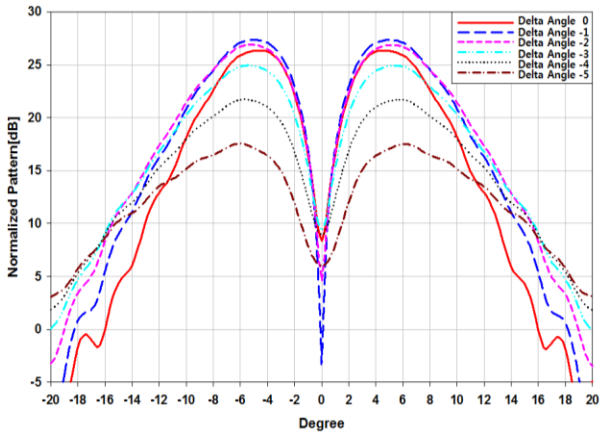

(b) Monopulse difference pattern

Fig. 8. Azimuthal section of the radiation pattern of the reflector varying elevation angles.

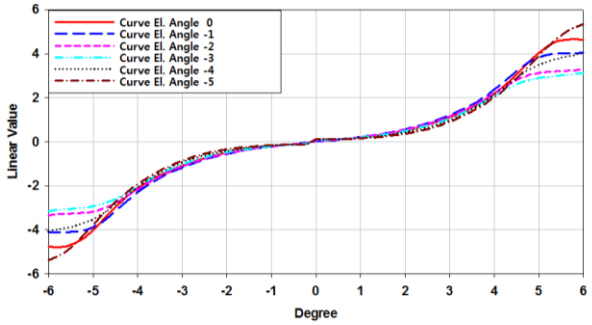

Fig. 9. Monopulse curve.

IV. CONCLUSION

The Ka-band shaped reflector antenna was designed based on a curve-deformation equation. The deformation of the surface was performed in the vertical and horizontal directions. The cosecant-squared patterns in the vertical and horizontal planes were obtained by simulation using the CATIA and CST software packages. These patterns satisfied the specifications of the antenna for a detection radar system for the road. The method herein presented can be used to design antennas for the detection of foreign-object debris on airport surfaces, for surveillance radar, and for the ship-mounted surface radar.

V. ACKNOWLEDGMENT

This work was supported by the Ministry of Education (MOE) and National Research Foundation of Korea through the Human Resource Training Program for Regional Innovation (NRF-2013H1B8A2032190).

REFERENCES

[1] S. Futatsimori, K. Morioka, A. Kohmura, and N. Yonemoto, "Design and measurement of W-band offset stepped parabolic reflector antennas for airport surface foreign object debris detection radar systems," *International Workshop on Ant. Tech. Conference*, pp. 4-6, 2014.

[2] A. Dastranj, H. Abiri, and A. Mallahzadeh, "Design of a broadband cosecant-squared pattern reflector antenna using IWO algorithm," *IEEE Ant. and Propag*., vol. 61, pp. 3895-3900, 2013.

[3] R. S. Elliott, *Antenna Theory and Design*. Wiley, 2003.

[4] A. Brunner, "Possibilities of dimensioning doubly curved reflectors for azimuth-search radar antennas," *IEEE Trans. Ant. and Propag*., Ap-19, pp. 52-57, 1971.

[5] A. S. Turk, "Analysis of aperture illumination and edge rolling effects for parabolic reflector antenna design," *Int. J. Electron. Commun*., vol. 60, pp. 257-266, 2006.

[6] G. A. Suedan and E. J. Edward, "Beam diffraction by planar and parabolic reflectors," *IEEE Trans. Ant. and Propag*., vol. 39, pp. 521-527, 1991.

[7] L. Shung-Wu and Y. Rahmat-Samii, "Simple formulas for designing an offset multibeam parabolic reflector," *AP-29*, pp. 472-478, 1981.

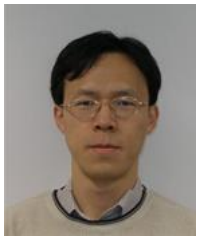

Ki-Bok Kong received the B.S. degree from Kyung-Pook National University, in 1992, and the M.S. and Ph.D. degree from Korea Advanced Institute of Science and Technology, Daejeon, in 1999 and 2003, respectively, all in Applied Mathematics. Since 2011, he has been with Kukdong Telecom as a Leader of Development Team. His research interests include parabolic antenna, and analytical and numerical method of electromagnetics.

Compact Broad Band-Stop Filter with Circular Fractal-Shaped Stubs for X-Band Radar Applications

Mohammad Pourbagher, Javad Nourinia, and Changiz Ghobadi

Depertment of Electrical Engineering
Urmia University, Urmia, Iran
armanpurbaqer@yahoo.com, ch.ghobadi@urmia.ac.ir, j.nourinia@urmia.ac.ir

Abstract ─ In this letter, we use the fractal structures to design a novel compact band-stop filter with prominent cut-off sharpness and wide stop-band for X-band applications. By cutting five U-shaped slots on the ground plane and by inserting five Fractal- Shaped stubs in the microstrip transmission line, the proposed structure is created hence a constant and flat impedance bandwidth at the X-band can be produced. The operating frequencies of the filter can be easily controlled by changing the protruded fractal-shaped stubs dimensions, without changing the area taken by the structure. The experimental results show good agreement with simulation results and demonstrate that excellent stop-band performance could be obtained through the proposed band stop filter.

Index Terms ─ Band-stop filter, circular fractal-shaped stubs, defected ground plane, X-band applications.

I. INTRODUCTION

Conventionally the microwave Band-Stop Filter (BSF) is implemented either by all shunt stubs or by series connected high-low stepped-impedance microstrip line sections. However, generally these are not easily available in microwave band due to the high impedance microstrip line and the spurious pass-bands. To remove these disadvantages, defected ground structures for microstrip lines have been presented in recent years. They have been presented in a number of different shapes for filter applications [1-2]. This technique is suitable for periodic structures, and for both band-stop and band-pass filters, e.g., [3]-[4]. The Defected Ground Structure (DGS) applied to a microstrip line causes a resonant character of the structure transmission with a resonant frequency controllable by changing the shape and size of the slot.

This paper introduces a DGS with U-shaped slots. The resonant behavior of the DGS used here introduces transmission zeroes to the filter response and consequently improves its stop-band performance. The proposed structure is designed based on the fractal structures. By using this priodical structure, we have a constant and flat impedance bandwidth at the X-band frequency range. The designed filter has a small dimension of $10\times15\times0.635\ mm^3$.

II. BAND-STOP FILTER DESIGN AND CONFIGURATION

The proposed quasi-elliptic band-stop filter configuration with apertures under the high-impedance transmission lines is shown in Fig. 1. In general, the cut-off frequency of the microwave band-stop filter can be adjusted by setting proper values of the lumped elements of the filter [5]. In addition, to realize the desired capacitive and inductive values of the filter elements by the stubs of the high/low impedance transmission lines, the characteristic impedance and effective dielectric constant of these transmission lines have to be determined. The band-stop filter in Fig. 1 was designed and fabricated on a Rogers RT/Duroid 5880 substrate with 0.635 mm in thickness and with a relative dielectric constant of 2.2. Defected Ground Structure (DGS) evolved from Photonic Band Gap (PBG) is realized by etching defected pattern and slot in the ground plane. The etched defect in ground plane disturbs the shield current distribution in the ground plane. This disturbance can increase the effective capacitance and inductance of a transmission line respectively. Thus, an LC equivalent circuit can represent the proposed unit DGS circuit [1-2]. The proposed DGS slot is shown in Fig. 1 (b). The slot is etched in the ground metallization under the microstrip line. This slot has a major advantage in providing tighter capacitive coupling to the line in comparison to known microstrip DGS. Moreover, the resonant frequency of the structure can be controlled by changing the distance between the U-shaped slots. The resonant frequency of the slot can be modified by changing the overall slot size, which shifts the cut-off frequency of the filter down. To shift the frequency up instead of frequency back, it is necessary to reduce the inductance of the narrow strip-line that is located over the slot. This can easily be done by increasing the width of the strip [6]. The final values of presented band-stop filter design parameters are specified in Table 1.

Submitted On: January 9, 2016
Accepted On: October 4, 2016

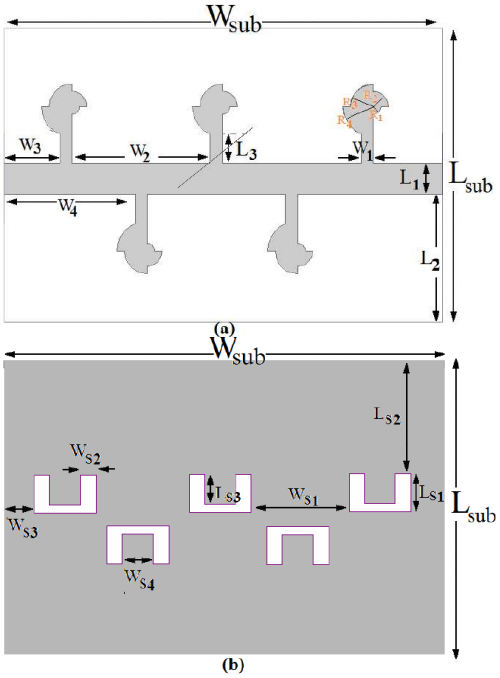

Fig. 1. Geometry of proposed microstrip filter: (a) top view and (b) bottom view.

Table 1: Optimal dimensions of proposed filter

Parameter	Value (mm)	Parameter	Value (mm)	Parameter	Value (mm)
W_1	0.4	L_2	4.5	W_{S1}	3
W_2	4.6	R_1	0.25	W_{S2}	0.5
W_3	2.3	R_2	0.5	W_{S3}	1.5
W_4	4.8	R_3	0.75	W_{S4}	1
L_1	1	R_4	1	L_{S1}	1.25
L_{S2}	3.5				

III. RESULTS AND DISCUSSIONS

The microstrip band-stop filter, as shown in Fig. 1, was designed on both substrate sides by opening apertures in the ground metallization under the high-impedance transmission line. Replacing some of the apertures by the proposed U-shaped structure introduces transmission zeroes. The number of transmission zeroes is equal to the number of apertures pairs according to centre in this case this number is three [6]. For the input/output connections 50-Ohm microstrip lines are used. The simulated results are obtained using the Ansoft simulation software high-frequency structure simulator (HFSS) [7], [8]. To minimize physical size of the proposed low-pass filter and increase its bandwidth, five U-shaped slots on the ground plane and five fractal-shaped stubs in the microstrip transmission line inserted to alter the input impedance characteristics. Figure 2 shows the return/ insertion loss characteristics of the various filter used for simulation studies. From the result in Fig. 2 (a), it is observed that when five U-shaped slots on the ground plane and five fractal-shaped stubs in the microstrip transmission line are used, the return loss of the proposed filter is increased amount of transmission zeros in the insertion loss. As shown in Fig. 2 (b), the five U-shaped slots on the ground plane and five fractal-shaped stubs in the microstrip transmission line also influence the bandwidth of the insertion loss. The proposed transmission line structure can be used to extend the lower edge frequency and the upper edge frequency of the insertion loss bandwidth.

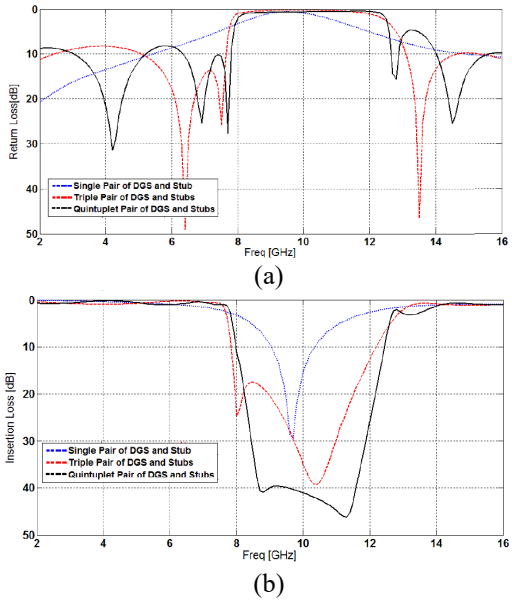

Fig. 2. Simulated return/insertion loss characteristics for the various filter structures: (a) return loss and (b) insertion loss.

To minimize physical size of the proposed band-stop filter and increase its bandwidth, four steps of semi-circular fractal-shaped open stubs are introduced into the microstrip transmission line to alter the input impedance characteristics.

Return/insertion loss characteristics for the structure of the various filter used for simulation studies are compared in Figs. 3 (a) and (b). From the result in Fig. 3 (a), it is observed that when four steps of semi-circular fractal-shaped open stubs are used, the return loss of the proposed filter is changed at lower frequencies. As shown in Fig. 3 (b), the semi-circular fractal-shaped open stubs also influence the bandwidth of the insertion loss.

The proposed transmission line structure can be used to extend the lower edge frequency and the upper edge frequency of the insertion loss bandwidth. The proposed filter with optimal design, as shown in Fig. 4, was fabricated and tested in the Antenna Measurement Laboratory at Urmia University. Figure 5 shows the

simulated and measured insertion and return loss of the filter.

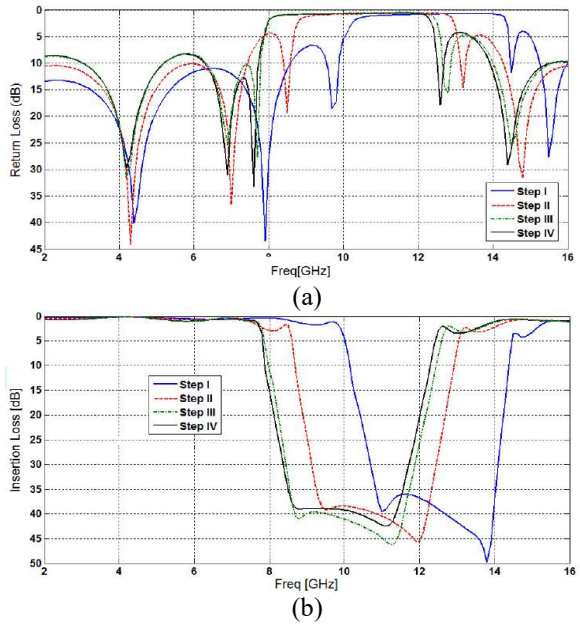

Fig. 3. Simulated return/insertion loss characteristics for the various steps of Koch-Snowflake fractal structures: (a) return loss and (b) insertion loss.

Fig. 4. Photograph of the realized printed band stop filter: (a) top view and (b) bottom view.

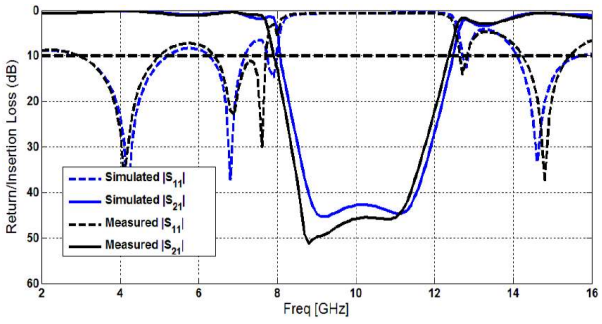

Fig. 5. Measured and simulated return/insertion loss for the proposed band stop filter.

As shown in Fig. 5, a flat insertion and return losses are introduced to the filter response at about 8.02 to 12.07 GHz. Consequently a wide stop-band was achieved. Additionally, the proposed DGS band-stop filter also has characteristics of wider and deeper stop-band than those of conventional band-stop filters [9], [10]. As shown in Fig. 5, there exists a discrepancy between measured data and the simulated results. This discrepancy is mostly due to a number of parameters such as the fabricated filter dimensions as well as the thickness and dielectric constant of the substrate on which the filter is fabricated, the wide range of simulation frequencies and also the effect of SMA [10], [11]. In order to confirm the accurate return loss characteristics for the designed antenna, it is recommended that the manufacturing and measurement process need to be performed carefully, besides, SMA soldering accuracy and RT/Duroid substrate quality needs to be taken into consideration.

IV. CONCLUSION

In this paper, a novel band-stop microstrip filter by using a modified defected ground structure is presented for satisfying X-band applications. By cutting five U-shaped slots on the ground plane and by inserting five fractal-shaped stubs in the microstrip transmission line, the proposed structure is created; hence, a constant and flat impedance bandwidth at the X-band can be produced. The desired resonant frequencies are obtained by adjusting the number of U-shaped slots on the ground plane. Also, in order to enhance the impedance bandwidth characteristic five fractal-shaped stubs are inserted in the microstrip transmission line. Prototypes of the proposed filter have been constructed and studied experimentally. The measured results showed good agreement with the numerical prediction and good flat insertion and return losses characteristics.

REFERENCES

[1] D. S. La, Y. H. Lu, S. Y. Sun, N. Liu, and J. L. Zhang, "A novel compact bandstop filter using defected microstrip structure," *Microw. Opt. Tech. Lett.*, vol. 53, pp. 433-435, Feb. 2011.

[2] X.-H. Wang, B.-Z. Wang, H. Zhang, and K. J. Chen, "A tunable band-stop resonator based on a compact slotted ground structure," *IEEE Trans Microwave Theory Tech.*, vol. 55 pp. 1912-1918, 2007.

[3] A. Faraghi, M. N. Azarmanesh, and M. Ojaroudi, "Small microstrip low-pass filter by using novel defected ground structure for UWB applications," *Applied Computational Electromagnetics Society (ACES) Journal*, vol. 28, no. 4, pp. 341-347, Apr. 2013.

[4] J Mazloum, A Jalali, and M Ojaroudi, "Miniaturized reconfigurable band-pass filter with electronically controllable for WiMAX/WLAN applications," *Microwave and Optical Technology Letters*, vol. 56, no. 2, pp. 509-512, 2014.

[5] L. H. Weng, Y. C. Guo, X. W. Shi, and X. Q. Chen, "An overview on defected ground structure," *Progress In Electromagnetics Research B*, vol. 7, pp. 173-189, 2008.

[6] W. D. Yan and R. R. Mansour, "Compact tunable bandstop filter integrated with large deflected actuators," *IEEE MTT-S International Microwave Symposium*, Honolulu, HI, pp. 1611-1614, 2007.

[7] Ansoft Corporation, Ansoft High Frequency Structure Simulation (HFSS), Ver. 13, Ansoft Corporation, Pittsburgh, PA, 2010.

[8] S. Pirani, J. Nourinia, and C. ghobadi, "Design of a small modified microstrip lowpass filter with folded U-shaped defected ground structure," *18th Iranian Conference on Electrical Engineering (ICEE)*, Tehran, 2011.

[9] M. Ojaroudi, N. Ojaroudi, R. Habibi, and H. Ebrahimian, "Microstrip low-pass filters by using novel defected ground structure slot with a pair of protruded T-shaped strips inside the slot," *Advanced Electromagnetic Symposium, AES 2012*, Paris, France, Apr. 16-19, 2012.

[10] M. Pourbagher, N. Ojaroudi, J. Nourinia, and C. Ghobadi, "Compact band-stop filter for X-band transceiver in radar applications," *Applied Computational Electromagnetics Society (ACES) Journal*, vol. 30, no. 4, pp. 423-428, Apr. 2015.

[11] A Faraghi, M. Ojaroudi, and N. Ghadimi, "Compact microstrip low-pass filter with sharp selection characteristics using triple novel defected structures for UWB applications," *Microwave and Optical Technology Letters*, vol. 56, no. 4, pp. 1007-1010, 2014.

RCS Validation of Asymptotic Techniques Using Measured Data of an Electrically Large Complex Model Airframe

Ciara Pienaar [1], Johann W. Odendaal [1], Johan Joubert [1], Johan C. Smit [2], and Jacques E. Cilliers [2]

[1] Department of Electrical Electronic and Computer Engineering
University of Pretoria, Pretoria, South Africa
u11175070@tuks.co.za, wimpie@up.ac.za, jjoubert@up.ac.za

[2] Defence Peace Safety and Security
Council for Scientific and Industrial Research, Pretoria, South Africa
jcsmit@csir.co.za, jcilliers@csir.co.za

Abstract ― This paper validates the accuracy with which various asymptotic techniques including RL-GO and SBR can calculate the RCS of an electrically large complex airframe. This target has a maximum electrical length of 106λ. Two CEM packages are utilized namely, CST MWS and FEKO. The simulated RCS results are compared to measured RCS data, obtained in a compact range. The effect of the 3D CAD model accuracy on the simulation accuracy is also investigated. Comparisons between simulated and measured RCS data are provided using RCS plots and ISAR images.

Index Terms ― Asymptotic methods, CAD model accuracy, RCS measurements, validation.

I. INTRODUCTION

Radar cross section (RCS) modelling and simulation has a wide range of applications in the field of radar and electronic warfare (EW). These include platform detectability analysis, the generation of test data for development and testing of radar and EW systems, as well as signature database generation for applications such as non-cooperative target recognition (NCTR). For these applications it is important that calculated radar signatures of targets are accurate and obtained within reasonable timeframes. The accuracy of calculated RCS results depends on a few factors. Two of the factors, investigated in this study, include the accuracy of the 3-dimensional (3D) computer aided design (CAD) model of the target, as well as the computational electromagnetic (CEM) method utilized.

It was shown in [1] that the overall shape of targets CAD models, as well as small geometric features on the models can have an impact on the RCS scattering characteristics. The differences between four aircraft CAD models were investigated using simulated data and quantified using different contour-based shape descriptors. The four targets included a Pilatus PC-21, an F-16 fighter jet, and two models of the same aircraft, namely a Cessna 172.

The second factor contributing to the simulation accuracy is the CEM method. Asymptotic CEM techniques are generally used for RCS predictions of electrically large complex targets. Numerous asymptotic techniques are available, which are capable of solving electrically large scattering problems within timeframes that are a fraction of the time required by full-wave methods. Some of these methods include physical optics (PO), geometrical optics (GO), the physical theory of diffraction (PTD), ray-launching GO (RL-GO), as well as shooting and bouncing rays (SBR).

In [2], a new efficient ray-tracing algorithm for the calculation of RCS, based on PO and PTD, was presented. This method was evaluated by comparing the monostatic RCS simulations of a few different targets, with either full-wave method of moments (MoM) results or RCS measurements used as reference. The targets investigated included a thin and thick flat plate, trihedral corner reflector, generic cruise missile and two aircraft models. The RCS results obtained for the first four targets were compared to MoM simulation results. Good agreements between the results were observed. The first aircraft target was a 1:32 scaled model with an electrical length of 60λ. The simulated results for this aircraft were compared to measured RCS data, with rather good agreement observed. The physical model used in the RCS measurements was manufactured using the simulated CAD model. High range resolution (HRR) profiles of both aircraft targets, scaled to original size, were generated using the data calculated with the PO and PTD algorithm, and compared to one another. It was observed that the objects could be distinguished based on these profiles.

Recently a study evaluated the suitability of three

Submitted On: February 25, 2016
Accepted On: November 27, 2016

CEM techniques, including the multilevel fast multipole method (MLFMM), PO and PO with SBR, for RCS calculations of electrically large targets [3]. Three targets were used for the analyses, and included a trihedral corner reflector, generic cruise missile similar to that used in [2], and the high fidelity Cessna 172 model used in [1]. Only simulated RCS results were considered, with MLFMM data used as reference for the comparisons. It was shown that the RCS of the corner reflector and generic cruise missile calculated with the PO and PO with SBR methods compared well with the MLFMM results.

In [4], the measured and simulated RCS data of a Boeing 777 scale model, with electrical length of 20λ, was compared. A commercially available 3D CAD model of the aircraft was simulated using the CADRCS software package. This package implements PO combined with ray-tracing and shadowing to calculate the RCS of objects. Although good correspondence between the main features in the RCS diagrams were obtained, differences were still observed which highlighted the need for different techniques to fully represent the RCS of an object.

In [5], the accuracy and efficiency with which full-wave and asymptotic CEM methods could predict the RCS of a large complex airframe was investigated. This study utilized the same physical 1:25 scale model of a Boeing 707 that was used in an installed antenna performance investigation [6]. RCS measurements of this target were obtained in a compact range at the University of Pretoria, South Africa. The methods that were validated included PO, PO with SBR and MLFMM. Three EM simulation packages were utilized in this study, viz. CST Microwave Studio (MWS), FEKO and SigmaHat. All of the methods showed good agreement with the measured data over the important azimuth ranges where the main features were found.

This paper serves to illustrate the effects of different options and asymptotic technique implementations on the simulated RCS results for a realistic representation of a large and complex model airframe. Measured RCS data of a conducting Boeing 707 scale model, with an electrical length of 106λ, is used to illustrate the effect of the geometrical accuracy of CAD models on calculated RCS results. Simulated data of a generic CAD model, constructed from canonical structures [6], and a laser scanned CAD model, generated from the physical airframe, are compared to the measured RCS results obtained in a compact range. Secondly, the accuracies of a few different implementations of asymptotic techniques to calculate the RCS of the large complex airframe are validated against the measured results. The methods include RL-GO as implemented in FEKO [7] and SBR using CST [8]. For the RL-GO method the effect of using different mesh types, consisting of linear and curvilinear triangles, is illustrated. The differences between the measured and simulated RCS results using the SBR method with rays and ray-tubes are also presented. Comparisons of the measured and simulated datasets are conducted using RCS graphs and inverse synthetic aperture radar (ISAR) images to gain more insight into the scattering mechanisms.

II. CAD MODEL ACCURACY

RCS measurements of the scale model Boeing 707 were conducted in the compact range at the University of Pretoria, South Africa. This setup is shown in Fig. 1. An investigation of the effect of the geometrical accuracy of two different 3D CAD models of the target, on the simulation accuracy, was conducted. These models included the scanned and generic CAD models.

Fig. 1. Scale model setup in the compact range at the University of Pretoria, South Africa.

The scanned model was developed by converting the 3D point cloud, generated with a handheld laser scanner, to a mesh model using 3D processing software [5]. The mesh model was imported into FEKO where a simulation mesh was created. The scanned model has an average accuracy of better than 0.2 mm relative to the actual scale model. An overlay of these two models, with a zoomed in view of the engines, is provided in Fig. 2. The scanned CAD model is shown in yellow and the generic CAD model in orange.

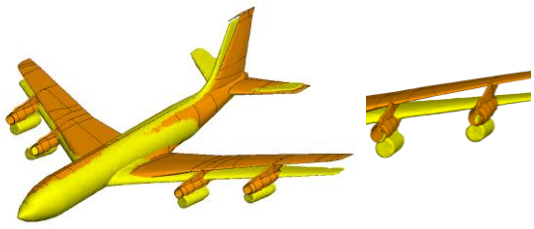

Fig. 2. Overlay of scanned (yellow) and generic (orange) CAD models and zoomed-in view of engines.

The geometrical differences between the two CAD models are clearly observed in Fig. 2. The largest discrepancies are the wing alignments, the engine positions and the details within the engines. It can further be observed that the scanned CAD model is a more realistic and accurate representation of the actual scale model of the target that was used for the measurements, shown in Fig. 1.

Experiments were conducted to determine which CAD model of the target would be the preeminent model for validating the asymptotic methods. It was shown in [5] that the RCS of the Boeing 707, calculated with PO compared very well with the RCS calculated with the full-wave MLFMM method at 10 GHz and 17 GHz. Consequently it was decided to analyze the effect of the geometrical accuracy of the two CAD models, relative to the scale model, on the simulation accuracy with the PO method implemented in FEKO, at both these frequencies as well as at a lower frequency of 3 GHz. Figures 3, 4 and 5 provides a comparison between the measured data and PO simulated data generated with the scanned and generic CAD models at 3 GHz, 10 GHz and 17 GHz, respectively.

The PO simulations of both the scanned and generic CAD models produced comparable results to the measured data as seen in Figs. 3, 4 and 5. Larger discrepancies between both PO simulated data sets and the measured data are observed over 40º and 60º. It is however clear that, the scanned CAD model yields overall more accurate RCS results compared to the measured data than the results obtained with the generic CAD model. This is particularly evident in the nose (0º) and tail (180º) regions of the airplane where the RCS values are lower. As the frequency increases, the smaller details on the models play larger roles in the RCS signatures.

Further analyses of the structural behavior of the scale model and the scattering centers of the two CAD models were conducted. This was done by generating ISAR images of the measured and PO simulated targets that were illuminated form the front (-30º to 30º) and from the port broadside (60º to 120º). The ISAR measurements and simulations were conducted for VV-polarized monostatic RCS centered at 10 GHz using 801 frequencies in steps of 8 MHz, and 101 frequencies in steps of 60 MHz, respectively. Figures 6 and 7 provides the ISAR images of the physical scale model measured in the compact range and the PO simulation of the 3D scanned CAD model as well as the generic 3D CAD model illuminated from the front and side, respectively.

It is evident from the ISAR image of the measured data in Fig. 6 (a) that there are certain areas on the target that produce dominant scattering when illuminated in this range, such as the engines. The wings and nose of the aircraft also produce some scattering. Even though the wooden mounting rod used to position the model in the compact range was covered with radar absorbing material (RAM), it still produces some scattering, not present in the simulations. Almost no scattering is observed on the stabilizers of the aircraft. Very similar scattering patterns located at the nose and cockpit area of the measured scale model and scanned CAD model are observed in Figs. 6 (a) and (b). A different scattering pattern is observed in this area of the generic CAD model seen in Fig. 6 (c). A lot less scattering is observed from the wings of the generic CAD model than with the measured data. Although the scattering produced by the engines of the scanned CAD model is slightly less than that of the physical scale model, these scattering patterns are very similar. The cavities in the engines of the generic CAD model produce slightly different scattering patterns than the enclosed engines of the scale model and scanned CAD model.

It is clear in Fig. 7 that the main parts contributing to the RCS of the aircraft, in this range, include the two visible port side engines, the fuselage, and the vertical stabilizer. The scattering produced by the fuselage of the CAD models are very similar to the measured data, however slightly less scattering is produced by the fuselage of the generic CAD model, Fig. 7 (c). The scattering center located on the vertical stabilizer of the generic CAD model is larger than that of the measured data. The obscured starboard side engines of the scale model and the scanned CAD model also contribute somewhat to the RCS patterns observed in Figs. 3, 4 and 5, whereas no scattering is observed from this part of the generic CAD model. The wingtip and the tip of the horizontal stabilizer of the scale model and the scanned CAD model produce scattering not observed with the generic CAD model.

The differences between the measured and simulated scattering centers observed in the ISAR images in Fig. 6 and Fig. 7, clarifies some of the discrepancies observed in the angular RCS data provided in Figs. 3, 4 and 5. It is evident that the scanned CAD model delivers more accurate scattering results compared to the measured data when comparing the various scattering centers. This can be attributed to the fact that the scanned CAD model is a more accurate geometrical representation of the actual scale model used for measurements than the generic CAD model. Additional scattering analysis of the scanned CAD model was therefore conducted to investigate the reason for the discrepancies observed between 40º and 60º. The ISAR images of measured and simulated data illuminated from 30º to 60º are provided in Figs. 8 (a) and (b).

A few main scattering points are observed in the image of the measured data, Fig. 8 (a). These are found at the leading edge of the wing, the juncture between the wing and the fuselage, the engines and the leading edge of the horizontal stabilizer of the aircraft. The corner reflector created between the wing and the fuselage is the dominant scattering center over this azimuth range. Some of the same scattering centers, although with lower intensity, are observed in the simulated data in Fig. 8 (b). The dominant measured scattering center located at the corner reflector, formed between the wing and the fuselage of the airplane, is

not present in the PO simulated data. This explains why the simulated RCS is lower than the measured data over this range.

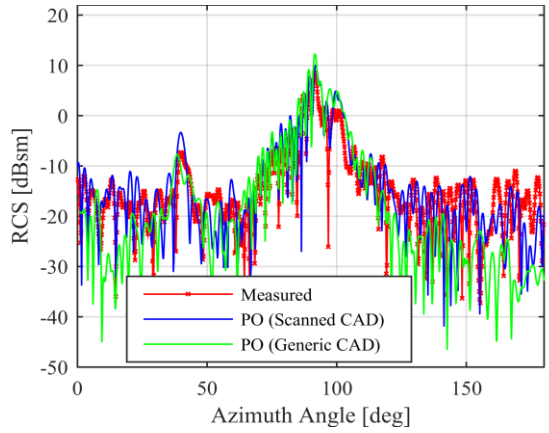

Fig. 3. RCS at 3 GHz measured and simulated in FEKO with PO using the scanned and generic CAD models.

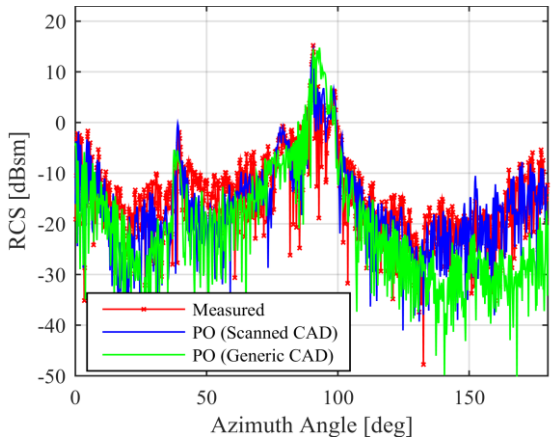

Fig. 4. RCS at 10 GHz measured and simulated in FEKO with PO using the scanned and generic CAD models.

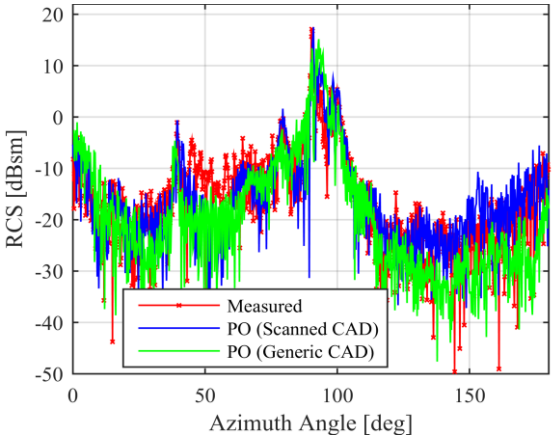

Fig. 5. RCS at 17 GHz measured and simulated in FEKO with PO using the scanned and generic CAD models.

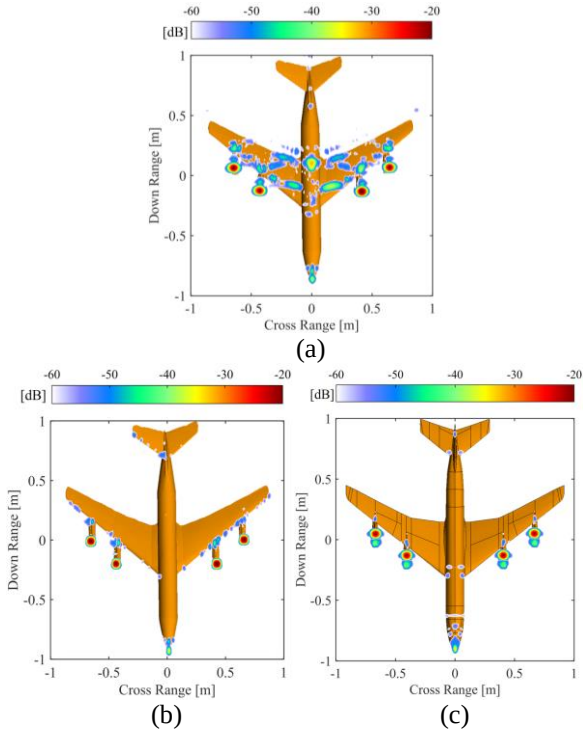

Fig. 6. ISAR images of: (a) measured data, (b) PO simulation of scanned CAD model, and (c) generic CAD model illuminated from the front.

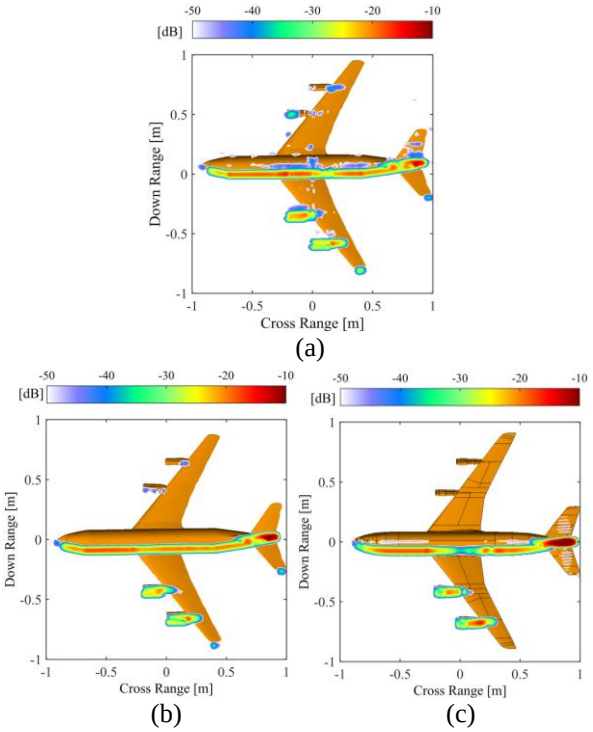

Fig. 7. ISAR images of: (a) measured data, (b) PO simulation of scanned CAD model, and (c) generic CAD model illuminated from the side.

Further analysis of the RCS capabilities of the other asymptotic methods were conducted exclusively with the scanned CAD model to minimize the errors introduced in the radar signature due to geometrical differences between the measured and simulated targets.

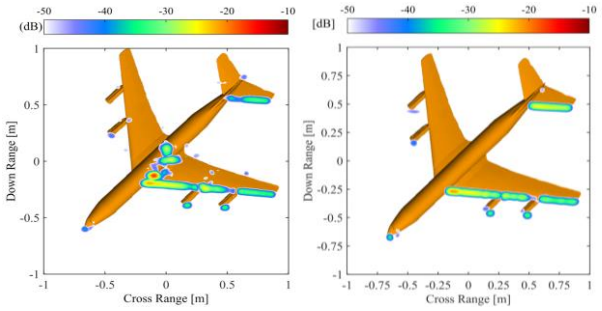

Fig. 8. ISAR images of: (a) measured data, and (b) PO simulation illuminated from 30º to 60º.

III. VALIDATION OF ASYMPTOTIC METHODS

A. RL-GO as implemented in FEKO

RL-GO (FEKO) simulations were performed at 3 GHz and 17 GHz and were validated against measured data. No edge-diffractions were taken into account. The effects of two different mesh types, compatible with this method, on the simulation accuracy were investigated. These meshes included a linear and curvilinear triangular mesh that is available with the FEKO Suite 7.0.2 Feature Update [9, 10]. The RCS of the CAD model, meshed with both types of meshes, was computed with the RL-GO method at both frequencies. One and three interactions were considered. It was found that the RL-GO data using a curvilinear mesh was very inaccurate with multiple interactions and is therefore not shown. The RCS results obtained with the linearly meshed model considering three interactions are provided in Figs. 9 and 10, respectively. The RCS results using both mesh types with one interaction are provided in Figs. 11 and 12, respectively.

It is clear from Figs. 9 and 10 that the RL-GO data using a linear mesh with three interactions follows a similar trend as the measured RCS data. However, large discrepancies are observed between the nose region of the airplane and the broadside reflection (20º to 70º) as well as the broadside reflection and the tail region of the aircraft (110º to 170º).

The simulation accuracy clearly increased significantly with respect to the measured data when only one interaction is considered, especially over the range of 110º to 170º, as seen in Figs. 11 and 12. There is overall excellent agreement between this simulated RCS data and the measured data, especially in the ranges where the RCS values are higher (above -5 dBsm). Some ranges are still slightly inaccurate, 40º to 60º and 110º to 170º. The RL-GO data of the linearly and curvilinearly meshed models are almost identical. These RL-GO results are also very similar to the PO results shown in Figs. 3 and 5.

Further scattering analysis of the RL-GO method with three interactions is conducted with the linearly meshed target. Scattering analyses are also conducted of the RL-GO method when only one interaction is considered with both mesh types. The same ISAR measurement and simulation setups as described in Section II were implemented, with the illumination from 110º to 170º. Because the RCS calculated with the linearly and curvilinearly meshed model, considering a single interaction, are so similar only the curvilinear data is shown. The three ISAR images are provided in Fig. 13.

It is clear from the ISAR image of the measured data seen in Fig. 13 (a) that the main scattering is produced by the corner reflector created between the trailing edge of the wing and the fuselage, the vertical stabilizer, and the trailing edges of the engines. Most of these main scattering centers are also observed in the RL-GO simulation image in Fig. 13 (b). However, the calculated scattering produced by the engines and the trailing edge of the wing are much higher than the measured data. This explains the larger simulated RCS value over this range in the angular RCS data provided in Figs. 9 and 10. When only one interaction is considered the scattering centers are very similar to the measured data as seen in Fig. 13 (c). The reason for the reduced error in the angular RCS data over this range as seen in Fig. 11 and 12 is due to the less noisy scattering observed between the fuselage and wing of the airplane. The calculated RCS is still slightly higher than the measured data due to the higher scattering produced by the engines and the trailing edge of the wing.

A summary of computational resources required by this method is provided in Table 1.

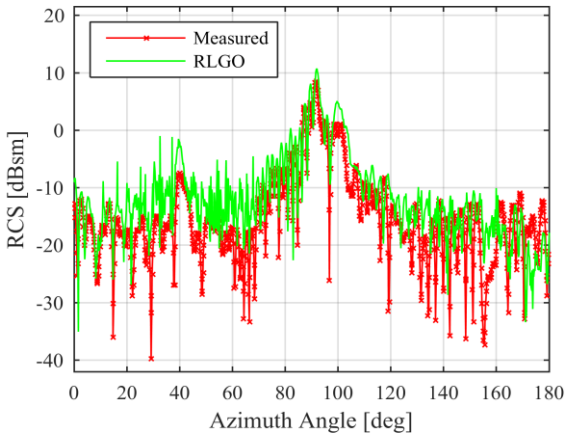

Fig. 9. RCS at 3 GHz measured and simulated in FEKO with RL-GO using a linear mesh considering 3 interactions.

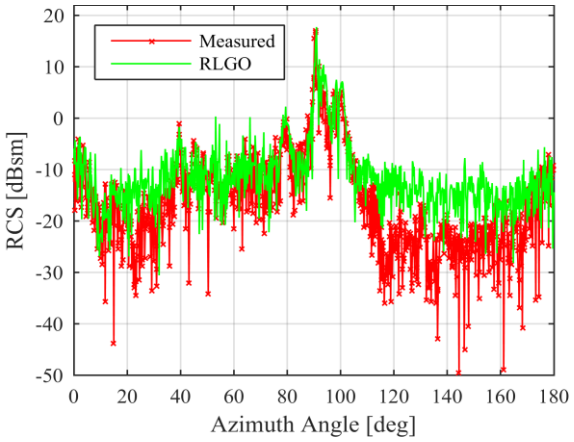

Fig. 10. RCS at 17 GHz measured and simulated in FEKO with RL-GO using a linear mesh considering 3 interactions.

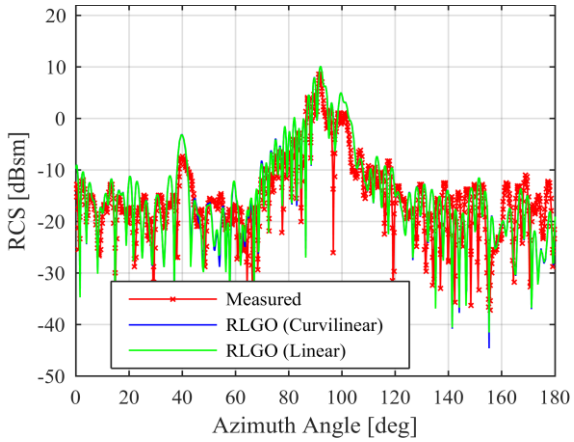

Fig. 11. RCS at 3 GHz measured and simulated in FEKO with RL-GO using linear and curvilinear meshes considering 1 interaction.

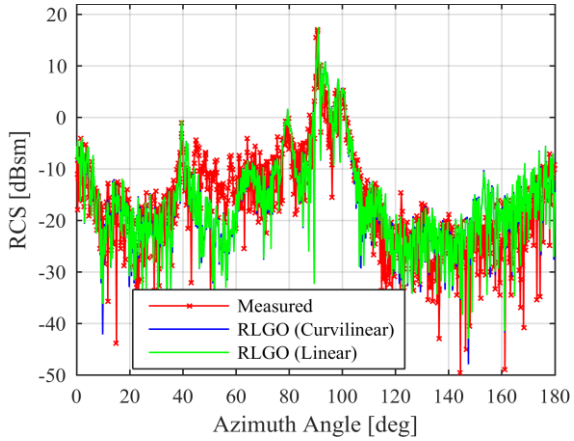

Fig. 12. RCS at 17 GHz measured and simulated in FEKO with RL-GO using linear and curvilinear meshes considering 1 interaction.

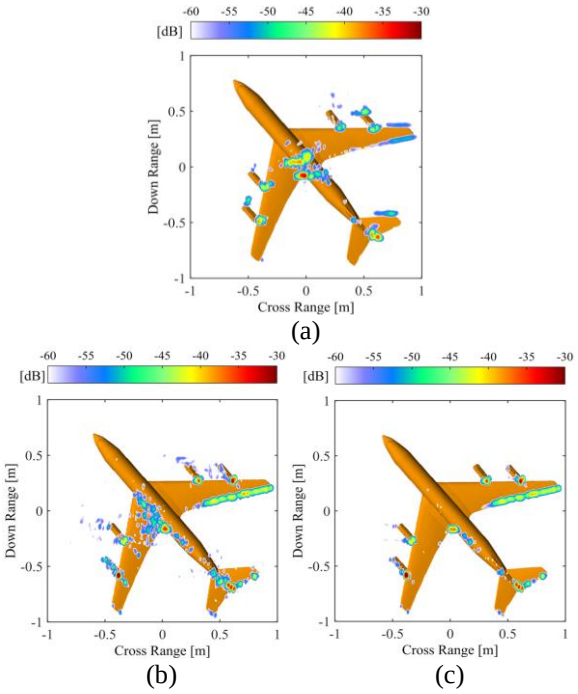

Fig. 13. ISAR images of: (a) measured data, (b) RL-GO simulation using a linear mesh with 3 interactions, and (c) using a curvilinear mesh with 1 interaction, illuminated from 110º to 170º.

B. SBR as implemented in CST MWS

The SBR method implemented in CST MWS 2015 was validated. The ability of this method to calculate the RCS of the airframe was investigated using rays and ray-tubes at 3 GHz and 17 GHz. The optimum number of reflections required, in terms of solution accuracy and execution time, was found to be three. The RCS results are provided in Figs. 14 and 15, respectively.

It is clear from Fig. 14 and Fig. 15 that there is overall excellent agreement between the measurements and the RCS calculated with the SBR method using rays. The RCS calculated with the SBR method using ray-tubes does not compare as well with the measured RCS over the entire azimuth range. Large discrepancies are observed between 40º to 60º where this simulated data is larger than the measured data. In this range, the RCS calculated with the SBR method using rays was slightly lower than the measured data. ISAR images of the measured and SBR simulated data using rays and ray-tubes were generated to examine the disagreements in this range. Figure 16 provides the ISAR images of the measured data, and the SBR simulation using rays, and ray-tubes illuminated from 30º to 60º. A few main scattering points are observed in the image of the measured seen in Fig. 16 (a). These are found at the leading edge of the wing, the juncture between the wing and the fuselage, the engines, the horizontal stabilizer, and the nose of the aircraft. The corner reflector created

between the wing and fuselage is the dominant scatterer over this azimuth range. There is overall excellent agreement between the scattering centers observed in the measured data and the simulated data generated with the SBR method using rays, shown in Fig. 16 (b). The scattering produced by the corner reflector, formed between the wing and the fuselage of the airplane, is slightly lower in this simulated data than in the measured data. This explains the slightly lower simulated RCS values observed in this range seen in Fig. 14 and Fig. 15. The main scattering centers found in the measured data are also observed in the ISAR image produced by the SBR method using ray-tubes, seen in Fig. 16 (c). However, the scattering center produced by the corner reflector, found between the wing and fuselage of the airplane, has a much higher value than the measured data. The simulation data is also noisier, possibly due to cross range smear [11]. This explains why the RCS calculated with this method is higher than the measured data from 40° to 60°.

A summary of computational resources required by this method is provided in Table 1.

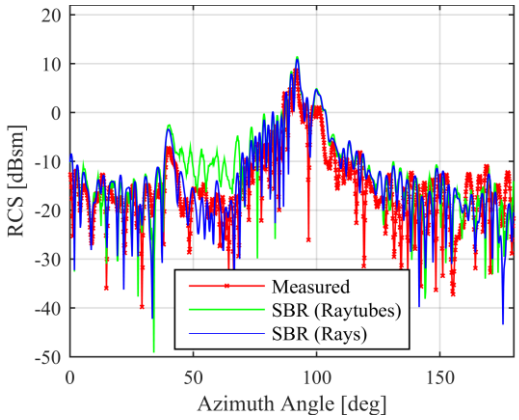

Fig. 14. RCS at 3 GHz measured in the compact range and simulated in CST with SBR using rays and ray-tubes.

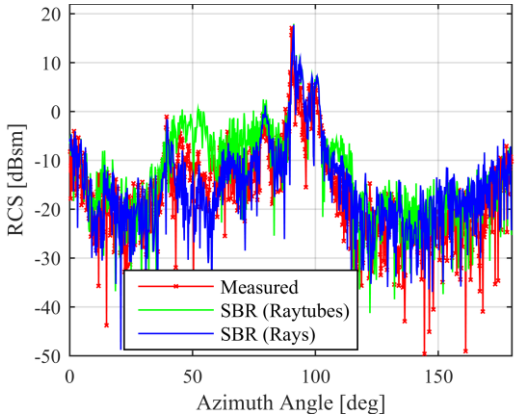

Fig. 15. RCS at 17 GHz measured in the compact range and simulated in CST with SBR using rays and ray-tubes.

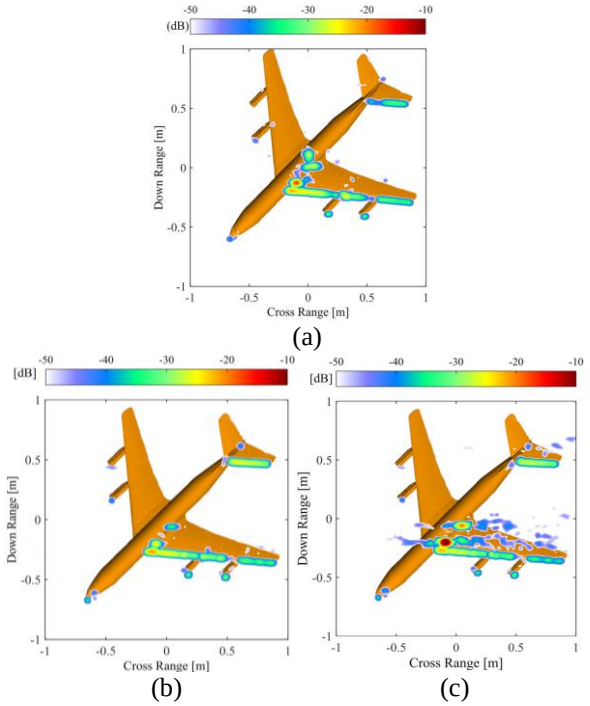

Fig. 16. ISAR images of: (a) measured data, (b) SBR simulation with rays, and (c) with ray-tubes illuminated from 30° to 60°.

Table 1: Summary of computational requirements

Method	Run Time [hrs]	CPU Time [hrs]	RAM [GB]	Mem. Read [GB]	Mem. Write [GB]
RL-GO	2.4	14	2.49	1.58	0.14
SBR rays	0.82	2.52	3.96	6.38	5.97
SBR tubes	1.28	5.53	4.03	6.43	10.10

IV. CONCLUSION

The effect of the geometrical accuracy of the 3D CAD, with respect to the scale model, on the accuracy of the calculated RCS data was investigated. This was done by calculating the RCS of two CAD models and comparing the results with measured RCS data generated in a compact range. A conducting scale model of a Boeing 707, with a maximum electrical length of 106λ, was measured. The two CAD models utilized in this investigation included a laser scanned and a generically constructed CAD model of the target. It was found that the laser scanned CAD model produced more accurately calculated RCS results compared to the measured data than the generic CAD model. Therefore, if measured data is used for validation purposes, the numerical model of the target has to be a very accurate approximation of the measured target. This can be achieved by either laser scanning the physical target or by accurately manufacturing the target from the CAD model specifications. Consequently, the validation of the

asymptotic methods was conducted with the scanned CAD model of the target.

The accuracy with which the RL-GO and SBR asymptotic CEM techniques calculated the RCS of the electrically large complex target was validated. This was done by comparing the simulated RCS results with measured data using RCS plots and ISAR images. Almost all of the simulated RCS data, generated with the various asymptotic methods, followed the same trend as the measurements and had excellent agreement over the ranges where the projected area of the aircraft was large. The accuracy also increased with frequency. Very poor RCS results were obtained when a curvilinear mesh model was simulated with multiple reflections using the RL-GO method in FEKO. However, the accuracy of the RCS results increased when this method was applied to a linearly meshed model. The accuracy of this method increased significantly, with both mesh types, when only one interaction was considered. These results were very similar to the PO results generated with the scanned CAD model. The SBR method as implemented in CST MWS produced accurate RCS results when rays were used and less accurate results when ray-tubes were used.

It was also shown that ISAR imaging provided a handy tool to examine the differences between the measured and simulated radar signatures.

The simulations were performed on a computer with six 3.2 GHz processors and 64 GB RAM. It is clear from Table 1 that the SBR method with rays (CST 2016) was the most time efficient method, and RL-GO (FEKO 14.0.420-552) was the most time demanding. However the RL-GO method (FEKO) was the most memory efficient method whereas the SBR method with ray-tubes (CST) was the least.

ACKNOWLEDGMENT

The authors are grateful for the support received from B. Jacobs for providing the generic CAD model of the target, CST MWS (A. Bhattacharya, A. Ibbotson, and M. Ruetschlin), and FEKO (E. Burger).

REFERENCES

[1] J. E. Ciliers, J. M. Steyn, J. C. Smit, C. Pienaar, and M. Pienaar, "Considering CAD model accuracy for radar cross section and signature calculations of electrically large complex targets," in *International Radar Conference*, Lille, 2014.

[2] F. Weinmann, "Ray tracing with PO/PTD for RCS modeling of large complex objects," *IEEE Transactions on Antennas and Propagation*, vol. 54, no. 6, pp. 1797-1806, June 2006.

[3] J. C. Smit, J. E. Cilliers, and E. H. Burger, "Comparison of MLFMM, PO and SBR for RCS investigations in radar applications," in *IET International Conference on Radar Systems*, Glasgow, 2012.

[4] I. M. Martin, M. A. Alves, G. G. Peixoto, and M. C. Rezende, "Radar cross section measurements and simulations of a model airplane in the X-band," *PIERS Online*, vol. 5, no. 4, pp. 377-380, 2009.

[5] B. Jacobs and D. E. Baker, "Validation of a computational electromagnetic model of a Boeing 707 aircraft by comparison to scale model measurements," in *Conference on Antennas and Propagation in Wireless Communications*, Cape Town, 2012.

[6] C. Pienaar, J. W. Odendaal, J. C. Smit, J. Joubert, and J. E. Cilliers, "RCS results for an electrically large realistic model airframe," Accepted for Publication in the *Applied Computational Electromagnetic Society Express Journal*, 2016.

[7] FEKO Suite, Altair, South Africa, www.feko.info, 2015.

[8] CST STUDIO SUITE® 2015, CST AG, Germany, www.cst.com

[9] U. Jakobus, "Advances in EM simulations," in *Altair Technology Conferences*, Dearborn, MI, USA, 6 May 2015.

[10] FEKO Altair, "FEKO Suite 7.0.2 Feature Update," 6 May 2015. [Online]. Available: https://www.feko.info/about-us/News/feko-suite-7.0.2-feature-update/view. [Accessed Aug. 2015].

[11] R. Bhalla and H. Ling, "Cross range streaks in ISAR images generated via the shooting-and-bouncing ray technique: Cause and solutions," *IEEE Antennas and Propagation Magazine*, vol. 39, no. 2, pp. 76-80, 1997.

A Novel UWB Monopole Antenna with Controllable Band-Notch Characteristics

Nasrin Tasouji, Javad Nourinia, Changiz Ghobadi, and Farnaz Mirzamohammadi

Department of Electrical Engineering, Urmia University, Urmia, Iran
nasrin.tasouji@gmail.com, javad.nourinia@urmia.ac.ir, changiz.ghobadi@urmia.ac.ir,
mirzamohamadi.farnaz@gmail.com

Abstract ─ A novel microstrip monopole antenna for Ultra Wide Band applications with switchable band-notch function is presented. For this purpose, elliptical radiator and a half circular shape ground plane are modified. Using these modifications, including a rectangular and an arc-shaped slots on ground plane and a complex form of slot, etched on the patch, new resonances are excited and hence bandwidth is enhanced. In addition, by adding one rectangular step to patch, wide fractional bandwidth of more than 124% (2.7-11.61 GHz), defined by 10 dB return loss is achieved, in following part effects of the rectangular step is investigated. The rejection of 3.01-3.9 GHz, WiMAX and 5.07-6 GHz, WLAN bands is achieved using small connections as switches across the circular slot and rectangular arm on the radiation patch in specific positions. The total size of antenna is only 21×26 mm^2. Parametric simulation of the proposed modifications and measurement results of the manufactured antenna are presented and discussed.

Index Terms ─ Frequency band-notched, microstrip-fed monopole antenna, switches, Ultra Wide Band (UWB).

I. INTRODUCTION

Due to rapid growth of Ultra Wide Band communication systems and their inherent properties such as low-spectral-density radiated power and positional for accommodating higher data rate [1], there is essential call for efficient communication devices to work in such environments. Special frequency band, 3.1 to 10.6 GHz, has allocated by FCC for unlicensed use of ultra-wide band devices [2]. Printed monopole antennas are potential candidates in emerging UWB applications because of their low cost and compact size and stable radiation properties. To avoid the electromagnetic interference between UWB systems and narrowband communication systems, such as Worldwide Interoperability for Microwave Access (WiMAX) operating at 3.4-3.69 GHz and the wireless local area network (WLAN) operating at 5.15-5.825 GHz, band-notched characteristic should be considered in UWB antenna design. For this purpose, recently, modified UWB monopole antennas with frequency band-notched function have been attempted. To get Reconfigurable capability, various electronic switches such as p-i-n diodes [3], radio frequency micro-electromechanical systems (RFMEMS) [4], and varactor [5] can be used. Extensive discussions of reconfigurable antenna, switches and their advantages were investigated in [6]. Also different shapes of the slots are used to obtain desired rejected bands [7-9]. In [10], using SRRs elements leads to triple band-notched characteristics. Parasitic strips with dual band notches in [11], band stop filter in [12], fractal structure [13] and DGS structure [14] are other methods used for band-notch characteristics.

In this letter, a new microstrip-fed monopole antenna with modified radiation patch and ground plane is suggested to provide UWB characteristics and band-notch function. Etching a rectangular and an arc shaped slot on the ground plane, leads to improvement of bandwidth. Additionally, a circular slot with three arms is employed on radiating patch to get much wider impedance bandwidth. Small connections as switches across the circular slot and one of arms on the patch, lead to desired reconfigurable frequency band-notches covering 3.01-3.9 GHz WiMAX and 5.07-6 GHz WLAN. Dimensions of designed antennas are small, also its structure has less complexity and better functionality. Additionally novelty in comparison to previously presented antennas is another specification of this design.

II. ANTENNA CONFIGURATION AND DESIGN

The configuration of proposed monopole antenna is illustrated in Fig. 1, which is fabricated on a FR4 substrate with the size of 21 (x-axis) × 26 (y-axis) × 1 mm^3, relative dielectric constant of 4.4, and loss tangent of 0.018. The basic antenna structure is made up of a half circular shape ground plane, feed line and elliptical radiating patch. On the front surface of substrate, the radiuses of elliptical patch are 10 mm and 8 mm

Submitted On: May 19, 2013
Accepted On: September 5, 2014

respectively. On the other side of the substrate, ground plane has radius of R. The width of the microstrip feed line is fixed at W_f = 2 mm to obtain 50 Ω characteristic impedance. The ground plane with a rectangular and an arc-shaped slot has substantial efficacy on controlling frequency response. In this case, the main parameter of these slots is H_g which will be investigated in the following part. A circular slot with three arms is employed on the elliptical radiation patch to enhance the impedance bandwidth and provide notch function. One of these arms is placed on the feed line and by optimizing its length (Y_f), surface currents are dispersed in new paths, so notch function focuses on desired frequency bands. Furthermore, the rectangular step is added on the patch to achieve smooth transition between frequency bands and avoid unwanted notched bands as considered by parametric study in Fig. 2. The location of rectangular step, K_n, is critical parameter to control UWB bandwidth. Also α connects feed line to radiation patch with angle of 45 degrees. Optimal dimensions of desired antenna are as shown in Table 1.

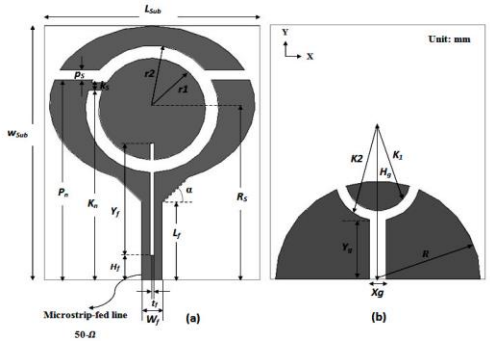

Fig. 1. Geometry of the proposed microstrip monopole antenna: (a) front view (including a microstrip-fed slotted patch) and (b) bottom view (including ground plane with slots).

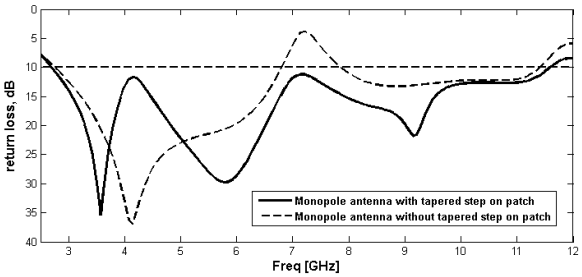

Fig. 2. Simulated return loss characteristics of the proposed monopole antenna with and without rectangular step.

Table 1: Parameters of antenna (Unit: mm)

L_{Sub} = 21		W_{Sub} = 26
Patch		Ground Plane
r_1= 5.2	R_S = 17.5	Y_g = 6.08
r_2 = 6.5	Y_f = 11.5	X_g = 1.6
P_n = 20.5	L_f = 8	H_g = 10.2
P_s = 1	H_f = 2.5	R = 10
K_s= 0.8	t_f = 0.4	K_2 = 4.2
K_n = 19.4		K_1 = 3.2

III. RESULTS AND DISCUSSION

A. Full band UWB monopole antenna

Ansoft simulation software high frequency structure simulator (HFSS) [15] is used for design and parametric analysis of antenna.

The optimized parameters are defined by changing selected parameter while fixing others. Figure 3 illustrates the structure of the various antennas used for simulation studies. Return loss characteristics for ordinary modified monopole antenna [Fig. 3 (a)], defected ground plane [Fig. 3 (b)], and the proposed antenna with slotted elliptical patch [Fig. 3 (c)], respectively are compared in Fig. 4. As shown in Fig. 4, slotted ground plane has an important effect on exciting new resonances and achieving different frequency responses. In this case, the new coupling paths between the modified patch and slotted ground plane can be obtained. Therefore the number of resonances, matching and bandwidth of antenna can be controlled. In this case, the covered bandwidth is from 2 to 8.35 GHz. To work in UWB frequency band, the simple elliptical patch is changed to slotted patch and in following, a tapered step is added to the patch. By this modification, it is found that good impedance bandwidth and matching is achieved at upper frequencies. Essential parameters for ultra wide band characteristics of proposed antenna are H_g, R, r_1, r_2, K_n and α. By carefully adjusting these parameters, ultra wide band operation is achieved. K_n is a key parameter in controlling the resonances of antenna. As shown in Fig. 5 (a), while K_n swaps form 16.4 mm to 19.4 mm, additional resonance will be added at 9.5 GHz but first and second resonances have almost fixed position. By selecting K_n = 19.4 mm, good matching in all frequency bands is realized. The other main parameter is H_g. Its effect on antenna performance is indicated in Fig. 5 (b).

By increasing Hg, the matching of high frequencies is considerably improved. In optimal value of Hg, frequency bands from 2.7 to 11.61 GHz are covered.

Fig. 3. (a) The ordinary elliptical patch and half circular shape ground plane. (b) The antenna with slotted ground plane. (c) Proposed antenna with defected ground plane and slotted patch.

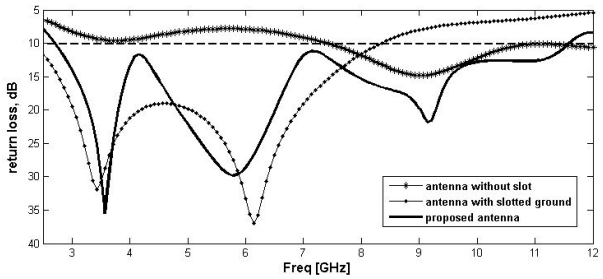

Fig. 4. Simulated return loss characteristics for antennas shown in Fig. 3.

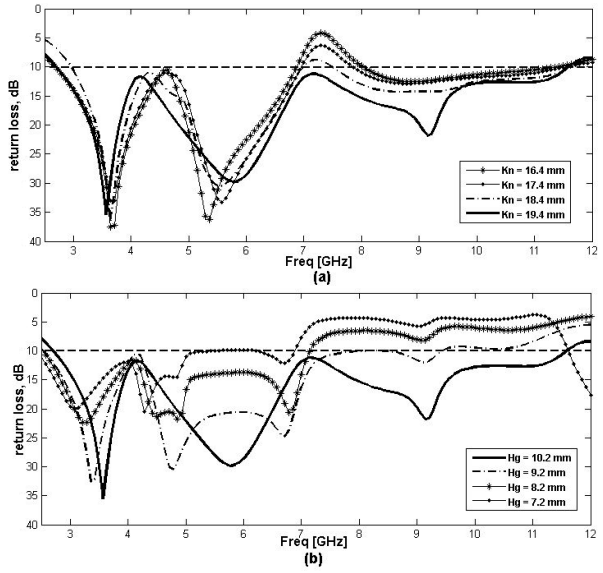

Fig. 5. Simulated return loss characteristics of the proposed antenna with different values of: (a) K_n (H_g is fixed at 10.2 mm), and (b) H_g (K_n is fixed at 19.4 mm).

B. UWB monopole antenna with switchable frequency band-notch characteristics

UWB monopole antenna with two band-notch modes is introduced here by using proposed structure depicted in Fig. 1 and adding two slots across the circular slot and rectangular arm on radiation patch with connections used as switches. Positions of connections, *D1* and *D2*, are adjusted appropriately to create desirable frequency notched bands. For the proposed structure, two operating states are investigated. At first, *D1* is connected as a switch. By selecting *D1*= 8.3 mm, first rejected band of 3.01-3.9 GHz, WiMAX is obtained. In second configuration, when other connection as a switch at *D2* =2 mm is attached, band-notch of 5.07-6 GHz WLAN is clearly seen. In this case, as shown in Fig. 6 (a) and Fig. 6 (b) simulated return loss curves with various values of *D1* and *D2* are optimized to reach desired notched bands. The phenomenon of switching between UWB and band-notch performances is clarified here by simulated current distributions on the radiation patch of proposed antenna according to the switching conditions. As shown in Fig. 7 (a), at 4.5 GHz, main part of surface current flows on the transmission line and dispersed by the means of rectangular slit, while around the circular slot current is small. The simulated current distributions at frequencies 3.5 and 5.5 GHz are illustrated in Figs. 7 (b) and (c). It can be observed that the current distributions mainly concentrate around the specific parts of circular slot. Impedance nearby feed-point changed markedly making considerable reflection at the desired rejected frequencies in three optimal designs. UWB antenna and two single band-notch antennas were built and tested. The photographs of fabricated prototypes are presented in Fig. 8. Simulated and measured reflection coefficients of selected designs are considered in Fig. 9. From this figure, it is clear that in all of designs, the simulated and measured results are in acceptable agreement. In first design, as indicated in Fig. 9 (a), fabricated antenna shows UWB performance from 2.8 to 12 GHz. In Fig. 9 (b), the results of second proposed antenna design with a connection on rectangular arm is shown. It reveals that measured rejected band from 3 to 4.1 GHz is obtained. Finally, Fig. 9 (c) illustrates the third design with a connection across circular slot. In this case, the antenna has measured notched frequency band from 5 to 6.2 GHz. The discrepancy between the measured and simulated values may be due to the errors of the manufactured antenna and the effects of the SMA port which is not considered in simulated results. Figure 10 indicates that gain of dual and single band-notched antenna is between 0 dB to 5dB and has comprehensive level during frequency bands except for two notched bands. Figure 11 shows the measured and simulated patterns including the co and cross polarization in the H-plane (x-z plane) and E-plane (y-z plane). It is clear that radiation patterns in H-plane are nearly omni-directional in the four frequencies and by such results antenna behavior is alike to the usual printed monopole antennas.

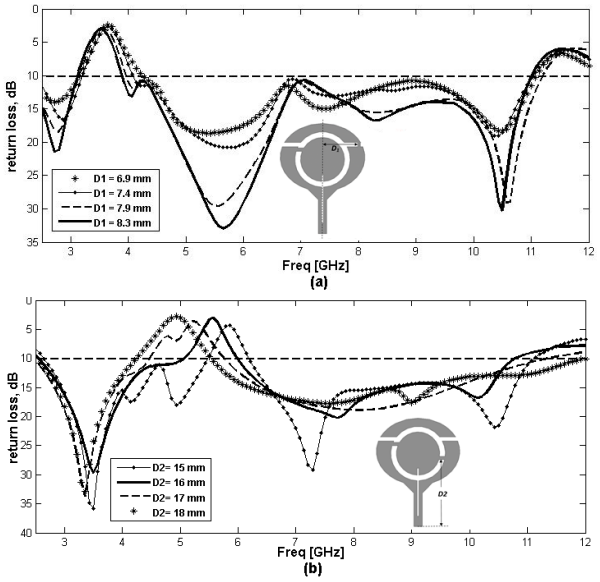

Fig. 6. Simulated return loss characteristics of the proposed antenna with different values of: (a) D1 and (b) D2.

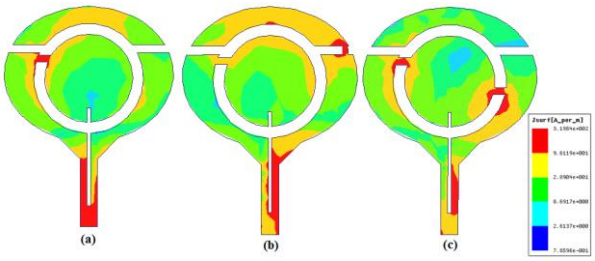

Fig. 7. Simulated surface current distributions on radiation patch: (a) UWB monopole antenna at 4.5 GHz, (b) single band-notch antenna with connected D1 at 3.5 GHz, and (c) single band-notch antenna with connected D2 at 5.5 GHz.

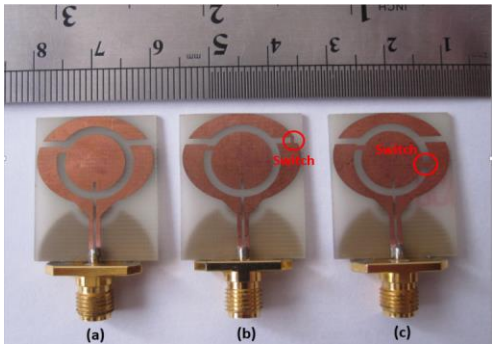

Fig. 8. Prototype antennas: (a) UWB monopole antenna, (b) single band-notch monopole antenna (WiMAX), and (c) single band-notch monopole antenna (WLAN).

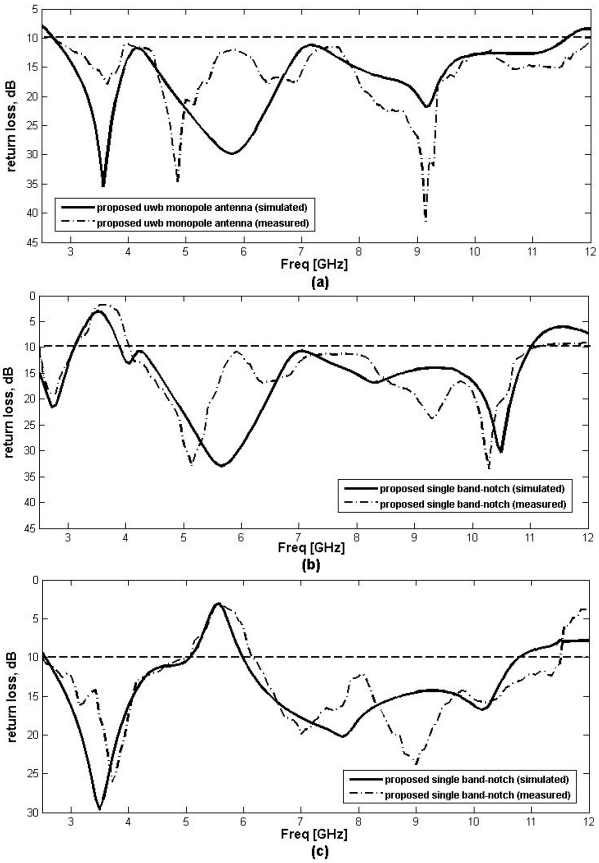

Fig. 9. Measured and simulated return loss results of: (a) UWB monopole antenna, (b) single band-notch (WiMAX), and (c) single band-notch (WLAN).

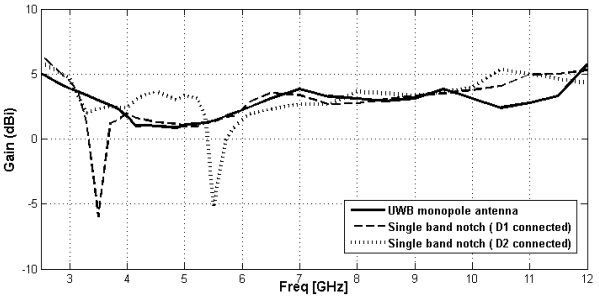

Fig. 10. Measured antenna gain of the proposed antennas.

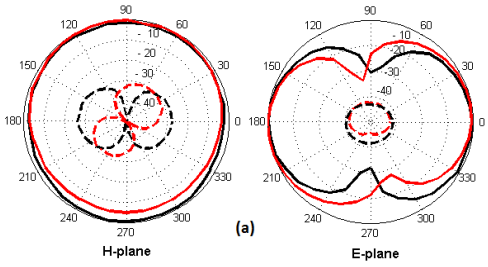

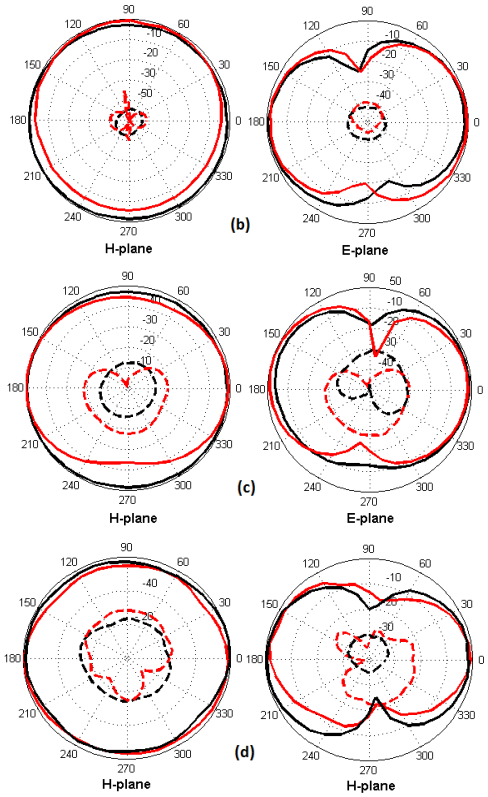

Fig. 11. Simulated and measured H- and E-planes radiation patterns of proposed antenna: (a) 3 GHz, (b) 4 GHz, (c) 5 GHz, and (d) 10 GHz.

IV. CONCLUSION

This letter has presented a novel printed UWB monopole antenna with switchable band-notch characteristics supporting various wireless applications. It has been shown that using circular slots with three arms etched on patch can enhance bandwidth from 2.7 to 11.61 GHz. In addition, using defected ground plane by inserting two rectangular and arc-shaped slots can also improve input reflection coefficient. By embedding a pair of connections as switches in proper situations, across the slotted patch, two single stop-bands will be created, which exempt from interfaces with existing WiMAX and WLAN bands.

REFERENCES

[1] G. P. Gao, M. Li, S. F. Niu, X. J. Li, B. N. Li, and J. S. Zhang, "Study of a novel wideband circular slot antenna having frequency band-notched function," *Progress In Electromagnetic Research, PIER*, vol. 96, pp. 141-154, 2009.

[2] G. R. Aiello and G. D. Roberson, "Ultra-wideband wireless systems," *IEEE Microwave*, pp. 36-38, June 2003.

[3] N. Tasouji, J. Nourinia, Ch. Ghobadi, and F. Tofigh, "A novel printed UWB slot antenna with reconfigurable band-notch characteristics," *922-5-1536-1225 © 2013 IEEE*, 2013.

[4] S. Nikolaou, N. D. Kingsley, G. E. Ponchak, J. Papapolymerou, and M. M. Tentzeris, "UWB elliptical monopoles with a reconfigurable band notch using MEMS switches actuated without bias lines," *IEEE Trans. Antennas Propag.*, vol. 57, no. 8, pp. 2242-2251, Aug. 2009.

[5] B. Trad, J. M. Floch, H. Rmili, M. Drissiand, and H. Zangar, "Design of a planar reconfigurable band-rejected UWB antenna," *2012 Loughborough Antennas & Propagation Conference 978-1-4673-2220-1/12/$31.00 © 2012 IEEE*, 2012.

[6] S. Yang, Ch. Zhang, H. K. Pan, A. E. Fathy, and V. K. Nair, "Frequency-reconfigurable antennas for multiradio wireless platforms," *IEEE Microwave Magazine*, pp. 66-83, Feb. 2009.

[7] M. Ojaroudi, N. Ojaroudi, and Y. Ebazadeh, "Dual band-notch small square monopole antenna with enhanced bandwidth characteristics for UWB applications," *420-6-1054-4887 © 2012 ACES*, 2012.

[8] G. Zhang, J.-S. Hong, B.-Z. Wang, and G. Song, "Switched band-notched UWB/WLAN monopole antenna," *256-260-1054-4887 © 2012 ACES*, 2012.

[9] D. Jiang, Y. Xu, R. Xu, and W. Lin, "A compact ultra-wideband antenna with improved triple band-notched characteristics," *130-6-1054-4887 © 2013 ACES*, 2013.

[10] J. Zhang, H. Yang, and H. Liang, "Band-notched split-ring resonators loaded monopole antenna for ultrawideband applications," *137-142-1054-4887 © 2013 ACES*, 2013.

[11] X.-L. Ma, W. Shao, and G.-Q. He, "A novel dual narrow band-notched CPW-fed UWB slot antenna with parasitic strips," *581-6-1054-4887 © 2012 ACES*, 2012.

[12] J. Zhang, X. L. Sun, S. W. Cheung, and T. I. Yuk, "Simple dual-band notched design for CPW-coupled-fed elliptical UWB monopole antenna," *Antennas and Propagation Society International Symposium (APSURSI), 2012 IEEE*, 2012.

[13] W. J. Lui, C. H. Cheng, Y. Cheng, and H. Zhu, "Frequency notched ultra-wideband microstrip slot antenna with fractal tuning stub," *Electronic Lett.*, vol. 41, no. 6, pp. 294-296, Mar. 2005.

[14] X. Wang, G. Fu, J. Zhao, and J. Dong, "A novel UWB patch antenna with dual notched band by etching DGS on the ground plane," *Microwave and Millimeter Wave Technology (ICMMT), 2012 International Conference*, 2012.

[15] Ansoft High Frequency Structure Simulation (HFSS), ver. 10, Ansoft Corporation, 2005.

Nasrin Tasouji was born on April 6, 1985 in Urmia, Iran. She received her B.Sc. degree in Electrical Communication Engineering from Urmia University, Iran in 2010 and M.Sc. degree in Electrical Communication Engineering from Urmia University, Iran in 2013. Her research interests are in designing of UWB antenna, impedance bandwidth enhancement techniques and reconfigurable structures.

Javad Nourinia received his B.Sc. in Electrical and Electronic Engineering from Shiraz University and M.Sc. degree in Electrical and Telecommunication Engineering from Iran University of Science and Technology, and Ph.D. degree in Electrical and Telecommunication from University of Science and Technology, Tehran Iran in 2000. From 2000, he was an Assistant Professor and now he is an Associated Professor in the Department of Electrical Engineering of Urmia University, Urmia, Iran. His primary research interests are in antenna design, numerical methods in electromagnetic, microwave circuits.

Changiz Ghobadi was born on June 1, 1960 in Iran. He received his B.Sc. in Electrical Engineering Electronic and M.Sc. degrees in Electrical Engineering Telecommunication from Isfahan University of Technology, Isfahan, Iran and Ph.D. degree in Electrical-Telecommunication from University of Bath, Bath, UK in 1998. From 1998, he was an Assistant Professor and now he is an Associated Professor in the Department of Electrical Engineering of Urmia University, Urmia, Iran. His primary research interests are in antenna design, radar and adaptive filters.

Farnaz Mirzamohammadi was born in Urmia, Iran 1986. She received her B.Sc. degree in Electrical Communication Engineering from Urmia University, Iran in 2009 and M.Sc. degree in Electrical Communication Engineering from Urmia University, Iran in 2012. Her research interests are in designing of UWB antenna, circular polarization and impedance bandwidth enhancement techniques, reconfigurable structures.

A Novel Compact Polarization Diversity Ultra-Wideband MIMO Antenna

Saeid Karamzadeh [1,2]

[1] Application & Research Center for Advanced Studies, Istanbul Aydin University, Turkey
[2] Department of Electrical and Electronics Engineering, Istanbul Aydin University, Turkey

Abstract ─ A very compact modified simple structure Ultra-Wideband (UWB) antenna with a size of 18 mm by 30 mm is presented for polarization diversity applications. The antenna employs two orthogonal monopole antenna to achieve polarization diversity over the UWB. The antenna was fabricated to study the performance such as S-parameters, radiation pattern, radiation efficiency, peak gain, envelope correlation coefficient and group delay. The measured results demonstrated that the proposed antenna has not only UWB (147.96% impedance bandwidth) but also good isolation less than about -25 dB. Moreover, the system fidelity factor is sufficient for pulse transmission with average 89.6% and 85.3% for ports 1 and 2, respectively. Furthermore, a low envelope correlation coefficient of less than 0.001 occurred, too. All these features show that the proposed UWB MIMO antenna can meet the requirement of MIMO/diversity of communication applications well.

Index Terms ─ Microstrip feed, monopole antenna, polarization diversity, UWB.

I. INTRODUCTION

The rapid developments in modern wireless communication systems demand a high data rate, strong dependability and heftiness. Ultra-wideband (UWB) technique is one of the most important technologies in indoor communications in order to have benefits such as low susceptibility to multipath fading, reduced probability of detection and intercept, and potentially high data rates [1-7]. But similar to most of the wireless communication systems, UWB systems usually suffer from channel fading caused by multipath environment [1-7]. To solve this problem, Multiple-Input-Multiple-Output (MIMO) technology is developed to supply best coverage and to become better performance over multipath wireless channels by utilizing multiple antennas at the transmitter and receiver [5-9]. The main problem facing the implementation of MIMO technology is the limited space available at each end of the communication link. Saving this extra space may cause performance degradation; therefore, polarization diversity needs to be considered in true wireless channels. These advantages enable UWB antenna to change polarization diversity by its capability attractive for wireless body area networks (WBANs). An appropriate UWB-WBAN diversity antenna must have low mutual coupling, i.e., high isolation between its branches [10]. The higher isolation leads to better diversity performance and higher efficiency of each branch. Hitherto, various techniques to attain UWB diversity antennas have been investigated and reported, aimed at reducing the antenna size and increasing the isolation [1-7]. In [1], a uniplanar, UWB dual-polarized antenna embedded with narrowband reject filter is presented. A style of designing ground plane has resulted in an enhance antenna foot print to 58×58×1.524 mm^3. Isolation between two ports is less than -15 dB. In [3, 4], by using a similar radiation patch, two type of UWB polarization diversity antenna in different large size and number in elements are provided (details is given in Table 1). In [5], a large size (50×50×1.524 mm^3) CPW fed uniplanar antenna with frequency range from 2.76 to 10.75 GHz and a rejection performance in the frequency band 4.75–6.12 GHz, along with isolation better than 15 dB, is reported. In [11] and [12], two UWB tapered slot antennas (TSAs) and mutual coupling below 15 dB are developed. That design utilizes a spatial diversity technique and, to the authors' knowledge, has the smallest size (27×47 mm^2) among the recently designed UWB diversity antennas. It should be noted that although a printed cantor set fractal antenna using spatial diversity, proposed in [13], has a smaller size (25×48 mm^2), its bandwidth is 80% of the UWB frequency defined range. In [7], a smaller UWB polarization antenna than reported works until the time of its release was worked. That is 52×27 mm^2 in size, and isolation between two input ports is less than -22 dB. In this work, we present a low profile 18×30×1.6 mm^3, small size polarization diversity antenna with covering impedance bandwidth from 2.97 to 19.86 GHz. This antenna with isolation less than about -25 dB between two ports and correlation coefficient less than -30 dB is a good choice for wireless systems which needs polarization diversity application. The proposed antenna has an area of 540 mm^2, which is significantly less than the recently published UWB polarization diversity antenna, as summarized in Table 1. Compared to other

Submitted On: October 9, 2016
Accepted On: December 6, 2016

similar types of antennas, the proposed antenna displays an impedance bandwidth which is significantly larger and shows no reduction in the gain performance as well as having better other results.

Table 1: Comparison of the proposed antenna with same works (IBW is Impedance Bandwidth, Sij is Isolation, ECC is Envelope Correlation Coefficient, FF is Fidelity Factor, GD is Group Delay, PW is Proposed Work, and RE is Radiation Efficiency)

Ref.	Size (mm)	IBW (GHz)	S_{ij} (dB)	ECC	FF (%)	Gain (dBi)	GD (ns)	RE (%)
[1]	58×58	8.2 GHz	-14	0.025	80	2.2	1	85
[3]	48×48	8.7 GHz	-15	0.04	--	~3	--	80
[4]	65×65	8.25 GHz	-40	--	--	~6.5	--	--
[5]	50×50	7.99 GHz	-15	0.025	95	~5.5	1	75
[6]	64×64	8 GHz	-40	0.006	--	~6.5	1	75
[7]	27×52	8.75 GHz	-22	0.01	85	--	--	--
[8]	40×40	8 GHz	-20	--	--	5	--	85
[9]	38.5×38.5	8.72 GHz	-15	0.02	--	7.5	--	50
[16]	45×50	8.2 GHz	-25	0.02	76	4	1	85
[17]	30×60	7.5 GHz	-20	0.01	--	4.2	--	80
[22]	~90×90	9.4 GHz	-20	--	--	~5	--	--
PW	18×30	16.89 GHz	~-25	0.001	88.2	4.7	0.86	83

II. ANTENNA DESIGN AND CONFIGURATION

Figure 1 displays the geometry of the proposed antenna. It includes two similar monopoles that are perpendicular to each other and printed on FR4 substrate with thickness of 1.6 mm, relative permittivity of (εr =) 4.4 and loss tangent of (tanδ=) 0.02. Spacing between two monopole antennas (center to center) is 12 mm. Each antenna is fed by a width of 2 mm microstrip line in order to attain 50Ω input impedance.

The patch of the antenna consists of a Trapezius- and a rectangular-shape which is united together. The ground of antenna comprises a rectangular and two symmetrical L-shape slot inside it. Details of other dimension are given in Table 2. Figure 2 demonstrates the structure of the various antennas employed for simulation studies. S11 characteristics for ordinary square monopole antenna [Fig. 2 (step 1)], the antenna with an improved patch [Fig 2. (step 2)] and the proposed antenna by cutting ground [Fig. 2 (step 3)] structures are compared in Fig. 3. As shown in Fig. 3, by using the modified radiating patch and two L-shape slots in defected ground inserted on the other side of substrate, additional third and fourth resonances are excited respectively, and hence, the bandwidth is increased. As exposed in Fig. 3, in the offered antenna configuration, the ordinary square monopole can provide the fundamental and next higher resonant radiation band at 4 and 7.9 GHz, respectively, in the absence of two L-shaped slots and without modifying the edges of the patch. The upper frequency bandwidth is significantly affected by using the radiating patch because by improving the edge of the patch, surface current which is focused in the edge of the ordinary square patch (as seen in Fig. 4 (a)) is eliminated and, therefore, surface current spreads in the total surface of patch conductor (see Fig. 4 (b)). By inserting two L-shaped slots in ground plane, the antenna bandwidth increases. The two L-shaped slots prevent the spreading of power in microstrip feed line on the ground conductive surface and, also, causes an increase in the surface current rotation in ground conductive (see Fig. 4 (c)).

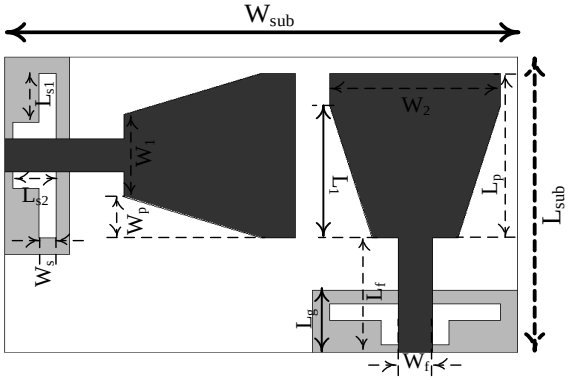

Fig. 1. Structure and dimension of proposed antenna.

Table 2: Parameters dimension

Parameter	Value	Parameter	Value
W_f	2 mm	W_1	5 mm
L_f	7 mm	W_2	10 mm
L_{s1}	3 mm	g	0.8 mm
L_{s2}	2.5 mm	h	1.6 mm
L_p	8 mm	W_{sub}	12 mm
W_p	2.5 mm	L_{sub}	17 mm
W_s	1 mm	L_g	3.8 mm

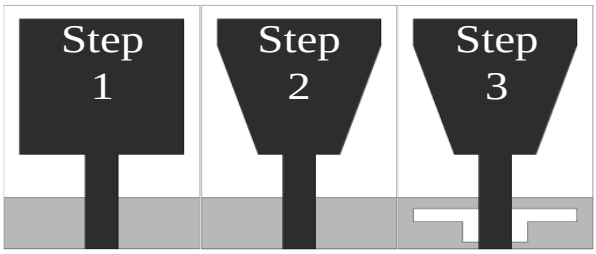

Fig. 2. Three steps of designing proposed monopole antenna.

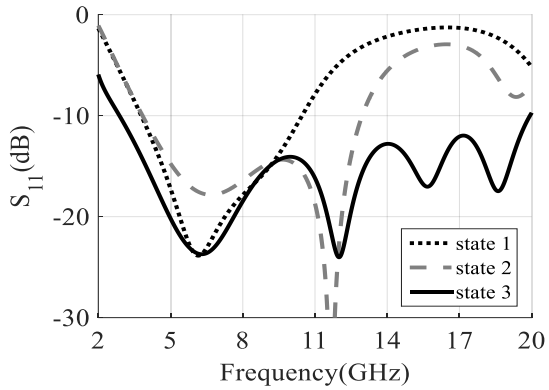

Fig. 3. Simulation S_{11} three steps of designing proposed monopole antenna.

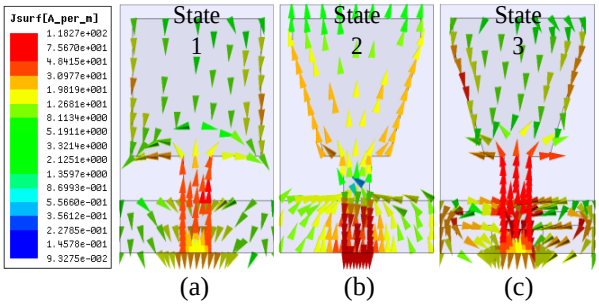

Fig. 4. Distribution of surface current: (a) simple square patch, (b) modified patch, and (c) modified ground and patch, at 8 GHz.

III. STUDY OF DGS EFFECT AT TDR

In order to comprehend defected ground structure effect in antenna performance Figs. 5 (a) and (b) are displayed. In order to calculate the TDR results for the proposed equivalent circuits, the impedance of these circuits in Laplace domain can be represented as in Equation (1):

$$Z_{DGS} = \frac{L_s+R}{LCs^2+RCs+1}. \quad (1)$$

Assuming that the characteristic impedance of the microstrip line is Z_0, we can write the reflection coefficient through a defected structure as in Equation (2), which is observed at the source end, i.e., port 1,

$$\Gamma_Z(s) = \frac{Z(s)}{Z(s)+2Z_0}. \quad (2)$$

Therefore, the reflected waveform for the proposed DGS can be written as:

$$\Gamma_{DGS}(s) = \frac{Ls+R}{2Z_0LCs^2+(2Z_0RC+L)s+R+2Z_0}. \quad (3)$$

A step voltage source with rise time τ_r and amplitude V0, can be expressed as in [18-21],

$$V_{in}(s) = \frac{V_0}{2\tau_r}\frac{1}{s^2}(1-e^{-(\tau_r s)}). \quad (4)$$

Therefore, the reflected waveform in Laplace domain can be written as:

$$V_{TDR}(s) = V_{in}(s)\Gamma_{DGS}(s). \quad (5)$$

In TDR measurements, the impedance follows as:

$$Z_{TDR} = \frac{Z_0(V_{in}(t)+V_{TDR}(t))}{V_{in}(t)-V_{TDR}(t)}. \quad (6)$$

In which Z_0 is the characteristic impedance of the transmission line at the terminal.

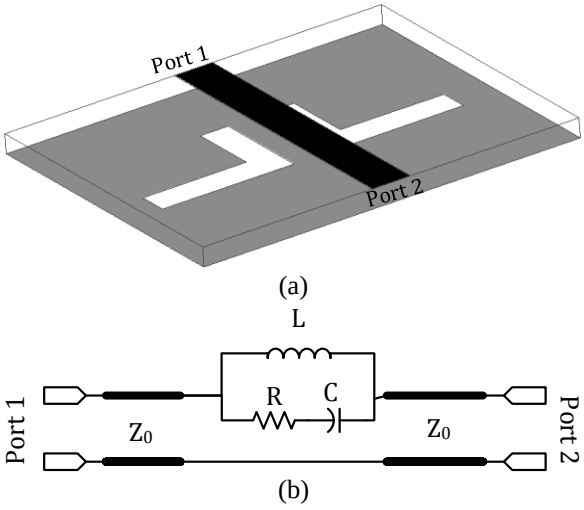

Fig. 5. (a) Geometry of the proposed DGS, and (b) equivalent circuit model.

The computed R, L and C of equivalent are 1.41Ω, 0.72nH and 16.01pF, respectively. In additionally, as mentioned with attention to LC circuit in equivalent circuit causes to creation of resonance in antenna performance.

IV. RESULT AND DISCUSSION

The proposed antenna was simulated by High Frequency Structure Simulator (HFSS) ver. 14, and then was optimized since the validation of results was fabricated and measured in frequency- and time-domain. In Fig. 6 (a) simulation results of insertion and isolation of two ports is indicated. As shown in this figure, simulated S11<-10 dB covered a frequency range from 2.98 to 20 GHz, and in this region of bandwidth, simulated S21 is less than about -25 dB. Scattering parameters of antenna was measured using Agilent EM 8722ES vector network analyzer. Measured results of S11 and S12 are

displayed in Fig. 6 (b). By comparing simulation and measured scattering results, it can be concluded that there is good matching between them in the expanding region. Measured results indicate that the antenna supplies an impedance bandwidth (S11&S22≤-10 dB) from 2.97 to 19.86 GHz, and it can also be realized that the measured port isolations (S21 & S12) are less than about -25 dB throughout the band. Thus, the bandwidth prerequisite for UWB applications is realized. Due to the effects of manufacturing tolerance, imperfect solder joints of the SMA connector to the feed-line and measurement environment, measured port is slightly worse than the simulation at frequencies from 3 to 11 GHz. Figure 7 depicts measured radiation patterns at 3, 6, 10, 14, and 19 GHz when port 2 is excited, while port 1 is terminated with a 50Ω load, and vice versa.

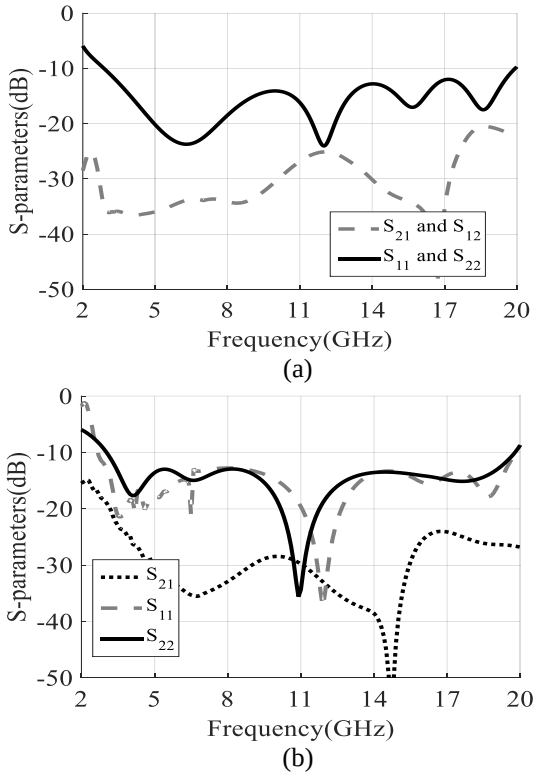

Fig. 6. Comparison between simulated and measured S11, S22 and S21: (a) Simulated and (b) measured.

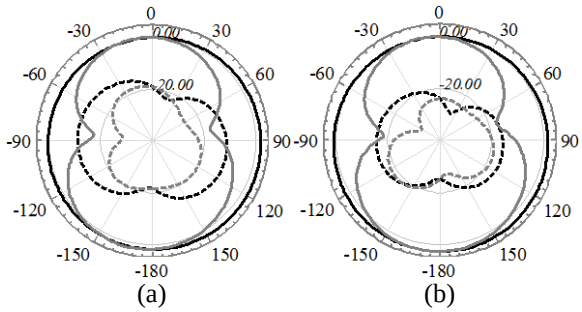

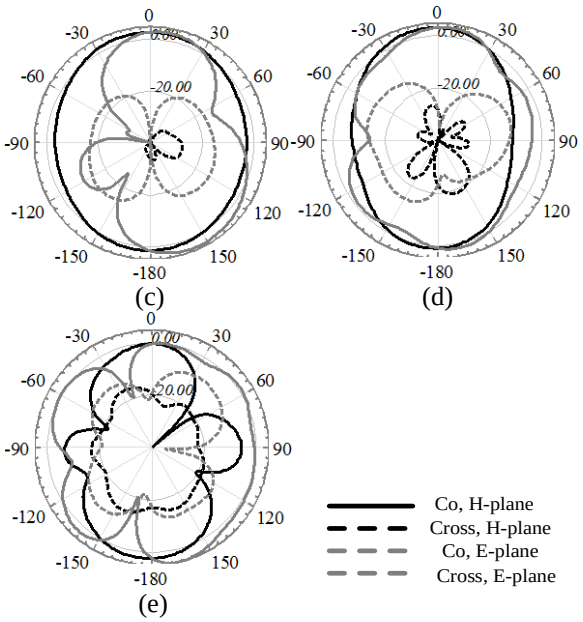

Fig. 7. Depicts measured radiation patterns at 3, 6, 10, 14 and 19 GHz when port 2 is excited: (a) 3 GHz, (b) 6 GHz, (c) 10 GHz, (d) 14 GHz, and (e) 19 GHz.

Figure 8 illustrates the simulated electric field distribution at 4, 8, and 12 GHz of the diversity antenna when two ports are excited respectively at different frequencies. It can be observed that the electric field is X-direction when port 1 is excited while the electric field shifts to Y-direction when port 2 is excited, which is consistent with the aforementioned current analysis. However, the polarization worsens at high frequency, which is attributed to the complicated current distribution on the radiator [8]. Gains and radiation efficiencies of the antennas for port 1 and 2 are measured. Figure 9 shows the measured gains of two antenna elements within the UWB band that are larger than 3.8 dB and have a peak gain of 4.7 dBi.

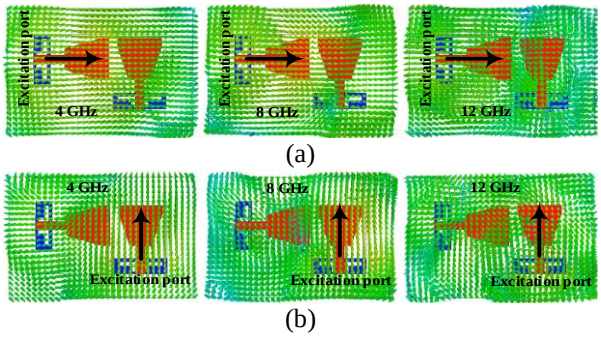

Fig. 8. The simulated far field electric field distribution at 4, 8, and 12 GHz of the diversity antenna when two ports are excited: (a) port 1 directed in X-direction, and (b) port 2 directed in Y-direction.

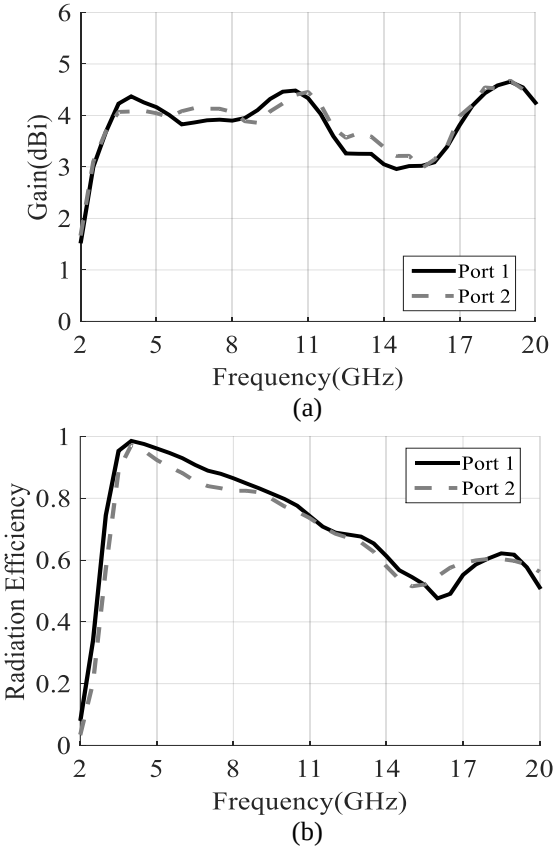

Fig. 9. Measured gains and radiation efficiencies of antennas for port 1 and 2: (a) gain and (b) radiation efficiencies.

It is essential to evaluate the Envelope Correlation Coefficient (ECC) since an ECC greater than 0.05 (less than -13 dB) can typically degrade the diversity performance. The ECC of the proposed antenna is also calculated [10, 23] using:

$$\rho_e = \frac{|S_{11}^* S_{12} + S_{21}^* S_{22}|^2}{(1-(|S_{11}|^2+|S_{21}|^2))(1-(|S_{22}|^2+|S_{12}|^2)}, \quad (7)$$

and is plotted in Fig. 10. The measurement and simulated values of ECC remain low throughout the UWB spectrum, which indicates that the proposed antenna is a good candidate for wireless communication systems with polarization diversity.

In a UWB system, the antenna needs to possess a high level of pulse-handling capability to handle high-frequency impulses. Hence, the time-domain properties are equally as important as frequency domain [1]. The group delay of the antenna is measured by exciting two identical antennas kept in the far field with face-to-face orientation (when one of the ports is excited, another port is terminated with 50 load, and vice versa). It is clear from Fig. 11 that the antenna displays a group delay that remains almost constant with variations less than 1 ns.

The HFSS default Gaussian pulse with spectrum covering from 2 GHz to 20 GHz band was employed as the input signal, as it completely complies with the FCC indoor and outdoor power masks [15]. Figure 12 displays the antenna impulse reply for the two measured directions.

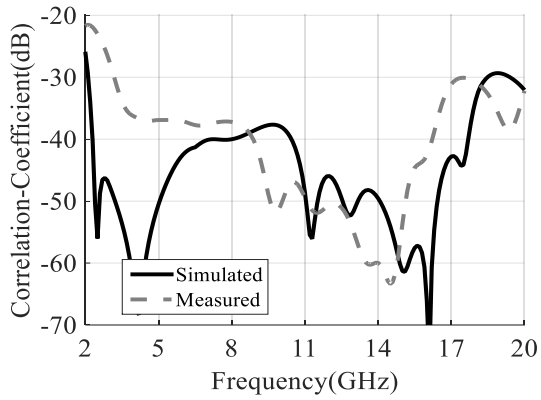

Fig. 10. Comparison between simulation and measurement values of ECC.

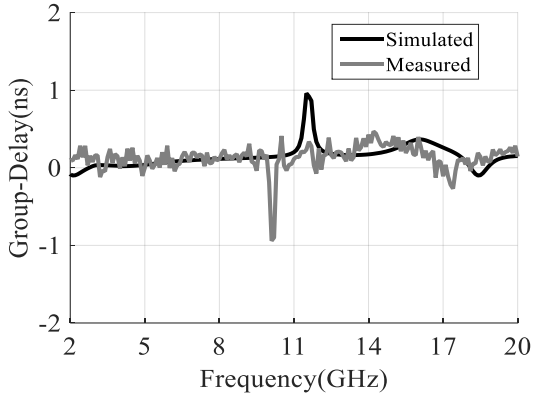

Fig. 11. Comparison between simulation and measurement values of proposed antenna group delay.

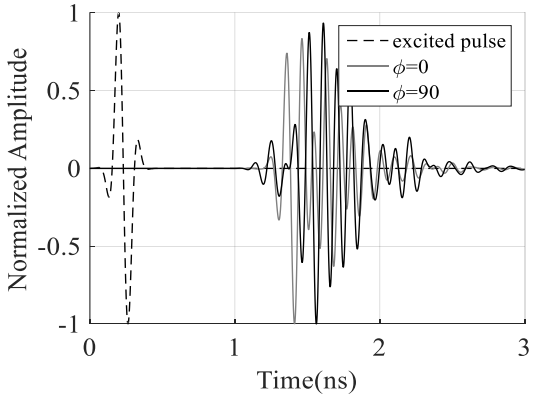

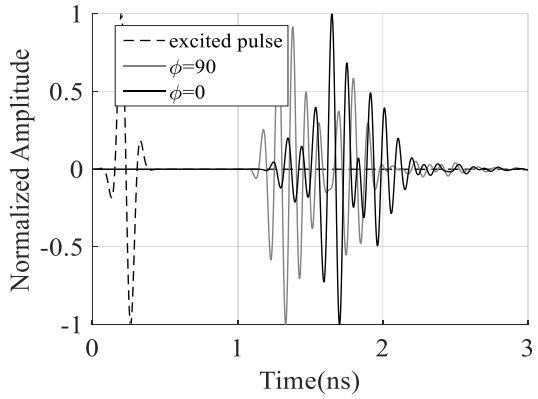

Fig. 12. Normalized amplitude measurement of Gaussian pulse response of antenna.

To compute the level of distortion, the system fidelity factor has been considered as in [14], and results are specified in Table 3. The measured average system fidelity factors, for the considered directions, of ports 1 and 2 are 88.2% and 84.3%, respectively, which shows that the level of signal distortion is quite suitable for UWB signals transmission [7]. The footprint of fabricated proposed compact polarization diversity MIMO antenna is illustrated in Fig. 13.

Table 3: Measured of system fidelity factor

Port 1	φ=0	89.6%
	φ=90	86.8%
Port 2	φ=0	85.3%
	φ=90	83.2%

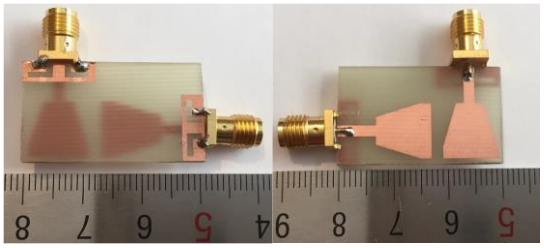

Fig. 13. Photograph of fabricated antenna.

V. CONCLUSION

An UWB MIMO antenna for polarization diversity applications has been proposed. The antenna prototype (with a size of 18×30 mm^2) in compared with same articles [1-9] have very compacted size and better results. Results show that the proposed antenna achieves an impedance bandwidth of larger than 147.96% (2.97 to 19.86 GHz). A high isolation between two ports has been achieved. Besides, low envelope correlation coefficient less than 0.001 was obtained. In the future, the proposed diversity UWB antenna mentioned above can be a promising candidate for wireless communication systems where a challenge such as multipath fading is a major concerns.

REFERENCES

[1] B. P. Chacko, G. Augustin, and T. A. Denidni, "Uniplanar slot antenna for ultrawideband polarization-diversity applications," in *IEEE Antennas and Wireless Propagation Letters*, vol. 12, pp. 88-91, 2013.

[2] S. Zhang, B. K. Lau, A. Sunesson, and S. He, "Closely-packed UWB MIMO/diversity antenna with different patterns and polarizations for USB dongle applications," in *IEEE Transactions on Antennas and Propagation*, vol. 60, no. 9, pp. 4372-4380, Sept. 2012.

[3] H. Huang, Y. Liu, S. Zhang, and S. Gong, "Uniplanar ultrawideband polarization diversity antenna with dual band-notched characteristics," in *IEEE Antennas and Wireless Propagation Letters*, vol. 13, pp. 1745-1748, 2014.

[4] H. Huang, Y. Liu, and S. Gong, "Uniplanar differentially driven UWB polarisation diversity antenna with band-notched characteristics," in *Electronics Letters*, vol. 51, no. 3, pp. 206-207, Feb. 5, 2015.

[5] B. P. Chacko, G. Augustin, and T. A. Denidni, "Uniplanar polarisation diversity antenna for ultrawideband systems," in *IET Microwaves, Antennas & Propagation*, vol. 7, no. 10, pp. 851-857, July 16, 2013.

[6] H. Huang, Y. Liu, S. Zhang, and S. Gong, "Uniplanar differentially driven ultrawideband polarization diversity antenna with band-notched characteristics," in *IEEE Antennas and Wireless Propagation Letters*, vol. 14, pp. 563-566, 2015.

[7] M. Koohestani, A. A. Moreira, and A. K. Skrivervik, "A novel compact CPW-fed polarization diversity ultrawideband antenna," in *IEEE Antennas and Wireless Propagation Letters*, vol. 13, pp. 563-566, 2014.

[8] C. X. Mao and Q. X. Chu, "Compact co radiator UWB-MIMO antenna with dual polarization," in *IEEE Transactions on Antennas and Propagation*, vol. 62, no. 9, pp. 4474-4480, Sept. 2014.

[9] L. Kang, H. Li, X. Wang, and X. Shi, "Compact offset microstrip-fed MIMO antenna for band-notched UWB applications," in *IEEE Antennas and Wireless Propagation Letters*, vol. 14, pp. 1754-1757, 2015.

[10] W. K. Toh, Z. N. Chen, Q. Xianming, and T. S. P. See, "A planar UWB diversity antenna," *IEEE Trans. Antennas Propag.*, vol. 57, no. 11, pp. 3467-3473, Nov. 2009.

[11] Q. H. Abbasi, M. M. Khan, S. Liaqat, M. Kamran, A. Alomainy, and Y. Hao, "Experimental investigation of ultra wideband diversity techniques for

on-body radio communications," *Prog. Electromagn. Res. C*, vol. 34, pp. 165-181, 2013.

[12] Q. H. Abbasi, A. Alomainy, and Y. Hao, "Ultra wideband antenna diversity techniques for on/off-body radio channel characterization," in *Proc. IEEE iWAT*, pp. 209-212, 2012.

[13] Y. Li, W. X. Li, Ch. Liu, and T. Jiang, "A printed diversity cantor set fractal antenna for ultra wideband communication applications," in *Proc. Antennas, Propag., EM Theory*, pp. 34-38, 2012.

[14] G. Quintero, J.-F. Zürcher, and A. K. Skrivervik, "System fidelity factor: A new method for comparing UWB antennas," *IEEE Trans. Antennas Propag.*, vol. 59, no. 7, pp. 2502-2512, July 2011.

[15] M. Koohestani, N. Pires, A. K. Skrivervik, and A. A. Moreira, "Time domain performance of patch-loaded band-reject UWB antenna," *Electron. Lett.*, vol. 49, no. 6, pp. 385-386, 2013.

[16] B. S. Femina and S. K. Mishra, "Compact WLAN band-notched printed ultrawideband MIMO antenna with polarization diversity," in *Progress In Electromagnetics Research C*, vol. 61, pp. 149-159, 2016.

[17] H. Huang, Y. Liu, S.-S. Zhang, and S.-X. Gong, "Compact polarization diversity ultrawideband mimo antenna with triple band-notched characteristics," *Microw. Opt. Technol. Lett.*, vol. 57, iss. 4, pp. 946-953, Apr. 2015.

[18] M. Ojaroudi and E. Mehrshahi, "Bandwidth enhancement of small square monopole antennas by using defected structures based on time domain reflectometry analysis for UWB applications," *Applied Computational Electromagnetics Society Journal*, vol. 28, iss. 7, pp. 620-627, July 2013.

[19] R. Azim, M. T. Islam, and N. Misran, "Design of a planar UWB antenna with new band enhancement technique," *Appl. Comp. Electro. Society (ACES) Journal*, vol. 26, no. 10, pp. 856-862, Oct. 2011.

[20] G. Zhang, J. S. Hong, B. Z. Wang, and G. Song, "Switched band-notched UWB/ WLAN monopole antenna," *Appl. Comp. Electro. Society (ACES) Journal*, vol. 27, no. 3, pp. 256-260, Mar. 2012.

[21] W. C. Weng, "Optimal design of an ultra-wideband antenna with the irregular shape on radiator using particle swarm optimization," *Appl. Comp. Electro. Society (ACES) Journal*, vol. 27, no. 5, pp. 427-434, May 2012.

[22] X.-S. Yang, S.-G. Qiu, and J.-L. Li, "Triangular-arranged planar multiple-antenna for UWB-MIMO applications," *Applied Computational Electromagnetics Society Journal*, vol. 29, iss. 1, pp. 62-66, Jan. 2014.

[23] P. Zibadoost, J. Nourinia, C. Ghobadi, S. Mohammadi, A. Mousazadeh, and B. Mohammadi, "Full band MIMO monopole antenna for LTE systems," *Applied Computational Electromagnetics Society Journal*, vol. 29, iss. 1, pp. 54-61, Jan. 2014.

Saeid Karamzadeh received his M.S. and Ph.D. degrees in Department of Communication Systems, Satellite Communication & Remote Sensing program at Istanbul Technical University in 2013 and 2015 respectively. He won the most successful Ph.D. thesis award of Istanbul Technical University. Currently, he is an Assistant Professor in the Istanbul Aydin University, Department of Electrical and Electronics Engineering. He is also with Application & Research Center for Advanced Studies in the Istanbul Aydin University, Turkey. His research interests include remote sensing, radar, microwave, and Antenna design.

Dual-Band Wide-Angle Circularly-Polarized Microstrip Antenna by Ferrite Ring Inserted in Its Cavity Domain

Fazel Rangriz Rostami [1], Gholamreza Moradi [1,2], and Reza Sarraf Shirazi [1]

[1,2,3] Department of Electrical Engineering
Amirkabir University of Technology, Tehran, Iran
fazel.rangriz@aut.ac.ir, ghmoradi@aut.ac.ir, sarraf@aut.ac.ir

[2] Department of Mechanical Engineering
University of Alberta, Alberta, Canada

Abstract ─ In this paper coaxially-fed circular microstrip patch antenna with ferrite ring in its cavity domain is presented in order to obtain dual-band circularly-polarized antenna in X-band having wide angle axial ratio in both bands. A mode matching approach is used to see the effects of each mode on input impedance of the antenna and is validated numerically by finite element method. The theoretical calculations for input impedance are in good agreement with full-wave simulation. The scattering and radiation parameters of the antenna are investigated. The antenna patch radius and height are 8 and 1 mm, respectively. The ferrite ring was made of yttrium iron garnet (YIG) and the substrate of antenna is Rogers RT5880. In the first band the antenna has 7 dB gain and the ratio of Copol/Xpol is about 24 dB and in the second band has 5 dB gain and the XPD, i.e., the ratio of Copol to Xpol is about 20 dB.

Index Terms ─ Dual-band circularly-polarized antenna, microstrip antennas, mode-matching, wide-angle antenna.

I. INTRODUCTION

Circular polarization (CP) is extensively used in wireless and satellite communications. In many papers, ferrite substrate was used to generate CP [1]-[2]. In [3], circularly polarized microstrip antenna based on the unidirectional resonant modes of a ferrite disk has been introduced which produce wide angle circular polarization for GPS application. In [4], circularly polarized microstrip antenna has been obtained by small ferrite disks inserted in its cavity domain. In order to have single-feed dual-band CP antenna various configurations have been investigated for GPS application [5]-[6]. A compact CP dual-band antenna was successfully designed for Meteosat satellite in L and X communication bands [7]. In [8], a compact dual-band CP multilayer microstrip antenna using LTCC technology has been proposed and implemented, due to the stacked-patch structure and inserted slits, the designed antenna has a small volume compared to the conventional dual-band CP antennas. A crossed asymmetric dipole antenna over a dual-band AMC surface has been introduced in [9] in which, the proposed antenna yields a low profile, good impedance matching, good CP radiation, and an improved 3-dB AR bandwidth at both operating bands. Sun *et al.* have introduced a dual-feed stacked annular-ring patch antenna which is dual-band, dual-layer; and is excited by two orthogonal H-shaped slots, fed by a 3-dB hybrid [10]. In [4], it is shown that dual-band CP antennas can be obtained by insertion of two or more ferrite disks in the cavity region of the antenna along with appropriate optimization of the bias magnetic field.

In this letter, a new configuration to achieve single-feed dual-band CP microstrip antenna is presented. Antenna has been excited via coaxial port; in addition, a ferrite ring is inserted in antenna cavity domain in order to produce circular polarization.

This paper is organized as follows. Section II introduces the structure of complete antenna. The theoretical analysis of input impedance of antenna is described in Section III and the results are validated by full-wave simulations and discussed. In Section IV radiation characteristics of antenna are simulated with CST Studio and discussed.

II. ANTENNA STRUCTURE

Figure 1 (a) shows the proposed antenna, which consists of a ferrite ring inserted in the cavity domain of the substrate. The ferrite disk is magnetized normal to the ground plane by a dc bias magnetic field H_0, which can be provided by a permanent magnet placed underneath the ground plane. The substrate of antenna is made of RT5880, permeability (μ) of the substrate is equal to that of the air, i.e., $\mu = \mu_0$, and has relative permittivity 2.2 and its loss tangent $\tan(\delta)$ is about 0.0009. The cavity domain of antenna has four regions as it can be seen from Fig. 1 (b). Region I is defined by

Submitted On: July 14, 2016
Accepted On: November 19, 2016

$0 < r < a$, which is from the center of the patch to the current probe that is fed at $r = a$. Region II is defined by $a < r < b$. This region is between feed probe and ferrite ring. Region III is defined by $b < r < c$, which contains ferrite ring, and finally, region IV is defined by $c < r < d$, which is between ferrite ring and edge of the patch. The ferrite ring with thickness 1 mm and height 1 mm is inserted in the cavity domain of patch antenna with radius 8 mm, and its substrate height is 1 mm.

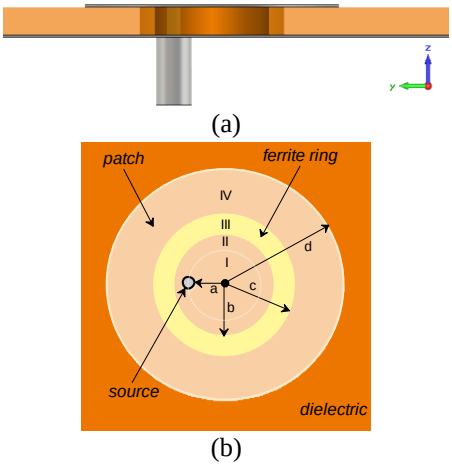

Fig. 1. (a) Side view of the antenna, and (b) top view of the antenna.

Permeability of the ferrite ring is defined as the following:

$$\mu = 1 + \frac{(\omega_H + j\,\omega\alpha)\omega_M}{\left(\omega_H + j\,\omega\alpha\right)^2 - \omega^2}, \tag{1}$$

$$\mu_a = \frac{\omega_M\,\omega}{\left(\omega_H + j\,\omega\alpha\right)^2 - \omega^2}, \tag{2}$$

$$\mu_\perp = \mu - \frac{\mu_\alpha^2}{\mu}, \tag{3}$$

in which μ and μ_α are the diagonals and off-diagonal elements of the permeability tensor of the ferrite, respectively, where $\omega_H = \gamma H_0$ and $\omega_M = \gamma M_s$, with M_s the saturation magnetization of the ferrite, and γ the gyromagnetic ratio, and also α is the Gilbert damping constant, and $\left(\Delta H = 2\alpha\omega/\gamma\right)$ is magnetic line width of the ferrite material, and also $\mu_\perp$ is effective permeability of ferrite material. The material properties of the ferrite ring are according to the Table 1.

Table 1: Ferrite material properties

H_0	ΔH	$4\pi M_s$	ε_{fer}
600 (Oe	20 (Oe)	1780 (Gauss)	15

Real and imaginary parts of ferrite permeability in desired frequency range are plotted in Fig. 2.

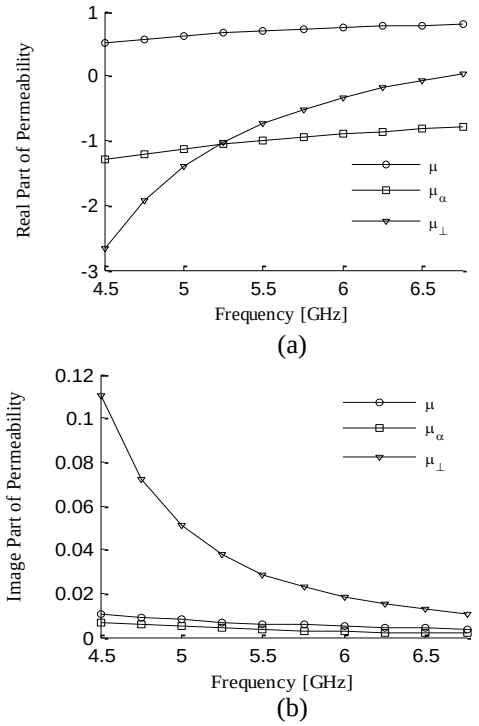

Fig. 2. Permeability of ferrite: (a) real part, and (b) imaginary part. Ferrite parameters are the same as Table 1.

III. INPUT IMPEDANCE

To determine the input impedance of the antenna, it is necessary to find the field solution beneath the circular patch. In general, these solutions take the form of a cylindrical mode expansion, with each mode being determined by arbitrary constants. To find all of these constants, additional boundary conditions are required, which are obtained by considering the wall admittances. The electric and magnetic field solution in each region can be written as following, in which for simplification purposes, the variations of the fields in z direction are ignored:

$$E_z^I(r,\phi) = \sum_n -j\omega A_n e^{jn\phi} J_n(kr), \tag{4}$$

$$H_\phi^I(r,\phi) = \sum_n -A_n \frac{1}{\mu_0} e^{jn\phi} \frac{\partial}{\partial r} J_n(kr), \tag{5}$$

$$E_z^{II}(r,\phi) = \sum_n -j\omega e^{jn\phi} \left(B_n J_n(kr) + C_n Y_n(kr)\right), \tag{6}$$

$$H_\phi^{II}(r,\phi) = \sum_n -\frac{1}{\mu_0} e^{jn\phi} \left(B_n \frac{\partial}{\partial r} J_n(kr) + C_n \frac{\partial}{\partial r} Y_n(kr)\right), \tag{7}$$

where J_n and Y_n are Bessel function of the first kind and second kind, respectively. In region I, II and IV, we have ordinary substrate and $k = k_0\sqrt{\varepsilon_r}$ in which, k_0 is

the free space wave number. In region III, due to the presence of the ferrite material electric and magnetic fields are written as following:

$$E_z^{III}(r,\phi)=\sum_n -j\omega e^{jn\phi}\left(D_n J_n(k_\perp r)+E_n Y_n(k_\perp r)\right), \quad (8)$$

$$H_\phi^{III}(r,\phi)=\sum_n -\frac{j}{\mu_0}e^{jn\phi}\left(\frac{\mu r\frac{\partial}{\partial r}E_z^{III}(r,\phi)+n\mu_\alpha E_z^{III}(r,\phi)}{\omega r\mu_\perp}\right), \quad (9)$$

in which $k_\perp = k_0\sqrt{\varepsilon_{fer}\mu_\perp}$. In region IV, we have the next ordinary substrate, will then result to:

$$E_z^{IV}(r,\phi)=\sum_n -j\omega e^{jn\phi}\left(F_n J_n(kr)+G_n Y_n(kr)\right), \quad (10)$$

$$H_\phi^{IV}(r,\phi)=\sum_n -\frac{1}{\mu_0}e^{jn\phi}\left(F_n\frac{\partial}{\partial r}J_n(kr)+G_n\frac{\partial}{\partial r}Y_n(kr)\right). \quad (11)$$

In order to take the feed probe into account, neglecting the variation of the probe current in the $z-$ direction, an infinitely thin electric current line source carrying a constant current I_0 is assumed. The current density of the line source is:

$$\boldsymbol{J}=\hat{z}\,J_z=\hat{z}\frac{I_0}{r_0}\delta(r-a)\delta(\phi).$$

Boundary conditions on the tangential components of the electric and magnetic fields are applied as following:

$$E_z^I(a,\phi)=E_z^{II}(a,\phi), \quad (12)$$

$$H_\phi^{II}(a,\phi)-H_\phi^I(a,\phi)=J_z, \quad (13)$$

$$E_z^{II}(b,\phi)=E_z^{III}(b,\phi), \quad (14)$$

$$H_\phi^{II}(b,\phi)=H_\phi^{III}(b,\phi), \quad (15)$$

$$E_z^{III}(c,\phi)=E_z^{IV}(c,\phi), \quad (16)$$

$$H_\phi^{III}(c,\phi)=H_\phi^{IV}(c,\phi). \quad (17)$$

By considering wall admittance on the side wall of the microstrip antenna, the next boundary condition can be written as following:

$$H_\phi^{IV}(d,\phi)=-y_n E_z^{IV}(d,\phi). \quad (18)$$

By using Equations (11) through (17), the constants A_n, B_n, C_n, D_n, E_n, F_n, and G_n will be evaluated. The input impedance can be written as following:

$$Z_{in}=-\frac{1}{I_0}\int_0^h E_z^I(r=a,\phi=0)dz. \quad (19)$$

In this paper the wall admittance, described in [11] is used, this wall admittance y_n fix the ratio between the $z-$directed electric field and the $\phi-$directed magnetic field for each mode. The antenna parameters are considered as Table 2.

Table 2: Antenna parameters

a	*b*	*c*	*d*
2.5 mm	4 mm	5 mm	8 mm

In the absence of ferrite ring, the superposition of two azimuthally travelling waves in opposite direction, have the same amplitude and resonance frequency, results in a standing wave behavior of the electric field. In order to show the effect of ferrite ring on the separation of resonance frequency of the right-handed and left-handed azimuthal modes, input impedance of each mode is individually plotted in Fig. 3. As it can be seen, modes of $n=\pm1$ do not have the same resonance frequency. These two modes have the most influence on the input impedance, and the other modes have a negligible effect on the real part of input impedance but increase the imaginary part of the input impedance.

Figures 4 and 5 show the comparison between our theoretical results for the input impedance and return loss, and those obtained by CST studio full wave simulator. For each calculation, we have considered 5 modes, the modes having order of greater than 5 were found to have insignificant effect on the calculated input impedance. It is seen that the mode matching results are close to that obtained by the CST studio simulation. The antenna has impedance bandwidth between (5.26 GHz-5.34 GHz) or 1.5% and (6 GHz-6.2 GHz) or 1.7% in first and second band, respectively.

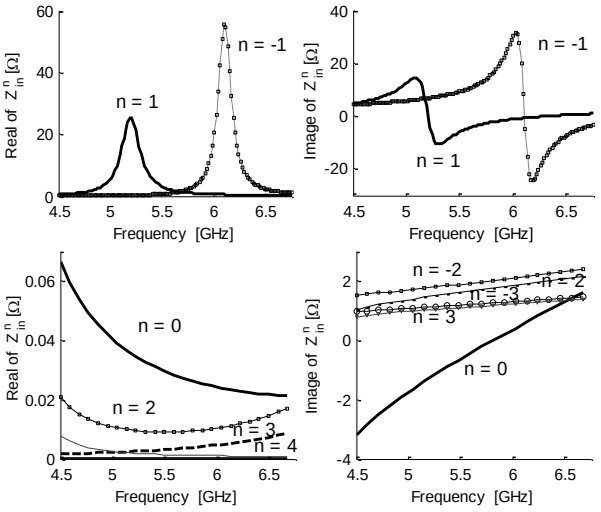

Fig. 3. Input impedance of each mode.

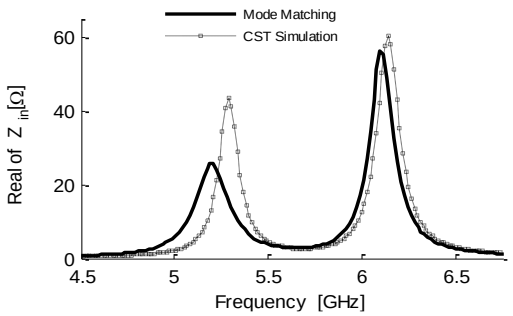

(a)

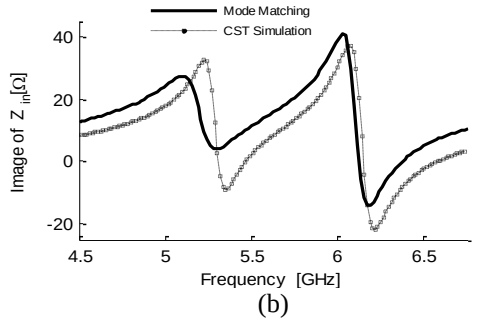

(b)

Fig. 4. Comparison between mode matching method and CST studio results: (a) real part and (b) imaginary part.

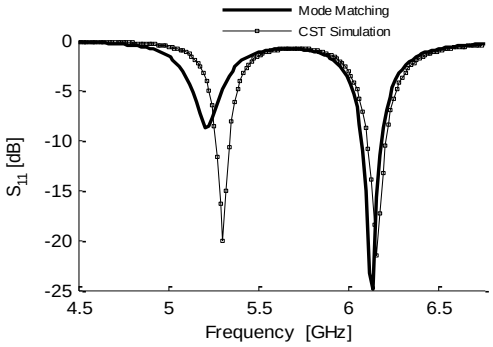

Fig. 5. Comparison of return loss between mode matching method and CST studio results.

The proposed dual-band CP antenna can be designed by adjusting the thickness of ferrite ring and by varying the dc bias field H_0 of ferrite.

Figure 6 shows the effect of ring thickness on the first and second band resonance frequency. By increasing the ring thickness, both resonance frequencies decrease which is due to the increasing of the effective permittivity and permeability of the substrate. Also, the separation between two resonance frequencies increases because the ferrite region which has anisotropic behavior is increased.

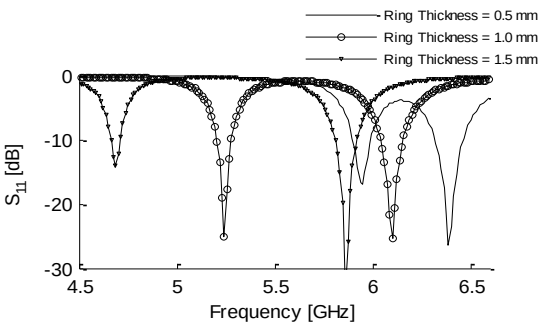

Fig. 6. Full-wave simulation result of the return loss against the ring thickness. The other design parameters are the same as in Fig. 4.

Figure 7 shows the effect of dc bias field H_0 on the resonance frequency. As it can be seen, by increasing the bias field, the resonance frequencies, and especially the second can be controlled.

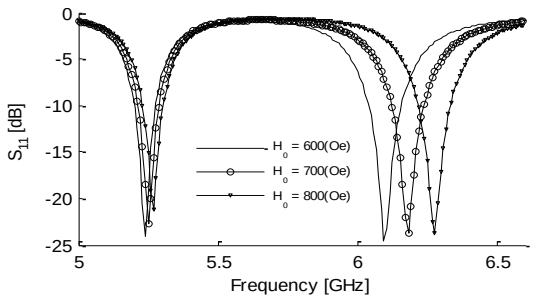

Fig. 7. Full-wave simulation result of the return loss against the magnetic bias field. The other design parameters are the same as in Fig. 4.

IV. RADIATION PROPERTIES

In order to examine radiation properties of the antenna, we consider a structure whose patch and ground plane are made of copper and having thickness of 50 microns. The ground dimensions in full wave simulation are considered $60\times60\ mm^2$.

Figure 8 shows the simulation results of axial ratio of the antenna on broadside direction versus frequency. As it can be seen, 3 dB axial ratio at first and second band is between (5.06 GHz-5.42 GHz) or 6.87% and (6.04 GHz-6.27 GHz) or 3.74%, respectively. The axial ratio bandwidth is wider than the impedance bandwidth which is given in Fig. 5. In Fig. 9, simulated axial ratio of the proposed antenna versus θ, at the first and second resonance frequencies are shown, the wide angle behavior of the antenna can be seen in this figure.

In Fig. 10, the gain of the antenna as a function of frequency is shown, the antenna has 7 dB gain in first band and 5 dB gain in second band.

In Fig. 11, simulated radiation patterns for RHCP and LHCP at first and second resonance frequency in the XOZ plane ($\phi=0$) and YOZ ($\phi=90$) plane are shown.

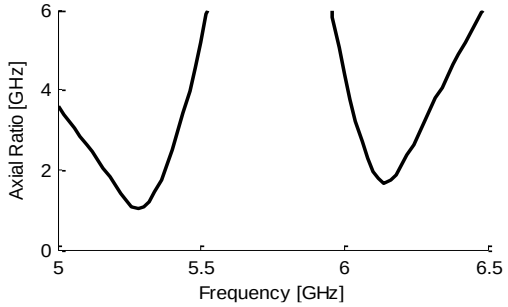

Fig. 8. The simulated broadside axial ratio versus frequency.

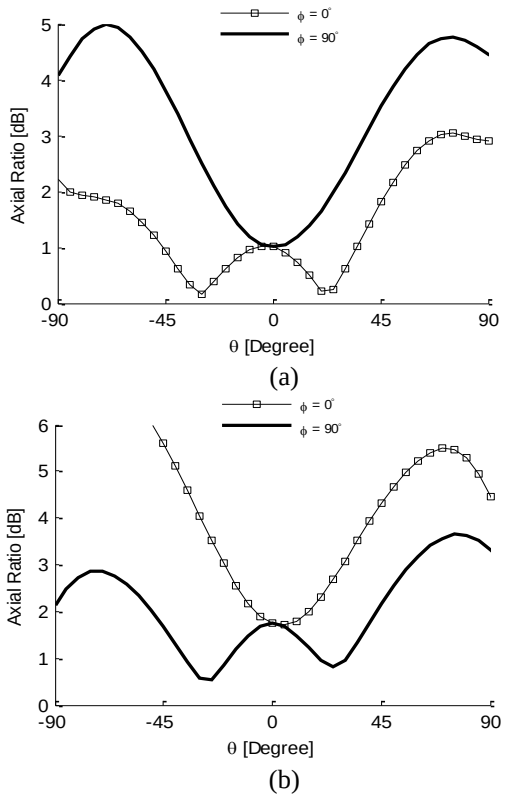

Fig. 9. Simulated axial ratio of the proposed antenna versus θ: (a) 5.3 GHz and (b) 6.16 GHz.

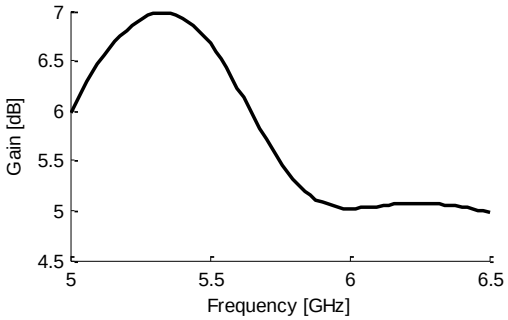

Fig. 10. The simulated broadside gain versus frequency.

It can be observed that the antenna has LHCP polarization in the first band and RHCP polarization in the second band. The Co-pol/Xpol is about 24 dB and 20 dB in the first and second bands, respectively. It is noticeable that the state of polarization can be switched by reversing the direction of the DC magnetic bias field. The efficiency of the antenna in first and second bands are 90% and 60%, respectively. The decrease in efficiency of the second band is due to the increase in ferrite loss. In Fig. 12, the loss of each part the antenna is plotted as a function of frequency. Here, the total input power in full-wave simulation is 500 mW. As it can be seen, the loss of ferrite ring is more than other losses and it plays the major role in antenna efficiency.

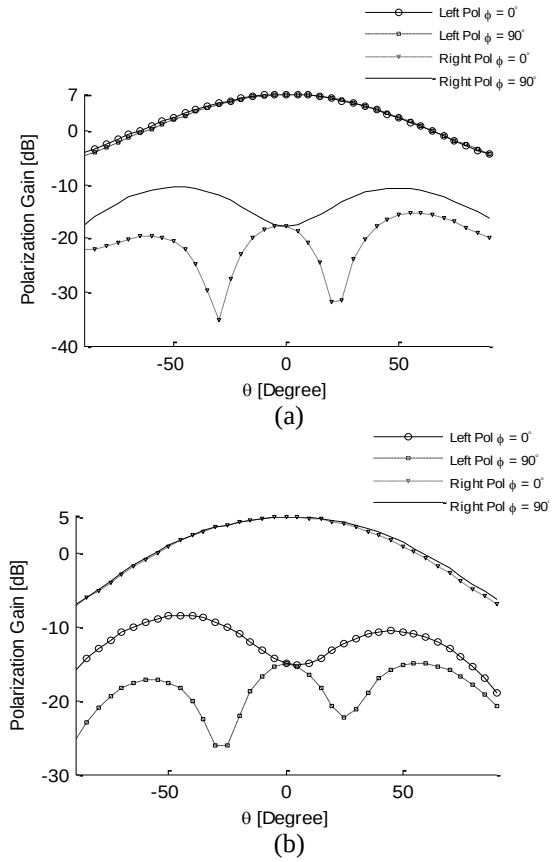

Fig. 11. Simulated radiation patterns for RHCP and LHCP at 5.3 GHz and 6.16 GHz in the XOZ plane ($\phi = 0$) and YOZ ($\phi = 90$) plane: (a) 5.3 GHz and (b) 6.16 GHz.

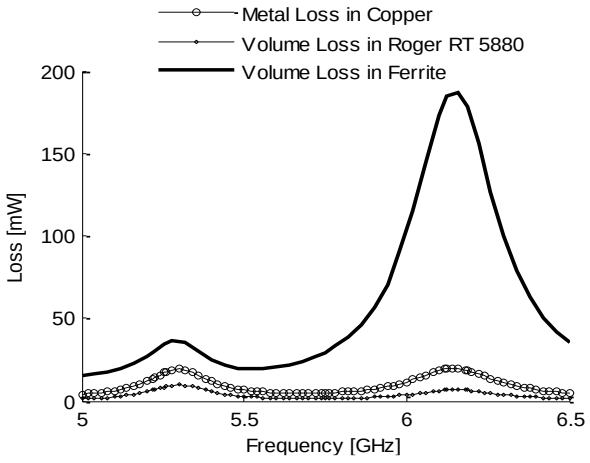

Fig. 12. Loss in each part of the antenna (total input power is 500 [mW])

V. CONCLUSION

A new single-layer single-feed dual-band CP antenna with wide-angle axial ratio in both frequency bands by inserting a ferrite ring in cavity domain has been proposed. This antenna has 6.87% axial ratio bandwidth, and 1.5% impedance bandwidth in the first band. It also has 3.74% axial ratio bandwidth and 1.7% impedance bandwidth in the second band and can be used as a frequency tunable antenna. Proposed structure is compact, easy to design and fabricate, and does not require a complicated feeding network. Therefore, it could be a good candidate for realizing wide-angle dual-band CP antennas.

REFERENCES

[1] D. M. Pozar, "Radiation and scattering characteristics of microstrip antennas on normally biased ferrite substrates," in *IEEE Transactions on Antennas and Propagation*, vol. 40, no. 9, pp. 1084-1092, Sep. 1992.

[2] A. D. Brown, J. L. Volakis, L. C. Kempel, and Y. Botros, "Patch antennas on ferromagnetic subtrates," in *IEEE Transactions on Antennas and Propagation*, vol. 47, no. 1, pp. 26-32, Jan. 1999.

[3] J. Ghalibafan, B. Rejaei, and N. Komjani, "A circlarly polarized antenna based on the unidirectional resonant modes of a Ferrite disk," in *IEEE Transactions on Magnetics*, vol. 50, no. 3, pp. 88-95, Mar. 2014.

[4] M. Sigalov, R. Shavit, R. Joffe and E. O. Kamenetskii, "Manipulation of the radiation characteristics of a patch antenna by small Ferrite disks inserted in its cavity domain," in *IEEE Transactions on Antennas and Propagation*, vol. 61, no. 5, pp. 2371-2379, May 2013.

[5] W. T. Hsieh, T. H. Chang, and J. F. Kiang, "Dual-band circularly polarized cavity-backed annular slot antenna for GPS receiver," in *IEEE Transactions on Antennas and Propagation*, vol. 60, no. 4, pp. 2076-2080, Apr. 2012.

[6] M. Maqsood, et al., "Low-cost dual-band circularly polarized switched-beam array for global navigation satellite system," in *IEEE Transactions on Antennas and Propagation*, vol. 62, no. 4, pp. 1975-1982, Apr. 2014.

[7] F. Ferrero, C. Luxey, G. Jacquemod, and R. Staraj, "Dual-band circularly polarized microstrip antenna for satellite applications," in *IEEE Antennas and Wireless Propagation Letters*, vol. 4, no. , pp. 13-15, 2005.

[8] K. Qian and X. Tang, "Compact LTCC dual-band circularly polarized perturbed hexagonal microstrip antenna," in *IEEE Antennas and Wireless Propagation Letters*, vol. 10, pp. 1212-1215, 2011.

[9] S. X. Ta and I. Park, "Dual-band low-profile crossed asymmetric dipole antenna on dual-band AMC surface," in *IEEE Antennas and Wireless Propagation Letters*, vol. 13, pp. 587-590, 2014.

[10] X. Sun, Z. Zhang, and Z. Feng, "Dual-band circularly polarized stacked annular-ring patch antenna for GPS application," in *IEEE Antennas and Wireless Propagation Letters*, vol. 10, pp. 49-52, 2011.

[11] F. R. Rostami, G. Moradi, and R. S. Shirazi, "Mode matching in microstrip antenna with both electric and magnetic surface current on sidewall in cavity model," *Applied Computational Electromagnetics Society Journal*, vol. 31, no. 7, 2016.

Computationally Efficient Technique for Wide-Band Analysis of Grid-Like Spatial Shields for Protection Against LEMP Effects

Andrzej Karwowski, Artur Noga, and Tomasz Topa

Institute of Electronics
Silesian University of Technology (SUT), Gliwice, 44-100, Poland
andrzej.karwowski@polsl.pl, artur.noga@polsl.pl, tomasz.topa@polsl.pl

Abstract ─ This paper introduces a heterogeneous CPU+GPU co-processing implementation of the method of moments (MoM) for broadband full-wave electromagnetic analysis of grid-like spatial shields for protecting structures against LEMP effects. Broadband capacity of the approach is achieved through supporting MoM by adaptive frequency sampling and implicit rational interpolation of the observed quantity via Stoer-Bulirsch algorithm. The overall application performance is increased by hardware acceleration, i.e., by employing CPU+GPU co-processing. Sample numerical results for a lightning protection system directly hit by lightning show that reliable rational interpolation can be done at substantially reduced computational effort compared to that of conventional uniform sampling, and the CPU+GPU co-processing offers additional noticeable speedup over the CPU single-thread implementation of the method.

Index Terms ─ CPU+GPU co-processing, grid-like shield, lightning protection system, method of moments, rational interpolation, Stoer-Bulirsch algorithm.

I. INTRODUCTION

Wire meshes in the form of spatial grid-like structures are widely used as lightning protection systems (LPS) designed to reduce aggressive high-intensity electromagnetic (EM) effects caused by lightning strikes. For effective design of LPS, prediction of its response to lightning induced electromagnetic excitation is of vital importance. Therefore, a considerable research effort has been devoted over the last years to the development of accurate and efficient techniques for EM analysis of complex LPSs. For spatial grid-like structures composed of arbitrarily arranged conductors, perhaps the best choice is the full-wave method of moments (MoM) formulated in the frequency domain (FD) [1]. When a wideband response of a structure is required, the investigation is usually carried out by point-by-point frequency swept computations, i.e., evaluation of samples of the required physical observable over a predefined set of uniformly spaced frequency nodes. The approach is computationally inefficient, since EM simulation must be performed repeatedly at many frequencies resulting in that the computation time can be unacceptably long for complex resonant structures. Among available approaches aimed at reducing the number of EM simulations needed for reconstruction of the system response, and thus, minimizing the overall processing time is the rational-function interpolation approach based upon the assumption that the system response can be represented by a rational polynomial [2]. The approach usually involves adaptive procedures for selecting the interpolation nodes and the rational interpolant order. In this study, we employ an adaptive frequency sampling (AFS) technique based upon interval halving (bisection) in combination with the rational interpolation implemented through Stoer-Bulirsch (SB) algorithm [3]. The details of the formulation are given in [4, 5].

Till the end of Pentium IV era, the possibility of MoM-based wide-band simulation of LPS structures on PC-based workstations was seriously limited. For example, the runtime needed for a wide-band simulation from 1 kHz to 20 MHz of a single-layer grid-like LPS type 1 (10 m × 10 m × 10 m) [6] discretized into 2224 wire segments was about one week [7]. The situation has changed dramatically with the introduction, about 2006, of powerful multi-core CPU technologies and the unified graphics and computing Graphics Processing Unit (GPU) architecture known as Nvidia CUDA (Compute Unified Device Architecture). Multi-core processors and CUDA-enabled GPUs offer an inexpensive massively parallel programmable hardware platform very attractive for use in scientific computing. It is now well known that by extending a traditional CPU-based computation model through adoption of the General-Purpose computing on GPU (GPGPU) paradigm, the performance of EM simulations can be remarkably increased.

In this paper, a CUDA-enabled heterogeneous CPU+GPU co-processing implementation of the method of moments supported by AFS and implicit rational interpolation for electromagnetic simulation of grid-like lightning shields over a wide frequency band is outlined.

Submitted On: October 24, 2015
Accepted On: November 5, 2016

The approach employs the technique described in [8] for mapping CPU sequential MoM procedures to parallel GPU platform. For consistence of presentation, we briefly summarize partial concepts of the overall approach including AFS-SB algorithm and CUDA-based CPU+GPU implementation of the relevant computer program. The potential of the approach is demonstrated by a numerical example involving grid-like LPS under direct strike.

The key components of a hardware platform engaged in this study were the Intel Core i7-3820 Quad-Core Processor and GeForce GTX 680 graphics card. Software tools included Intel Fortran, PGI Fortran, CULA and Intel MKL libraries. The overall approach constitutes an example of the integration of the advanced computational electromagnetics technique with modern architecture of a rather typical low-cost PC-style workstation for the purpose of increasing efficiency of the application-oriented EM simulator.

II. METHOD

A. Matrix approximant to the integral equation

The approach outlined in this paper adopts (for wires) the frequency-domain mixed-potential electric field integral equation (EFIE) formulation developed in [9] for analyzing an arbitrary configuration of conducting bodies and wires. For the sake of completeness, the formulation is briefly outlined here.

For a wire residing in a simple medium (ε, μ) and illuminated by an incident time-harmonic (exp (jωt)) EM field $(\mathbf{E}^i, \mathbf{H}^i)$, the EFIE for the total axial current $\mathbf{I}(l)$ excited on the wire can be written as [9]:

$$(j\omega\mathbf{A} + \nabla\phi)\cdot\mathbf{1}_l = \mathbf{1}_l\cdot\mathbf{E}^i, \tag{1}$$

with conventional notation $\mathbf{A}$ and ϕ employed for the magnetic vector potential and electric scalar potential, respectively, and $\mathbf{1}_l$ denoting the unit vector locally parallel to the wire axis. For the wire approximated by a series of broken line segments, the unknown current is expanded as a linear combination of one-dimensional (triangle) RWG-type functions:

$$\mathbf{I}(l) \cong \sum_{n=1}^{N} I_n \mathbf{T}_n(l)\,, \tag{2}$$

where

$$\mathbf{T}_n(l) = \begin{cases} \mathbf{1}_n^+(l - l_{n-1})/\Delta_n^+ & \text{if } \ l_{n-1} \le l \le l_n\,, \\ \mathbf{1}_n^-(l_{n+1} - l)/\Delta_n^- & \text{if } \ l_n \le l \le l_{n+1}\,, \\ 0 & \text{otherwise,} \end{cases} \tag{3}$$

and

$$\Delta_n^+ = |\mathbf{r}_n - \mathbf{r}_{n-1}| \quad \text{and} \quad \Delta_n^+ = |\mathbf{r}_{n+1} - \mathbf{r}_n|, \tag{4}$$

with l and $\mathbf{r}_i$ denoting the arc length along the wire axis and a position vector of the i-th point subdividing the wire into segments, respectively. The EFIE-MoM procedure leads to the matrix equation:

$$\mathbf{Z}(f)\mathbf{I}(f) = \mathbf{V}(f), \tag{5}$$

in which $\mathbf{Z}_{N\times N}$ denotes the MoM-generated system matrix with elements (m, n = 1, 2, …, N):

$$\begin{aligned} Z_{mn} = j\omega\big[&\mathbf{A}_n(\mathbf{r}_{m-1/2})\cdot(\mathbf{r}_m - \mathbf{r}_{m-1/2}) \\ &+ \mathbf{A}_n(\mathbf{r}_{m+1/2})\cdot(\mathbf{r}_{m+1/2} - \mathbf{r}_m)\big] \\ &+ \phi_n(\mathbf{r}_{m+1/2}) - \phi_n(\mathbf{r}_{m-1/2}), \end{aligned} \tag{6}$$

where $\mathbf{A}_n(\mathbf{r})$ and $\phi_n(\mathbf{r})$ denote $\mathbf{A}$ and ϕ values from n-th basis function at the observation point specified by $\mathbf{r}$, respectively, with

$$\mathbf{r}_{m-1/2} = \frac{\mathbf{r}_{m-1} + \mathbf{r}_m}{2} \quad , \quad \mathbf{r}_{m+1/2} = \frac{\mathbf{r}_m + \mathbf{r}_{m+1}}{2}. \tag{7}$$

The unknown current expansion coefficients constitute a column vector $\mathbf{I}_{N\times 1}$, and the elements of a column vector $\mathbf{V}_{N\times 1}$ representing the excitation are given by (m = 1, 2, …, N):

$$\begin{aligned} V_m = &\mathbf{E}^i(\mathbf{r}_{m-1/2})\cdot(\mathbf{r}_m - \mathbf{r}_{m-1/2}) \\ &+\mathbf{E}^i(\mathbf{r}_{m+1/2})\cdot(\mathbf{r}_{m+1/2} - \mathbf{r}_m). \end{aligned} \tag{8}$$

The complex valued dense impedance matrix $\mathbf{Z}$ is frequency, $f(=\omega/2\pi)$, dependent and, therefore, the matrix equation must be set up and then solved repeatedly for each individual frequency within a set of discrete frequencies of interest. The Equation (5) can be solved by standard methods of linear algebra. In this paper, only the LU decomposition is considered in GPU context, since the technique is widely used in MoM simulations.

B. Adaptive frequency sampling

An adaptive frequency sampling scheme employed in this study consists in performing repetitive bisection of each of initially chosen frequency intervals until a specified convergence criterion is met for the observable $H(f)$. The efficiency of sampling process is noticeably improved by way of interpolation of the quantity of interest by a rational function, $R(f)$, fitting the support point $\{f_i\,, H_i; i = 0, 1, 2, \cdots, N\}$. Such the function is defined as a quotient of polynomials $P_L(f)$ and $Q_M(f)$ of orders L and M, respectively, that is

$$R_{L,M}(f) = \frac{P_L(f)}{Q_M(f)} = \frac{\sum_{i=0}^{L} p_i f^i}{1 + \sum_{j=1}^{M} q_j f^j}, \tag{9}$$

where $L + M = N$. Instead of constructing $R_{L,M}$ explicitly, we employ in this study a recursive tabular algorithm developed by Stoer and Bulirsch, which generates implicitly the so-called diagonal rational interpolant [3]. A combination of SB algorithm with bisectional AFS results in the AFS-SB adaptive frequency sampling scheme. This latter is controlled by error

surrogates. To be precise, for the interval $[f_{i-1}, f_i]$, three approximate values for H: $\widehat{H}_m$, $\widehat{H}_m^+$ and $\widehat{H}_m^-$ are computed at the midpoint f_m from three rational fitting models $R_{L,M}$, $R_{L+1,M-1}$ and $R_{L-1,M+1}$, respectively. Then, the absolute values of relative errors between $\widehat{H}_m^+$ and $\widehat{H}_m$, and $\widehat{H}_m^-$ and $\widehat{H}_m$, respectively, are computed for the purpose of controlling the AFS-SB process. When one of the errors (or both of them) exceed(s) the assumed convergence tolerance, δ, a new sample H_m is computed at f_m via MoM, the number of support points for the rational fitting model is thus increased by one, and the bisection process continues until the convergence criterion is met.

C. GPU+CPU co-processing

As already mentioned in the introductory section, the GeForce GTX 680 CUDA-capable device has been used to accelerate the MoM solution process. The device has 4 GB of GDDR5 memory and 8 Kepler-based Streaming Multiprocessors (SMXs) comprised of 8×192 CUDA cores. Each SMX has access to 64 KB of on-chip memory configured as 48 KB of shared memory and 16 KB of L1 cache. The device has the capability to overlap kernel execution and data transfer between the device and host memory, offers fully IEEE-754 compliant single and double precision floating point operations, supports concurrent kernel execution, and employs a dynamic voltage and frequency scaling (DVFS) technique [10].

Solution of the integral equation via MoM involves two computationally intensive phases, i.e., assembling the system matrix $\boldsymbol{Z}$ and the solution of the linear system given by (5). Correspondingly, the CPU+GPU implementation of the MoM scheme has been divided into two relevant parts. The matrix assembly part is ported on the GPU device and handled by a highly optimized CUDA Fortran kernels [8]. To maximally exploit the compute capability of the device, blocks of 16×16 threads using 40 registers each are employed in computing the system matrix $\boldsymbol{Z}$. The SMX with 64 K register file accommodates six such blocks, resulting in thread capacity of 1536 threads in each SMX utilizing 61440 registers, that is, 94% of the register file.

For the solution of the linear system given by (5), the routine `cula_device_zgesv()` from a commercial library CULA Tools [11] is employed when the matrix $\boldsymbol{Z}$ fits into GPU memory. When the matrix is too big to reside in GPU memory, an out-of-core-like approach described in [12] is followed. In brief, the LU decomposition process of the $\boldsymbol{Z}$ matrix is divided into numerous tasks on top of blocks of its columns called panels. The panels are factorized on the CPU using a multi-core routine such as `zgetf2()` from the MKL library, while the trailing submatrices are updated on both the CPU and GPU with the use of highly optimized MKL/CUDA kernels. The pseudo-code for the proposed LU decomposition scheme is presented in Fig. 1. Note that four different CUDA streams are created to manage the computations (line 8). The initial data is assumed to be on the CPU, and when the GPU is executing the task, the data need to be copied from the host and sent back to be used for updating the impedance matrix. All data transfers are asynchronous, allowing the overlapping with kernel executions (line 16 and 19). To reduce CPU idle time, a concept known as a look-ahead is employed [13]. After performing LU factorization of the matrix, the backward substitution executed on the CPU yields a solution to the matrix equation (line 27).

Various aspects of GPU+CPU co-processing in solving dense linear algebra problems are discussed from general and CEM perspectives in [13, 14] and [15-17], respectively.

```
1.  ! Perform factorization and update panel size
2.  call set_size(nf0, nu1, nu2)
3.  nw = n  ! number of rows of the trailing submatrix
4.  ! Create CUDA streams and events to manage block LU
5.  ! decomposition and record the timings
6.  istat = cudaEventCreate()
7.  do i = 1, 4
8.   istat = cudaStreamCreate(nStream(i))
9.  end do
10. ! Update and factorize the impedance matrix
11. do while (i<n-n_d)
12.  call zgetf2(m-s*nf0/nw,nf0/nw)
13.  call ztrsm(nu1/nw, nu1/nw)
14.  call ztrsm(nb2,m-(i+1)*nu1/nw,nu1/nw)
15.  do i = 1, 4
16.   istat = cudaMemcpy2DAsync(d_cz(m1,n1), &
      (h_cz(n-s*nf0/nw,i+(i-1)*nu1/nw:i*nu1/nw),nStream(i))
17.   call cula_device_Ztrsm(n-s*nu2,nw,nu2/nw,nStream(i))
18.   call cula_device_Zgemm(n-(i+1)*nu2/nw), &
      n-(i+1)*nu2/nw,nu2/nw,nStream(i))
19.   istat = cudamemcpy2DAsync(h_cz(n-s*nf0/nw, &
      i+(i-1)*nu2/nw:i*nu2/nw),d_cz(m1,n1),nStream(i))
20.   istat = cudaStreamSynchronize()
21.  end do
22.  ! check the update order
23.  call upd_nw(nw) ! update nw
24.  i=i+incr(nw, nf0)
25. end do
26. ! Perform backward substitution
27. call zgetrs(h_cz,n,ipv,ci,n)
28. istat = cudaEventDestroy()
29. istat = cudaStreamDestroy()
```

Fig. 1. Pseudo-code for out-of-core-like LU decomposition of MoM matrix.

III. RESULTS

To demonstrate the efficiency of the proposed approach, a lightning protection system directly hit by lightning is considered. The LPS, serving as a building shielding structure from the lightning electromagnetic pulse (LEMP), is modeled by a grounded wire-mesh cage. A perfectly electrically conducting (PEC) ground plane is assumed and taken into account by the method of images. The dimensions of the building are (length × width × height) 10 m × 10 m × 50 m. The model is based on the type 3 grid-like large volume shield considered in

[6]. The shield is assumed to be made of perfectly conducting wires of radius 4 mm forming a square mesh of 0.5 m × 0.5 m (see Fig. 2 (a)). The lightning is assumed to strike a corner of the building. The lightning channel is represented by a vertical lossy monopole antenna of the height 2 km and radius 5 cm, loaded with the distributed inductance of 4.5 μH/m in series with the resistance of 1 Ω/m [18]. The monopole is fed at its base by a delta-gap unit-voltage generator. The entire structure including LPS and lightning channel is discretized into linear segments of 1 m in length. The total number of segments is 18710, and the number of unknowns (basis functions) associated with the structure is 27109.

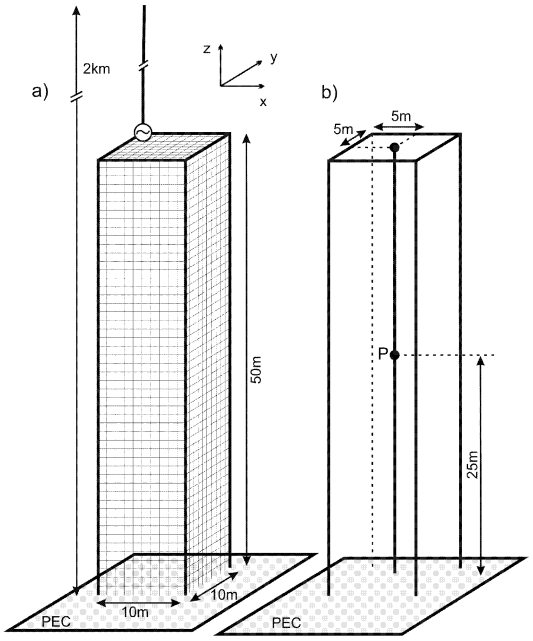

Fig. 2. Model of grid-like LPS with lightning channel and vertical wire located inside the protected volume.

As a numerical example, the electric field/current transmittance:

$$T_{E/I}(f) = |\mathbf{E}(f)|/\left|I_g(f)\right|, \tag{10}$$

where $\mathbf{E}(f)$ denotes the electric field intensity at the centre of the shielded volume ($x = 5\text{m}, y = 5\text{m}, z = 25\text{m}$) and I_g is the current at the channel base (i.e., at the feed-point of the equivalent monopole antenna) has been computed. The resulting frequency run of the transmittance in the range from 1 kHz to 20 MHz is shown in Fig. 3 in the linear and logarithmic scales. The empty circles represent data points (EM samples) generated by the AFS-SB/GPU algorithm outlined in Section II. As can be seen, the AFS-SB/GPU results compare very well with those derived from FEKO [19].

The computations of $T_{E/I}$ were performed for the frequency range from 1 kHz to 20001 kHz with the initial frequency step $\Delta f = 2$ MHz and the convergence tolerance $\delta = 0.01$. The AFS-SB algorithm generated totally 149 non-uniformly spaced frequency samples of $T_{E/I}$ with the frequency step locally decreased to 3.90625 kHz. To achieve the same convergence level with uniform sampling, 5121 samples taken with $\Delta f = 3.90625$ kHz would be required so that the AFS-SB algorithm offers about 34.4x reduction of the number of EM samples. Moreover, engaging GPU device in both phases of MoM solution, that is, assembling the system matrix $\boldsymbol{Z}$ and solving the system of linear Equations (5), accelerates computations by a factor of 6.7 for each frequency sample. The total wall-clock simulation time was 16 h 16 min, and the improvement in performance with a speedup ratio of about 34.4×6.7 = 230x was achieved compared to a reference single-thread sequential CPU implementation of the uniform sampling scheme. When a parallel four-core CPU OpenMP version of the code is taken as a reference, the above figure drops to about 64x.

The knowledge of voltages induced in electrical circuits inside a protected volume/building is crucial for the design of LPS. To mimic the situation of interest, a long vertical cylindrical wire of radius 0.89 mm was placed in the protected volume parallel to the down conductors of the LPS system and connected directly between midpoints of the roof and the floor coinciding with PEC ground (see Fig. 2 (b)). The wire was discretized into 100 0.5-m segments resulting in that the total number of basis functions associated with the considered structure increased to 27210. The task was to calculate the voltage/current transmittance defined as:

$$T_{U/I}(f) = \left|U(f)/I_g(f)\right|, \tag{11}$$

where U is the open-circuit voltage at point P located in the middle of the wire (see Fig. 2 (b)) and I_g denotes the current at the lightning channel base. Figure 4 shows the frequency run of the transmittance of interest in the range from 1 kHz to 20 MHz using a convention similar to that applied for $T_{E/I}$. Again, the AFS-SB/GPU results are in excellent agreement with the results derived from a commercial full-wave EM simulator FEKO [19]. This time the AFS-SB algorithm launched for the frequency range from 1 kHz to 20001 kHz with the initial Δf= 2 MHz and δ = 0.01 generated 70 non-uniformly spaced frequency samples of $T_{U/I}(f)$ with the frequency step locally refined to 31.25 kHz. This implies that 641 samples uniformly spaced at every 31.25 kHz would be required to achieve the same convergence level. Hence, the number of samples needed for reconstruction of $T_{U/I}(f)$ is reduced by a factor of about 9.2. The overall improvement in performance with a speedup ratio of about 17x was achieved compared to the four-core parallel OpenMP version of the code. The total wall-clock simulation time was 7 h 41 minutes.

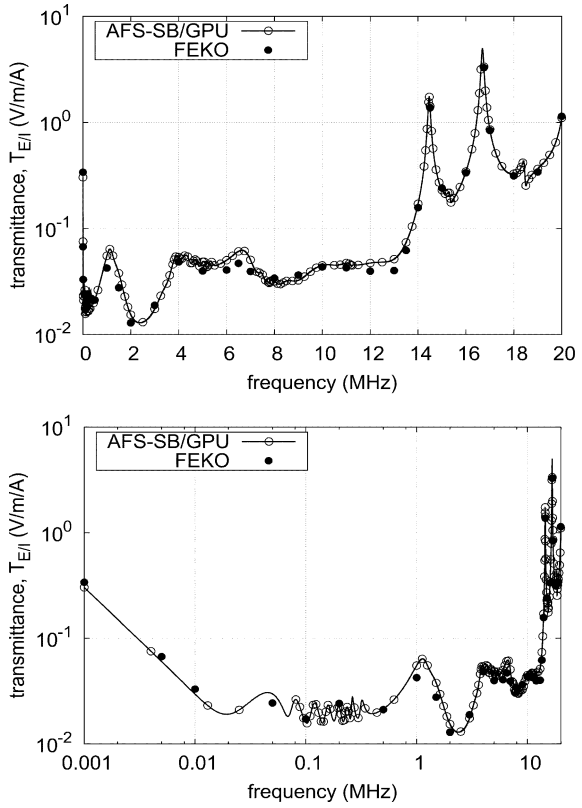

Fig. 3. Electric field/current transmittance $T_{E/I}$.

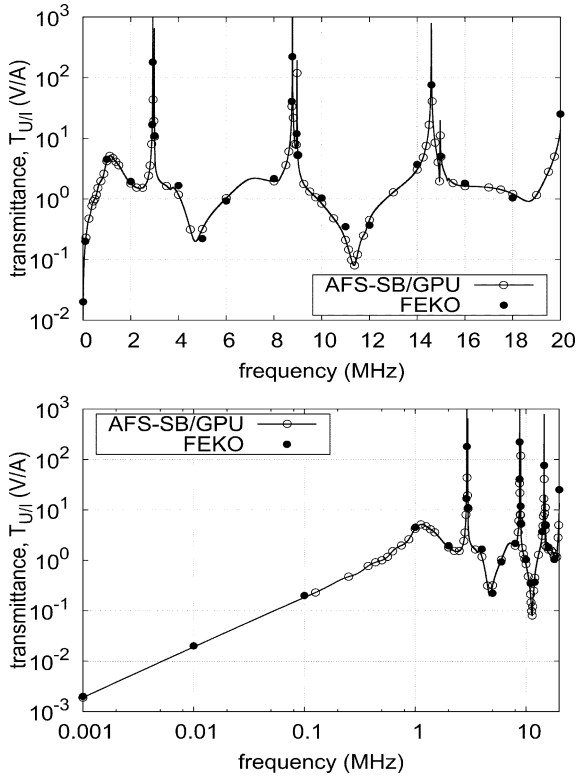

Fig. 4. Voltage/current transmittance $T_{U/I}$.

IV. CONCLUSION

The fast technique based on method of moments for wideband analysis of lightning protection systems is presented in the paper. Broadband capability of the technique is attained through supporting MoM by the dynamic adaptive frequency sampling employing the interval halving scheme backed by the recursive tabular Stoer-Bulirsch rational interpolation algorithm. The approach offers significant reduction in the number of EM samples needed for reconstruction of the response of the system. Further speedup of numerical MoM-based simulations is achieved by GPU hardware acceleration. In case of GeForce GTX 680 CUDA-capable device used in this study, the improvement in performance with a speedup ratio of about 6.7x for each frequency sample is reached compared to the single-thread sequential CPU implementation of the algorithm. Numerical examples for the grid-like LPS directly hit by lightning are presented to illustrate the usefulness and efficiency of the approach. From a broader perspective, the approach described in this paper represents an example of utilizing the potential for technical computing provided by CPU+GPU architectures of low-cost PC-based workstations.

ACKNOWLEDGMENT

This work was supported by the Ministry of Science and Higher Education Republic of Poland (decision no. 8686/E-367/S/2016).

REFERENCES

[1] R. F. Harrington, *Field Computation by Moment Methods*, MacMillan, New York, 1968.

[2] R. S. Adve, T. K. Sarkar, S. M. Rao, E. K. Miller, and D. R. Pflug, "Application of the Cauchy method for extrapolating/interpolating narrow-band system responses," *IEEE Trans. Microw. Theory Techn.*, vol. 45, pp. 837-845, May 1997.

[3] J. Stoer and R. Bulirsch, *Introduction to Numerical Analysis*, Springer-Verlag, New York, 1980.

[4] A. Karwowski, "Efficient wide-band interpolation of MoM-derived frequency responses using Stoer-Bulirsch algorithm," *IEEE Int. Symp. on Electromagn. Compat., EMC 2009*, Austin, TX, pp. 249-252, Aug. 2009.

[5] A. Karwowski and A. Noga, "Interpolating broadband shielding behavior of wire-grid cages from full-wave electromagnetic simulation," *Int. Symp. on Electromagn. Compat., EMC Europe 2012*, Rome, Sept. 2012.

[6] IEC 62305-4, Protection Against Lightning - Part 4: Electrical and electronic system within structures.

[7] A. Metwally and F. H. Heidler, "Reduction of lightning-induced magnetic fields and voltages inside struck double-layer grid-like shields," *IEEE Trans. Electromagn. Compat.*, vol. 50, no. 4, pp.

905-912, Nov. 2008.
[8] T. Topa, A. Karwowski, and A. Noga, "Using GPU with CUDA to accelerate MoM-based electromagnetic simulation of wire-grid models," *IEEE Antennas Wireless Propag. Lett.*, vol. 10, pp. 342-345, 2011.
[9] S. U. Hwu and D. R. Wilton, Electromagnetic Scattering and Radiation by Arbitrary Configurations of Conducting Bodies and Wires, Tech. Doc. 1325, AEL, Univ. of Houston, Aug. 1988.
[10] NVIDIA Corporation, *CUDA Programming Guide*, Santa Clara, 2014.
[11] EMPhotonics, *CULA Tools – GPU Accelerated LAPACK*, http://www.culatools.com/
[12] T. Topa, "Efficient out-of-GPU memory strategies for solving matrix equation generated by method of moments," *Elect. Lett.*, vol. 51, no. 19, pp 1542-1544, Sept. 2015.
[13] J. Kurzak, D. A. Bader, and J. Dongarra (Eds.), *Scientific Computing with Multicore and Accelerators*, CRC Press, Boca Raton, 2011.
[14] W. W. Hwu (Ed.), *GPU Computing Gems. Jade Edition*, Elsevier, 2012.
[15] M. J. Inman, A. Z. Elsherbeni, and C. J. Reddy, "CUDA based LU decomposition solvers for CEM applications," *ACES Journal*, vol. 25, no. 4, pp. 339-347, Apr. 2010.
[16] B. M. Kolundzija, M. S. Tasic, D. I. Olcan, D. P. Zoric, and S. M. Stevanetic, "Advanced techniques for efficient modeling of electrically large structures on desktop PCs," *ACES Journal*, vol. 27, no. 2, pp. 123-131, Feb. 2012.
[17] U. Jakobus, "Benefits and challenges of GPU accelerated electromagnetic solvers from a commercial point of view," *ACES Express Journal*, vol. 1, no. 4, pp. 117-120, Apr. 2016.
[18] S. Bonyadi-Ram, R. Moini, S. H. H. Sadeghi, and V. A. Rakov, "On representation of lightning return stroke as a lossy monopole antenna with inductive loading," *IEEE Trans. Electromagn. Compat.*, vol. 50, no. 1, pp. 118-127, Feb. 2008.
[19] https://www.feko.info/

Andrzej Karwowski received the Ph.D. and D.Sc. degrees in Electronic Engineering from the Wrocław University of Technology (WUT), Wrocław, Poland, in 1976 and 1984, respectively. Since 1987, he has been with the Faculty of Automatic Control, Electronics and Computer Science, Silesian University of Technology (SUT), Gliwice, Poland, where he now holds a position of a Professor. His professional interests are mainly in antennas, electromagnetic compatibility, transmission lines, passive microwave components with emphasis on development and application of relevant CEM methods and tools. He is a Senior Member of the IEEE and a Member of the IET. He was the Founder of the Polish IEEE EMC Society Chapter and its first Chairperson. From 2010 to 2015 he served the European EMC community as a Member of the International Steering Committee EMC Europe.

Artur Noga received the M.Sc. and Ph.D. degrees in Electrical Engineering from the Silesian University of Technology, Gliwice, Poland, in 2002 and 2007, respectively. His professional interests are primarily in computational electromagnetics with applications in the field of antennas and electromagnetic compatibility.

Tomasz Topa received the M.Sc. and Ph.D. degrees in Electrical Engineering from the Silesian University of Technology, Gliwice, Poland, in 2002 and 2007, respectively. His professional interests are primarily in numerical simulation of electromagnetic fields with particular emphasis on parallel computing, high-performance computing, CPU-GPU hybrid and cooperative computing and multicore computing.

Shape Reconstruction of Three Dimensional Conducting Objects Using Opposition-Based Differential Evolution

Mojtaba Maddahali [1], Ahad Tavakoli [1], and Mojtaba Dehmollaian [2]

[1] Department of Electrical Engineering
Amirkabir University of Technology, Tehran, 15875-4413, Iran
tavakoli@aut.ac.ir, maddahali@aut.ac.ir

[2] School of Electrical and Computer Engineering
University of Tehran, Tehran, 14395-515, Iran
m.dehmollaian@ece.ut.ac.ir

Abstract ─ In this paper, shape reconstruction of three dimensional conducting objects using radar cross section (RCS) of the scatterer and opposition-based differential evolution is investigated. The shape of the scatterer is modeled with nonuniform rational B-spline (NURBS) surfaces composed of more than one Bezier patches. NURBS are piecewise polynomial with unknown coefficients that are determined in the procedure of shape reconstruction. Opposition-based differential evolution (ODE) is then employed as an optimization tool to find the unknown coefficients. Physical optics approximation is used to predict RCS of the large conducting scatterer in various directions and at multiple frequencies. The effect of noise is also considered in the inverse process.

Index Terms ─ Inverse scattering, NURBS modeling, opposition-based differential evolution, physical optics approximation.

I. INTRODUCTION

The objective of inverse scattering methods is to discover features of an object by means of the electromagnetic (EM) scattered field. These methods have several applications such as nondestructive testing, biomedical imaging, and ground-penetrating radars. The complexity encountered in inverse scattering is mostly due to ill-posed and nonlinear problems. Mathematical algorithms of inverse scattering problems are mostly categorized into the time-domain or the frequency-domain solutions. The time-reversal method is an example of time-domain solutions [1]. Optimization methods are mostly utilized in widely used frequency-domain approaches. Optimization methods are commonly used for reconstruction of two dimensional conducting and dielectric objects [2-5]. In [2], the shape of the scatterer is modeled with the cubic B-spline curves. These curves are piecewise polynomial where their coefficients are determined by control points. The control points are found such that a specific measure of difference between reconstructed and original scattered fields is minimized. This approach could be generalized to three dimensional problems. In this case, the structure is modeled with non-uniform rational B-spline (NURBS) surfaces. NURBS are also piecewise polynomials where their coefficients are defined by a set of control points and associated weights. For computational purposes, NURBS surfaces are decomposed into Bezier surfaces. These surfaces are also piecewise polynomials. In [6], a NURBS surface composed of only one Bezier patch is considered and genetic algorithm (GA) is used to reconstruct the shape of a three dimensional conducting object.

Generally, NURBS surfaces have a complex geometry and are composed of more than one Bezier surface. This paper tries to reconstruct a more complex structure composed of more than one Bezier surface. The geometrical continuity of the surfaces complicates the reconstruction approach. The proposed algorithm is based on opposition-based differential evolution (ODE) as an optimization tool, because unlike GA, the ODE is simple to implement; it does not require coding and decoding of population members. In each iteration of the optimization algorithm, RCS of the reconstructed conducting body is calculated using physical optics (PO) approximation. The paper is organized as follow. Section II presents a brief review of NURBS modeling. Computation of PO integral is discussed in Section III. The inverse problem is discussed in Section IV. Some simulation results are presented in Section V. Concluding remarks are given in Section VI.

II. GEOMETRIC DESCRIPTION OF THE BODIES

In this paper, non-uniform rational B-spline surfaces are used for geometric modeling of the bodies.

Submitted On: January 26, 2016
Accepted On: July 24, 2016

The main reason for this choice is that a small amount of information is needed for accurate representation of complex objects. NURBS surfaces are specified with a set of control points, associated weights, and knot vectors. A NURBS surface is expanded as a set of Bezier patches. Geometrical parameter calculation of Bezier patches is easier than the NURBS surfaces. In the following, we discuss the concept of rational Bezier curves and then extend it to the three-dimensional surfaces. Rational Bezier curves could be formulated as follows [7]:

$$\vec{r}(u) = \frac{\sum_{i=0}^{m} w_i \vec{b}_i B_i^m(u)}{\sum_{i=0}^{m} w_i B_i^m(u)}, \quad (1)$$

where $\vec{b}_i \in R^3$, $i = 0,\ldots,m$, are the control points, $w_i \in R$, $i = 0,..,m$, are the associated weights, the integer m is the curve degree, and $B_i^m(u)$, $i = 0,\ldots,m$, are the Bernstein polynomials given by:

$$B_i^m(u) = \frac{m!}{i!(m-i)!} u^i (1-u)^{m-i}, 0 \le u \le 1, \quad (2)$$

u is a parameter between zero and one that shapes the curve. When these control points move through space on another Bezier curve, a Bezier surface is formed. The resultant surface could be formulated as follows:

$$\vec{r}(u,v) = \frac{\sum_{i=0}^{m}\sum_{j=0}^{n} w_{ij} \vec{b}_{ij} B_i^m(u) B_j^n(v)}{\sum_{i=0}^{m}\sum_{j=0}^{n} w_{ij} B_i^m(u) B_j^n(v) w_{ij}}, \quad (3)$$

where $\vec{b}_{ij} \in R^3$, $i = 0,\ldots,m$, $j = 0,\ldots,n$, are the control points, $w_{ij} \in R$, $i = 0,\ldots,m$, $j = 0,\ldots,n$, are the associated weights, and the integers *m* and *n* are degrees of the surface. Similar to *u*, *v* is a parameter between zero and one that shapes the other dimension of the surface. When a set of Bezier surfaces are connected by a specific continuity rule, a B-spline surface is formed. The resulting B-spline surface has an appealing property of local control ability [7]. A B-spline surface can be expanded as a linear combination of B-spline basis functions [9].

III. PHYSICAL OPTICS

When the dimensions of the conducting object are large compared to the wavelength, the backscattering electric field is specified by [9]:

$$\vec{E}_s(r) = -\frac{j}{\lambda}\frac{\exp^{-jk_0 r}}{r}(\hat{k}.\vec{I})\vec{E}_0, \vec{I} = \int n(r')\exp^{j2\vec{k}.\vec{r}'} ds', \quad (4)$$

where λ is the operating wavelength, $\vec{E}_0$ is the polarization of the incident field, $\hat{k}$ is the wave vector, $\vec{r}'$ is the position vector, ds' is the differential element of the surface, $\hat{n}$ is the normal vector at the surface point, k_0 is the wave number, and $\vec{I}$ is the physical optics integral. For a Bezier surface, $\vec{I}$ is written as follows:

$$\vec{I} = \int_{u=0}^{u=1}\int_{v=0}^{v=1} g(u,v)\exp[jkf(u,v)]dudv, \quad (5)$$

where

$$\vec{g}(u,v) = \vec{r}_u \times \vec{r}_v, \quad f(u,v) = 2\vec{k}.\vec{r}'(u,v). \quad (6)$$

Any surface can be formed with composition of three kinds of Bezier surfaces, (a) singly curved, (b) doubly curved, and (c) plane patch. PO integral can be evaluated for these kinds of surfaces as explained in continue.

A. Singly curved surfaces

When the degree of a Bezier surface is equal to one, then a singly curved surface is formed as shown in Fig. 1 (a). In other words, this surface is formed when a curve moves on a straight line in space. Suppose that the surface is linear along parameter *v*, then the phase term in PO integral can be written as follows:

$$f(u,v) = f_0(u) + vf_1(u) = 2\vec{k}.\vec{r}_0(u) + v2\vec{k}.\vec{r}_1(u), \quad (7)$$

thus, the PO integral is

$$\vec{I} = \int_{u=0}^{u=1}\exp[jkf_0(u)]\int_{v=0}^{v=1}\vec{g}(u,v)\exp[jkvf_1(u)]dudv. \quad (8)$$

Integration with respect to the parameter v can be computed by expanding $g(u,v)$ in Taylor series around $v_0 = 0.5$ and then calculating the integral of each term in the series analytically, then we have,

$$\vec{I} = \int_{u=0}^{u=1}\exp[jkf_0(u)]G(u), \quad (9)$$

where $G(u)$ is

$$G(u) = \sum_{n=0}^{n=N}\sum_{k=n}^{N}\frac{g^k(u,v_0)(v_0)^{k-n}}{(k-n)!n!}A_n(u), \quad (10)$$

and

$$A_n(u) = \int_{v=0}^{v=1} v^n \exp[jk(v)f_1(u)]dv = \frac{n!}{-jkf_1^{n+1}(u)} - \sum_{i=0}^{n}\frac{n!\exp[jkf_1(u)]}{(n-i)![-jkf_1(u)]^{i+1}}. \quad (11)$$

Integration with respect to the parameter u can be evaluated via a trapezoidal numerical method. In some references, this integral is computed with stationary phase method [8-10]; however our simulations show that numerical method is more accurate.

B. Doubly curved surfaces

When both degrees of a Bezier surface is greater than one, a doubly curved surface is formed as shown in Fig. 1 (b). In this case, currents near the certain critical points produce the main contribution of the scattered field. There are three kinds of critical points: stationary phase points, boundary points, and vertex

points as shown in Fig. 2. The phase term of the integrand is expanded in Taylor series around the critical points and then physical optics integral is easily calculated. This method is explained in [8-10].

C. Plane patches

When both degrees are equal to one, a plane patch is formed as shown in Fig. 1 (c). For plane patch, PO integral can be evaluated using Gordon method [11].

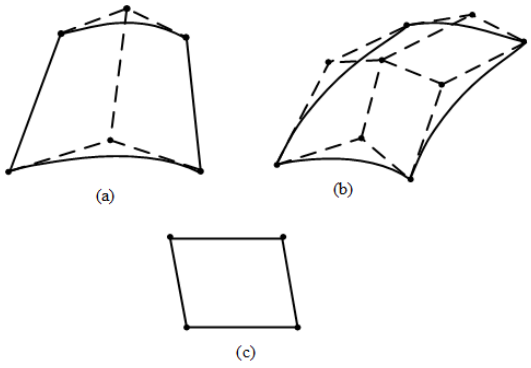

Fig. 1. Three kinds of Bezier surfaces and their control points: (a) singly curved surface, (b) doubly curved surface, and (c) plane patch [8].

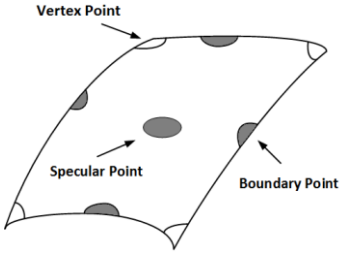

Fig. 2. critical points over the Bezier surface [5].

IV. INVERSE SCATTERING

In the inverse scattering procedure, the control points of the rational spline surface are optimally located such that the RCS of the reconstructed scatterer in multiple directions and at several frequencies approaches the RCS of the original scatterer. Here, the shape of the scatterer is approximated by a degree-n surface that is constructed by rational spline curves (Fig. 3). The shape of these curves and the distance between them are determined by an optimization algorithm. Therefore, arbitrary objects can be reconstructed. Compared to the reference [6], an exact algorithm for reconstruction is presented here, and some complex objects are rebuilt as well. In addition, in this case, other issues such as the effect of the shadowing of a surface by another surface, is taken into consideration by the authors while nothing is concerned in reference [6] regarding this effect.

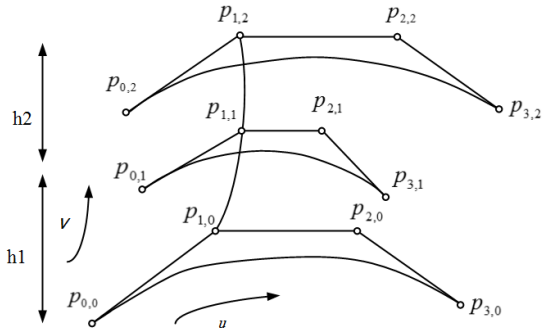

Fig. 3. Control points of the object.

A. Optimization algorithm

The opposition-based differential evolution is our optimization approach as follows. If the problem has D unknown parameters, then NP parameter vectors of D -dimension are produced in the first step [12]:

$$x_{i,j}, \qquad i = 1,....,NP. \tag{12}$$

Then, the opposite population is calculated by:

$$ox_{i,j} = a_j + b_j - x_{i,j}, \tag{13}$$

where a_j and b_j are the lower and upper bounds of the j^{th} dimension of the parameter vector respectively. If the cost function of $ox_{i,j}$ is lower than $x_{i,j}$, then $x_{i,j}$ is replaced by $ox_{i,j}$. According to probability principles, this happens 50% of the time. In the second step, a mutant vector is produced for each target vector as:

$$v_i^{G+1} = x_{r1}^G + F.(x_{r2}^G - x_{r3}^G), \tag{14}$$

where G is the generation index and r_1, r_2, r_3 are three mutually different integers that also differ from target index i. F is also the mutuant constant that is usually taken to be 0.8. Next, from the combination of the mutant vector and the target vector, the trial vector is produced:

$$u_i^{G+1} = (u_{1i}^{G+1}, u_{2i}^{G+1}, ..., u_{Di}^{G+1}), \tag{15}$$

where

$$u_{ji,G+1} = \begin{cases} v_{ji}^{G+1} & if \quad h_j \leqslant H \quad or \quad j = l \\ x_{ji}^{G+1} & if \quad h_j > H \quad and \quad j \neq l \end{cases}. \tag{16}$$

In this equation, h_j is a random number in the interval $[0,1]$, $H \varepsilon (0,1)$ is a crossover constant selected by the user, and l is a random integer $\in [1,2,...,D]$. If the cost function of u_i^{G+1} is smaller than x_i^{G+1}, then x_i^{G+1} is replaced by the trial vector. Similarly, opposite of the current population is generated by:

$$ox_{i,j}^G = MIN_j^G + MAX_j^G - x_{i,j}^G, \tag{17}$$

where MIN_j^G and MAX_j^G are the minimum and maximum of j^{th} dimension in the current population. Now, a random number between $[0,1]$ is generated and

if it is lower than the preselected jumping rate J_r, then $x_{i,j}^G$ is compared with $ox_{i,j}^G$ and the one with a lower cost function is selected as the member of the current population. Here, the selected parameters of the opposition-based differential evolution are listed in Table 1.

B. RCS based cost function

The cost function for this optimization is defined as:

$$f(p) = \frac{\sum_{\omega}\sum_{\theta}\sum_{\phi} |\sigma_{\theta\phi\omega}^{true} - \sigma_{\theta\phi\omega}^{rec}|}{\sum_{\omega}\sum_{\theta}\sum_{\phi} |\sigma_{\theta\phi\omega}^{true}|}, \quad (18)$$

where $\sigma_{\theta\phi\omega}^{true}$ and $\sigma_{\theta\phi\omega}^{rec}$ are radar-cross sections of the original and the reconstructed scatterer respectively. The cost function is minimized to find the location of control points, p and the distance between curves. For considering the noise effect, the original RCS is modified as follows [6]:

$$\sigma_{\theta,\phi,\omega}^{n} = \sigma_{\theta,\phi,\omega} + \sqrt{\sigma_{\theta,\phi,\omega}^{2}} \times (NL) \times (rand). \quad (19)$$

In this equation, $\sqrt{\sigma_{\theta,\phi,\omega}^{2}}$ is the rms of the original RCS, *NL* is the noise level, and *rand* is a random number picked from the interval $[0,1]$. In this paper, the radar cross section of the scatterer is used in the cost function, so that the phase of the scattered field is not taken into account, and the transmission of the object is obtained.

V. NUMERICAL RESULTS

For the first example, the reconstruction of perfectly conducting cone modeled with one NURBS surface composed of three Bezier surfaces is presented. The cone has the height of 1m and the bottom radius of 1m and the top radius of 0.5m as shown in Fig. 4 (a). In the reconstruction procedure, the degree of the surface and weight coefficients are selected a-priori. In addition, we assume that the curvature of the surface is negative. It should be noted that the weight of control points and the degree of surface can also be considered as the optimization parameters; however, in this state, the volume of computations is enormous and it is not considered here as just a generalized method for complex structures was aimed. This cone is modeled with 6x2 control points. The scattered filed is evaluated at 45 points that are uniformly located around the object at $\theta = 60^{\circ}, 75^{\circ}, 90^{\circ}$ and at frequencies of $0.4, 0.8, 1.2\,GHz$. Figure 4 (b) displays the reconstructed cone. The average cost function for five simulations as a function of number of iterations are depicted in Fig. 4 (c). The RCS of the original and the reconstructed cones are presented in Fig. 4 (d). A very good agreement between the original cone and the reconstructed cone is observed.

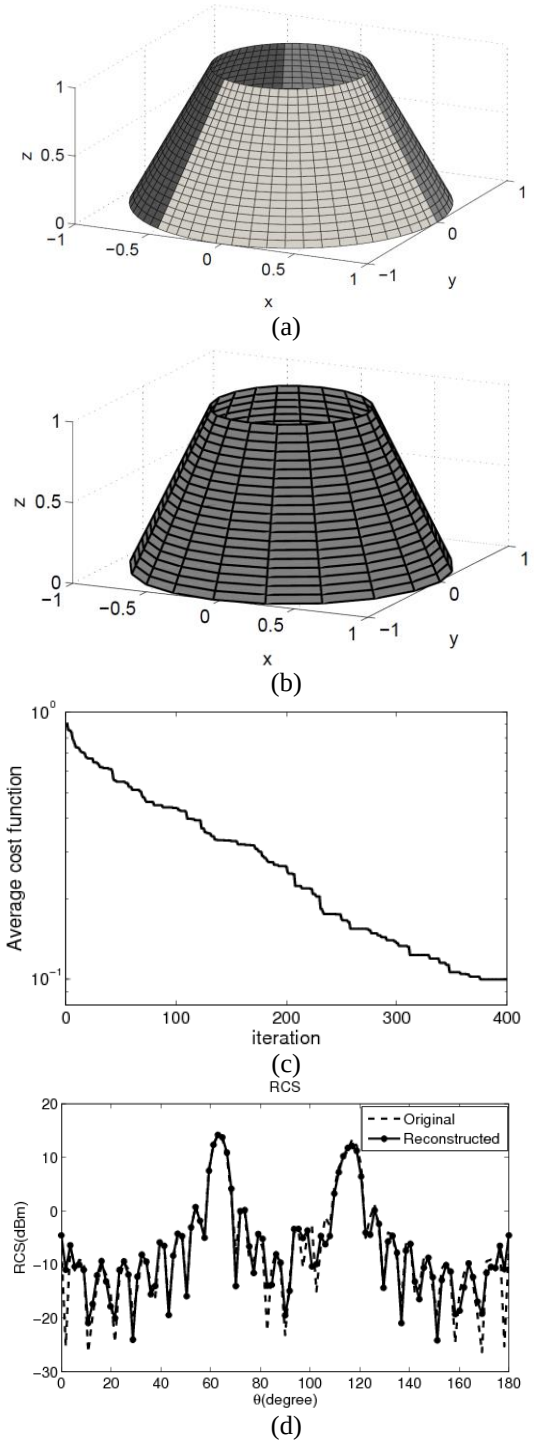

Fig. 4. (a) Original half cone, (b) reconstructed half cone, (c) average cost function, and (d) radar cross section of the original and the reconstructed cone at $f = 1.2\,GHz$ and $\phi = \pi/4$.

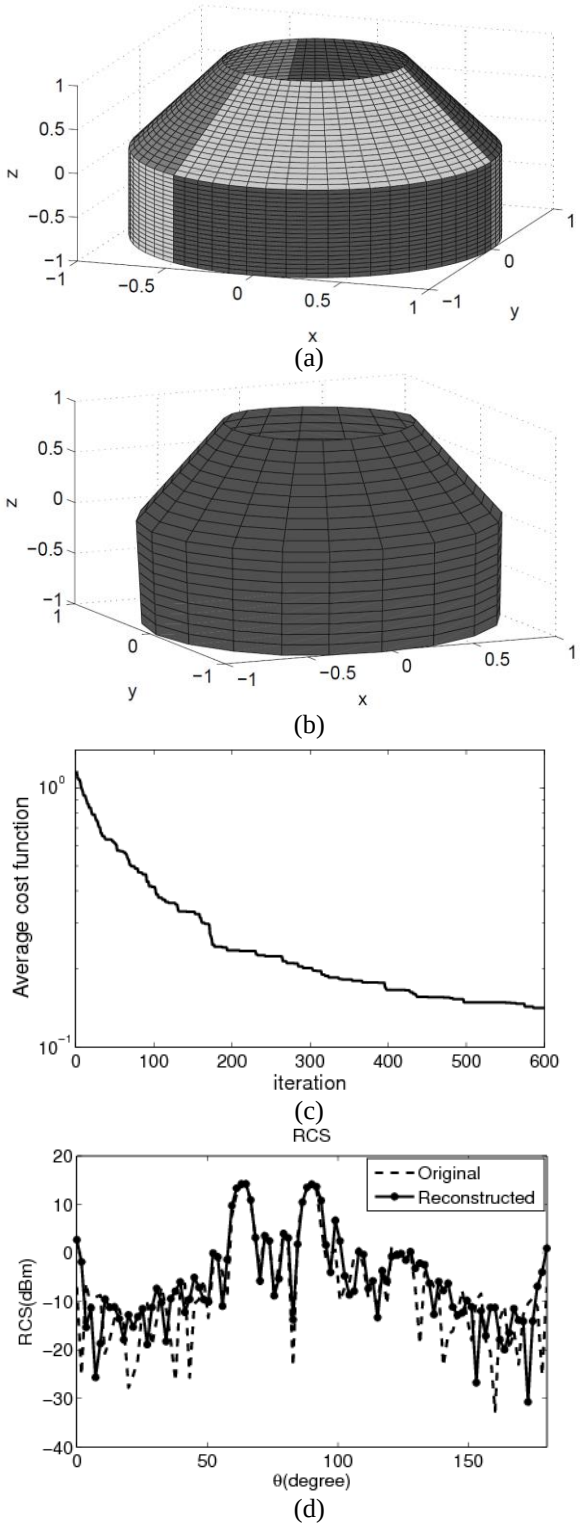

Fig. 5. (a) Original cone cylinder, (b) reconstructed cone cylinder, (c) average cost function, and (d) radar cross section of the original and the reconstructed cone-cylinder at $f = 1.2GHz$ and $\phi = \pi/4$.

Table 1: Opposition-based differential evolution parameters

Jumping Rate	Mutant Constant	Crossover Rate
0.5	0.8	0.5

To evaluate the accuracy of the reconstruction procedure, a shape error is defined as follow [6]:

$$RECP = \frac{1}{N_{vnet}}\left(\sum_{i=0}^{m}\sum_{j=0}^{n}\frac{\| \Delta^{0,1} p_{i,j}^{true} - \Delta^{0,1} p_{i,j}^{reco} \|^2}{\| \Delta^{0,1} p_{i,j}^{true} \|^2} + \frac{\| \Delta^{1,0} p_{i,j}^{true} - \Delta^{1,0} p_{i,j}^{reco} \|^2}{\| \Delta^{1,0} p_{i,j}^{true} \|^2}\right)^{1/2}, \quad (20)$$

where $N_{vnet} = 2mn + m + n$ is the number of elements in the vector net and $\| p_{i,j} \|$ is the Euclidean norm given by:

$$\| p_{i,j} \| = \sqrt{x_{i,j}^2 + y_{i,j}^2 + z_{i,j}^2}. \quad (21)$$

$\Delta^{0,1} p_{i,j}$ and $\Delta^{1,0} p_{i,j}$ are related to the control points as:

$$\Delta^{0,1} p_{i,j} = p_{i,j+1} - p_{i,j} \quad \Delta^{1,0} p_{i,j} = p_{i+1,j} - p_{i,j}. \quad (22)$$

In the simulation, the shape error for a half cone is calculated to be 0.04423. In the presence of a noise level of 10%, the shape error is 0.04725. For the second example, the reconstruction of perfectly conducting cone-cylinder modeled with one NURBS surface composed of six Bezier surfaces is presented. The cone-cylinder has the height of 1m for both the cone and the cylinder and radius of 1m at the bottom and 0.5m at the top. Similar to the previous example, Fig. 5 shows the target and the simulation results. Here, the shape error for cone-cylinder is calculated to be 0.071. In the presence of a noise level of 10%, the shape error is 0.1527. In the following, we can consider this issue for the reconstruction of buried objects by taking into account the effect of a background layer.

VI. CONCLUSION

In this paper, the PO approximation, the ODE algorithm, and NURBS modeling are used to reconstruct three-dimensional conducting objects. NURBS surface are used to model unknown scatterers by a minimum number of parameters. The reconstruction is done by applying the ODE algorithm as an optimization tool. Here, NURBS surfaces composed of more than one Bezier surface is reconstructed. A very good agreement between the original object and the reconstructed object is achieved.

REFERENCES

[1] P. Kosmas and C. M. Rappaport, "Time reversal with the fdtd method for microwave breast cancer detection," *IEEE Transactions on Microwave Theory and Techniques*, vol. 53, no. 7, pp. 2317-

2323, July 2005.
[2] I. T. Rekanos, "Shape reconstruction of a perfectly conducting scatterer using differential evolution and particle swarm optimization," *IEEE Trans. Geosci. Remote Sens.*, vol. 46, no. 7, pp. 1967-1974, July 2008.
[3] A. Semnani, I. T. Rekanos, M. Kamyab, and M. Moghaddam, "Solving inverse scattering problems based on truncated cosine fourier and cubic b-spline expansions," *IEEE Trans. Antennas Propagat.*, vol. 60, no. 12, pp. 5914-5923, 2012.
[4] C.-C. Chiu and R.-H. Yang, "Inverse scattering of biaxial cylinders," *Microwave and Optical Technology Letters*, vol. 9, no. 5, pp. 292-302, 1995.
[5] I. T Rekanos, "On-line inverse scattering of conducting cylinders using radial basis-function neural networks," *Microwave and Optical Technology Letters*, vol. 28, no. 6, pp. 378-380, 2001.
[6] A. Saeedfar and K. Barkeshli, "Shape reconstruction of three-dimensional conducting curved plates using physical optics, nurbs modeling, and genetic algorithm," *IEEE Trans. Antennas Propagat.*, vol. 54, no. 9, pp. 2497-2507, Sept. 2006.
[7] G. E. Farin, *Curves and Surfaces for Computer-Aided Geometric Design: A Practical Guide*. Number v. 1 in Computer Science and Scientific Computing. Academic Press, 1997.
[8] J. Perez and M. F. Catedra, "Application of physical optics to the rcs computation of bodies modeled with nurbs surfaces," *IEEE Trans. Antennas Propagat.*, vol. 42, no. 10, pp. 1404-1411, Oct. 1994.
[9] F. S. de Adana and O. Gutierrez, *Practical Applications of Asymptotic Techniques in Electromagnetics*. Artech House Electromagnetic Analysis Series. Artech House, 2010.
[10] F. S. de Adana, I. G. Diego, O. G. Blanco, P. Lozano, and M. F. Catedra, "Method based on physical optics for the computation of the radar cross section including diffraction and double effects of metallic and absorbing bodies modeled with parametric surfaces," *IEEE Trans. Antennas Propagat.*, vol. 52, no. 12, pp. 3295-3303, Dec. 2004.
[11] W. Gordon, "Far-field approximations to the kirchoff-Helmholtz representations of scattered fields," *IEEE Trans. Antennas Propagat.*, vol. 23, no. 4, pp. 590-592, July 1975.
[12] S. Rahnamayan, H. R. Tizhoosh, and M. M. A. Salama, "Opposition-based differential evolution," *IEEE Transactions on Evolutionary Computation*, vol. 12, no. 1, pp. 64-79, Feb. 2008.

Mojtaba Maddah-ali was born in Isfahan, Iran, on December 5, 1987. He received B.Sc. degree in Electrical Engineering from Isfahan University of technology, Isfahan, Iran, in 2009, the M.Sc. degrees from the Amirkabir University of Technology, Tehran, Iran, in Electrical Engineering, in, 2013.

Ahad Tavakoli was born in Tehran, Iran, on March 8, 1959. He received the B.S. and M.S. degrees from the University of Kansas, Lawrence, and the Ph.D. degree from the University of Michigan, Ann Arbor, all in Electrical Engineering, in 1982, 1984, and 1991, respectively.

He is currently a Professor in the Department of Electrical Engineering at Amirkabir University of Technology.

Mojtaba Dehmollaian was born in Iran in 1978. He received the B.S. and M.S. degrees in Electrical Engineering from the University of Tehran, Tehran, Iran, in 2000 and 2002, respectively. He received the M.S. degree in Applied Mathematics and Ph.D. degree in Electrical Engineering from the University of Michigan, Ann Arbor, in 2007. Currently, he is an Assistant Professor with the Department of Electrical and Computer Engineering, University of Tehran.